NUMERICAL AND ASYMPTOTIC APPROACHES TO BOUNDARY-LAYER RECEPTIVITY AND TRANSITION

A thesis

submitted to the School of Mathematics

of the University of East Anglia

in fulfilment of the requirements

for the degree of

Doctor of Philosophy

By

Matthew Ray Turner

November 2005

Abstract

We consider the interaction of a uniformly pulsating free-stream with the leading edge of a body, and consider its effect on transition. The free-stream is assumed to be incompressible, high Reynolds number flow parallel to the chord of the body, with a small, unsteady, perturbation of a single harmonic frequency. We present a method which calculates Tollmien-Schlichting (T-S) wave amplitudes downstream of the leading edge, by a combination of an asymptotic receptivity approach in the leading edge region and a numerical method which marches through the Orr-Sommerfeld region. The asymptotic receptivity analysis produces a three deck eigenmode which, in its far downstream limiting form, produces an upstream initial condition for our numerical Parabolized Stability Equation (PSE).

Downstream T-S wave amplitudes are calculated for the flat plate, and good comparisons are found with the Orr-Sommerfeld asymptotics available in this region. The importance of the $O(Re^{-\frac{1}{2}})$ term of the asymptotics is discussed, and, due to the complexity in calculating this term, we show the importance of numerical methods in the Orr-Sommerfeld region to give accurate results.

We also discuss the initial transients present for certain parameter ranges, and show that their presence appears to be due to the existence of higher T-S modes in the initial upstream boundary condition.

Extensions of the receptivity/PSE method to the parabola and the Rankine body are considered, and a drop in T-S wave amplitudes at lower branch is observed for both bodies, as the nose radius increases. The only exception to this trend occurs for the Rankine body at very large Reynolds numbers, which are not accessible in experiments, where a double maximum of the T-S wave amplitude at lower branch is observed.

The extension of the receptivity/PSE method to experimentally realistic bodies is also considered, by using slender body theory to model the inviscid flow around a modified super ellipse to compare with numerical studies.

Acknowledgements

The production of this thesis relied on a number of people either directly, through comments made, or indirectly, through support given.

I would like to thank all my family for their encouragement and especially for their words of wisdom such as ‘What do you actually do?’ and ‘How do you research Maths?’. I offer a big thank you to all my friends in the department who make up the eating out, Friday football, drinking and pitch and putt clubs, without whom I would have had many a dull summers afternoon working rather than being out on the golf course. These include Mark Blyth, Mark Cooker, Nigel Scott, Jean-Marc Vanden-Broeck, Richard Purvis, Graham Everest, Scott Grandison, Emilian Parau, Helene Gleeson and Peter Hicks. A special thank you must go to Helen King, because without her friendship and support, my PhD would have been much harder, and nowhere near as much fun.

But most of all I would like to thank my supervisor, Paul Hammerton. Paul has always been there for every problem and mini crisis, as well as being there as a good friend. Without his help this thesis would not be what it is, and I would not be heading in the direction that I am, so I thank you very much.

Contents

List of Tables

List of Figures

Chapter 1

Introduction

The solutions to the Navier-Stokes equations, are in general smooth or laminar, up to some critical value of the Reynolds number, Re_c, above which the flow becomes unstable, and the flow is then irregular or turbulent after this value. The instability occurs in the fluid due to the growth of initially small perturbations of the mean flow and the resulting turbulent flow leads to strong mixing of the fluid. Solutions to problems such as shear layers and boundary-layers generally satisfy the above rule, however the stability criterion of these flows also depends upon other features of the flow such as the frequency or wavenumber of the perturbation. The change from laminar flow to turbulent flow is know as 'transition', and is of great importance in the subject of fluid dynamics.

The process of transition was first noted by Reynolds (1883), who conducted experiments on liquid flow down a glass pipe. Reynolds set up the experiments so that water was drawn through the tube out of a large glass tank, in which the tube was immersed, and it was conducted so that a streak or streaks of coloured water entered the tube with the clear water. He also fitted a funnel at the entrance to the pipe so that the water entered with the smallest possible disturbance. Reynolds noted three main results from his experiments:

(i) When the fluid velocity was sufficiently small, the streak of coloured fluid extended right the way along the pipe.

(ii) If the water in the tank had not quite come to rest, then for low velocities, the coloured streak would move about in the tube, but would do so without any regularity.

(iii) As the velocity of the fluid down the tube was increased in small increments, at some point far down the tube, the coloured streak would suddenly mix up with the surrounding water, and fill the whole pipe downstream of this point with coloured dye. Once this had occurred, if the velocity of the fluid was increased further, then the point at which the mixing occurred would move towards the inlet point of the pipe, however the mixing point never reached the inlet for any velocities tried. When the tube was lit with an electric spark, the region of mixed water was seen to contain vortices and eddies.

Reynolds went on to show experimentally that the pipe flow breaks down beyond a critical value of the dimensionless number, defined by

$$Re = \frac{Ud}{\nu},$$

where U is the velocity down the pipe, d is the diameter of the pipe, and ν is the kinematic viscosity of water. This dimensionless number is the 'Reynolds number', as mentioned earlier.

One area of fluid dynamics where the understanding of transition is very important is boundary-layer theory. For example a boundary-layer is formed next to a rigid impermeable boundary when a large Reynolds number flow acts parallel to the boundary. The boundary-layer is defined by where, the velocity of the fluid is reduced from the tangential slip velocity of the inviscid free-stream, to zero at the boundary. The flow within the boundary-layer can also undergo transition. There are two forms of boundary-layer transition, the first is when the mean flow contains small unsteady disturbances which grow within the boundary-layer, until transition occurs. The second is when the disturbances are so large, that nonlinear interactions become important, and the flow breaks down faster. This is known as bypass. The transition point in a boundary-layer can be detected by a sudden growth in the boundary-layer, and this point is strongly dependent on the unsteady nature of the free-stream disturbances. Other factors which affect the position of transition include the addition of an external pressure gradient, the surface of the body, i.e. surface roughness and curvature, and the angle of attack of the body to the free-stream (Reshotko, 1976). The importance of the transition point usually depends on

the type of problem being solved. For example, sometimes early transition is required, as this delays boundary-layer separation, and reduces the drag on a body, such as a golf ball. Other times it is desirable to delay transition, so that laminar flow occurs along the whole length of the body, as is desirable for an airfoil.

For the first kind of boundary-layer transition, where the disturbance in the free-stream is small, the process of transition can be split into three stages of theory. The first stage is the development of instability waves by a transfer of energy from the external disturbance, known as **receptivity** (Morkovin, 1969). The second stage is related to the slow linear growth of the instability wave, known as **stability theory**. Mathematically this stage is an eigenvalue problem, and the solution to this problem are know as Tollmien-Schlichting waves (T-S waves). Only one of these waves grows as we move downstream, the rest decay, and it is the one growing wave which is important in boundary-layer transition, because it is this wave which eventually leads to turbulence. The third and final stage is the nonlinear breakdown of these instability waves. The second and third stages will be discussed in more detail later, but for now we concentrate our attention on the first stage, receptivity.

1.1 Receptivity theory

Here we consider only receptivity of the first kind, where the external free-stream disturbance is assumed to be small. In this region of the flow, the mathematical problem is an initial value problem (IVP), and hence any numerical solution requires an initial condition to march though this region. There are two types of receptivity:

(i) Forced receptivity - is when the disturbance is introduced locally into the boundary-layer, by means of a vibrating ribbon, wall suction/blowing or by heating the boundary.

(ii) Natural receptivity - is when the disturbance source is located far from the boundary-layer, such as acoustic waves within the free-stream.

For the case of forced receptivity, the wavelength of the induced disturbance is matched

to that of the T-S wave, so that the T-S wave can be excited immediately, and then the problem can be considered as a stability problem. In the natural receptivity problem however, the external disturbance usually has a much longer wavelength than the T-S wave, hence a wavelength shortening mechanism is required so that the external disturbance can transfer energy and excite the shorter wavelength T-S wave.

The wavelength shortening process of natural receptivity is often associated with areas where the non-parallel effects of the mean base flow are important. These exist where there are rapid changes in the streamwise variation of the boundary-layer, or where there are rapid changes in the surface boundary conditions, which produce diffracted disturbances. Rapid variations in the mean flow occur at a leading edge, where the boundary-layer is thin and grows rapidly (Goldstein, 1983 and Hammerton and Kerschen, 1996), or at a point further downstream, where the boundary-layer is forced to make a sudden adjustment due to the presence of a surface roughness element (Goldstein and Hultgren, 1989). Other mechanisms which can produce rapid streamwise changes to the boundary-layer needed for wavelength conversion are, any discontinuities in surface curvature and the angle the body makes to the mean flow, which produces an area of low wall shear, where the boundary-layer is close to separation. All of the above mechanisms invalidate the assumption that the boundary-layer is parallel to the surface of the body, and hence the equation governing stability calculations becomes invalid. In places where the boundary-layer is thin and rapidly growing, the unsteady boundary-layer equation becomes the correct approximation to the Navier-Stokes equations over the whole region. In areas of sudden changes to the boundary's surface or boundary conditions, the flow is governed by a triple-deck solution, where, in a small region centered on the variation, the unsteady boundary-layer equation is the correct approximation to the Navier-Stokes equations in the lower deck.

Overall reviews of the receptivity topic have been provided by Reshotko (1976), Goldstein and Hultgren (1989) and Saric *et al.* (2002). Nishioka and Morkovin (1986) reviewed the process of boundary-layer receptivity to unsteady pressure gradients including Soviet experiments and views on receptivity. Kachanov (1994) reviewed the physical

mechanisms of laminar boundary-layer transition.

The main receptivity mechanism of interest to us in this work is that of leading edge receptivity. However, a brief overview of two of the other mechanisms are given before we concentrate on leading edge receptivity.

1.1.1 Streamwise variations in surface geometry

Goldstein (1985), Goldstein and Hultgren (1987) and Bodonyi *et al.* (1989) showed that small streamwise variations in the surface geometry far downstream of the leading edge are mechanisms for receptivity. Goldstein (1985) considered changes in the surface slope, and introduced a turning angle of $O(Re^{-\frac{1}{4}})$, which is the downward angle the surface makes with the horizontal part of the surface, at the point at which the curvature changes. Goldstein and Hultgren (1987) considered a discontinuity in curvature of the surface, over a vertical height of $O(Re^{-\frac{5}{8}}l)$, where the Reynolds number, which is assumed to be large, is defined in terms of l, which is the distance between the leading edge and the discontinuity. Both these methods were assumed to act over a streamwise length scale of $O(Re^{-\frac{3}{8}}l)$, which is of the same order of magnitude as the T-S wave's wavelength. The disturbance wave was taken to be an acoustic wave with frequency of $O(Re^{\frac{1}{4}}U/l)$, which corresponds to the T-S wave frequency at the lower branch neutral stability point (the point at which the T-S wave starts to grow). The flow in the vicinity of the surface variations has a triple-deck structure, as in Smith (1979), where the bottom deck is governed by the unsteady boundary-layer equation. The influence of the variation in surface geometry acts so as to 'scatter' the long wavelength acoustic waves into the shorter wavelength T-S waves which are of similar magnitude to the initial acoustic wave. The fact that these T-S waves occur closer to the neutral stability point means that they have less time to decay (than T-S waves generated at the leading edge) before they start to grow. Hence they are important to the overall receptivity problem when combined with the leading edge problem. Goldstein and Hultgren (1987) define the coupling effect as a measure of the size of the resulting T-S wave. For a $6:1$ aspect ratio ellipse (ratio of the major to the minor axis) stuck onto a flat plate, considered in the experiments of Shapiro (1977)

and Leehey and Shapiro (1980), Goldstein and Hultgren found that this coupling effect due to the discontinuity in curvature is of $O(Re^{-\frac{1}{8}}\sigma)$ where σ is the thickness ratio of the ellipse ($\sigma = \frac{1}{6}$ for the Shapiro body). In comparison to this, the coupling coefficient due to the leading edge receptivity is of $O(Re^{\frac{\tau}{4}})$, where $\tau = -0.6921$. Hence the weak static pressure gradients set up by the small streamwise fluctuations in surface geometry, produce a large coupling effect at lower branch, and this is in fact larger than the effect due to the leading edge, when the respective damping factors are also taken into consideration. The asymptotic analysis of this localized receptivity region is also supplemented by a numerical 'finite-Reynolds-number-approach' (Choudhari and Streett, 1992 and Crouch, 1992).

1.1.2 Regions of marginal separation

Goldstein *et al.* (1992) considered a relatively thin two-dimensional body at an angle of attack to the free-stream. The angle of attack was assumed to be close to the critical angle where boundary-layer separation occurs along the upper surface of the body, so that the minimum of the non-dimensional wall shear is of $O(Re^{-\frac{1}{5}})$, where the Reynolds number is based on the distance, l, from the leading edge to the point of minimum wall shear. The flow has a triple-deck structure on a length scale of $O(Re^{-\frac{1}{5}}l)$, centered on the minimum wall shear, but the individual layer thicknesses are different from traditional triple-deck theory. Stewartson *et al.* (1982) named the flow on this length scale, 'marginal separation', where the wall shear is almost zero but immediately recovers to an $O(1)$ value downstream. Fully unsteady, triple-deck, interaction occurs when the frequency of the disturbance is of $O(Re^{\frac{1}{7}}U/l)$. Initially the disturbance amplitude is exponentially small compared with the free-stream amplitude, but it rapidly grows in the triple-deck region. However, the solution in the triple-deck region does not match directly onto the T-S wave, and there is a region of $O(Re^{-\frac{1}{14}}l)$, where the disturbance's wavelength grows with x, where x is the coordinate measured along the body from the leading edge. Finally, there is a streamwise outer region of $O(l)$, where the disturbance evolves into eigenmodes similar to the Lam-Rott eigenmodes, which will be discussed in more detail in §1.1.3.

These eigenmodes have a wavelength which decays like $x^{-\frac{1}{2}}$, which is the required decay rate to match onto the T-S waves in the stability region.

Experiments have shown that the transition Reynolds number is strongly dependent on the angle of attack of the body. The angle of attack has little effect on the pressure gradients at the lower branch point, however it makes steep pressure gradients at the leading edge (Polykov, 1973a, Polykov, 1973b and Vorob'Yev *et al.*, 1976). Goldstein *et al.* (1992) suggest that this is because marginal separation has occurred.

1.1.3 Leading-edge receptivity

As was mentioned earlier, we primarily concentrate on the receptivity occurring at the leading-edge for this work, where the rapidly growing boundary-layer produces the relevant change in energy from the unsteady free-stream to the short wavelength T-S waves. It was the pioneering theoretical work of Goldstein (1983) which first discovered the physical mechanism behind the wavelength shortening procedure which leads to receptivity at the leading edge. Goldstein considered the interaction of small disturbances in the free-stream acting on the boundary-layer on an infinitely thin, semi-infinite flat plate. The mean flow was considered to be two-dimensional, incompressible, and with a large Reynolds number, $Re = U_\infty^2/\nu\omega$, where U_∞ is the free-stream velocity, and ω is the frequency of the free-stream. The free-stream disturbance is assumed to be small compared to the free-stream, and to have frequency ω. This means that the unsteady flow can be considered as a linear perturbation of the free-stream, with the a single harmonic frequency.

Close to the nose of the plate, the unsteady boundary-layer flow is governed by the linearized unsteady boundary-layer equation (LUBLE). This problem was first studied by Lighthill (1954), who derived solutions to the LUBLE both close to, and far from the leading-edge. He then went on to connect these two solutions by means of a Kármán-Pohlhausen method. Lam and Rott (1960) and Ackerberg and Phillips (1972) re-derived Lighthill's results, and demonstrated that the far downstream form of the solution develops a two layer structure, where the inner wall layer is a Stokes shear-wave type of flow,

to lowest order, and the upper layer is a modified Blasius solution. Lam and Rott (1960) point out from their analytical work that the Stokes-type solution is not complete, as it is uniquely determined independently of the upstream condition, which is imposed for the solution of a parabolic partial differential equation. This lead Lam and Rott to conclude that the far downstream form of the LUBLE must consist of a Stokes-type solution, and an infinite sum of asymptotic eigenmodes. Lam and Rott (1960) went on to construct such a family of eigenmodes, which decay exponentially fast as we move down the plate. Ackerberg and Phillips (1972) obtained equivalent expressions for these eigenmodes by the use of separation of variables and matched asymptotic expansions. These Lam-Rott eigenmodes are inversely ordered, with the first eigenmode having the greatest amplitude, and the slowest decay rate. Goldstein (1983) found that these Lam-Rott eigenmodes have a wavelength proportional to $x^{-\frac{1}{2}}$, where $x = \omega x^*/U_\infty$ is the dimensionless streamwise distance from the leading-edge non-dimensionalised with respect to the aerodynamic length scale U_∞/ω. This wavelength has the correct shortening mechanism required for them to generate the short wavelength T-S waves. Goldstein, however, showed that the Lam-Rott eigenmodes still satisfy the LUBLE when multiplied by x^τ, where τ is a constant, which is determined by a solvability condition at the next order of the asymptotics.

Further downstream, the LUBLE becomes an invalid approximation to the Navier-Stokes equations, because the boundary-layer, which grows like $x^{\frac{1}{2}}$, allows the eigenmodes to keep oscillating more and more rapidly, until the neglected streamwise variations become important, and the LUBLE solution breaks down. The appropriate approximation to the Navier-Stokes equations in this region is the Orr-Sommerfeld equation, and Goldstein (1983) showed that there exists a matching region between the two regimes, where the Lam-Rott eigenmodes match, in the matched asymptotic expansion sense (Van Dyke, 1964b), to the T-S waves of the Orr-Sommerfeld equation. Each Lam-Rott eigenmode matches precisely to one T-S wave, with the lowest order Lam-Rott eigenmode matching to the T-S wave which exhibits spatial growth downstream of the lower branch neutral stability point. All the other T-S waves exhibit exponential decay all the way along the plate.

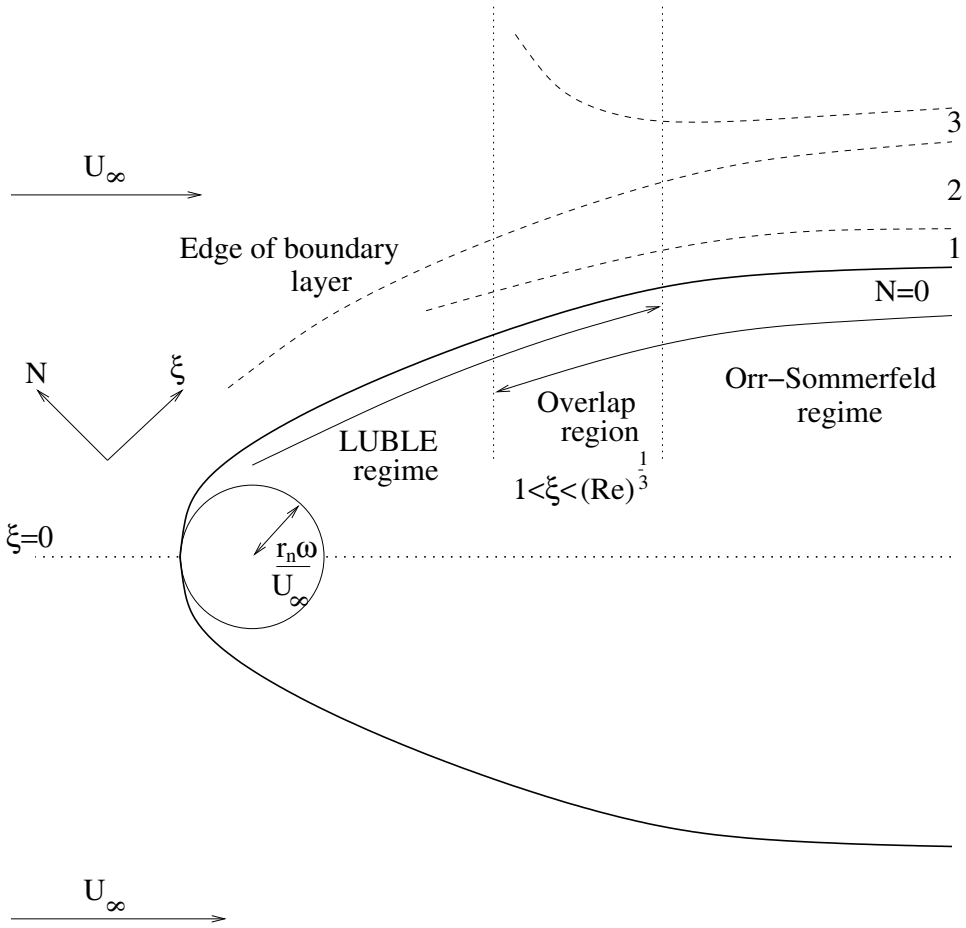

Figure 1.1: An illustration of the boundary-layer structure for a general body with dimensional nose radius r_n at zero angle of attack. The three decks in the Orr-Sommerfeld region are 1- the viscous wall layer; 2- the main inviscid layer; 3- the outer irrotational layer.

These results are also valid for finite thickness bodies, where the nose radius of curvature is of $O(U_\infty/\omega)$ or smaller, as shown in figure 1.1. Nose radii larger than this invalidate the small curvature condition stipulated in chapter 2. In a region of length $O(Re^{-\frac{1}{6}})$ near the stagnation point at the nose of the body, the fluid motion is governed by the full Navier-Stokes equations. Further downstream, on an $O(1)$ length scale, the motion is governed by the LUBLE, and the solution exhibits a two deck structure. Further downstream still, on a length scale of $O(Re^{\frac{1}{3}})$, the LUBLE solution brakes down, and the governing equation is then the Orr-Sommerfeld equation. The solution to the Orr-Sommerfeld equation has a triple-deck structure, which is also the correct behaviour for

the solution at the lower branch point. The triple-deck structure consists of a viscous wall layer, a main inviscid layer, and a irrotational outer layer.

Lam and Rott (1993) re-derived their asymptotic eigenmodes to the LUBLE, with the missing x^{τ} term included, found by Goldstein (1983). Lam and Rott found that with the inclusion of this extra multiplication factor, their 'outer' eigensolution was now valid for arbitrary pressure gradients, and their 'inner' eigensolution was also valid without requiring that the pressure gradient of the basic steady flow be zero. Brown and Stewartson (1973) showed that the Lam and Rott (1960) eigenmodes are not the only asymptotic eigenmodes which satisfy the LUBLE. The Brown-Stewartson eigenmodes in contrast to the Lam-Rott modes are correctly ordered, in that the amplitude of the fist eigenmode is the smallest, and it decays the slowest. Both sets of eigenmodes are valid solutions to the LUBLE, and both sets are visible in the numerical solution to the LUBLE (Hammerton, 1999), however they have different properties. The real part of the mode shape of the Lam-Rott eigenmodes have their maxima close the wall, whereas the Brown-Stewartson eigenmodes have their maxima close to the outer edge of the boundary-layer. It was also pointed out by Goldstein (1983), that the Brown-Stewartson eigenmodes have a much stricter criterion for their validation, and in fact are only valid for $\sqrt{\ln(x/3)} \gg 1$. The Lam-Rott eigenmodes on the other hand have a much weaker validation criterion of $x \gg 1$. Although we acknowledge the existence of the Brown-Stewartson eigenmodes, we concentrate our attention on the Lam-Rott modes because they have the required exponential decay, and wavelength shortening to transfer energy to the T-S waves. It has been speculated that the Brown-Stewartson eigenmodes may be obtainable by re-expanding, for large x, an appropriate sum of the Lam-Rott eigenmodes (Goldstein *et al.*, 1983), however this idea has not yet been validated.

By showing that the Lam-Rott eigenmodes match to the T-S waves, Goldstein (1983) proved that the information from the leading edge is only transmitted downstream by the unique constants multiplying each eigenmode. Moreover, as it is the *first* of these eigenmodes which matches to the spatially growing T-S wave, we are most interested in this coefficient. We call this coefficient, C_1, the 'receptivity coefficient', and it is uniquely

determined by the form of the free-stream. For the semi-infinite flat plate, Goldstein *et al.* (1983) found the receptivity coefficient to be $C_1 = -0.45 + 0.855i$ for acoustic disturbances, in two ways. Firstly a curve-fitting technique was used identical to the method of Ackerberg and Phillips (1972), where the numerical and asymptotic solutions for the displacement thickness were assumed to agree at certain pre-selected points. Secondly it was determined by assuming that the solution to the unsteady boundary-layer equation is an analytic function of x, when extended into the complex plane (Lam and Rott, 1960). Thus the numerical solution to the unsteady boundary-layer equation can be extended into a region where the lowest order eigenmode is dominant, and then the receptivity coefficient can be easily determined by comparison with the asymptotic form of the eigenmode.

In general, airfoils used for subsonic flow have finite thickness, and so cannot be modeled as a semi-infinite flat plate. Hammerton and Kerschen (1996) were first to treat analytically the receptivity on a more general body. They considered a parabola at zero angle of attack to the free-stream, with an acoustic disturbance incident at an angle θ to the chord of the airfoil. The leading edge curvature of the body enters the problem through the Strouhal number, $S = \omega r_n / U_\infty$, where the dimensional nose radius is, r_n, non-dimensionalised with respect to the aerodynamic length scale U_∞/ω. Hammerton and Kerschen consider the case $S = O(1)$, and $\xi \ll O(Re^{\frac{1}{3}})$, where ξ is the coordinate along the body. These limits were such that the flow is governed by the LUBLE, hence the flow in the vicinity of the leading edge could be treated. The parabolic nose produces everywhere a favourable pressure gradient, which decreases monotonically from its maximum value at the stagnation point, and approaches zero far downstream. The resulting eigenmodes of the LUBLE, in their far downstream form, are the same as the Lam-Rott eigenmodes, but they are modified to include the effect of the mean pressure gradient. As the nose radius increases, the strong favourable pressure gradient near the nose, extends over a larger number of disturbance wavelengths and acts as a stabilizing influence on the solution. Thus this produces a rapid decrease in the value of the modulus of the receptivity coefficient, C_1, as S increases, and in fact the modulus of the receptivity coefficient is approximately 12% of the flat plate value when $S = 0.3$. Hammerton and Kerschen

(1996) go on to suggest that this rapid decrease in the modulus of the receptivity coefficient should be valid for other streamlined bodies. For the parabola, Hammerton and Kerschen also observed a small rise in the receptivity coefficient for small S, before the monatonic decrease as S increases. When the angle of incidence of the acoustic wave is considered, the receptivity coefficient can be written in the form of a symmetric component and an antisymmetric component, both of which are determined separately. Two cases for the incident angle were studied: one where the acoustic wavelength is long compared with both the hydrodynamical wavelength, U_∞/ω, and the airfoil chord, and the second where the acoustic wavelength is long compared to the hydrodynamic wavelength, but short compared to the length of the chord. For the first case, the absolute value of the symmetric receptivity coefficient, C_s, as a function of θ, increases to a value of 18 for $S = 0$ and 3 for $S = 0.2$, both of which occur at $\theta \approx \pm\pi/2$, before decreasing again to approximately the $\theta = 0$ values at $\theta = \pi$. For the second case however, the absolute value of the symmetric receptivity coefficient increases to 20 for $S = 0$ and to 4 for $S = 0.2$, which occur at approximately $\theta = \pm\pi$.

The curious behaviour of the receptivity coefficient increasing slightly before decreasing was further studied by Hammerton and Kerschen (1997), where they analysed the limit $S \longrightarrow 0$ for the parabola considered above. It was shown that the symmetric part of the receptivity coefficient, C_s, grows like S, hence proving the increase in receptivity coefficient from the flat plate value, and the antisymmetric component, C_a, decreases like $S^{\frac{1}{2}}$, hence giving a very rapid decrease in value compared to the flat plate value. Also as $S \longrightarrow 0$, it was noted that the antisymmetric receptivity coefficient is approximately five time the value of the symmetric receptivity coefficient, and hence the antisymmetric component proves much more important in evaluating the receptivity coefficient than the symmetric component.

Hammerton and Kerschen (2005) extended their previous work to consider a cambered parabolic airfoil at a non-zero angle of attack to the free-stream. In this case there is a favourable pressure gradient at the stagnation point, followed by an even stronger favourable pressure gradient as the flow travels around the leading edge. The pressure

gradient on the upper surface then becomes adverse and the boundary-layer either separates, or reaches a point of minimum wall shear followed by a relatively slow recovery downstream. The boundary-layer is assumed to be attached, so the wall stress is everywhere positive and finite, and the airfoil is assumed not to be near the critical angle of attack where marginal separation occurs. Modest amounts of aerodynamic loading in the leading edge region causes a decrease in the receptivity coefficient for the flow over the upper surface of the airfoil and an increase for the flow under the lower surface. In fact, on the upper surface, the absolute value of the symmetric receptivity coefficient decreases from its value when the aerodynamic loading parameter, μ, equals zero until approximately $\mu \approx 0.7$ where it increases again, and the absolute value of the antisymmetric coefficient decays to $\mu \approx 0.4$ before increasing again. Conversely, on the lower surface, the symmetric and antisymmetric receptivity coefficients increase to a maximum at $\mu \approx 0.4$ before decaying again. The lower surface receptivity is of less interest however, because the pressure gradient is typically favourable and the instability waves have smaller growth rates. The effect of the aerodynamic loading is more pronounced for higher Strouhal numbers where the region of receptivity is concentrated closer to the stagnation point. Also the introduction of the aerodynamic loading moves the stagnation point towards the lower surface, which increases the favourable pressure gradient between the stagnation point and the leading edge.

The finite thickness airfoil theory was extended further by Nichols (2001), she extended the theory to general bodies for which the inviscid slip velocity tends to a constant far downstream, and the curvature is assumed to be small. The body is at a zero angle of attack, and the disturbance is considered to act parallel to the body. The unsteady flow, on a length scale along the body of, $\xi = O(1)$, is again governed by the LUBLE, and as $\xi \longrightarrow \infty$ it has a Stokes-like solution which is determined locally (i.e. it is independent of the upstream disturbance), and a sum of eigenmodes, which are modified versions of the Lam-Rott eigenmodes, to take into account the mean pressure gradient. The propagation of information from the leading edge occurs only through the coefficient multiplying the lowest order eigenmode, and Nichols (2001) calculated this value

for different geometries. Only acoustic waves flowing parallel to the free-stream were considered, however this work is valid for other free-stream disturbances, such as convected gusts (Buckingham, 2004), as the resulting difference only occurs in the value of the receptivity coefficient. Solutions are also valid as long as the minimum wall shear is greater than $O(Re^{-\frac{1}{5}})$, so marginal separation doesn't occur, and as long as any surface variation acts with a streamwise length of variation greater than $O(Re^{-\frac{3}{8}}l)$, where l is the distance from the leading edge to the centre of the variation. Nichols (2001) considered a Rankine body whose nose radius of curvature is proportional to A. She found that the receptivity coefficient decreases rapidly from the flat plate value as A increases, then exhibits a local rise centered on $A = 0.035$, followed by a further gradual decline. This was then extended to consider bodies which are equivalent to a flow formed by a source and a sink in a uniform flow, which are parameterized by two parameters. Nichols showed that two bodies which have the same thickness but subtly different body shapes, can have pressure gradients which are very similar close to the nose and downstream, but very different in the region of the minimum pressure gradient. The source/sink formulation leads to two different types of bodies. For monotonically increasing bodies, there was a fall in the receptivity coefficient with increasing thickness/nose radius. Hence the receptivity depends not only on the minimum of the pressure gradient, but also on its location and the variation of the pressure gradient in the region of the minimum. However, bulbous bodies, without boundary-layer separation, observed a rapid fall in the receptivity coefficient, followed by a rapid increase. Hence when a change of wall slope occurs in the leading edge region, it acts as another source of receptivity, and so has to be treated as such.

The analytic receptivity analysis on its own is very difficult to compare with experimental analysis, as the experiments generally calculate receptivity by calculating the magnitude of the growing T-S wave at some point downstream of the leading edge. Mathematically, this region is on a length scale of $O(Re^{\frac{1}{3}})$, and so the LUBLE is no longer the governing equation, and the correct approximation to the Navier-Stokes equations is now the Orr-Sommerfeld equation. Goldstein (1983) derived the asymptotic solution in this Orr-Sommerfeld region for the case of a semi-infinite flat plate, hence T-S wave am-

plitudes downstream are available. However a semi-infinite flat plate is not a physically reasonable body to preform experiments on, and extending Goldstein's asymptotics to general finite thickness bodies is not simple. Hence the receptivity analysis has to be used in conjunction with stability analysis to produce results which are comparable with experiments and full Navier-Stokes numerical schemes.

1.2 Stability theory

Stability theory accounts for the linear growth of the T-S wave, after it has been excited in the receptivity region. For the case of the airfoil problems we have considered so far, this occurs on a streamwise length scale of $O(Re^{\frac{1}{3}})$. The correct approximation to the Navier-Stokes equations in this region is the Orr-Sommerfeld equation. This equation was first derived when considering the flow between two solid walls, and the derivation of the Orr-Sommerfeld equation can be found in Appendix A. The Orr-Sommerfeld equation is solved as an eigenvalue problem, with the first accurate solution for Poiseuille flow offered by Orszag (1971). Chebyshev polynomials (Appendix C) were used to approximate the mode shape across the fluid domain, and an eigenvalue algorithm was used to find the linear temporal eigenvalues. The more complex problem of solving for the non-linear spatial eigenvalues was addressed by Bridges and Vaserstein (1986) and Bridges and Morris (1984) who extended the Chebyshev polynomial technique to simplify the non-linear eigenvalue problem to a linear one, and proved that the results were consistent with those of Orszag (1971).

If it is assumed that the boundary-layer is parallel to the surface of the body, then the Orr-Sommerfeld equation, derived in Appendix A, is the correct approximation to the Navier-Stokes equations. An example of the spatial eigenvalues, $\alpha = \alpha_r + i\alpha_i$, for parallel Blasius flow can be seen in figure 1.2. The eigenvalue close to the point $\alpha_r = 0.3$ is the most unstable eigenvalue, and it corresponds to the T-S wave which eventually grows downstream. For small Reynolds numbers, this eigenvalue lies very close to the continuous spectrum of eigenvalues at $\alpha_r = 0.12$, but as the Reynolds number increases, this eigenvalue moves away from the continuous spectrum, and closer to the line $\alpha_i = 0$.

When $\alpha_i > 0$ the corresponding T-S wave is decaying, and when $\alpha_i < 0$ it is growing, and at the point when $\alpha_i = 0$, the T-S wave neither grows or decays, it is said to be neutrally stable, and the corresponding value of the Reynolds number at this point is known as the critical Reynolds number. The main drawback to the parallel flow theory is that the boundary-layer over an airfoil's surface is not strictly parallel, and so extra terms are needed to give more accurate comparisons with experimental and full numerical results.

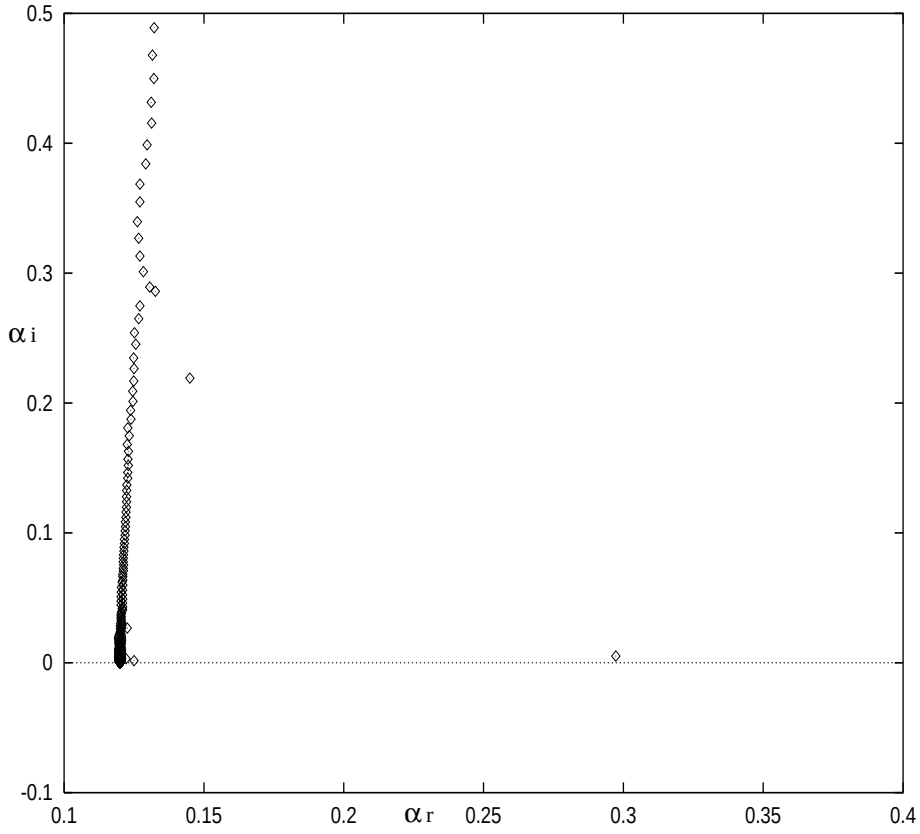

Figure 1.2: Spatial eigenvalues, $\alpha = \alpha_r + i\alpha_i$, for Blasius flow, for the case $\omega = 0.12$ and $Re = 519.4$

Gaster (1974) attempted to resolve this problem by leaving a streamwise dependent function, rather than a constant, multiplying the normal mode solution, and forming a solution in powers of $Re^{-\frac{1}{2}}$. The resulting equations were solved with an iterative scheme, and showed that this method was valid in the large Reynolds number limit.

Itoh (1974a) developed a different numerical method for solving the parallel Orr-Sommerfeld equation, based on power series, and this method provided good agreement

for the critical Reynolds numbers for both Poiseuille and Blasius flow. Itoh then extended this method to take into account the thickening of the boundary-layer downstream, and the normal component of velocity that this produces (Itoh, 1974b). The solution was sought by expanding the stream function as a Fourier series with the omission of components higher than the 3^{rd} order. Itoh (1974b) found fairly good agreement with the results of Klebanoff *et al.* (1962) when the initial amplitude of the disturbance is relatively small. However for large initial amplitudes this is not the case, and the difference is attributed to the fact that the experimental disturbance is three-dimensional, whereas the disturbance is assumed to be two-dimensional.

Saric and Nayfeh (1975) devised another method of formulating the non-parallel boundary-layer flow, which accounts for the non-parallel behaviour in a different manner to Itoh (1974b). The method is a multiple scales method, based on the work of Nayfeh (1973), where the flow is split into a base flow, and a small perturbation, of frequency ω. The base flow is assumed to be a slowly varying function of the streamwise variable x, hence $x_1 = \epsilon x$ is introduced as a slow streamwise variable, where $\epsilon \ll 1$. The resulting analysis produces two equations, one at $O(1)$ and the other at $O(\epsilon)$, both of which are solved iteratively, and the results provide a neutral curve which is in good agreement with the experiments of Schubauer and Skramstad (1947) and Ross *et al.* (1970). This method is very similar to that of Bridges and Morris (1984), who use a numerical method similar to their nonlinear spatial eigenvalue solver and they also obtain results in good agreement with the experiments. Saric and Nayfeh (1977) later extended this method to incorporate boundary-layer flows with pressure gradients and surface suction.

The triple-deck structure of the Orr-Sommerfeld solution at the lower branch neutral stability point, on a flat plate was analytically derived by Smith (1979), and Goldstein (1983) showed that the solution in the Orr-Sommerfeld region has the triple-deck structure throughout the entire region. Goldstein derived the asymptotic form of the wavenumber and mode shape in this region, which proved that the calculation of T-S wave amplitudes at lower branch is possible. Up to now, all the eigenvalue methods for numerically solving the Orr-Sommerfeld equation, have been correct only up to an arbitrary multiplicative

constant, and in fact contain no information from the leading edge. Goldstein showed that the asymptotic T-S wave solutions matched, in the matched asymptotic sense, to the large downstream form of the Lam-Rott eigenmodes of the LUBLE. This suggests that information from the leading edge can be passed downstream to the T-S waves via these asymptotics. However, it is not yet apparent if the asymptotic solution in the Orr-Sommerfeld region is actually correct to order $Re^{-\frac{1}{2}}$, and hence the accuracy of these asymptotics is not fully known. Also any attempt to extend the analysis to bodies such as the parabola have been difficult due to the fact that the asymptotics to $O(Re^{-\frac{1}{2}})$ on a flat plate are complex enough, without the introduction of a non-zero pressure gradient.

Itoh (1986) extends Goldstein's theory in the Orr-Sommerfeld region to numerical evaluations of the eigenmodes for a wider range of Reynolds numbers. Itoh derives a parabolic partial differential equation governing small disturbances with fixed frequency from an expansion procedure essentially similar to the boundary-layer approximation. The PDE was shown to be valid for both the upstream region where the unsteady boundary-layer equation is approximately applicable, to the far downstream region, where the Orr-Sommerfeld equation based on the parallel flow approximation is applicable. If the value of the Reynolds number and the frequency of the disturbance are above a certain value, then the PDE is decomposed into a set of ordinary differential equations.

The method behind the derivation of the parabolic PDE of Itoh (1986) was extended by Bertolotti *et al.* (1992) who used the assumptions that the mean flow is governed by the boundary-layer approximation, and moreover, the second derivatives of the disturbance wavenumber and mode shape with respect to the streamwise direction are sufficiently small, and thus can be neglected. The resulting Parabolized Stability Equation (PSE) describes the evolution of linear or non-linear, two- or three-dimensional disturbances in flows with slowly changing streamwise properties such as non-parallelism. The PSE is solved with an upstream boundary condition, usually given by local theory. The solution is then found by marching downstream, along with the fixing of a normalization condition, solving for the disturbance wavenumber and mode shape, in a similar fashion to the multiple scales method. The linear form of the PSE is identical to the partial differen-

tial equation derived by Itoh (1986), however the advantage of the PSE over the other multiple scales methods is, that it is relatively easy to include weakly non-linear effects, which prove to be important when the disturbances approach upper branch. The PSE can reproduce the results of Saric and Nayfeh (1977), but the analysis shows that their definitions of growth rates are not based on relevant physical quantities, hence should not be compared with the existing experimental measurements.

Bertolotti *et al.* (1992) derive their PSE equation in terms of a stream function, which gives rise to some numerical stability problems, but not as many as the primitive variables approach adopted by Herbert (1993) (Andersson *et al.*, 1998). Herbert (1993) derives a three-dimensional version of the PSE in terms of the primitive variables (u, v, w, p), where u, v and w are the velocity components in the x, y and z directions, respectively, and p is the pressure. When marching downstream with a streamwise step size less then some given amount, this form of the PSE experiences numerical instabilities which increase until numerical divergence occurs. Herbert (1993) discusses uses for the PSE other than non-parallel boundary-layer calculations. The incompressible version can model vortices in Blasius flow, receptivity to Hiemenz flow, and nonlinear vortices whereas the compressible version of the PSE can model high Mach number flows. The numerical instability for the primitive variable form of the PSE is due to the equations being ill-posed, due to the pressure gradient term. Li and Malik (1994) and Li and Malik (1996) offer a solution to this problem, by giving the minimum streamwise step size for which the PSE is ill-posed. They suggest either marching with a step size bigger than this minimum, or equivalently set the pressure gradient to zero, which removes some of the ellipticity from the PSE, hence makes the minimum step size smaller. However this does not remove all of the ellipticity, and hence the PSE is still ill-posed. The mathematical nature of the branch cuts and eigenvalues of the PSE in the complex plane are discussed by Li and Malik (1997).

A stabilization procedure for the primitive variable form of the PSE is offered by Andersson *et al.* (1998). They suggest the addition of a term of the same magnitude as the neglected truncation error to the first order backward Euler scheme. With this added term, multiplied by an arbitrary real number s, the PSE step size restriction can

be changed by a suitable value for s. Andersson *et al.* (1998) comment that the stream function formulation of the PSE has a less severe step size restriction. This was first noted by Li and Malik (1996), who suggests that this step size restriction can be relaxed if the streamwise derivative of the wavenumber is set to zero. This doesn't affect the overall wavenumber result, as long as we are not near a region where the wavenumber is changing reasonable quickly, for example close to the leading edge. Herbert (1997) offers an extensive review of the PSE and its applications.

An alternative approach to solving the stability problem was considered by Hill (1995), who used adjoint methods to solve the Orr-Sommerfeld problem. Salwen and Grosch (1981) developed a theory of temporal and spatial eigenfunction expansions for the solution of the Orr-Sommerfeld equation. The linear Navier-Stokes equations are not self-adjoint, hence a bi-orthogonal eigenfunction set is required (Schensted, 1960). For every eigensolution to the Orr-Sommerfeld equation, there exists an adjoint which has equal and opposite frequency and wavenumber, and also the adjoint eigensolution can be used to filter a general disturbance field to identify the amplitude of the corresponding eigensolution. The adjoint solution defines the sensitivity of a chosen disturbance to the modification of the base flow or boundary conditions, and Hill (1995) found that the unsteady forcing in the vicinity of the critical layer will induce the largest response of the T-S wave. Other parallel work on the adjoint methods has been studied by Zhigulev and Fedorov (1987) and Nayfeh and Ashour (1994).

Herbert (1997) first proposed the use of the Adjoint Parabolized Stability Equation (APSE), and it was first formulated by Collis and Dobrinsky (1999). The adjoint methods show that for 2-D disturbances in 2-D boundary-layers, the non-parallel effects are almost negligible over a wide range of frequencies, while adverse pressure gradients increase receptivity and favourable pressure gradients reduce receptivity. Adjoint methods also show that 3-D oblique modes have greater receptivity than 2-D waves, which are both in contrast to well known effects of pressure gradients on T-S instability growth rates (Dobrinsky and Collis, 2000). All the work on adjoint methods, except for Luchini and Bottaro (1998) and Hill (1997), rely on the expansion of the homogeneous solution to

the locally parallel flow into a bi-orthogonal set of eigenfunctions. Luchini and Bottaro (1998) solved the receptivity problem of Görtler vortices using the adjoint of the linearized boundary-layer equations. The advantage of this method is that it naturally includes the non-parallel effects within the receptivity predictions which are important for streamwise orientated disturbances. Hill (1997) extends the adjoint parallel theory approach to utilize the PSE and presents results based on the APSE along with comparisons for forced PSE and direct numerical solutions (DNS) results of Crouch (1995). The numerical solution to the APSE is solved by marching upstream, and used to provide a direct measure of the receptivity (e.g. to a suction strip at a certain location).

The method of adjoint solutions was extended by Giannetti (2002), who marches receptivity results given by the numerical solution to the LUBLE, downstream via an adjoint multiple scales approach. This approach is similar to the approach taken in this thesis, except we use the asymptotic form of the result in the leading edge region, and we use the PSE to march the solution through the Orr-Sommerfeld region (Turner and Hammerton, 2006). The bi-orthogonality properties on the adjoint operators are used to extract the receptivity coefficient, before the Orr-Sommerfeld modes are marched downstream. This method is used for an acoustic wave impinging on an incompressible flat plate boundary-layer. For moderate values of the non-dimensional frequency $F = \omega\nu/U_\infty^2$, no matching region between the leading edge region and the Orr-Sommerfeld region exists, however for low frequencies there is a well defined matching region.

Although receptivity and stability problems are in general solved separately, they have been solved simultaneously in direct numerical schemes and compared with experiments. Haddad and Corke (1998) compute full numerical solutions to the flow over a parabolic body, where the mean flow is perturbed by a small acoustic disturbance. The flow around the parabolic edge is linearised with respect to the small acoustic perturbation, and then the base flow and the perturbation flow are solved separately. To separate out the T-S wave behaviour from the perturbation flow, the unsteady Stokes flow is solved separately, subtracted from the total perturbation flow, and the remaining disturbance is assumed to be the T-S wave. The T-S wave amplitude is extracted back to the leading

edge, where Haddad and Corke (1998) define the leading edge receptivity coefficient as $K_{LE} = |(u'_{TS})_{LE}|/|u'_{\infty}|$, which is the ratio of the maximum T-S amplitude at the leading edge to the amplitude of the free-stream disturbance. Note this is a different definition to the receptivity coefficient, C_1, defined earlier as the coefficient of the lowest order Lam-Rott eigenmode.

In the limiting case of the semi-infinite flat plate, Haddad and Corke found good agreement between their results and those of Murdock (1980), who numerically modeled the flow using a parabolized form of the unsteady Navier-Stokes equations. They found agreement with the streamwise wavelengths of the T-S waves and the locations of the lower and upper branch neutral stability points of the neutral stability curve. Other results show an increase in leading-edge receptivity with decreasing nose radius, with the maximum occurring for the infinitely thin flat plate, and an increase in receptivity with an increase in the angle of attack. This work was extended by Erturk and Corke (2001) who considered more frequencies than Haddad and Corke, and a non-zero disturbance incident angle. They found results which agree qualitatively with Hammerton and Kerschen (1996), including the occurrence of maximum receptivity at an incident angle of 90° to the horizontal, and an asymmetrical variation in receptivity.

Erturk *et al.* (2004) and Haddad *et al.* (2005) went on to consider parabolic bodies at an angle of attack, where the aerodynamic loading was increased until separation occurred, followed downstream by reattachment. The separation point was shown to move downstream with increasing angle of attack, and the separation zone increased in size as the nose radius increased. This demonstrates the importance of aerodynamic loading and flow separation on acoustic receptivity.

Finite thickness bodies have also been considered, where the leading edge is elliptic in shape. These bodies have a pressure gradient on their upper surface which starts off favourable, but quickly becomes adverse, before decaying to zero far downstream. Numerical studies of these bodies have been conducted by Reed *et al.* (1990), Lin *et al.* (1992), Fuciarelli *et al.* (1998), Wanderley and Corke (2001) and a summary of the early numerical work can be found in Reed (1994). The experiments on these bodies have been

carried out by Saric and Rasmussen (1992), Saric *et al.* (1994), Saric *et al.* (1995) and Saric and White (1998). Reed *et al.* (1990) computed full solutions of the Navier-Stokes equations for a finite thickness flat plate with half an ellipse joined onto the front. Two different aspect ratios (ratio of major to minor axis) of 3 and 9 were studied at two different frequencies, and the measure of receptivity was chosen to be the maximum of the ratio of the T-S wave amplitude with the amplitude of the free-stream. The smaller aspect ratio produced the highest receptivity, which occurred between the junction of the ellipse and the flat plate and the neutral stability point. The body with aspect ratio of 3, had a sharp minimum in pressure gradient with a fast recovery, whereas the body with aspect ratio 9 had a smaller minimum and slower recovery. Lin *et al.* (1992) considered full numerical solutions to the Navier-Stokes equations in the same way, except they used a finite thickness flat plate with an elliptical edge where the discontinuity in curvature at the join has been mathematically removed. This body is known as a Modified Super Ellipse (MSE). Similarly to Reed *et al.* (1990), the smaller aspect ratio produced the larger receptivity, where the receptivity is the same ratio used by Reed *et al.* Lin *et al.* (1992) compared the body with a discontinuity in curvature in Reed *et al.* with the MSE and found that the MSE gave lower receptivity at the junction. Hence a discontinuity in curvature enhances the receptivity. However the MSE was found to be as receptive downstream of the junction, and this was attributed to the steeper adverse pressure gradient at the junction. Hence rapid changes in adverse pressure gradients are as important as discontinuities in curvature to the receptivity of bodies.

Fuciarelli *et al.* (1998) extended the DNS work by Lin *et al.* (1992), and calculated T-S wave amplitudes at the lower branch neutral stability point to compare with the experiments of Saric *et al.* (1995). In the experiments of Saric *et al.* (1995) and Saric and White (1998), T-S wave amplitudes at lower branch were calculated by first finding their amplitude at upper branch, and then extracting back this information using linear stability theory. Wanderley and Corke (2001) use the same method as Haddad and Corke (1998), where the flow is linearised and then the base and perturbation flows are solved separately, to model flow over a MSE. Again the largest aspect ratio MSE of $40:1$ produced

the largest amount of receptivity at branch I when compared to a $20:1$ MSE. Wanderley and Corke also found good agreement with the experiments of Saric *et al.* (1995) for the surface pressure coefficient, wall normal eigenfunction of the streamwise perturbation velocity, and the locations of the upper branch neutral stability point, as well as the receptivity value at lower branch given by Saric and White (1998) and Fuciarelli *et al.* (1998).

The aim of this thesis is to use the existing asymptotic theory from the leading edge region (Goldstein, 1983, Hammerton and Kerschen, 1996, Nichols, 2001), for acoustic waves, and extend it downstream through the Orr-Sommerfeld region to the lower branch neutral stability point, we will then be able to compare amplitudes with existing studies, both numerical (Haddad and Corke, 1998, Wanderley and Corke, 2001) and experimental (Saric and White, 1998). To do this, we hope to incorporate the use of the PSE, and extend the derivation of this equation to include body geometry, as Nichols (2001) did for the leading edge problem. The primary reason for wanting to compare with these experiments is to try and help with the understanding behind T-S wave propagation, and the mechanisms behind transition. The main topics in this work are outlined in the next section.

1.3 Outline for thesis

In chapter 2, we derive the LUBLE in the leading edge region, and produce the large downstream asymptotic form of the Lam-Rott eigenmodes for the case of a body with a rounded leading edge where the inviscid slip velocity tends to a constant far downstream. This asymptotic form can then be used as an initial upstream boundary condition, for the numerical solution to the PSE (Bertolotti *et al.*, 1992), which we extend to bodies, as discussed above. We compare the different variables used in both the leading edge region and the Orr-Sommerfeld region, and derive a relation between the two. In chapter 3 we give the numerical algorithms for solving the Orr-Sommerfeld equation for both the temporal and spatial eigenvalues. The algorithm is also given for the numerical solution of the PSE.

Chapter 4 deals with the special case of an infinitely thin, semi-infinite flat plate, for which Goldstein (1983) has derived asymptotic solutions for both the wavenumber and mode shape in the Orr-Sommerfeld region. We look extensively at the derivation of these asymptotic expansions, including the very complicated $O(Re^{-\frac{1}{2}})$ term, which, because of its complexity, makes it very difficult to extend the asymptotic analysis to more general bodies with non-zero nose radii. Using the existing asymptotics, we demonstrate the existence of an overlap region between the leading edge region and the Orr-Sommerfeld region, where both sets of equations are valid. We compare the results in the Orr-Sommerfeld region for the PSE, with Goldstein's asymptotics, and show that these are consistent in the large Reynolds number limit. We discuss the limitations of the PSE, and suggest an appropriate means to overcome amplitude calculations for slightly smaller values of the Reynolds number, where the PSE cannot be initiated right back in the matching region. We discuss the problem of initial transients appearing in the PSE calculations from the initial condition, and suggest a mechanism behind their appearance. We compare our PSE results with those of Haddad and Corke (1998) in the limit as the parabola's nose radius goes to zero, in an attempt to relate the different numerical schemes.

In chapters 5 and 6 we extend our PSE calculations to finite thickness bodies with non-zero nose radii. Chapter 5 deals with the parabola, where we calculate T-S wave amplitudes at lower branch for a range of values of Reynolds number, and Strouhal number. Chapter 6 compares similar calculations for the Rankine body, which can be defined in terms of one dimensionless parameter, related to the nose radius. We finish off by extending our analysis to the Modified Super Ellipse (MSE), and use slender body theory to model the influence of the geometry of this body, as a prerequisite to using the receptivity/PSE method.

Chapter 2

Formulation

In this chapter, we consider the two-dimensional flow over a body with nose radius r_n as shown in figure 2.1. The free-stream velocity is assumed to have magnitude, U_∞, and act parallel to the horizontal x^*-axis. It is also assumed to have a high Reynolds number, and a small perturbation of a single frequency acting parallel to the free-stream. Figure 2.1 shows the structure of the two regions discussed in chapter 1, with some overlap region occurring where the equations in both the leading edge and Orr-Sommerfeld region are valid. We shall use the existence of this overlap region to march the solutions from the leading edge region, downstream via the Parabolized Stability Equation (PSE).

To be able to use the PSE as a way of determining the downstream propagation information, we must first derive the asymptotic form of the disturbance in the leading edge receptivity region to use as our upstream boundary condition for the PSE. We derive the governing equation in this region, which is known as the linearised unsteady boundary-layer equation (LUBLE), and seek large ξ asymptotic solutions of this equation, where ξ is the coordinate in the streamwise direction along the body. It was first pointed out by Lam and Rott (1960) that the solutions to this equation consists of a Stokes flow part, and a linear combination of unsteady eigenmodes. It was shown (Goldstein, 1983) that it's the first of these eigenmodes which matches onto the Tollmien-Schlichting (T-S) wave in the Orr-Sommerfeld region, which eventually grows downstream of the lower branch neutral stability point, and hence is of interest to us.

This method was first conducted on a semi-infinite flat plate, but was later extended

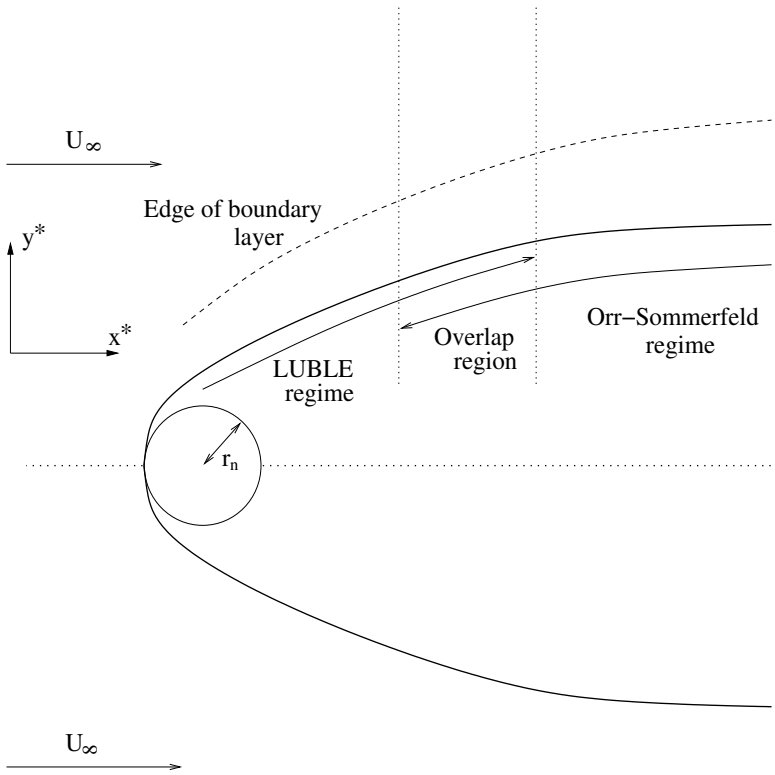

Figure 2.1: An illustration of the region structure on a body with a nose radius, r_n, at zero angle of attack to the free-stream, U_∞.

by Hammerton and Kerschen (1996) and Nichols (2001) to a more general family of eigenmodes, which are valid on bodies which have curved leading edges.

We shall extend the PSE derived by Bertolotti *et al.* (1992) to incorporate bodies with curvature, and hence, as in the LUBLE region, we shall derive the PSE from the Navier-Stokes equations using the coordinates (ξ, N), where ξ is a coordinate along the body, and N is a coordinate normal to the surface of the body, to be defined later. In later chapters, we shall use the PSE to march the asymptotic form of the leading edge eigenmodes downstream from the leading edge.

2.1 Leading edge region

2.1.1 Derivation of the steady and unsteady flow equations

The two dimensional Navier-Stokes equations modeling incompressible flow beside a plane wall at $y^* = 0$, in dimensional form, are given by

$$\frac{\partial u^*}{\partial t^*} + u^*\frac{\partial u^*}{\partial x^*} + v^*\frac{\partial u^*}{\partial y^*} = -\frac{1}{\rho}\frac{\partial p^*}{\partial x^*} + \nu\left(\frac{\partial^2 u^*}{\partial x^{*2}} + \frac{\partial^2 u^*}{\partial y^{*2}}\right), \tag{2.1}$$

$$\frac{\partial v^*}{\partial t^*} + u^*\frac{\partial v^*}{\partial x^*} + v^*\frac{\partial v^*}{\partial y^*} = -\frac{1}{\rho}\frac{\partial p^*}{\partial y^*} + \nu\left(\frac{\partial^2 v^*}{\partial x^{*2}} + \frac{\partial^2 v^*}{\partial y^{*2}}\right), \tag{2.2}$$

$$\frac{\partial u^*}{\partial x^*} + \frac{\partial v^*}{\partial y^*} = 0, \tag{2.3}$$

where x^* is measured along the wall, and y^* is measured normal to the wall. The components of velocity (u^*, v^*) are in the directions of (x^*, y^*) respectively. The pressure is denoted by p^*, density by ρ and the kinematic viscosity by ν. The boundary conditions for this flow are

$$u^* = v^* = 0 \qquad \text{on} \qquad y^* = 0, \tag{2.4}$$

$$u^* \longrightarrow U_\infty \qquad \text{as} \qquad y^* \longrightarrow \infty, \tag{2.5}$$

where U_∞ is the velocity of the undisturbed free-stream.

We consider the problem for which the free-stream U_∞ is not completely undisturbed, but has a small free-stream forcing component of frequency ω. Hence we introduce non-dimensional variables based on the velocity scale, U_∞, length scale, U_∞/ω, and time scale, ω^{-1}, into (2.1) to (2.3), which leads to

$$\frac{\partial \bar{u}}{\partial \bar{t}} + \bar{u}\frac{\partial \bar{u}}{\partial \bar{x}} + \bar{v}\frac{\partial \bar{u}}{\partial \bar{y}} = -\frac{\partial \bar{p}}{\partial \bar{x}} + \frac{1}{Re}\left(\frac{\partial^2 \bar{u}}{\partial \bar{x}^2} + \frac{\partial^2 \bar{u}}{\partial \bar{y}^2}\right), \tag{2.6}$$

$$\frac{\partial \bar{v}}{\partial \bar{t}} + \bar{u}\frac{\partial \bar{v}}{\partial \bar{x}} + \bar{v}\frac{\partial \bar{v}}{\partial \bar{y}} = -\frac{\partial \bar{p}}{\partial \bar{y}} + \frac{1}{Re}\left(\frac{\partial^2 \bar{v}}{\partial \bar{x}^2} + \frac{\partial^2 \bar{v}}{\partial \bar{y}^2}\right), \tag{2.7}$$

$$\frac{\partial \bar{u}}{\partial \bar{x}} + \frac{\partial \bar{v}}{\partial \bar{y}} = 0, \tag{2.8}$$

where the bar denotes a dimensionless quantity, and Re is the Reynolds number defined

as

$$Re = \frac{U_\infty^2}{\omega\nu}. \tag{2.9}$$

The non-dimensional boundary conditions for this problem are $\bar{u} = \bar{v} = 0$ on $\bar{y} = 0$, and $\bar{u} \longrightarrow 1$ as $\bar{y} \longrightarrow \infty$.

In this work we are only interested in large Reynolds number flows. In this case a boundary-layer is formed adjacent to the wall, of thickness $\delta = O(Re^{-\frac{1}{2}})$ (Acheson, 1990, p268). Hence we introduce boundary-layer variables scaled on this thickness as

$$x = \bar{x}, \quad y = Re^{\frac{1}{2}}\bar{y}, \quad u = \bar{u}, \quad v = Re^{\frac{1}{2}}\bar{v}, \quad t = \bar{t}, \quad p = \bar{p}. \tag{2.10}$$

Substituting these into the non-dimensional Navier-Stokes equations gives the following boundary-layer equations at leading order

$$\frac{\partial u}{\partial t} + u\frac{\partial u}{\partial x} + v\frac{\partial u}{\partial y} = -\frac{\partial p}{\partial x} + \frac{\partial^2 u}{\partial y^2}, \tag{2.11}$$

$$0 = -\frac{\partial p}{\partial y}, \tag{2.12}$$

$$\frac{\partial u}{\partial x} + \frac{\partial v}{\partial y} = 0. \tag{2.13}$$

Outside the boundary-layer, viscous effects are negligible, and hence the flow is governed by inviscid theory. The inviscid solution cannot satisfy the no-slip condition at the boundary, hence we obtain a tangential slip velocity, $U_s(x,t)$, even though the normal component of velocity at the boundary is zero. Matching the boundary-layer flow to the inviscid flow gives the outer boundary condition as

$$u \longrightarrow U_s(x,t), \quad v \longrightarrow 0 \quad \text{as} \quad y \longrightarrow \infty. \tag{2.14}$$

From (2.12), we note that, $p = p(x,t)$, hence the pressure is constant throughout the boundary-layer. Therefore applying (2.11) at the edge of the boundary-layer gives

$$\frac{\partial p}{\partial x} = -\left(\frac{\partial U_s}{\partial t} + U_s\frac{\partial U_s}{\partial x}\right), \tag{2.15}$$

and the non-dimensional boundary-layer equations become

$$\frac{\partial u}{\partial t} + u\frac{\partial u}{\partial x} + v\frac{\partial u}{\partial y} = \frac{\partial U_s}{\partial t} + U_s\frac{\partial U_s}{\partial x} + \frac{\partial^2 u}{\partial y^2}, \tag{2.16}$$

$$\frac{\partial u}{\partial x} + \frac{\partial v}{\partial y} = 0, \tag{2.17}$$

with the boundary conditions for a rigid and impermeable plate at $y = 0$, $u = v = 0$, and $u \longrightarrow U_s(x,t)$ as $y \longrightarrow \infty$.

The equations above have been derived in the case of a flat plate, however these same equations hold, to leading order, for flows past curved boundaries, as long as the curvature of the boundary, κ, is such that $\kappa U_\infty \delta/\omega$ and $(U_\infty^2 \delta/\omega^2)(\partial\kappa/\partial x^*)$ are small (Rosenhead, 1963). The coordinates x and y are now defined as being along the boundary and normal to the boundary, respectively. For the curved boundary, $\partial p^*/\partial y^*$ is no longer zero, but equals $\kappa\rho u^{*2}$, to balance the centrifugal force. However (2.15) still holds, as the total change in pressure across the boundary-layer, $\Delta p^* = O(\kappa\rho U_\infty^2 \delta)$, is still negligible when $\kappa\delta$ is small.

With our new definition of (x, y), we solve (2.16) by noting that from (2.17) there exists a stream function, $\psi = Re^{\frac{1}{2}}\omega\psi^*/U_\infty^2$, with the properties

$$u = \frac{\partial\psi}{\partial y} \quad \text{and} \quad v = -\frac{\partial\psi}{\partial x}. \tag{2.18}$$

Thus (2.16) becomes

$$\frac{\partial^2\psi}{\partial y\partial t} + \frac{\partial\psi}{\partial y}\frac{\partial^2\psi}{\partial y\partial x} - \frac{\partial\psi}{\partial x}\frac{\partial^2\psi}{\partial y^2} = \frac{\partial U_s}{\partial t} + U_s\frac{\partial U_s}{\partial x} + \frac{\partial^3\psi}{\partial y^3}, \tag{2.19}$$

with the boundary conditions

$$\psi = \frac{\partial\psi}{\partial x} = \frac{\partial\psi}{\partial y} = 0 \quad \text{on} \quad y = 0, \tag{2.20}$$

$$\frac{\partial\psi}{\partial y} \longrightarrow U_s(x,t) \quad \text{as} \quad y \longrightarrow \infty. \tag{2.21}$$

For this work it is assumed that the external disturbance is small compared to the free-stream, and is of a single dimensional frequency, ω. Therefore we assume that the slip velocity can be written as a steady base part and a linear perturbation due to the external disturbance,

$$U_s(x,t) = U_f(x) + \epsilon U_d(x)e^{-it}, \tag{2.22}$$

where $\epsilon \ll 1$ is a small constant, and $U_f(x)$ and $U_d(x)$ are $O(1)$. Here the function $U_f(x)$ is the slip velocity due to the undisturbed free-stream, and can be calculated by inviscid theory.

To simplify (2.19), it is assumed that the stream function takes the following form

$$\psi = h(x)\phi(x, N, t) \quad \text{where} \quad N = g(x)y, \tag{2.23}$$

where $g(x)$, $h(x)$ and $\phi(x, N, t)$ will be determined below.

On substituting this into (2.19), we get

$$\begin{aligned} \frac{\partial^2\phi}{\partial N\partial t} &+ \frac{d(gh)}{dx}\left(\frac{\partial\phi}{\partial N}\right)^2 + gh\left(\frac{\partial\phi}{\partial N}\frac{\partial^2\phi}{\partial N\partial x} - \frac{\partial^2\phi}{\partial N^2}\frac{\partial\phi}{\partial x}\right) \\ &= \frac{1}{gh}\left(\frac{\partial U_s}{\partial t} + U_s\frac{\partial U_s}{\partial x}\right) + g^2\frac{\partial^3\phi}{\partial N^3} + g\frac{dh}{dx}\phi\frac{\partial^2\phi}{\partial N^2}, \end{aligned} \tag{2.24}$$

with the boundary conditions

$$\phi = \frac{\partial\phi}{\partial N} = 0 \qquad \text{on} \qquad N = 0, \tag{2.25}$$

$$\frac{\partial\phi}{\partial N} \longrightarrow \frac{U_s(x,t)}{g(x)h(x)} \qquad \text{as} \qquad N \longrightarrow \infty. \tag{2.26}$$

The functions $h(x)$ and $g(x)$ are chosen in such a way as to satisfy the boundary condition at the edge of the boundary-layer, and to simplify (2.24). Thus because of the form of (2.22), we choose

$$g(x)h(x) = U_f(x), \tag{2.27}$$

to simplify the boundary condition (2.26) to

$$\frac{\partial\phi}{\partial N} \longrightarrow 1 + \epsilon\frac{U_d(x)}{U_f(x)}e^{-it} \quad \text{as} \quad N \longrightarrow \infty.$$

We also choose

$$g(x) = \frac{dh}{dx}, \tag{2.28}$$

so that the last two terms in (2.24) both have the same coefficient. This gives the equation a form similar to that of the standard equation for steady boundary-layer evolution. Solving (2.27) and (2.28) leads to the arbitrary functions having the form

$$g(x) = U_f(x)\left(2\int_0^x U_f(x')dx'\right)^{-\frac{1}{2}}, \tag{2.29}$$

$$h(x) = \left(2\int_0^x U_f(x')dx'\right)^{\frac{1}{2}}. \tag{2.30}$$

We assume that $\phi(x, N, t)$ takes the same linear form as the slip velocity, hence

$$\phi(x, N, t) = \phi_1(x, N) + \epsilon\phi_2(x, N)e^{-it}, \tag{2.31}$$

where we shall label $\phi_1(x,N)$ as the steady solution, and $\phi_2(x,N)$ as the unsteady solution. Substituting this into (2.24), along with the definitions for $g(x)$ and $h(x)$, and equating powers of ϵ, we find the steady evolution equation is

$$\phi_{1NNN} + \phi_1\phi_{1NN} = f1(x)\left(\phi_{1N}^2 - 1\right) + f2(x)\left(\phi_{1N}\phi_{1Nx} - \phi_{1NN}\phi_{1x}\right), \tag{2.32}$$

where the subscripts x and N represent differentiation with respect to the appropriate variable. The functions $f1(x)$ and $f2(x)$ are functions of the slip velocity, and are given by

$$f1(x) = \frac{2\int_0^x U_f dx'}{U_f^2}\frac{dU_f}{dx}, \qquad f2(x) = \frac{2\int_0^x U_f dx'}{U_f}.$$

For (2.32) to be of the same form as the standard equation for the evolution of a steady boundary-layer,

$$\phi_{NNN} + \phi\phi_{NN} = \beta(\xi)\left(\phi_N^2 - 1\right) + 2\xi\left(\phi_N\phi_{N\xi} - \phi_{NN}\phi_\xi\right),$$

we introduce the further change of variables,

$$\xi = \int_0^x U_f(x')dx', \tag{2.33}$$

which on substitution into (2.29) and (2.30) leads to $g(\xi) = U_f(\xi)(2\xi)^{-\frac{1}{2}}$ and $h(\xi) = (2\xi)^{\frac{1}{2}}$.

Now with the new variables (ξ, N), we gain two equations for the evolution of a boundary-layer: one for the steady part ϕ_1 and a second for the coefficient ϕ_2 of the time-dependent part. The steady flow equation is

$$\phi_{1NNN} + \phi_1\phi_{1NN} = \beta(\xi)\left(\phi_{1N}^2 - 1\right) + 2\xi\left(\phi_{1N}\phi_{1N\xi} - \phi_{1NN}\phi_{1\xi}\right), \tag{2.34}$$

with the boundary conditions

$$\begin{aligned} \phi_1 = \phi_{1N} = 0 \qquad &\text{on} \qquad N = 0, \\ \phi_{1N} \longrightarrow 1 \qquad &\text{as} \qquad N \longrightarrow \infty. \end{aligned} \tag{2.35}$$

The function $\beta(\xi)$ is the mean pressure gradient, and is given by

$$\beta(\xi) = \frac{2\xi}{U_f}\frac{dU_f}{d\xi}. \tag{2.36}$$

The equation for the unsteady flow component ϕ_2 of ϕ in (2.31) is

$$\begin{aligned} \phi_{2NNN} + \phi_{2NN}\left(\phi_1 + 2\xi\phi_{1\xi}\right) &+ \phi_{2N}\left(i\Omega(\xi) - 2\beta(\xi)\phi_{1N} - 2\xi\phi_{1N\xi}\right) + \phi_2\phi_{1NN} \\ +2\xi\left(\phi_{1NN}\phi_{2\xi} - \phi_{1N}\phi_{2N\xi}\right) &= \frac{U_d}{U_f}\left(i\Omega(\xi) - \beta(\xi)\right) - \frac{2\xi}{U_f}\frac{dU_d}{d\xi}, \end{aligned} \tag{2.37}$$

where the function $\Omega(\xi)$ is known, and is given by

$$\Omega(\xi) = \frac{2\xi}{U_f^2}, \tag{2.38}$$

and the corresponding boundary conditions are

$$\phi_2 = \phi_{2N} = 0 \qquad \text{on} \qquad N = 0, \tag{2.39}$$

$$\phi_{2N} \longrightarrow \frac{U_d(x)}{U_f(x)} \qquad \text{as} \qquad N \longrightarrow \infty. \tag{2.40}$$

Equation (2.37), is known as the linearised unsteady boundary-layer equation (LUBLE), due to $\phi_2(\xi, N)$ being the linear correction term to $\phi_1(\xi, N)$.

In deriving the equations for boundary-layer flow, the only assumption we have made is that the inviscid slip velocity, $U_s(x)$, and the boundary-layer flow excited by the free-stream forcing can be written as a linear perturbation on the steady problem. Therefore (2.34) and (2.37) hold for more general two-dimensional bodies as long as these assumptions still hold.

2.1.2 Asymptotic solutions as $\xi \longrightarrow \infty$

In later chapters, we hope to utilise the solution to the LUBLE, and use it as an initial upstream boundary condition to our PSE solver, which is valid far downstream of the leading edge. Thus, we require the far downstream form of the LUBLE solutions, so in this section, we derive the large ξ asymptotic form of these solutions. The steady problem is completely determined through the mean pressure gradient $\beta(\xi)$, and the unsteady problem is determined by $\beta(\xi)$, the steady solution, and the function $\Omega(\xi)$, all of which are functions of the inviscid slip velocity $U_f(x)$. Hence to form the asymptotic solutions for these equations, we need only the asymptotic form of U_f in the large ξ limit.

We shall consider bodies for which it can be assumed that the slip velocity, U_f, acts parallel and symmetric to the body, and hence takes the following form in the large x

limit,

$$U_f(x) = 1 + \frac{\alpha}{x} + \frac{\gamma}{x^2} + O(x^{-3}). \tag{2.41}$$

This form of U_f holds true for the bodies we discuss in later chapters. This gives from (2.33)

$$\xi = x + \alpha \ln(x) - \frac{\gamma}{x} + O(x^{-2}). \tag{2.42}$$

However, we require $U_f(\xi)$, and hence we need $x(\xi)$. If we take the approximation that $\xi = x + \alpha \ln(x)$, and write that $x = \xi + \tilde{\xi}$, where $\tilde{\xi} \ll \xi$, then in the limit $\xi \longrightarrow \infty$ we find $\tilde{\xi} \sim -\alpha \ln(\xi)$. From this we can write the asymptotic relationship $x(\xi)$ as

$$x = \xi - \alpha \ln(\xi) + O(\xi^{-1}). \tag{2.43}$$

Using this relation in the asymptotic form of $U_f(x)$ and expanding for large ξ, we find

$$U_f(\xi) = 1 + \frac{\alpha}{\xi} + \frac{\alpha^2 \ln(\xi)}{\xi^2} + \frac{\gamma}{\xi^2} + O(\xi^{-3} \ln^2(\xi)). \tag{2.44}$$

From this we can now find the asymptotic forms of $\beta(\xi)$ and $\Omega(\xi)$ as $\xi \longrightarrow \infty$ from (2.36) and (2.38),

$$\beta(\xi) \sim \frac{a_1}{\xi} + a_2 \frac{\ln(\xi)}{\xi^2} + \frac{a_3}{\xi^2} + O(\xi^{-3} \ln^2(\xi)), \tag{2.45}$$

$$\Omega(\xi) \sim b_1 \xi + b_2 + b_3 \frac{\ln(\xi)}{\xi} + \frac{b_4}{\xi} + O(\xi^{-2} \ln^2(\xi)), \tag{2.46}$$

where the coefficients a_i and b_i are given by

$$a_1 = -2\alpha, \quad a_2 = -4\alpha^2, \quad a_3 = 4(\alpha^2 - \gamma), \tag{2.47}$$

$$b_1 = 2, \quad b_2 = -4\alpha, \quad b_3 = -4\alpha^2, \quad b_4 = 6\alpha^2 - 4\gamma. \tag{2.48}$$

To expand $\beta(\xi)$ and $\Omega(\xi)$ to higher powers of ξ^{-1}, we would need more terms in the expansion of $U_f(\xi)$. However, Nichols (2001) shows that the asymptotic form for the steady component $\phi_1(\xi, N)$ up to $O(\xi^{-1})$, only depends upon a_1, and the unsteady solution only depends upon a_1, b_1 and b_2. Thus to this required order, the expansions of $\beta(\xi)$ and $\Omega(\xi)$ are sufficient.

Asymptotic steady solution

From the analysis of Van Dyke (1964a) and Hammerton and Kerschen (1996) on a parabola, the steady solution $\phi_1(\xi, N)$ is assumed to have the following form as $\xi \longrightarrow \infty$,

$$\phi_1(\xi, N) \sim \phi_a(N) + \phi_b(N)\frac{\ln(\xi)}{\xi} + \frac{\phi_c(N)}{\xi} + O\left(\xi^{-1.887}\right) \tag{2.49}$$

The logarithmic term is essential, as it ensures exponential decay of the vorticity through the boundary-layer (Stewartson, 1957). The correction term with fractional power -1.887 arises as the next eigenmode of an infinite sequence discussed later (Libby and Fox, 1963). The boundary conditions on ϕ_1 translate to

$$\begin{aligned} \phi_a = \phi_b = \phi_c = \phi_{aN} = \phi_{bN} = \phi_{cN} = 0 \qquad &\text{on} \qquad N = 0, \\ \phi_{aN} \longrightarrow 1, \quad \text{and} \quad \phi_{bN}, \phi_{cN} \longrightarrow 0 \qquad &\text{as} \qquad N \longrightarrow \infty. \end{aligned} \tag{2.50}$$

Substituting (2.49) and (2.45) into the steady equation (2.34), and equating powers of ξ, gives us three differential equations for the three unknown functions $\phi_a(N), \phi_b(N)$ and $\phi_c(N)$. The order one term leads to

$$\phi_a''' + \phi_a\phi_a'' = 0, \tag{2.51}$$

where the prime denotes differentiation with respect to N. With the boundary conditions (2.50), the solution to (2.51) is $\phi_a(N) = f(N)$ where $f(N)$ denotes the Blasius solution for flow past a flat plate, with zero pressure gradient ($\beta(\xi) = 0$). At order $\ln(\xi)/\xi$, the equation for $\phi_b(N)$ is

$$\phi_b''' + f\phi_b'' + 2f'\phi_b' - f''\phi_b = 0, \tag{2.52}$$

which has the solution $\phi_b(N) = C(Nf' - f)$ (Lighthill, 1954), where C is an arbitrary constant. This constant will be determined later by a solvability condition. At order $1/\xi$, the equation for $\phi_c(N)$ is given by

$$\phi_c''' + f\phi_c'' + 2f'\phi_c' - f''\phi_c = a_1(f'^2 - 1) + 2Cff'', \tag{2.53}$$

where a_1 is the leading coefficient from the asymptotic form of the pressure gradient given in (2.45). The solution of (2.53) can be written as $\phi_c(N) = D(Nf' - f) + E(N)$, where D is a constant, and $E(N)$ is a particular solution of (2.53). We assume without loss of

generality that $E''(0) = 0$, and hence the constant D is unique. As $\phi_a(N) = f(N)$, then the asymptotic form of the steady solution, (2.49), can be considered as a perturbation about the Blasius solution. Libby and Fox (1963) considered such flows, and sought a solution of the form

$$\phi_1(\xi, N) \sim f(N) + \sum_{k=1}^{\infty} \phi_{1,k}(\xi, N),$$

where $\phi_{1,k+1} \ll \phi_{1,k}$ for $\xi \gg 1$. Libby and Fox found that the functions $\phi_{1,k}$, through linearisation and separation of variables, are of the form $\phi_{1,k} = S_k(\xi)T_k(N)$, where $S_k(\xi) \sim \xi^{-\frac{\lambda_k}{2}}$ and $T_k(N)$ satisfies the eigenvalue problem

$$T_k''' + fT_k'' + \lambda_k f'T_k' + (1 - \lambda_k)f''T_k = 0,$$

with boundary conditions $T_k(0) = 0$ and $T_k'(\infty) = 0$. They list the first ten eigenvalues of this equation, the first of which is $\lambda_1 = 2$ which is the only integer value among the eigenvalues. From comparison with (2.53), we see that the homogeneous form of this equation corresponds to the above equation with $\lambda_k = 2$. Therefore as the first eigensolution is $D(Nf' - f)/\xi$, we note that the constant D cannot be found using the asymptotic analysis, and hence it has to be found numerically. The next two eigenvalues are $\lambda_2 = 3.774$ and $\lambda_3 = 5.635$, whose corresponding eigensolutions are $O\left(\xi^{-1.887}\right)$ and $O\left(\xi^{-2.818}\right)$ respectively, correspond to higher order correction terms in $\phi_1(\xi, N)$.

The particular solution $E(N)$ cannot be found analytically, hence it is found by numerically solving

$$L_1(E) = a_1(f' - 1) + 2Cff'', \tag{2.54}$$

with the boundary conditions

$$E = E' = E'' = 0 \quad \text{on} \quad N = 0,$$

where the linear operator L_1 is given by

$$L_1(E) = E''' + fE'' + 2f'E' - f''E. \tag{2.55}$$

The solvability condition for C is found by applying adjoint linear operator theory at the $1/\xi$ order. For third-order linear operators,

$$vL(u) - u\hat{L}(v) = \frac{dP(u, v)}{dN},$$

where $\hat{L}(v)$ represents the homogeneous adjoint operator to $L(u)$. The general operators, L, $\hat{L}$ and the function $P(u,v)$ are given by

$$\begin{aligned} L(u) &= u''' + pu'' + qu' + su, \\ \hat{L}(v) &= -v''' + (pv)'' - (qv)' + sv, \\ P(u,v) &= vu'' + uv'' - v'u' + pvu' - (pv)'u + qvu. \end{aligned}$$

For the linear operator $L_1(E)$, the solution to the corresponding adjoint operator problem $\hat{L}_1(v) = 0$, is $v = f$, hence

$$f\left(a_1(f'^2 - 1) + 2Cff''\right) = \frac{d}{dN}\left(fE'' + Ef'' - f'E' + f^2E'\right). \tag{2.56}$$

Integrating this equation with respect to N between zero and infinity and using the boundary conditions on $f(N)$ and $E(N)$, gives the solvability condition that

$$\int_0^\infty f\left(a_1(f'^2 - 1) + 2Cf''f\right) dN = 0. \tag{2.57}$$

Therefore rearranging this we find

$$\frac{C}{a_1} = \frac{\int_0^\infty f(f'^2 - 1)dN}{2\int_0^\infty f^2 f''dN} \approx 0.60115, \tag{2.58}$$

and hence the general asymptotic form of the steady solution for general $\beta(\xi)$ is

$$\phi_1(\xi, N) \sim f + 0.60115a_1(Nf' - f)\frac{\ln(\xi)}{\xi} + \frac{D(Nf' - f) + E(N)}{\xi} + O\left(\xi^{-1.887}\right). \tag{2.59}$$

The undetermined constant D is obtained numerically (Hammerton and Kerschen, 1996) by noting that we can rearrange (2.59) to give

$$q(\xi) = \frac{\xi(\phi_{1NN}(\xi, 0) - f''(0))}{f''(0)\ln(\xi)} \sim 0.60115a_1 + \frac{D}{\ln(\xi)}. \tag{2.60}$$

Hence by plotting $q(\xi)$ against $1/\ln(\xi)$, the constant D can be evaluated as the gradient of the tangent to $q(\xi)$, in the limit $1/\ln(\xi) \longrightarrow 0$, whose intercept is $0.60115a_1$. However in the limit as $1/\ln(\xi) \longrightarrow 0$, the value of $\phi_{1NN}(\xi, 0)$ approaches that of $f''(0)$, and hence to avoid numerical error in this calculation, it's more convenient to use $\hat{\phi}(\xi, N) = \phi_1(\xi, N) - f(N)$. Substituting $\phi_1(\xi, N) = f(N) + \hat{\phi}(\xi, N)$ into (2.34) gives

$$\begin{aligned} \hat{\phi}_{NNN} + \hat{\phi}\hat{\phi}_{NN} &= \beta(\xi)\left(\hat{\phi}_N^2 - 1\right) + 2\xi\left(\hat{\phi}_N\hat{\phi}_{N\xi} - \hat{\phi}_{NN}\hat{\phi}_\xi\right) - f''\hat{\phi} - f\hat{\phi}_{NN} \\ &+ \beta(\xi)\left(f'^2 + 2\hat{\phi}f'\right) + 2\xi\left(f'\hat{\phi}_{N\xi} - f''\hat{\phi}_\xi\right), \end{aligned} \tag{2.61}$$

as the governing equation for $\hat{\phi}(\xi, N)$. The unknown constant D can now be determined from the plot of $\hat{q}(\xi)$ against $1/\ln(\xi)$, where $\hat{q}(\xi)$ is given by

$$\hat{q}(\xi) = \frac{\xi \hat{\phi}_{NN}(\xi, 0)}{f''(0)\ln(\xi)} \sim 0.60115 a_1 + \frac{D}{\ln(\xi)}. \tag{2.62}$$

Asymptotic unsteady eigenmode

Ackerberg and Phillips (1972) conducted work on flow past a flat plate, and they showed that a two-layer structure exists in the boundary-layer far from the leading edge. This two-layer structure consists of a main layer of width $N = O(1)$, and an inner layer of width $N = O(\xi^{-\frac{1}{2}})$. Within the boundary-layer, the unsteady solution is a combination of a Stokes-layer solution, that is fully determined, and a sum of eigenmodes, which take into account the initial conditions. These eigenmodes were first found by Lam and Rott (1960) for flow past a flat plate, and these authors later showed that these eigenmodes are also valid for arbitrary pressure gradients (Lam and Rott, 1993). Goldstein (1983) showed that it's these eigenmodes which provide the wavelength shortening process required for the external disturbance to excite T-S waves. This was demonstrated by showing that the unstable eigenmode from Orr-Sommerfeld theory matches, in the matched asymptotic sense, to the the first Lam-Rott eigenmode in a matching region which occurs on a streamwise length scale of the order $Re^{\frac{1}{3}}$. These eigenmodes were generalised by Hammerton and Kerschen (1996), for the case of a parabola, and further by Nichols (2001) who derived them for a general body for which the inviscid slip velocity tends to a constant far downstream.

There is another orthogonal set of eigenmodes, which are solutions to the LUBLE, found by Brown and Stewartson (1973), these modes decay more slowly than Lam-Rott modes, and have been less widely studied. We shall just consider the Lam-Rott modes in the present work, as they have been shown to match onto the unstable mode of the Orr-Sommerfeld equation. It has, however, been conjectured that the Brown-Stewartson modes are the Lam-Rott modes in the limit as $\xi \longrightarrow \infty$ (Goldstein *et al.*, 1983), although this will not be considered here.

The unsteady solution $\phi_2(\xi, N)$ is considered to have the form

$$\phi_2(\xi, N) \sim \phi_{ST}(\xi, N) + \sum_{i=1}^{\infty} C_i \phi_{2,i}(\xi, N), \tag{2.63}$$

where $\phi_{ST}(\xi, N)$ denotes the Stokes-layer solution to the LUBLE, and $\phi_{2,i}(\xi, N)$ are the eigenmodes. The Stokes solution, $\phi_{ST}(\xi, N)$, is found by solving the LUBLE using the boundary conditions (2.40). However the eigenmodes are found by solving the LUBLE (2.37) with the forcing terms on the right hand side set equal to zero, and with homogeneous boundary conditions. Goldstein (1983) showed that it's the lowest order eigenmode, $\phi_{2,1}$, which matches, in the matched asymptotic expansion sense, onto the growing T-S wave, and this will be important when applying our initial conditions to the PSE. This fact is important because we are interested in calculating the amplitude of the T-S mode which grows downstream of the neutral stability point, as it is assumed that this mode eventually leads to turbulence in the boundary-layer and consequently boundary-layer separation (Saric *et al.*, 2002).

To simplify the algebra, and to be consistent with work done by Ackerberg and Phillips (1972) and Hammerton and Kerschen (1996), we introduce a new variable $G(\xi, N)$ to replace $\phi_2(\xi, N)$ in the LUBLE. We define this variable as

$$G(\xi, N) = (2\xi)^{\frac{1}{2}} \phi_2(\xi, N), \tag{2.64}$$

which on introduction to the LUBLE with the forcing terms set equal to zero gives

$$G_{NNN} + (\phi_1 + 2\xi\phi_{1\xi})\, G_{NN} + (i\Omega(\xi) + (1 - 2\beta(\xi))\phi_{1N} - 2\xi\phi_{1N\xi})\, G_N \\ +2\xi\,(\phi_{1NN} G_\xi - \phi_{1N} G_{N\xi}) = 0. \tag{2.65}$$

As mentioned earlier, the Stokes solution, ϕ_{ST}, can be found by numerically solving (2.65) with homogeneous boundary conditions at the wall, but with the condition $\partial\phi_{ST}/\partial N \longrightarrow (2\xi)^{-\frac{1}{2}}$, for fixed ξ, as $N \longrightarrow \infty$. However we can also form the large ξ asymptotic form of ϕ_{ST}, which when evaluated at the outer edge of the boundary-layer is given by

$$\phi_{ST}(\xi, N) = N - \frac{1+i}{2}\frac{1}{\xi^{\frac{1}{2}}} + \frac{i\beta}{2}\frac{1}{\xi} + \frac{13U_0'}{32}\frac{1}{\xi^2} - \frac{39iU_0'}{64}\frac{1}{\xi^3} - \frac{4051(1-i)U_0'^2}{2048}\frac{1}{\xi^{\frac{7}{2}}} + O(Re^{-1}), \tag{2.66}$$

where $U_0' = f''(0) = 0.4696....$ and $\beta = \lim_{N\longrightarrow\infty}(Nf' - f) \approx 1.217$. This result provides a good check for the full numerical solution of ϕ_{ST}.

Solution in the inner and main layer

Close to the wall in the inner layer, a change of variable is required, and Nichols (2001) solved (2.65) in this layer, by changing to the inner variable

$$M = (2\xi)^{\frac{1}{2}} \left(\left(\frac{b_1}{2} \right)^{\frac{1}{2}} + \left(\frac{1}{2b_1} \right)^{\frac{1}{2}} \frac{b_2}{2\xi} \right) N, \tag{2.67}$$

and by looking for a solution in the form

$$G(\xi, M) = e^{T(\xi)} f(\xi, M), \tag{2.68}$$

where $f(\xi, M)$ and $T(\xi)$ are expanded in powers of 2ξ. The main deck solution needed no variable change, but again the solution was written in the form

$$G(\xi, N) = e^{T(\xi)} g(\xi, N), \tag{2.69}$$

where $g(\xi, N)$ is again expanded in powers of 2ξ. The solution in these two decks can be written, after matching, as

$$\psi = \begin{cases} \xi^{\tau_j} e^{T(\xi)} \left(U_0' \frac{\int_0^M (M - \widetilde{M}) Ai(\tilde{z}) d\widetilde{M}}{\int_0^\infty Ai(\tilde{z}) d\widetilde{M}} + O(\xi^{-\frac{3}{2}}) \right) & N = O(\xi^{-\frac{1}{2}}), \\ \xi^{\tau_j} e^{T(\xi)} \left((2\xi)^{\frac{1}{2}} f'(N) + \frac{U_0' i}{\lambda_j} + O(\xi^{-\frac{1}{2}}) \right) & N = O(1), \end{cases} \tag{2.70}$$

where

$$U_0' = f''(0) = 0.4696....., \tag{2.71}$$

$$\tilde{z} = -\rho_j + \rho_j^{-\frac{1}{2}} e^{\frac{i\pi}{4}} \widetilde{M}, \tag{2.72}$$

$$\lambda_j = \rho_j^{-\frac{3}{2}} e^{-\frac{i\pi}{4}}, \tag{2.73}$$

$$\tau_j = -\frac{889 - 16\rho_j^3}{1260} + a_1 \left(\frac{2}{b_1} \right)^{\frac{1}{2}} \frac{8\rho_j^3 - 27}{20 U_0'^2 \rho_j^3} i, \tag{2.74}$$

$$T_j(\xi) = -\frac{\lambda_j (2\xi)^{\frac{3}{2}}}{U_0'} \left(\frac{b_1}{2} \right)^{\frac{3}{2}} \left(\frac{1}{3} - 0.60115 a_1 \frac{\ln(\xi)}{\xi} + \left(1.2023 a_1 - D + \frac{3b_2}{2b_1} \right) \frac{1}{\xi} \right) + O(\xi^{-0.387}). \tag{2.75}$$

Here ρ_j are the solutions of the equation

$$Ai'(-\rho_j) = 0,$$

where Ai' is the derivative of the Airy function (Appendix B). The first 5 solutions for ρ_j are

$$\begin{aligned}\rho_1 &= 1.01879,\\ \rho_2 &= 3.24820,\\ \rho_3 &= 4.82010,\\ \rho_4 &= 6.16331,\\ \rho_5 &= 7.37281,\end{aligned}$$

and it's the first of these solutions which matches onto the growing T-S mode in the Orr-Sommerfeld region, so will provide most interest to us in this work (Abramowitz, 1964).

The solution (2.70) is valid within the boundary-layer, but does not take into account the slow decay of the eigenmode as $N \longrightarrow \infty$, however, we will see in the next section that the PSE equation is valid for $N \in [0, \infty)$. Thus to be able to use (2.70) as an upstream boundary condition, we need to find the outer solution to the leading edge problem, in the outer inviscid region. This solution has not been calculated before in previous work.

Solution in the outer inviscid layer

To find the solution in the outer inviscid region, we first go back to the non-dimensional form of the Navier-Stokes equations (2.6) and (2.7). Instead of introducing the boundary-layer variables and only taking the leading order terms, we instead consider all the terms. We then introduce a stream function (2.18) as before, to give the equations

$$\frac{\partial^2\psi}{\partial y\partial t}+\frac{\partial\psi}{\partial y}\frac{\partial^2\psi}{\partial x\partial y}-\frac{\partial\psi}{\partial x}\frac{\partial^2\psi}{\partial y^2} = -\frac{\partial p}{\partial x}+\frac{\partial^3\psi}{\partial y^3}+\frac{1}{Re}\frac{\partial^3\psi}{\partial x^2\partial y}, \tag{2.76}$$

$$\frac{1}{Re}\left(-\frac{\partial^2\psi}{\partial x\partial t}-\frac{\partial\psi}{\partial y}\frac{\partial^2\psi}{\partial x^2}+\frac{\partial\psi}{\partial x}\frac{\partial^2\psi}{\partial x\partial y}\right) = -\frac{\partial p}{\partial y}-\frac{1}{Re}\frac{\partial^3\psi}{\partial x\partial y^2}-\frac{1}{Re^2}\frac{\partial^3\psi}{\partial x^3}. \tag{2.77}$$

We can then eliminate the pressure by taking $\partial/\partial y$ (2.76)$-\partial/\partial x$ (2.77), to give

$$\begin{aligned}\frac{\partial^3\psi}{\partial y^2\partial t} &+ \frac{\partial\psi}{\partial y}\frac{\partial^3\psi}{\partial x\partial y^2}-\frac{\partial\psi}{\partial x}\frac{\partial^3\psi}{\partial y^3}-\frac{\partial^4\psi}{\partial y^4}\\ &= \frac{1}{Re}\left(\frac{\partial\psi}{\partial x}\frac{\partial^3\psi}{\partial x^2\partial y}-\frac{\partial^3\psi}{\partial x^2\partial t}-\frac{\partial\psi}{\partial y}\frac{\partial^3\psi}{\partial x^3}+2\frac{\partial^4\psi}{\partial x^2\partial y^2}\right)+\frac{1}{Re^2}\frac{\partial^4\psi}{\partial x^4}.\end{aligned} \tag{2.78}$$

As before, we split the stream function, ψ, into a steady base flow part, and an unsteady perturbation part. Hence we write

$$\psi(x,y,t) = \psi_1(x,y) + \delta\psi_2(x,y)e^{-it},$$

where $\delta \ll 1$, and $\psi_1(x,y)$ and $\psi_2(x,y)$ are $O(1)$. The leading order equation for ψ_1, after integration with respect to y, is given by equation (2.19), after changing variables from (x,y) to (ξ,N), with added correction terms of $O(Re^{-1})$.

The $O(\delta)$ equation is

$$-i\frac{\partial^2\psi_2}{\partial y^2} + \frac{\partial\psi_1}{\partial y}\frac{\partial^3\psi_2}{\partial x\partial y^2} + \frac{\partial^3\psi_1}{\partial x^2\partial y}\frac{\partial\psi_2}{\partial y} - \frac{\partial\psi_1}{\partial x}\frac{\partial^3\psi_2}{\partial y^3} - \frac{\partial\psi_2}{\partial x}\frac{\partial^3\psi_1}{\partial y^3} - \frac{\partial^4\psi_2}{\partial y^4} =$$
$$\epsilon^6\left(2\frac{\partial^4\psi_2}{\partial x^2\partial y^2} + i\frac{\partial^2\psi_2}{\partial x^2} - \frac{\partial\psi_1}{\partial y}\frac{\partial^3\psi_2}{\partial x^3} - \frac{\partial\psi_2}{\partial y}\frac{\partial^3\psi_1}{\partial x^3} + \frac{\partial\psi_1}{\partial x}\frac{\partial^3\psi_2}{\partial x^2\partial y} + \frac{\partial\psi_2}{\partial x}\frac{\partial^3\psi_1}{\partial x^2\partial y}\right)$$
$$+\epsilon^{12}\frac{\partial^4\psi_2}{\partial x^4}, \quad (2.79)$$

which is the y derivative of (2.37) after the appropriate change of variables, and with added terms due to viscosity, and $\epsilon^6 = Re^{-1}$, which is different to the value of ϵ introduced earlier.

We now change to the (ξ,N) variables defined in (2.33) and (2.23). To seek a solution in the outer inviscid region, we introduce the scaled variables

$$X = \epsilon^s\xi, \qquad M = \epsilon^t N, \quad (2.80)$$

into (2.79), where s and t are positive real numbers. We note that as we are outside the boundary-layer, $N \longrightarrow \infty$, therefore $\psi_1 \sim (2\xi)^{\frac{1}{2}}N$ and we seek a solution for ψ_2 in the form

$$\psi_2 = (2\xi)^{\frac{1}{2}}G(\xi,N)\exp\left(\frac{2(2\xi)^{\frac{3}{2}}\mu(\xi)}{3}\right) \quad \text{where} \quad \mu(\xi) = -\lambda_j/(U_0'\hat{\gamma}(\xi)),$$

and

$$\hat{\gamma} = \left(1 + 0.60115a_1\frac{\ln(\xi)}{\xi} + \frac{D}{\xi} - \frac{3b_2}{2b_1\xi}\right)\left(\frac{2}{b_1}\right)^{\frac{3}{2}} + O(\xi^{-1.887}), \quad (2.81)$$

which was motivated by the solution in the two lower decks (2.70).

We find the only appropriate choice for the balancing of terms which gives s and t both positive, and gives a non-trivial balance at leading order, is for $s+t=3$. Goldstein

(1983) discusses that the matching region between the leading edge region, and the Orr-Sommerfeld region occurs when $\xi = O(\epsilon^{-2})$, hence we set $s = 2$ and $t = 1$. This then gives the leading order equation for $G(X, M)$ as

$$U_f^2 \left(U_f^2 \mu - \epsilon i (2X)^{-\frac{1}{2}} \right) \left(G_{MM} + (2X)^2 \mu^2 G \right) = O(\epsilon^2). \tag{2.82}$$

We seek an asymptotic form of $G(X, M) = G_0(X, M) + \epsilon G_1(X, M)$. Hence at leading order

$$G_{0MM} + (2X)^2 \mu^2 G_0 = 0, \tag{2.83}$$

to which the bounded solution as $M \longrightarrow \infty$ is

$$G_0(X, M) = A_0 \exp \left(\frac{-\sqrt{2}(1+i)XM}{U_0' \hat{\gamma} \rho_j^{\frac{3}{2}}} \right), \tag{2.84}$$

as,

$$\mu(X) = \frac{-\lambda_j}{U_0' \hat{\gamma}(X)} = \frac{(1-i)}{\sqrt{2} U_0' \hat{\gamma}(X) \rho_j^{\frac{3}{2}}}.$$

At $O(\epsilon)$ we have from (2.82)

$$\begin{aligned} U_f^4 \mu (G_{1MM} + (2X)^2 \mu^2 G_1) &= i U_f^2 (2X)^{-\frac{1}{2}} (G_{0MM} + \mu^2 (2X)^2 G_0), \\ &= 0 \end{aligned} \tag{2.85}$$

by using the solution for G_0. This gives us the bounded solution

$$G_1 = A_1 \exp \left(\frac{-\sqrt{2}(1+i)XM}{U_0' \hat{\gamma} \rho_j^{\frac{3}{2}}} \right). \tag{2.86}$$

The functions of X, A_0 and A_1, are found by matching with the main deck given in (2.70). The outer inviscid solution as $M \longrightarrow 0$ is given from (2.84) and (2.86) as

$$\psi_{outer} \sim \frac{(2X)^{\frac{1}{2}}}{\epsilon} (A_0 + \epsilon A_1) e^{T_j(\xi)},$$

where

$$T_j(\xi) = -\frac{\lambda_j (2\xi)^{\frac{3}{2}}}{3 U_0' \hat{\gamma}},$$

which in the large ξ limit is given by (2.75). The main deck solution as $N \longrightarrow \infty$, given by (2.70) is

$$\psi_{main} \sim (\epsilon^{-2} X)^{\tau_j} e^{T_j(\xi)} \left(\frac{(2X)^{\frac{1}{2}}}{\epsilon} + \frac{U_0' i}{\lambda_j} \right),$$

therefore

$$A_0 = (\epsilon^{-2}X)^{\tau_j}, \quad A_1 = \frac{(\epsilon^{-2}X)^{\tau_j}}{(2X)^{\frac{1}{2}}}\left(\frac{U_0'i}{\lambda_j}\right),$$

and hence the solution for ψ in the outer inviscid region is

$$\psi = \xi^{\tau_j}e^{T_j(\xi)}\left((2\xi)^{\frac{1}{2}} + \frac{U_0'i}{\lambda_j}\right)\exp\left(\frac{-\epsilon^3\sqrt{2}(1+i)\xi N}{U_0'\hat{\gamma}(\xi)\rho_j^{\frac{3}{2}}}\right). \tag{2.87}$$

Now we have the complete form for the shape of the eigenmode over the full N domain, hence we can now use this as our initial condition to the PSE, which is derived in the next section.

2.2 Orr-Sommerfeld region

As we move downstream from the leading edge, the rapid boundary-layer growth close to the leading edge has diminished, and the boundary-layer has become almost parallel to the surface of the body. Goldstein (1983) showed that this region occurs when $\xi = O(\epsilon^{-2})$, where $\epsilon = Re^{-\frac{1}{6}} = (\nu\omega/U_\infty^2)^{-\frac{1}{6}}$. At leading order, this region is governed by the Orr-Sommerfeld equation. However, the Orr-Sommerfeld equation is only strictly valid for parallel flows, and although this is a good first approximation, in general this equation leads to unsatisfactory results when dealing with boundary-layers. It is also possible to use a non-parallel formulation of the Orr-Sommerfeld equation (Saric and Nayfeh, 1975), but this method has its limitations, as we shall discuss later. Instead, to incorporate the now slow growth in the boundary-layer, we model the flow in this region numerically, using the Parabolized Stability Equation, first introduced by Bertolotti *et al.* (1992). Goldstein (1983) solved the equations in this region asymptotically, and we shall use this result to compare with our numerics. We shall also discuss later the difficulty with extending the asymptotic method to bodies with curvature.

2.2.1 Parabolized Stability Equation

We consider a body in a uniform stream, U_∞, which has a small free-stream disturbance, of frequency, ω_P^*. The coordinates x_P^*, and y_P^* represent dimensional coordinates along

the body, and normal to the body respectively, where the subscript P denotes that we are in the PSE region.

We introduce non-dimensional quantities, based on the velocity scale U_∞ and boundary-layer thickness length scale $\delta_0 = \delta(x_0) = (\nu x_0^*/U_\infty)^{\frac{1}{2}}$, where x_0^* is a dimensional distance from the leading edge, which we take to be the starting point of our analysis, and ν is the kinematic viscosity. Based on these two quantities, we define our time scale as δ_0/U_∞.

The non-dimensional Navier-Stokes equations based on these non-dimensional quantities are

$$\frac{\partial u_P}{\partial t_P} + u_P\frac{\partial u_P}{\partial x_P} + v_P\frac{\partial u_P}{\partial y_P} = -\frac{\partial p_P}{\partial x_P} + \frac{1}{R_0}\left(\frac{\partial^2 u_P}{\partial x_P^2} + \frac{\partial^2 u_P}{\partial y_P^2}\right), \tag{2.88}$$

$$\frac{\partial v_P}{\partial t_P} + u_P\frac{\partial v_P}{\partial x_P} + v_P\frac{\partial v_P}{\partial y_P} = -\frac{\partial p_P}{\partial y_P} + \frac{1}{R_0}\left(\frac{\partial^2 v_P}{\partial x_P^2} + \frac{\partial^2 v_P}{\partial y_P^2}\right), \tag{2.89}$$

$$\frac{\partial u_P}{\partial x_P} + \frac{\partial v_P}{\partial y_P} = 0, \tag{2.90}$$

where R_0 is the Reynolds number based on the length scale δ_0, and is defined to be

$$R_0 = \frac{U_\infty \delta_0}{\nu} = \frac{x_0^*}{\delta_0} = x_0, \tag{2.91}$$

x_0 is the dimensionless distance from the leading edge, p_P is the pressure, and (u_P, v_P) is the velocity in the (x_P, y_P) direction. The subscript P on the variables, denote that we are in the PSE regime. As in the leading edge region, the Reynolds number is assumed to be large.

Eliminating the pressure by doing $\partial/\partial y_P$ (2.88)$-\partial/\partial x_P$ (2.89), and introducing a stream function Ψ_P, such that

$$\frac{\partial \Psi_P}{\partial y_P} = u_P \qquad \frac{\partial \Psi_P}{\partial x_P} = -v_P,$$

we find that the vorticity equation for the stream function is

$$\left(\frac{\partial}{\partial t_P} - \frac{1}{R_0}\nabla^2 + \frac{\partial \Psi_P}{\partial y_P}\frac{\partial}{\partial x_P} - \frac{\partial \Psi_P}{\partial x_P}\frac{\partial}{\partial y_P}\right)\nabla^2 \Psi_P = 0. \tag{2.92}$$

We also introduce the definition of the Reynolds number based on the length scale $\delta(x_P)$ to be $R = (x_P R_0)^{\frac{1}{2}} = (U_\infty x_P^*/\nu)^{\frac{1}{2}} = (x_P/x_0)^{\frac{1}{2}} R_0$.

We split the stream function $\Psi_P(x_P, y_P, t_P)$ into a time dependent disturbance part, $\psi_P(x_P, y_P, t_P)$, and the mean steady base flow, $\Psi_B(x_P, y_P)$, under the assumption that

$\psi_P \ll \Psi_B$. Inserting $\Psi_P = \Psi_B + \psi_P$ into (2.92), leads to the following equations for Ψ_B and ψ_P,

$$\left(\frac{\partial \Psi_B}{\partial y_P}\frac{\partial}{\partial x_P} - \frac{\partial \Psi_B}{\partial x_P}\frac{\partial}{\partial y_P}\right)\nabla^2\Psi_B = \frac{1}{R_0}\nabla^4\Psi_B, \tag{2.93}$$

$$\left(\frac{\partial}{\partial t_P} - \frac{1}{R_0}\nabla^2 + \frac{\partial \Psi_B}{\partial y_P}\frac{\partial}{\partial x_P} - \frac{\partial \Psi_B}{\partial x_P}\frac{\partial}{\partial y_P}\right)\nabla^2\psi_P + \frac{\partial^3\Psi_B}{\partial x_P^3}\frac{\partial \psi_P}{\partial y_P} + \frac{\partial^3\Psi_B}{\partial x_P \partial y_P^2}\frac{\partial \psi_P}{\partial y_P}$$
$$-\frac{\partial^3\Psi_B}{\partial x_P^2 \partial y_P}\frac{\partial \psi_P}{\partial x_P} - \frac{\partial^3\Psi_B}{\partial y^3}\frac{\partial \psi_P}{\partial x_P} = \left(\frac{\partial \psi_P}{\partial x_P}\frac{\partial}{\partial y_P} - \frac{\partial \psi_P}{\partial x_P}\frac{\partial}{\partial y_P}\right)\nabla^2\psi_P + O(R_0^{-2}). \tag{2.94}$$

As for the leading edge region in §2.1, these equations still hold at leading order, if the curvature of the body is small.

Motivated by our work in §2.1, we introduce the following change of variables

$$\xi_P = \int_0^{x_P} U_f(x')dx', \tag{2.95}$$

$$N_P = R_0^{\frac{1}{2}} g(\xi_P) y_P, \tag{2.96}$$

where $g(\xi_P) = U_f(\xi_P)(2\xi_P)^{-\frac{1}{2}}$. Under this change of variables, it's easy to show that the function for the base flow $\phi_B = (2\xi_P)^{-\frac{1}{2}}\Psi_B$ in fact satisfies (2.34), and hence we can write down its large ξ_P asymptotic form as

$$\Psi_B = R_0^{-\frac{1}{2}}(2\xi_P)^{\frac{1}{2}}\left(\phi_\alpha(N_P) + \phi_\beta(N_P)\frac{\ln(\xi_P)}{\xi_P} + \phi_\gamma(N_P)\frac{1}{\xi_P}\right). \tag{2.97}$$

Note that ϕ_α, ϕ_β, and ϕ_γ are different from ϕ_a, ϕ_b and ϕ_c as $\xi \neq \xi_P$, but we shall write down their full forms later.

We seek a solution to (2.94) in the form of traveling waves. A spatially evolving wave of constant angular frequency ω_P, is described by specifying the streamwise wavenumber $\alpha(\xi_P)$ and the velocity profiles as derivatives of the complex mode shape $\phi(\xi_P, N_P)$. These components combine to give the disturbance stream function in the form,

$$\psi_P(\xi_P, N_P, t_P) = \phi(\xi_P, N_P)\chi(\xi_P, t_P) + \text{complex conjugate}, \tag{2.98}$$

where

$$\chi(\xi_P, t_P) = \exp\left(i(\theta(\xi_P) - \omega_P t_P)\right),$$

and

$$\frac{d\theta}{d\xi_P} = \alpha(\xi_P).$$

In the parallel flow case, we assume that the mode shape ϕ is independent of ξ_P, and we derive the Orr-Sommerfeld equation. In the non-parallel case, our best chance to simplify the problem is to have ϕ and α as slowly varying functions of ξ_P. This cannot be assumed straight away, because both oscillations and growth, in ξ_P, can be absorbed into ϕ, as well as the phase function θ. We can remove this ambiguity by considering the variation of ϕ with ξ_P. Unlike the parallel case, we can't find ϕ independent of ξ_P, except in some average sense across the whole flow domain in N_P. In the simple 2D case, we could apply a simple norm such as, $|u_P(N_P^{max})| = \text{constant}$, at some suitable distance N_P^{max} from the boundary, but we prefer norms which are physically and mathematically meaningful. To that extent, we note that, from (2.98)

$$(\ln(\psi_P))_{\xi_P} = \frac{\phi_{\xi_P}}{\phi} + i\alpha,$$

which when multiplied by $|\phi|^2$ and integrated from $N_P = 0$ to ∞ gives,

$$-i\frac{\int_0^\infty (\ln(\psi_P))_{\xi_P}|\phi|^2 dN_P}{\int_0^\infty |\phi|^2 dN_P} = \alpha - i\frac{\int_0^\infty \phi_{\xi_P}\phi^\dagger dN_P}{\int_0^\infty |\phi|^2 dN_P}, \tag{2.99}$$

where † denotes the complex conjugate. From (2.99) it seems reasonable to choose as our norm,

$$\int_0^\infty \phi_{\xi_P}\phi^\dagger dN_P = 0, \tag{2.100}$$

which minimizes the streamwise variation of ϕ, weighted by its complex conjugate, when averaged between $N = 0$ and ∞. This normalization condition places most of the streamwise variation of the solution into the exponential term in (2.98). Thus from (2.99) we take as our definition for α

$$\alpha = -i\frac{\int_0^\infty (\ln(\psi_P))_{\xi_P}|\phi|^2 dN_P}{\int_0^\infty |\phi|^2 dN_P}.$$

From (2.97) and (2.91) we can see that $\Psi_B(\xi_P, N_P)$ varies on a short length scale of $O(R_0^{-1})$, i.e. $\partial\Psi_B/\partial\xi_P = O(R_0^{-1})$. Therefore in the derivation of the Parabolized Stability Equation, we assume that the disturbance ψ_P varies on a short length scale too, which is at most as large as the base flow's length scale. By this we mean that $\partial\phi/\partial\xi_p$ and $d\alpha/d\xi_P$ are at most $O(R_0^{-1})$. This assumption has also been seen to hold for T-S waves in experiments and numerical computations (Morkovin, 1985). Thus we assume that second

derivatives of ϕ and α with respect to ξ_P and the product of their first derivatives are of $O(R_0^{-2})$, and hence negligibly small. Also in the derivation of the PSE, we assume that the disturbances in the boundary-layer grow and decay as convected instabilities. That is that the mean base flow acts merely as an amplifier of the initial disturbances, and in the absence of these disturbances, the flow would return to its original state.

Neglecting the second and higher derivatives of α and ϕ with respect to ξ_P, attempts to change the character of the PDE (2.94) from elliptic to parabolic, and this is only permitted if the stability problem is governed by downstream propagating information, while the upstream propagation can be neglected. The formulation does this, by changing the eigenvalue of the problem to one which has no upstream propagating information (Andersson *et al.*, 1998). Attempting to parabolize the PDE (2.94) gives the resulting equation the name Parabolized Stability Equation, however, it is not fully parabolic, and still contains a small amount of ellipticity, and it is this ellipticity which gives rise to numerical problems which we discuss in chapter 4.

Using the assumptions, we can simplify derivatives of ψ_P with respect to ξ_P into the following form,

$$\frac{\partial^m \psi_P}{\partial \xi_P^m} = \left((i\alpha)^m \phi + m(i\alpha)^{m-1} \frac{\partial \phi}{\partial \xi_P} + im(m-1)(i\alpha)^{m-2} \frac{d\alpha}{d\xi_P} \phi \right) \exp\left(i(\theta - \omega_P t)\right). \tag{2.101}$$

For the purposes of this work, we shall only be considering the linear form of (2.94), which we can do if the disturbances to the base flow are suitably small, $\psi_P \ll 1$. Although we are not considering the non-linear case here, this work can easily be extended to incorporate weakly non-linear effects, which would become important if this work was extended to look at the amplitudes of disturbances at the upper branch neutral stability point. The non-linear PSE have been formulated by Bertolotti *et al.* (1992), and have been shown to yield good agreement with full numerical simulations in problems where weakly non-linear effects are important. However in only marching up to the lower branch neutral stability point, the non-linear effects are negligible, and hence the linear equation will be sufficient.

Introducing (2.95), (2.96), (2.98) and (2.101) into (2.94), and neglecting any terms of

$O(R_0^{-2})$, leads to the linear form of the PSE,

$$(L_0 + L_1 + L_2)\phi + M\frac{\partial\phi}{\partial\xi_P} + \frac{d\alpha}{d\xi_P}N\phi = 0, \tag{2.102}$$

where

$$\begin{aligned}
L_0 &= -\frac{1}{R_0}\left(\frac{R_0 D^2}{2\xi_P} - \alpha^2\right)^2 + \left(i\alpha\Psi_{B1} - i\omega_P U_f^{-2}\right)\left(\frac{R_0 D^2}{2\xi_P} - \alpha^2\right) \\
&- i\alpha\Psi_{B2}, && (2.103)\\
L_1 &= \frac{R_0^{\frac{1}{2}}}{(2\xi_P)^{\frac{1}{2}}}\Psi_{B3}D - \frac{R_0^{\frac{1}{2}}}{(2\xi_P)^{\frac{1}{2}}}\Psi_{B4}\left(\frac{R_0 D^3}{2\xi_P} - \alpha^2 D\right), && (2.104)\\
L_2 &= \left(\frac{U_f'}{U_f} - \frac{1}{2\xi_P}\right)N_P\left(\Psi_{B1}\left(\frac{R_0 D^3}{2\xi_P} - 3\alpha^2 D\right) + 2\omega_P\alpha U_f^{-2}D - \Psi_{B2}D\right) \\
&+ 2R_0\Psi_{B1}\left(\frac{U_f'}{2\xi_P U_f} - \frac{1}{4\xi_P^2}\right)D^2 + \omega_P\alpha U_f' U_f^{-3} - 3\Psi_{B1}U_f' U_f^{-1}\alpha^2, && (2.105)\\
M &= \Psi_{B1}\left(\frac{R_0 D^2}{2\xi_P} - 3\alpha^2\right) + 2\omega_P\alpha U_f^{-2} - \Psi_{B2}, && (2.106)\\
N &= \omega_P U_f^{-2} - 3\alpha\Psi_{B1}, && (2.107)
\end{aligned}$$

and $D \equiv d/dN_P$, and the dashes on the U_f terms denote derivatives with respect to ξ_P. The functions $\Psi_{Bn}(x_P, y_P)$ are defined as

$$\begin{aligned}
\Psi_{B1} &= \frac{1}{U_f}\frac{\partial\Psi_B}{\partial y_P}, \\
\Psi_{B2} &= \frac{1}{U_f^3}\frac{\partial^3\Psi_B}{\partial y_P^3}, \\
\Psi_{B3} &= \frac{1}{U_f^3}\frac{\partial^3\Psi_B}{\partial x_P\partial y_P^2}, \\
\Psi_{B4} &= \frac{1}{U_f}\frac{\partial\Psi_B}{\partial x_P},
\end{aligned}$$

which we shall write out using (2.97) later.

For the purposes of this work, we are only interested in the propagation of the eigenmodes of the LUBLE, which have homogeneous boundary conditions. Hence we solve

(2.102) subject to

$$v_P = 0 \text{ on } N_P = 0 \implies \phi(x_P, 0) = 0, \tag{2.108}$$

$$u_P = 0 \text{ on } N_P = 0 \implies \frac{\partial \phi}{\partial N_P}(x_P, 0) = 0, \tag{2.109}$$

$$v_P = 0 \text{ as } N_P \longrightarrow \infty \implies \phi(x_P, N_P) \longrightarrow 0 \text{ as } N_P \longrightarrow \infty, \tag{2.110}$$

$$u_P = 0 \text{ as } N_P \longrightarrow \infty \implies \frac{\partial \phi}{\partial N_P}(x_P, N_P) \longrightarrow 0 \text{ as } N_P \longrightarrow \infty. \tag{2.111}$$

We also need to stipulate an upstream boundary (initial) condition for the PSE, so we set

$$\phi(\xi_0, N_P) = F(N_P) \quad \alpha(\xi_0) = \alpha_0, \tag{2.112}$$

where ξ_0 is the dimensionless starting position on the body. There are various forms of upstream boundary conditions applicable to the PSE, the one we shall consider most of all is the leading edge asymptotic form, although we could use a parallel boundary-layer assumption at the initial point, or a locally non-parallel boundary-layer assumption at the initial point, both of which will be discussed in more depth in §4 when we consider a flat plate.

The structure of the eigenvalues in the Orr-Sommerfeld region is the same as shown in figure 1.2 of chapter 1. We have a continuous spectrum, and the most unstable eigenvalue moves from this continuous spectrum towards the line $Im(\alpha) = 0$. The fact that the most unstable eigenvalue approaches the continuous spectrum as we approach the leading edge, leads to numerical difficulties when solving the Orr-Sommerfeld equation and the local PSE equation described in the next section. The numerical problem occurs because we cannot distinguish between the unstable eigenvalue and the continuous spectrum as the leading edge is approached. Thus we are unable to solve these problems right back to the leading edge. This numerical problem is discussed more in chapter 4.

2.2.2 Local solution to the PSE

We can solve the PSE locally about some upstream position $\xi_P = \xi_0$, by writing the solution as a Taylor series expansion in powers of $\hat{\xi} = \xi_P - \xi_0$. We note that the higher derivatives can all be neglected because of the assumptions we made on the PSE that

$\phi_{\xi_P\xi_P}$, $\alpha_{\xi_P\xi_P}$ and the product of first derivatives are $O(R_0^{-2})$. Expanding $\phi(\xi_P, N_P)$ and $\alpha(\xi_P)$ about ξ_0, we obtain

$$\phi(\xi_P, N_P) = \phi(\xi_0, N_P) + \hat{\xi}\left.\frac{\partial\phi(\xi_P, N_P)}{\partial\xi_P}\right|_{\xi_P=\xi_0} + O(\hat{\xi}^2) = \phi_0 + \hat{\xi}\phi_1, \quad (2.113)$$

$$\alpha(\xi_P) = \alpha(\xi_0) + \hat{\xi}\left.\frac{d\alpha(\xi_P)}{d\xi_P}\right|_{\xi_P=\xi_0} + O(\hat{\xi}^2) = \alpha_0 + \hat{\xi}\alpha_1, \quad (2.114)$$

where the $O(\hat{\xi}^2)$ terms are zero due to the PSE assumption on ϕ and α.

Substituting these into (2.102) and requiring that the equation be valid for varying $\hat{\xi}$ produces two equations

$$(L_0 + L_1 + L_2 + \alpha_1 N)\phi_0 + M\phi_1 = 0, \quad (2.115)$$

$$(L_4 + i\alpha_1 M)\phi_0 + L_0\phi_1 = 0, \quad (2.116)$$

where

$$L_4 = -\frac{R_0}{2\xi_0^2}\left(i\alpha_0\Psi_{B1} - i\omega U_f^{-2}\right)D^2 + \left(i\alpha_0\Psi_{B1\xi_P} + \frac{2i\omega U_f'}{U_f^3}\right)\left(\frac{R_0 D^2}{2\xi_0} - \alpha_0^2\right) - i\alpha_0\Psi_{B2\xi_P} + \frac{R_0 D^4}{2\xi_0^3}, \quad (2.117)$$

and in the operators, L_0, L_1, L_2, M and N, α is replaced by α_0. The local form of the PSE is commonly used as the initial condition to the PSE, to take into account some of the non-parallel effects (Bertolotti *et al.*, 1992, Herbert, 1993).

2.3 Comparison of leading edge and PSE variables

The leading edge receptivity results, and the Parabolized Stability Equation derived in sections §2.1 and §2.2, were derived using different non-dimensional variables, via a different length scale. This was done to keep the general derivations simple, and to keep them in accord with the form in which they were originally derived in their original contexts. This means it's difficult to change the leading edge solution into the PSE variables to act as the initial condition to the PSE. Thus in this section we link the two sets of variables in both regions, so that we can change the leading edge solution into the PSE variables,

Quantity	PSE	leading edge
Length scale	δ_0	U_∞/ω
Velocity scale	U_∞	U_∞
Time scale	δ_0/U_∞	ω^{-1}
Reynolds number	$R_0 = U_\infty\delta_0/\nu$	$Re = \epsilon^{-6} = U_\infty^2/\omega\nu$

Table 2.1: Table comparing dimensional quantities for the leading edge and PSE schemes.

and after the PSE calculation, change back to the leading edge variables to compare with other results such as those of Goldstein (1983).

Table 2.1 gives a comparison of the major scalings for the two schemes used. If we compare the two streamwise, x, coordinates, we find

$$\begin{aligned} x^* &= \delta_0 x_P, \\ x^* &= \frac{U_\infty}{\omega} x, \end{aligned}$$

where * again signifies a dimensional quantity. Now, as both these dimensional quantities are the same, we can equate them to give

$$\frac{x}{x_P} = \frac{\delta_0\omega}{U_\infty} = \frac{R_0}{Re}. \tag{2.118}$$

To compare the streamwise variables ξ and ξ_P, we note from (2.33) and (2.95) that

$$\frac{d\xi}{dx} = U_f(x) = \frac{d\xi_P}{dx_P},$$

therefore using (2.118) we find

$$\frac{d\xi}{dx} = \frac{R_0}{Re}\frac{d\xi_P}{dx}.$$

Integrating, and setting the arbitrary constant to 0 without loss or generality, we find

$$\frac{\xi}{\xi_P} = \frac{R_0}{Re}, \tag{2.119}$$

which is of the same form as (2.118).

Equating the dimensional y^* coordinates, we find

$$\begin{aligned} \frac{\delta_0(2\xi_P)^{\frac{1}{2}}N_P}{U_f R_0^{\frac{1}{2}}} &= \frac{U_\infty(2\xi)^{\frac{1}{2}}N}{\omega Re^{\frac{1}{2}}}, \\ \frac{R_0}{Re}\frac{(2\xi_P)^{\frac{1}{2}}N_P}{R_0^{\frac{1}{2}}} &= \frac{R_0^{\frac{1}{2}}}{Re^{\frac{1}{2}}}\frac{(2\xi_P)^{\frac{1}{2}}N}{Re^{\frac{1}{2}}}, \\ N_P &= N. \end{aligned}$$

Hence from now on we will refer only to N as the normal coordinate, as this is the same for both schemes.

Comparing the dimensional frequencies in a similar fashion leads to the relation

$$\omega_P = \frac{Re}{R_0}. \tag{2.120}$$

A stream function Ψ has dimensions of a length $\times$ a velocity, hence it's easy to show that any stream function, Ψ_P in the PSE scheme satisfies

$$\Psi_P = \frac{Re^{\frac{1}{2}}}{R_0}\Psi. \tag{2.121}$$

We can now use this information to write Ψ_B in terms of the leading edge base flow functions ϕ_a, ϕ_b and ϕ_c. Thus using (2.121) and (2.119), we find

$$\Psi_B = R_0^{-\frac{1}{2}}(2\xi_P)^{\frac{1}{2}}\left(\phi_a(N) + \frac{Re}{R_0}\frac{\phi_b(N)\ln(\frac{R_0\xi_P}{Re})}{\xi_P} + \frac{Re}{R_0}\frac{\phi_c(N)}{\xi_P}\right) + O(\xi_P^{-1.887}). \tag{2.122}$$

Using this new form of Ψ_B, we can write Ψ_{Bn}, for $n = 1, 2, 3, 4$, as

$$\Psi_{B1} = \phi_{aN} + \frac{Re}{R_0}\frac{\phi_{bN}\ln(R_0\xi_P/Re)}{\xi_P} + \frac{Re}{R_0}\frac{\phi_{cN}}{\xi_P}, \tag{2.123}$$

$$\Psi_{B2} = \frac{R_0}{2\xi_P}\left(\phi_{aNNN} + \frac{Re}{R_0}\frac{\phi_{bNNN}\ln(R_0\xi_P/Re)}{\xi_P} + \frac{Re}{R_0}\frac{\phi_{cNNN}}{\xi_P}\right), \tag{2.124}$$

$$\begin{aligned}\Psi_{B3} &= \frac{R_0^{\frac{1}{2}}}{2\xi_P}\left(\frac{\phi_{aNN}}{(2\xi_P)^{\frac{1}{2}}} - \frac{2Re}{R_0}\frac{\phi_{bNN}\ln(R_0\xi_P/Re)}{(2\xi_P)^{\frac{3}{2}}} + \frac{2Re}{R_0}\frac{(2\phi_{bNN} - \phi_{cNN}))}{(2\xi_P)^{\frac{3}{2}}}\right)\\ &+ \frac{R_0^{\frac{1}{2}}N}{(2\xi_P)^{\frac{1}{2}}}\left(\frac{U_f'}{U_f} - \frac{1}{2\xi_P}\right)\left(\phi_{aNNN} + \frac{Re}{R_0}\frac{\phi_{bNNN}\ln(R_0\xi_P/Re)}{\xi_P} + \frac{Re}{R_0}\frac{\phi_{cNNN}}{\xi_P}\right)\\ &+ \frac{2R_0^{\frac{1}{2}}}{(2\xi_P)^{\frac{1}{2}}}\left(\frac{U_f'}{U_f} - \frac{1}{2\xi_P}\right)\left(\phi_{aNN} + \frac{Re}{R_0}\frac{\phi_{bNN}\ln(R_0\xi_P/Re)}{\xi_P} + \frac{Re}{R_0}\frac{\phi_{cNN}}{\xi_P}\right),\end{aligned} \tag{2.125}$$

$$\begin{aligned}\Psi_{B4} &= \frac{1}{R_0^{\frac{1}{2}}}\left(\frac{\phi_a}{(2\xi_P)^{\frac{1}{2}}} - \frac{2Re}{R_0}\frac{\phi_b\ln(R_0\xi_P/Re)}{(2\xi_P)^{\frac{3}{2}}} + \frac{2Re}{R_0}\frac{(2\phi_b - \phi_c))}{(2\xi_P)^{\frac{3}{2}}}\right)\\ &+ \frac{(2\xi_P)^{\frac{1}{2}}N}{R_0^{\frac{1}{2}}}\left(\frac{U_f'}{U_f} - \frac{1}{2\xi_P}\right)\left(\phi_{aN} + \frac{Re}{R_0}\frac{\phi_{bN}\ln(R_0\xi_P/Re)}{\xi_P} + \frac{Re}{R_0}\frac{\phi_{cN}}{\xi_P}\right).\end{aligned} \tag{2.126}$$

If we compare the forms of the disturbance stream function, and use (2.121), we find that

$$\phi(\xi_P, N)\exp(i(\theta(\xi_P) - \omega_P t_p)) = \frac{Re^{\frac{1}{2}}}{R_0}f(\xi, N)\exp(T_j(\xi) - it), \tag{2.127}$$

where $f(\xi, N)$ has a three layer structure. Hence we note that

$$\alpha(\xi_P) = -i\frac{R_0}{Re}\frac{dT_j}{d\xi}, \tag{2.128}$$

and therefore our upstream boundary condition for α takes the form

$$\alpha_0 = \frac{R_0}{Re}\frac{i\lambda_j(2\xi)^{\frac{1}{2}}}{U_0'}\left(\frac{b_1}{2}\right)^{\frac{3}{2}}\left(1 - 0.60115a_1\frac{\ln(\xi)}{\xi} + \frac{(\frac{3b_2}{2b_1} - D)}{\xi}\right). \tag{2.129}$$

We also note from (2.127) that

$$\phi(\xi_P, N) = \frac{Re^{\frac{1}{2}}}{R_0}f(\xi, N),$$

which we shall use in our numerical calculations.

2.4 Summary

In this chapter, we have considered a two-dimensional, incompressible flow over an airfoil with a high Reynolds number, which has a small harmonic perturbation of frequency ω. We have shown that the flow in the leading edge region can be split into a base flow and a linear perturbation flow. The base flow, $\phi_1(\xi, N)$, is fully determined by the form of the inviscid slip velocity at the edge of the boundary layer, U_f. The perturbation flow $\phi_2(\xi, N)$, up to the receptivity coefficient, is also fully determined by U_f, through ξ, $\beta(\xi)$, $\Omega(\xi)$ and the steady solution $\phi_1(\xi, N)$. The particular form of the disturbance, U_d, enters the problem through the receptivity coefficient, C_1, which for our work is an acoustic wave. Hence the results in the leading edge region are valid for all geometries where the inviscid slip velocity tends to a constant far downstream, as long as the curvature, κ, satisfies the properties that both $\kappa U_\infty \delta/\omega$ and $(U_\infty^2\delta/\omega^2)(\partial\kappa/\partial x^*)$ remain small. The form of the solution in this leading edge region, in the limit as the streamwise variable $\xi \longrightarrow \infty$, is a Stokes layer solution, dependent on the form of U_d, and an infinite sum of homogeneous eigenmodes. The eigenmodes are a generalization of the Lam-Rott eigenmodes (Lam and Rott, 1960), where a non-zero pressure gradient along the body has been incorporated, which is generated by a non-zero nose radius.

In this chapter, we also derived the PSE, which is valid in the Orr-Sommerfeld region, and is solved numerically to produce an infinite set of eigenmodes, one of which displays the required streamwise growth in amplitude, characteristic of the T-S wave. We generalized the flat plate form of the PSE to include surface curvature, and it is valid as long as

the curvature, κ, satisfies the same conditions as for the leading edge problem. These conditions guarantee that the boundary-layer equations are the correct approximation to the Navier-Stokes equations at leading order. As in the leading edge region, the PSE is fully determined by the form of the inviscid slip velocity in this region and the exact form of the free-stream disturbance is not required. Unlike Bertolotti *et al.* (1992) we formulate the PSE in terms of ξ and N instead of x and y, so that the slow growth in the boundary-layer thickness is taken into account by the numerical mesh.

The PSE is solved numerically by means of a streamwise marching procedure, from a stipulated initial condition. The local PSE is valid in a region about some ξ_0, and provides an initial condition to the PSE, however, the local PSE contains no information of the initial magnitude of the T-S wave. Therefore to transfer information about the T-S wave's amplitude downstream, we use the leading edge asymptotics as the initial condition to the PSE.

It's the lowest order Lam-Rott eigenmode which is of most interest to us, because it is this mode which experiences spatial growth in the Orr-Sommerfeld region, and could eventually lead to transition. Hence we examine the propagation of this mode using the PSE. Because the exact form of the free-stream disturbance only enters through the receptivity coefficient, C_1, the equations in both regions are valid for general disturbances, and not just for the acoustic ones examined here. The numerical algorithms for solving the PSE and parallel stability problems are discussed in the next chapter.

Chapter 3

Numerical scheme

The numerical schemes used for stability type calculations in boundary-layer problems are based on eigenvalue solvers, as these problems are eigenvalue problems. The methods we consider for parallel boundary-layer problems are eigenvalue solvers, based on collocation methods. Iterative methods can be used for parallel problems (Cebeci and Cousteix, 2005), however as their results are identical to the collocation methods, they are not considered here.

3.1 Parallel stability problems

The numerical schemes behind the parallel flow problems, are in general very simple. Spectral collocation is used, with Chebyshev polynomials, and the number of polynomials used determines the accuracy of the results. Before we consider solving the Orr-Sommerfeld equation, let us first consider a simple example to examine how the spectral collocation method works for solving differential equations.

3.1.1 Spectral collocation method

Consider the Poisson problem for $u = u(x)$ in one dimension,

$$\frac{d^2u}{dx^2} = f(x), \tag{3.1}$$

where $f(x)$ is a given function, and with boundary conditions

$$u(-1) = u(1) = 0. \tag{3.2}$$

In a finite difference approach, we look to find the values of u at a discrete set of points x_m, say,

$$x_m = -1 + \frac{2m}{M},$$

for $m = 0, 1, ..., M$, where M determines the spread of the set of points. Algebraic equations are found by approximating the differential operator, d^2u/dx^2, in (3.1) with terms like,

$$\frac{d^2u}{dx^2}(x_m) \approx \frac{u_{m+1} - 2u_m + u_{m-1}}{(\Delta x)^2},$$

for $m = 1, 2, ..., M-1$, where

$$\begin{aligned} u_m &= u(x_m), \\ \Delta x &= \frac{2}{M}. \end{aligned}$$

This form of (3.1) yields $M-1$ equations for the $M+1$ unknowns u_m. The two boundary conditions, (3.2), give two more equations which complete the problem.

The spectral collocation approach approximates the solution at all points, by a sum over a finite set of orthogonal basis functions. Here, we consider a Chebyshev basis, hence we write

$$u(x) = \sum_{i=0}^{M} a_i T_i(x), \tag{3.3}$$

where $T_i(x)$ is the i^{th} Chebyshev polynomial of the first kind, defined by equation (C.2).

Now we insist that u satisfies the differential equation and boundary conditions exactly at the collocation points

$$x_m = \cos\left(\frac{m\pi}{M}\right),$$

for $m = 0, 1, ..., M$. Hence we require the solution to satisfy

$$u(x_0) = 0, \tag{3.4}$$

$$u(x_M) = 0, \tag{3.5}$$

$$\frac{d^2u}{dx^2}(x_m) = f(x_m), \tag{3.6}$$

for $m = 1, ..., M-1$.

To solve (3.6), we first note that

$$\frac{d^2u}{dx^2} = \sum_{i=0}^{M} a_i T_i''(x).$$

The second derivatives of the Chebyshev polynomials can then be found by using the recurrence relations

$$\begin{aligned}
T_0^{(k)}(x_m) &= 0, \\
T_1^{(k)}(x_m) &= T_0^{(k-1)}(x_m), \\
T_2^{(k)}(x_m) &= 4T_1^{(k-1)}(x_m), \\
T_s^{(k)}(x_m) &= 2sT_{s-1}^{(k-1)}(x_m) + \frac{s}{s-2}T_{s-2}^{(k)}(x_m) \quad s = 3, 4, ...,
\end{aligned}$$

where $T_s^{(k)}$ is the k^{th} derivative of the s^{th} Chebyshev polynomial. These relations can be easily derived from (C.5). Satisfying (3.6) at the collocation points, along with (3.4) and (3.5), gives a system of $M+1$ equations for the $M+1$ unknowns, which can be solved by a linear system solver, such as the following.

The $M+1$ equations can be written in the following form

$$\mathbf{Ba} = \mathbf{c},$$

where the $(M+1) \times (M+1)$ matrix, $\mathbf{B}$, is the coefficients of the LHS of (3.4), (3.5) and (3.6), $\mathbf{a}$ is the vector of the constants a_i, and the vector $\mathbf{c}$, is the coefficients of the RHS of (3.4), (3.5) and (3.6). We wish to find

$$\mathbf{a} = \mathbf{B^{-1}c},$$

but the calculation of an inverse matrix is hard to compute for large systems. The numerical solution to $\mathbf{a}$ can be calculated in many ways, the following method is known as LU factorisation.

First of all, $\mathbf{B}$ is transformed, using partial pivoting with row interchanges, into

$$\mathbf{B} = \mathbf{PLU},$$

where $\mathbf{P}$ is a permutation matrix, $\mathbf{L}$ is a lower triangular matrix with unit diagonal elements, and $\mathbf{U}$ is an upper triangular matrix. Once in this form

$$\mathbf{PLUa} = \mathbf{c},$$

$\mathbf{PLd} = \mathbf{c}$ is solved for $\mathbf{d}$, and then $\mathbf{Ua} = \mathbf{d}$ is solved for $\mathbf{a}$. Both these systems are easy to solve because the matrices are upper or lower diagonal (Anton, 1994).

3.1.2 Orr-Sommerfeld equation

The equation we have to solve for parallel flow problems is the Orr-Sommerfeld equation, which is derived in Appendix A. The Orr-Sommerfeld equation can be written as

$$(D^4 - 2\alpha^2 D^2 + \alpha^4)v = i\alpha Re\left((U-c)(D^2-\alpha^2) - U''\right)v, \tag{3.7}$$

where $D \equiv d/dy$. We can consider solutions to this equation in two ways. Firstly, we could input a real wavenumber α, and solve for the complex eigenvalues $c_r + ic_i$, in which case we end up with the solution for v from (A.10) with $l = 0$, as

$$v = v(y)e^{i\alpha x}e^{-i\alpha(c_r+ic_i)t}. \tag{3.8}$$

Alternatively, we could introduce a real frequency $\omega = \alpha c$, and solve for the complex wavenumber $\alpha = \alpha_r + i\alpha_i$, leading to solution

$$v = v(y)e^{-i\omega t}e^{i(\alpha_r+i\alpha_i)x}. \tag{3.9}$$

Solution (3.8) is unstable when $c_i > 0$, this is known as **temporal instability**, as the solution grows with increasing time.

Solution (3.9) is unstable when $\alpha_i < 0$, this is known as **spatial instability**, as the solution grows in space.

Temporal eigenvalue problem

Finding the temporal eigenvalues is a straightforward problem, as the eigenvalue appears linearly in the problem. We write the Orr-Sommerfeld equation as

$$\frac{d^4v}{dy^4} - 2\alpha^2\frac{d^2v}{dy^2} + \alpha^4 v - i\alpha Re\left(U\left(\frac{d^2v}{dy^2} - \alpha^2 v\right) - U''v\right) = c\left(-i\alpha Re\left(\frac{d^2v}{dy^2} - \alpha^2 v\right)\right), \tag{3.10}$$

and looking for a solution of the form

$$v = \sum_{i=0}^{M-1} a_i T_i(y),$$

it reduces to

$$\mathbf{A}\mathbf{a} = c\mathbf{B}\mathbf{a}, \tag{3.11}$$

where **a** is a vector of the constants a_i. By evaluating the left and right hand sides at the collocation points

$$y_i = \cos\left(\frac{i\pi}{(M-1)}\right),$$

for $i = 2, ..., M-3$, we can then use an eigenvalue solver to solve for c. The derivatives of v are again found using the recurrence relations

$$\begin{aligned}
T_0^{(k)}(y_i) &= 0, \\
T_1^{(k)}(y_i) &= T_0^{(k-1)}(y_i), \\
T_2^{(k)}(y_i) &= 4T_1^{(k-1)}(y_i), \\
T_m^{(k)}(y_i) &= 2mT_{m-1}^{(k-1)}(y_i) + \frac{m}{m-2}T_{m-2}^{(k)}(y_i) \quad m = 3, 4, ...,
\end{aligned}$$

where again $T_m^{(k)}$ is the k^{th} derivative of the m^{th} Chebyshev polynomial. This gives $M-4$ equations for the M unknowns a_i, which along with the 4 boundary conditions, and noting that

$$T_m(\pm 1) = (\pm 1)^m \qquad T'_m(\pm 1) = (\pm 1)^{m-1} m^2,$$

gives the required information to put into the matrix eigenvalue solver.

Spatial eigenvalue problem

The spatial eigenvalue problem is not as simple as the temporal one in the previous section, because in this case we stipulate an initial real frequency $\omega = c\alpha$, and solve for the complex eigenvalue α, which occurs nonlinearly, thus the problem can not be written in the matrix form (3.11). Thus we have to solve the eigenvalue problem of the form

$$\left(\mathbf{C_4}\alpha^4 + \mathbf{C_3}\alpha^3 + \mathbf{C_2}\alpha^2 + \mathbf{C_1}\alpha + \mathbf{C_0}\right)\mathbf{v} = \mathbf{0}.$$

To solve this problem we use a method developed by Bridges and Vaserstein (1986) and Bridges and Morris (1984), who introduce the quantities

$$\begin{aligned}\Gamma_1 &= \alpha v,\\ \Gamma_2 &= \alpha^2 v,\\ \Gamma_3 &= \alpha^3 v,\end{aligned}$$

into (3.7), which leads to the following system of equations in matrix form

$$\begin{bmatrix} \rho_{11} & \rho_{22} & \rho_{33} & \rho_{44} \\ I & 0 & 0 & 0 \\ 0 & 0 & I & 0 \\ 0 & 0 & 0 & I \end{bmatrix} \begin{bmatrix} v \\ \Gamma_1 \\ \Gamma_2 \\ \Gamma_3 \end{bmatrix} = \alpha \begin{bmatrix} 0 & 0 & 0 & \rho_{55} \\ I & 0 & 0 & 0 \\ 0 & I & 0 & 0 \\ 0 & 0 & I & 0 \end{bmatrix} \begin{bmatrix} v \\ \Gamma_1 \\ \Gamma_2 \\ \Gamma_3 \end{bmatrix}, \tag{3.12}$$

where

$$\rho_{11} = -\frac{1}{Re}D^4 - i\omega D^2, \tag{3.13}$$

$$\rho_{22} = iUD^2 - iU'', \tag{3.14}$$

$$\rho_{33} = i\omega + \frac{2}{Re}D^2, \tag{3.15}$$

$$\rho_{44} = -iU, \tag{3.16}$$

$$\rho_{55} = \frac{1}{Re}. \tag{3.17}$$

This system can again be solved using spectral collocation methods described in the previous section. The functions v, Γ_1, Γ_2 and Γ_3 are all expanded in terms of M Chebyshev polynomials, which are substituted into (3.12) to give a $4M \times 4M$ matrix system to solve using a linear system solver.

Finite and infinite domains

The temporal and spatial eigenvalue solvers using Chebyshev polynomials are fine as long as they are for functions defined in the domain $y \in [-1, 1]$, but the Blasius boundary-layer is defined for $\eta \in [0, \infty)$, after the change of variable $\eta = Re^{\frac{1}{2}}y/(2x)^{\frac{1}{2}}$, which is the change of variable for a flat plate, $U_f = 1$ in (2.23). To utilise Chebyshev polynomials,

we first map the semi-infinite domain $\eta \in [0, \infty)$ to the bounded domain $\bar{\eta} \in [-1, 1]$, using the mapping

$$\bar{\eta} = \frac{\eta - L}{\eta + L}, \tag{3.18}$$

where L denotes a constant map parameter, chosen to map the majority of the function being expanded to the region $[-1, 0]$. For our boundary-layer problem, we choose the map parameter, so that we get a concentration of points close to the boundary at $\eta = 0$, to resolve the rapid change of the mode shape in this region. We found a value of L in the region of 30 to 45 gave good results for the eigenvalues for Blasius boundary-layer flow, when compared with the work of Schmid and Henningson (2001). Now we can use the same methods as before, but we must note that the derivatives change to

$$\frac{\partial}{\partial \eta} = \frac{(1-\bar{\eta})^2}{2L}\frac{\partial}{\partial \bar{\eta}}, \tag{3.19}$$

$$\frac{\partial^2}{\partial \eta^2} = \frac{(1-\bar{\eta})^4}{4L^2}\frac{\partial^2}{\partial \bar{\eta}^2} - \frac{(1-\bar{\eta})^3}{2L^2}\frac{\partial}{\partial \bar{\eta}}, \tag{3.20}$$

$$\frac{\partial^3}{\partial \eta^3} = \frac{(1-\bar{\eta})^6}{8L^3}\frac{\partial^3}{\partial \bar{\eta}^3} - \frac{3(1-\bar{\eta})^5}{4L^3}\frac{\partial^2}{\partial \bar{\eta}^2} + \frac{3(1-\bar{\eta})^4}{4L^3}\frac{\partial}{\partial \bar{\eta}}, \tag{3.21}$$

$$\frac{\partial^4}{\partial \eta^4} = \frac{(1-\bar{\eta})^8}{16L^4}\frac{\partial^4}{\partial \bar{\eta}^4} - \frac{3(1-\bar{\eta})^7}{4L^4}\frac{\partial^3}{\partial \bar{\eta}^3} + \frac{9(1-\bar{\eta})^6}{4L^4}\frac{\partial^2}{\partial \bar{\eta}^2} - \frac{3(1-\bar{\eta})^5}{2L^4}\frac{\partial}{\partial \bar{\eta}}. \tag{3.22}$$

3.2 Parabolized Stability Equation

The Parabolized Stability equation (2.102) is a fourth-order quasi-parabolic differential equation, for which a marching procedure is used to march the solution downstream from the upstream boundary conditions defined by (2.112). The procedure is iterative, and works by fixing the value of the wavenumber and the mode shape, so that it satisfies both the PSE and the normalization condition.

The governing equation (2.102), along with its boundary conditions (2.108) to (2.111) and upstream boundary condition (2.112) are solved using a spectral collocation technique with Chebyshev polynomials.

We use a similar mapping as defined in the previous section to map the semi-infinite domain $N \in [0, \infty)$ to the bounded domain $\bar{N} \in [-1, 1]$,

$$\bar{N} = \frac{N - L}{N + L}. \tag{3.23}$$

In this problem, we found that we required a value of L in the region of 20 to 45 to give results which agree with those of Bertolotti *et al.* (1992), mainly because we are now not using an eigenvalue solver, but merely a linear system solver. We can then use spectral collocation to solve for $\phi(\xi_P, N)$ in terms of $M+1$ Chebyshev polynomials. We solve (2.102) for a vector $\boldsymbol{\phi}$ of ϕ evaluated at the $M+1$ collocation points

$$N_m = \cos\left(\frac{m\pi}{M}\right) \quad \text{for} \quad m = 0, 1, ..., M. \tag{3.24}$$

The operators in (2.102) contain α, hence we have a coupled set of equations. To solve them using a marching method in ξ_P, we use an iterative scheme at each value $\xi_P = \xi_j$, to solve for $\phi(\xi_j, N) = \phi_j(N)$ and $\alpha(x_j) = \alpha_j$. At each ξ_j, we solve (2.102) with an initial guess for α_j for ϕ_j and use the normalization condition (2.100) to update our guess for α_j. We also note at this point, that the mapping (3.23) changes the normalisation condition to

$$\int_{-1}^{1} \phi_{\xi_P} \phi^\dagger \frac{1}{(1-\bar{N})^2} d\bar{N} = 0.$$

Herbert (1993) found that the simplest, but effective way to evaluate the derivatives $d\alpha/d\xi_P$ and $\partial\phi/\partial\xi_P$ in (2.102) is to use a two-point backward-difference method,

$$\left(\frac{\partial\phi}{\partial\xi_P}\right)_{j+1} = \frac{\phi_{j+1} - \phi_j}{\Delta\xi_j}, \qquad \left(\frac{d\alpha}{d\xi_P}\right)_{j+1} = \frac{\alpha_{j+1} - \alpha_j}{\Delta\xi_j},$$

where $\Delta\xi_j = \xi_{j+1} - \xi_j$. Using these, the PSE equation becomes

$$\left\{\left[(L_0)_{j+1} + (L_1)_{j+1} + (L_2)_{j+1}\right]\Delta\xi_j + M_{j+1} + N_{j+1}\left[\alpha_{j+1} - \alpha_j\right]\right\}\phi_{j+1} = M_{j+1}\phi_j. \tag{3.25}$$

The scheme works by taking the initial data (2.112), and letting our initial guess for α_{j+1}, i.e α at the next spatial step, be $\alpha_{j+1}^{(1)} = \alpha_j$, where the superscript (1) signifies the first iteration. These values go into (3.25) and evaluate it at each of the $M+1$ collocation points, (3.24), to find $\phi_{j+1}^{(1)}$ at the $M+1$ collocation points. Then using the normalization condition (2.100), we arrive at a better estimate for α_{j+1}, which we label $\alpha_{j+1}^{(2)}$. We then resolve (3.25) for a better approximation for ϕ_{j+1}, which we label $\phi_{j+1}^{(2)}$. We then repeat these steps, until we have converged onto a solution. We say that we have converged onto a solution when $\alpha_{j+1}^{(n+1)} - \alpha_{j+1}^{(n)} < 10^{-6}$.

Hence our numerical scheme comes down to solving,

$$\left\{\left[(L_0)_{j+1}^{(n)} + (L_1)_{j+1}^{(n)} + (L_2)_{j+1}^{(n)}\right]\Delta\xi_j + M_{j+1}^{(n)} + N_{j+1}^{(n)}\left[\alpha_{j+1}^{(n)} - \alpha_j\right]\right\}\phi_{j+1}^{(n)} = M_{j+1}^{(n)}\phi_j, \tag{3.26}$$

where to update α, we utilise (2.99), and write

$$\alpha_{j+1}^{(n+1)} = \alpha_{j+1}^{(n)} - \frac{i}{\Delta\xi_j}\frac{\int_o^\infty \left(\phi_{j+1}^{(n)} - \phi_j\right)\left(\phi_{j+1}^{(n)}\right)^\dagger dN}{\int_0^\infty |\phi_{j+1}^{(n)}|^2 dN}, \tag{3.27}$$

where (n) is the number of iterations.

3.3 Summary

The numerical scheme for solving the PSE is outlined in this chapter. The scheme is very similar to the one given by Bertolotti *et al.* (1992), however we have N as our normal variable rather than y, which means that the slow growth of the boundary-layer is included in the formulation of the numerical mesh. This approach has not been used before, and the results it gives are identical to the ones given when y is chosen as the normal variable. The parallel Orr-Sommerfeld schemes are of the same format as the local PSE, which is solved as an eigenvalue problem.

These numerical schemes are now applied to bodies with different leading edge geometries, and the next chapter concentrates on the semi-infinite flat plate case.

Chapter 4

The semi-infinite flat plate

Before applying our PSE method to perturbed flow around general curved bodies, we first apply it to the semi-infinite flat plate, and compare our results with those of Goldstein (1983), who extended the leading edge asymptotics idea to derive the asymptotic form of the wavenumber and amplitude function in the Orr-Sommerfeld region. We shall discuss the accuracy of our results compared with Goldstein's up to and including $O(\epsilon^3 \ln \epsilon)$ terms, where $\epsilon = Re^{-\frac{1}{6}}$, and then include the $O(\epsilon^3)$ term (Goldstein, 1982), and discuss the difficulties in using the asymptotics, and extending this idea to more general bodies. We illustrate the key points for the derivation of Goldstein's asymptotics, but look more closely at the $O(\epsilon^3)$ correction term, where we have calculated the values of some undetermined constants to be able to calculate fully the $O(\epsilon^3)$ term.

As well as comparing the PSE results with Goldstein's asymptotics, we also illustrate the consistency of the PSE, by demonstrating that the PSE solution is independent of the choice of upstream boundary condition used, where the boundary condition comes from Orr-Sommerfeld theory, the local PSE and the leading edge asymptotics. Also we discuss the need to patch growth rate curves for moderately large ϵ, and show how this is possible, as well as demonstrating the step size independence of the PSE solution for small ϵ.

We shall also compare our results to the numerical studies of Haddad and Corke (1998) and Wanderley and Corke (2001), who consider flows over a parabola and a Modified Super Ellipse (MSE) respectively. We compare our results with Haddad and Corke in the limit as the parabola's nose radius goes to zero. We examine the work of Wan-

derley and Corke, who attempt to approximate the boundary-layer equations by the Orr-Sommerfeld equation close to the leading edge. However this approximation does not take into account the growth in the boundary-layer at this point, hence we use the PSE method to check the validity of this Orr-Sommerfeld approximation.

Further to this work, we also discuss the numerical problems which arise when solving the PSE. In particular we consider the occurrence of initial transients from the initial conditions, and hope to show that these arise as a consequence of higher eigenmodes being present in the composite form of the initial upstream boundary condition.

4.1 Equations on a flat plate

4.1.1 Leading edge region

For flow past a semi-infinite flat plate, the slip velocity due to the free-stream is $U_f = 1$. Thus from (2.36) and (2.38) we find

$$\beta(\xi) = 0, \quad \Omega(\xi) = 2\xi, \tag{4.1}$$

and hence (2.34) becomes

$$\phi_{1NNN} + \phi_1\phi_{1NN} = 2\xi\left(\phi_{1N}\phi_{1N\xi} - \phi_{1NN}\phi_{1\xi}\right), \tag{4.2}$$

with the same boundary conditions as in (2.35). At $\xi = 0$, the above equation reduces to the Blasius equation, which has solution $\phi_1(0, N) = f(N)$. However, as this solution satisfies the full steady equation, and the corresponding boundary conditions, it remains as the solution for all ξ. Now from (2.37) the LUBLE becomes

$$\phi_{2NNN} + f\phi_{2NN} + 2\xi i\phi_{2N} + f''\phi_2 + 2\xi\left(f''\phi_{2\xi} - f'\phi_{2N\xi}\right) = 2\xi i U_d - 2\xi\frac{dU_d}{d\xi}, \tag{4.3}$$

which when written in terms of the stream function $\psi_0 = h(\xi)\phi_2 = (2\xi)^{\frac{1}{2}}\,\phi_2$ becomes

$$\psi_{0NNN} + f\psi_{0NN} + 2\xi i\psi_{0N} + f'\psi_{0N} + 2\xi\left(f''\psi_{0\xi} - f'\psi_{0N\xi}\right) = (2\xi)^{\frac{3}{2}}\left(i - \frac{d}{d\xi}\right)U_d. \tag{4.4}$$

The variables (ξ, N) from (2.33) and (2.23) are equivalent to

$$\xi = x = x_G \quad \text{and} \quad N = (2\xi)^{-\frac{1}{2}}y = (2x_G)^{-\frac{1}{2}}\epsilon^{-3}y_G = \eta_G,$$

where the subscript G denotes the variables used by Goldstein (1982) and Goldstein (1983) and $\epsilon^6 = Re^{-1}$. Therefore the above form of the LUBLE is identical to equation (3.2) in Goldstein (1983). Since $U_f = 1$, comparison with the large ξ asymptotic form (2.41), gives the coefficients α and γ, which appear in the asymptotic eigenfunction, to be zero. The steady solution has already been determined as $f(N)$, hence from (2.59), $D = E(N) = 0$. Substituting these values into (2.74) and (2.75) gives

$$\tau_j = -\frac{889 - 16\rho_j^3}{1260}, \tag{4.5}$$

$$T_j(\xi) = \frac{-\lambda_j (2\xi)^{\frac{3}{2}}}{3U_0'}. \tag{4.6}$$

Also the variable M given by (2.67) is equivalent to the variable σ used by Goldstein (1983), hence the form of the unsteady eigenmode is identical to the one given by Goldstein.

4.1.2 Orr-Sommerfeld region - PSE

If we substitute $U_f = 1$ along with $D = E(N) = 0$ into (2.102) to (2.107), we recover the Parabolized Stability Equation for a semi-infinite flat plate,

$$(L_0 + L_1 + L_2)\phi + M\frac{\partial \phi}{\partial \xi_P} + \frac{d\alpha}{d\xi_P} N\phi = 0, \tag{4.7}$$

where

$$\begin{aligned} L_0 &= -\frac{1}{R_0}\left(\frac{R_0 D^2}{2\xi_P} - \alpha^2\right)^2 + \left(i\alpha\frac{\partial \Psi_B}{\partial y_P} - i\omega_P\right)\left(\frac{R_0 D^2}{2\xi_P} - \alpha^2\right) \\ &\quad - i\alpha\frac{\partial^3 \Psi_B}{\partial y_P^3}, \end{aligned} \tag{4.8}$$

$$L_1 = \frac{R_0^{\frac{1}{2}}}{(2\xi_P)^{\frac{1}{2}}}\frac{\partial^3 \Psi_B}{\partial x_P \partial y_P^2} D - \frac{R_0^{\frac{1}{2}}}{(2\xi_P)^{\frac{1}{2}}}\frac{\partial \Psi_B}{\partial x_P}\left(\frac{R_0 D^3}{2\xi_P} - \alpha^2 D\right), \tag{4.9}$$

$$\begin{aligned} L_2 &= -\frac{N}{2\xi_P}\left(\frac{\partial \Psi_B}{\partial y_P}\left(\frac{R_0 D^3}{2\xi_P} - 3\alpha^2 D\right) + 2\omega_P \alpha D - \frac{\partial^3 \Psi_B}{\partial y_P^3} D\right) \\ &\quad - R_0 \frac{\partial \Psi_B}{\partial y_P}\frac{1}{2\xi_P^2} D^2, \end{aligned} \tag{4.10}$$

$$M = \frac{\partial \Psi_B}{\partial y_P}\left(\frac{R_0 D^2}{2\xi_P} - 3\alpha^2\right) + 2\omega_P \alpha - \frac{\partial^3 \Psi_B}{\partial y_P^3}, \tag{4.11}$$

$$N = \omega_P - 3\alpha\frac{\partial \Psi_B}{\partial y_P}, \tag{4.12}$$

and $D \equiv d/dN$. The base flow $\Psi_B(\xi_P, N)$ is given by

$$\Psi_B(\xi_P, N) = \frac{(2\xi_P)^{\frac{1}{2}}}{R_0^{\frac{1}{2}}} f(N), \tag{4.13}$$

and the relationship between ξ_P and x_G, defined in §4.1.1, is

$$\xi_P = \frac{Re}{R_0} x_G.$$

If we change the PSE variables from (ξ_P, N) to (x_P, y_P), using the fact that $\xi_P = x_P$ and $N = (2x_P)^{\frac{1}{2}} y_P / R_0^{\frac{1}{2}}$, we derive a form of the PSE similar to the one derived by Bertolotti *et al.* (1992) for a semi-infinite flat plate,

$$(L_0 + L_1)\phi + M\frac{\partial \phi}{\partial x_P} + \frac{d\alpha}{dx_P} N\phi = 0, \tag{4.14}$$

where

$$\begin{aligned} L_0 &= -\frac{1}{R_0}\left(D^2 - \alpha^2\right)^2 + \left(i\alpha \frac{\partial \Psi_B}{\partial y_P} - i\omega_P\right)\left(D^2 - \alpha^2\right) \\ &- i\alpha \frac{\partial^3 \Psi_B}{\partial y_P^3}, \qquad (4.15) \\ L_1 &= \frac{\partial^3 \Psi_B}{\partial x_P \partial y_P^2} D - \frac{\partial \Psi_B}{\partial x_P}\left(D^3 - \alpha^2 D\right), \qquad (4.16) \\ M &= \frac{\partial \Psi_B}{\partial y_P}\left(D^2 - 3\alpha^2\right) + 2\omega_P \alpha - \frac{\partial^3 \Psi_B}{\partial y_P^3}, \qquad (4.17) \\ N &= \omega_P - 3\alpha \frac{\partial \Psi_B}{\partial y_P}, \qquad (4.18) \end{aligned}$$

and where, $D \equiv d/dy_P$. The difference between this form of the PSE, and the one given in Bertolotti *et al.* (1992), is that we have neglected the $O(R_0^{-1})$ terms given in the operators M and N, as these only contribute up to $O(R_0^{-2})$ to the final solution. We feel our form of (4.14) gives a more consistent equation than Bertolotti because all the $O(R_0^{-2})$ terms have then been neglected. We found in our calculations that these extra terms make no significant effect to the PSE solution far from the nose, and although these terms become significant close to the nose, they are as significant as the other $O(R_0^{-2})$ terms which have been neglected.

4.1.3 Upstream boundary conditions to the PSE

As we mentioned in §2.2, the PSE is solved with homogeneous boundary conditions to pick out the propagation of the unsteady eigenmodes, however the PSE is also subject to

an upstream boundary condition of the form (2.112). This boundary condition takes the form of an initial wavenumber, and an initial mode shape given at some upstream position $x_P = x_0$. This condition could come from a number of different sources, three of which are considered here.

Parallel flow assumption

The parallel flow assumption assumes that at the point x_0, both α and ϕ, along with the base flow Ψ_B are independent of x_P. In this case, the PSE (4.7) reduces to

$$L_0\phi = \left[-\frac{1}{R_0}\left(\frac{R_0 D^2}{2\xi_P} - \alpha^2\right)^2 + \left(i\alpha\frac{\partial \Psi_B}{\partial y_P} - i\omega_P\right)\left(\frac{R_0 D^2}{2\xi_P} - \alpha^2\right)\right]\phi = 0, \quad (4.19)$$

which is the usual Orr-Sommerfeld equation for parallel flows. This equation is solved using a matrix eigenvalue solver described in chapter 3, and the upstream boundary condition is taken as the most unstable discrete eigenvalue, and its corresponding eigenfunction. The main drawback of this boundary condition, is that it doesn't incorporate any of the boundary-layer growth. Therefore close to the leading edge region, this method produces an unsatisfactory boundary condition, because the wavenumber and mode shape would be in poor agreement with the actual wavenumber and growth rate at that point, which could be calculated via a full Navier-Stokes simulation.

Local PSE solution

The PSE contains all the information needed to resolve the boundary-layer growth, so as an upstream boundary condition, we consider the local solution to the PSE given in (2.115) and (2.116). In the case of a flat plate, the operators simplify to the ones given in (4.8) to (4.12), and the operator L_4 simplifies to

$$L_4 = -\frac{R_0}{2\xi_0^2}\left(i\alpha_0\Psi_{B1} - i\omega\right)D^2 - i\alpha_0\Psi_{B2\xi} + \frac{R_0 D^4}{2\xi_0^3}. \quad (4.20)$$

Similarly we could look for a local solution to (4.14) about the upstream point $x_P =$

x_0. Expanding the solution gives

$$\phi(x_P, y_P) = \phi(x_0, y_P) + \hat{x}\left.\frac{\partial\phi(x_P, y_P)}{\partial x_P}\right|_{x_P=x_0} + O(\hat{x}^2) = \phi_0 + \hat{x}\phi_1, \quad (4.21)$$

$$\alpha(x_P) = \alpha(x_0) + \hat{x}\left.\frac{d\alpha(x_P)}{dx_P}\right|_{x_P=x_0} + O(\hat{x}^2) = \alpha_0 + \hat{x}\alpha_1. \quad (4.22)$$

where $\hat{x} = x_P - x_0$, and the $O(\hat{x}^2)$ terms are zero due to the PSE assumptions on ϕ and α. Introducing these into (4.14) we find the two equations valid for varying $\hat{x}$ are

$$(L_0 + L_1 + \alpha_1 N)\,\phi_0 + M\phi_1 = 0, \quad (4.23)$$

$$(L_3 + i\alpha_1 M)\,\phi_0 + L_0\phi_1 = 0, \quad (4.24)$$

where

$$L_3 = i\alpha_0\frac{\partial^2\Psi_B}{\partial x_P\partial y_P}\left(D^2 - \alpha_0^2\right) - i\alpha_0\frac{\partial^4\Psi_B}{\partial x_P\partial y_P^3}, \quad (4.25)$$

and in L_0, L_1, M and N, α is replaced by α_0.

The standard approach for solving this type of problem (Bertolotti *et al.*, 1992) is to consider the approximation $\alpha = constant$, i.e. $\alpha_1 = 0$, which is a normalization condition for the problem, although it is different to the normalization condition (2.100). This approach cuts down on computation time, as we need only to solve a simple linear eigenvalue problem, rather than perform many iterations. Bertolotti *et al.* (1992) suggests other iterative methods for solving this problem, however we found no advantage when using these methods compared to the simpler one above. The simple $\alpha = constant$ approach leads to the eigenvalue problem

$$\begin{bmatrix} L_0 + L_1 & M \\ L_3 & L_0 \end{bmatrix}\begin{bmatrix} \phi_0 \\ \phi_1 \end{bmatrix} = \begin{bmatrix} 0 \\ 0 \end{bmatrix}, \quad (4.26)$$

which when solved at $x_P = x_0$ gives us our upstream boundary condition $\alpha = \alpha_0$ and $\phi = \phi_0$. The solution to this problem produces a pair of eigenvalues which approach the eigenvalue of the Orr-Sommerfeld equation in the limit $R_0 \longrightarrow \infty$. Thus it appears to be ambiguous as to which eigenvalue we take as our boundary condition, however we shall show later that both eigenvalues and mode shapes very quickly iterate on to the same solution when used as the boundary condition so either is acceptable. It is

also the case that although we get a pair of solutions, both solutions actually give the same growth rate when we consider the contribution from the mode shape as well as the eigenvalue (Bertolotti *et al.*, 1992). Hence the difference in the eigenvalues is not mapped to a difference in the growth rate, because the mode shape is adjusted accordingly for each solution.

If we examine the form of (4.26) in the large y_P limit, we find that the asymptotic form of $\phi(x_P, y_P)$ in the region of x_0 is

$$\phi(x_P, y_P \gg 1) = (x_P + Ay_P)\, e^{-\alpha_0 y_P} \tag{4.27}$$

where

$$A = \frac{i}{1 - V_\infty / i(1 - \omega_P/\alpha_0)},$$

and $V_\infty = -\Psi_{Bx_P}|_{y_P \longrightarrow \infty}$, is the transverse mean velocity far from the plate. This asymptotic behaviour is different to that of the Orr-Sommerfeld equation, in which the large y_P solution is $Be^{-\alpha_0 y_P}$, where B is a constant. Therefore the non-parallel effects slow the rate of decay outside the boundary-layer by an amount proportional to y_P.

4.2 Leading edge region

4.2.1 Illustration of the leading edge receptivity results

Earlier we stated that we wish to utilise the large ξ form of the leading edge receptivity analysis, by using it as our upstream boundary condition to the PSE. We use the lowest order eigenmode as our initial condition, as it is this mode which matches to the T-S wave downstream and exhibits spatial growth. The full form of the lowest order eigenmode, ψ_1, in this region, in the limit $\xi \longrightarrow \infty$, on a flat plate is given in chapter 2 by

$$\psi_1 = C\xi^{\tau_1} g(\xi, N) \exp\left(-\frac{\lambda_1 (2\xi)^{\frac{3}{2}}}{3U_0'} \right), \tag{4.28}$$

where $\tau_1 = -0.6921$. Hence for the flat plate, our initial wavenumber comes from (2.129), which becomes

$$\alpha_0 = \frac{R_0}{Re} \frac{i\lambda_1 (2x^{(0)})^{\frac{1}{2}}}{U_0'}, \tag{4.29}$$

where $x^{(0)} = R_0 x_0/Re$, i.e $x^{(0)}$ is the starting point in the leading edge $\xi = x_G$ variable. The initial mode shape is given by

$$\phi_0 = x^{(0)\tau_1} g(x^{(0)}, N), \tag{4.30}$$

where

$$g(x,N) = \begin{cases} U_0' \frac{\int_0^M \left(M - \widetilde{M}\right) Ai(\tilde{z}) d\widetilde{M}}{\int_0^\infty Ai(\tilde{z}) d\widetilde{M}} & \text{for} \quad N = O(x^{-\frac{1}{2}}), \\ \left(2x^{(0)}\right)^{\frac{1}{2}} f'(N) + \frac{iU_0'}{\lambda_1} & \text{for} \quad N = O(1), \\ \left(\left(2x^{(0)}\right)^{\frac{1}{2}} f'(N) + \frac{iU_0'}{\lambda_1}\right) \exp\left(-\frac{2\epsilon^3 \lambda_1 i x^{(0)} N}{U_0'}\right) & \text{for} \quad N = O(\epsilon^{-3} x^{-1}). \end{cases} \tag{4.31}$$

As it stands, we can't use (4.31) as our initial mode shape, as we need it in the form of a single function. This is achieved by forming a composite solution of the three layers. To see how a composite function works, consider the following example. Consider the function

$$h(x) = \begin{cases} h_1(x) & \text{for} \quad x = O(1) \\ h_2(x) & \text{for} \quad \text{large } x, \end{cases}$$

with the matching condition that

$$\lim_{x \longrightarrow \infty} h_1(x) = \lim_{x \longrightarrow 0} h_2(x) = R(x).$$

We form the composite solution $H(x)$ defined as

$$H(x) = h_1(x) + h_2(x) - R(x),$$

so as $x \longrightarrow 0$, $h_2(x) = R(x)$, hence $H(x) = h_1(x)$. However, as x gets large ($x \longrightarrow \infty$), $h_1(x) = R(x)$, therefore $H(x) = h_2(x)$, and there is a region in between where the two solutions are smoothly joined. A composite function of this form is exact in the two regions for which the original function was defined, but in the matching region between the two regions, the solution may not be exact. However the composite solution produces a smooth transition between the two regions, so as long as there are no discontinuities between the regions, the composite solution provides a good approximation.

Applying this to our three layer boundary-layer structure (4.31), we find our initial mode shape is

$$\begin{aligned} \phi_0 \quad = \quad & x^{\tau_1} \left[U_0' \frac{\int_0^M \left(M - \widetilde{M}\right) Ai(\tilde{z}) \widetilde{M}}{\int_0^\infty Ai(\tilde{z}) d\widetilde{M}} + (2x)^{\frac{1}{2}} f'(N) \right. \\ & \left. + \left((2x)^{\frac{1}{2}} + \frac{U_0' i}{\lambda_1}\right) \exp\left(-\frac{2\epsilon^3 i \lambda_1 x N}{U_0'}\right) - U_0' (2x)^{\frac{1}{2}} N - (2x)^{\frac{1}{2}} - \frac{U_0 i}{\lambda_1} \right], \end{aligned} \tag{4.32}$$

evaluated at $x = x^{(0)}$. We can check that this is the correct solution, by letting N vary over different length scales. When $N = O\left(x^{-\frac{1}{2}}\right)$, then

$$f'(N) \sim U_0' N + O(N^4), \quad \text{and} \quad \exp\left(-\frac{2\epsilon^3 i\lambda_1 x N}{U_0'}\right) \sim 1 + O(\epsilon^3 x^{\frac{1}{2}}),$$

so

$$\phi_0 \sim x^{\tau_1}\left[U_0' \frac{\int_0^M \left(M - \widetilde{M}\right) Ai(\tilde{z})\widetilde{M}}{\int_0^\infty Ai(\tilde{z}) d\widetilde{M}} + O(x^{-\frac{3}{2}})\right].$$

When $N = O(1)$, then

$$\exp\left(-\frac{2\epsilon^3 i\lambda_1 x N}{U_0'}\right) \sim 1 + O(\epsilon^3 x^{\frac{1}{2}}), \quad \text{and} \quad U_0' \frac{\int_0^M \left(M - \widetilde{M}\right) Ai(\tilde{z})\widetilde{M}}{\int_0^\infty Ai(\tilde{z}) d\widetilde{M}} \sim \frac{iU_0'}{\lambda_1} + U_0'(2x)^{\frac{1}{2}} N,$$

so

$$\phi_0 \sim x^{\tau_1}\left[\frac{iU_0'}{\lambda_1} + (2x)^{\frac{1}{2}} f'(N) + O(x^{-\frac{3}{2}})\right].$$

Finally when $N = O(\epsilon^{-3} x^{-1})$,

$$f'(N) \sim 1 + \text{EST}, \quad \text{and} \quad U_0' \frac{\int_0^M \left(M - \widetilde{M}\right) Ai(\tilde{z})\widetilde{M}}{\int_0^\infty Ai(\tilde{z}) d\widetilde{M}} \sim \frac{iU_0'}{\lambda_1} + U_0'(2x)^{\frac{1}{2}} N,$$

so

$$\phi_0 \sim x^{\tau_1}\left(\frac{iU_0'}{\lambda_1} + (2x)^{\frac{1}{2}}\right) \exp\left(-\frac{2\epsilon^3 i\lambda_1 x N}{U_0'}\right).$$

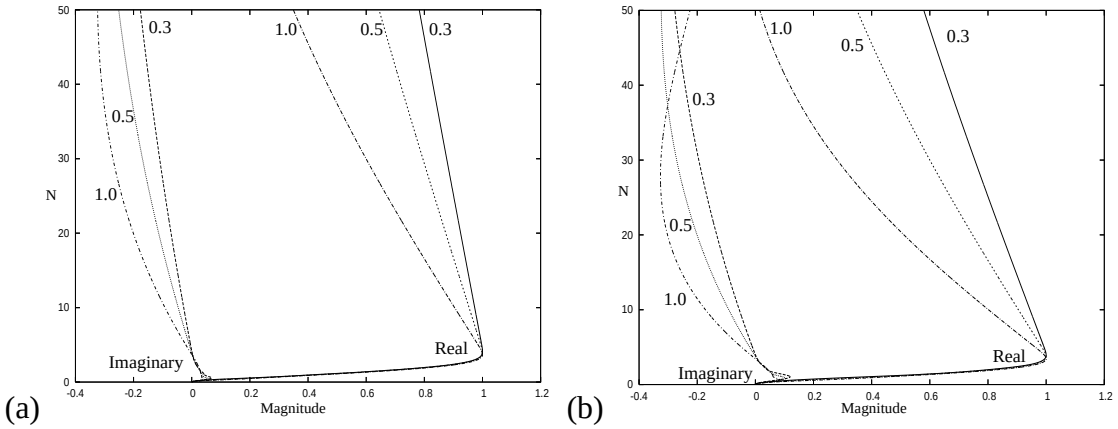

Figure 4.1: Plot of leading edge mode shape, given by (4.32), at $\tilde{x}_1 = 2\epsilon^2 x/U_0'^2 = 0.3, 0.5$ and 1.0 for (a) $\epsilon = 0.05$ and (b) $\epsilon = 0.1$, where the mode shapes have been normalised so that $Re(\phi_0) = 1$.

In figure 4.1, we compare the evolution of the leading edge mode shape, given by (4.32) at the scaled variable positions $\tilde{x}_1 = 2\epsilon^2 x/U_0'^2 = 0.3, 0.5$ and 1.0, for $\epsilon = 0.05$ and 0.1, where the mode shapes have been normalised so that $Re(\phi_0) = 1$. We note that as we move further from the leading edge, $\tilde{x}_1 = 0$, in both cases the real part of the mode shape tends to 0 faster as $N \longrightarrow \infty$. Also, for both values of ϵ it appears that the inner layers are about the same thickness, but since the width of the outer layer in the matching region is $O(\epsilon^{-1})$, we note that the $\epsilon = 0.1$ outer layer is much thinner, so the mode shapes are more concentrated near to the wall than for $\epsilon = 0.05$. The reason that the outer layer is $O(\epsilon^{-1})$ in this case is because the matching region occurs on an x length scale of $O(\epsilon^{-2})$.

4.3 Orr-Sommerfeld region

For the flat plate, which is the simplest geometry to consider, Goldstein (1982) and Goldstein (1983) calculated the large Re asymptotic solution for both the wavenumber and mode shape in the Orr-Sommerfeld region. This will provide us with a means of checking our numerical scheme. In section §4.3.1, we shall demonstrate the key stages in the derivation of the asymptotics, but for the full derivation, the reader is referred to Goldstein (1982).

4.3.1 Goldstein's asymptotics up to $O(\epsilon^3 \ln \epsilon)$

Goldstein derived the governing equation for the motion of the boundary-layer from the vorticity-stream function form of the non-dimensional Navier-Stokes equations, and wrote the equation as

$$-i\tilde{\nabla}^2\psi + x^{\frac{1}{2}}\left[\frac{\partial(x^{-1}\tilde{\nabla}^2\psi, x^{\frac{1}{2}}f)}{\partial(x,\eta)} + \frac{\partial(x^{-\frac{1}{2}}f'', \psi)}{\partial(x,\eta)}\right] = \tilde{\nabla}^2\left(\frac{1}{2x}\tilde{\nabla}^2\psi\right) + O(\psi\epsilon^6\Lambda) \quad (\eta, x > 0), \quad (4.33)$$

where

$$\begin{aligned}
\tilde{\nabla}^2 &= \frac{\partial^2}{\partial\eta^2} + 2\epsilon^6 x\frac{\partial^2}{\partial x^2} + \epsilon^6\frac{\partial}{\partial x}, \\
\Lambda &= max\left(\frac{\eta^2}{x}, x^{-1}\right), \\
\epsilon^6 &= Re^{-1},
\end{aligned}$$

and the variables (x, η) are equivalent to (ξ, N) used in chapter 2 with $U_f = 1$. This equation is solved with the boundary conditions

$$\psi = \frac{\partial \psi}{\partial \eta} = 0 \quad \text{on} \quad \eta = 0,\ x > 0.$$

In the limit $\epsilon \longrightarrow 0$ with $x = O(1)$, (4.33) reduces to the linearised unsteady boundary-layer equation (4.4), and gives the Lam-Rott eigenmodes as part of its solution. However, the leading edge solution breaks down when $x = O(\epsilon^{-2})$, therefore, to look for a solution to (4.33) in the Orr-Sommerfeld region, we introduce the scaled variable

$$x_1 = \epsilon^2 x, \tag{4.34}$$

and look for solutions in the form of traveling waves

$$\psi = \epsilon^s G(x_1, \eta) \exp\left(\frac{i}{\epsilon}\int_0^x \kappa(x_1, \epsilon) dx\right), \tag{4.35}$$

where κ and G are $O(1)$, and the constant $s = -(2\tau_j + 1)$, where τ_j is given by (4.5). We write the function $G(x_1, \eta)$ as a product:

$$G(x_1, \eta) = A(x_1)\gamma(x_1, \eta),$$

where $A(x_1)$ is a slowly varying function of x_1, to be determined by the analysis, and $\gamma(x_1, \eta)$ is the mode shape.

The equation for the evolution of the wavenumber κ up to $O(\epsilon^3 \ln \epsilon)$ is

$$\begin{aligned}\tilde{x}_1^{\frac{3}{2}} + (\epsilon e^{\frac{1}{4}i\pi}\zeta_0^{\frac{3}{2}})\tilde{x}_1\left(2 - \frac{\tilde{x}_1^{\frac{3}{2}}J_1}{i\zeta_0^3}\right) + (\epsilon e^{\frac{1}{4}i\pi}\zeta_0^{\frac{3}{2}})^2\tilde{x}_1^{\frac{1}{2}}\left(1 + \frac{2\tilde{x}_1^{\frac{3}{2}}J_2}{i\zeta_0^3} - \frac{\tilde{x}_1^3 J_3}{\zeta_0^6}\right) \\ - \frac{e^{\frac{1}{4}i\pi}(\tilde{x}_1\zeta_0)^{\frac{3}{2}}\epsilon^3}{2U_0'^2}\ln\left(\frac{\epsilon e^{\frac{1}{4}i\pi}\zeta_0^{\frac{3}{2}}}{\tilde{x}_1^{\frac{1}{2}}U_0'}\right) = H(\zeta_0) \equiv \frac{e^{\frac{5}{2}i\pi}\zeta_0^2 Ai'(\zeta_0)}{\int_{\infty_1}^{\zeta_0} Ai(\zeta)d\zeta},\end{aligned} \tag{4.36}$$

where

$$\tilde{x}_1 \equiv \frac{2x_1}{U_0'^2}, \tag{4.37}$$

$$\zeta_0 = e^{-\frac{5}{6}i\pi}\left(\frac{\tilde{x}_1^{\frac{1}{2}}}{\kappa}\right)^{\frac{2}{3}}, \tag{4.38}$$

$$J_1 \equiv U_0'\int_0^\infty \left(U^2 - \frac{1}{U^2} + \frac{1}{U_0'^2\eta^2}\right)d\eta, \tag{4.39}$$

$$J_2 = -U_0'\int_0^\infty \left(\frac{1}{U^3} - \frac{2}{U^2} + U - \frac{1}{(U_0'\eta)^3} + \frac{2}{(U_0'\eta)^2}\right)d\eta, \tag{4.40}$$

$$J_3 = J_1^2 - 2U_0'^2\int_0^\infty U^2\int_\eta^\infty \left(U^2 - \frac{1}{U^2}\right)d\eta d\eta, \tag{4.41}$$

$$U = f'(\eta), \tag{4.42}$$

and the subscript 1 on ∞ is used to indicate that the path of integration tends to infinity in the sector $-\frac{1}{3}\pi < \arg(\zeta) < \frac{1}{3}\pi$. Equation (4.36) is the same as equation (4.52) of Goldstein (1983).

We solve (4.36) using a complex-plane eigenvalue search method at each step. At the initial step, $\tilde{x}_1 = 0$, we set $\zeta_0 = -1.0188$, as this is the first root of $Ai(\zeta_j) = 0$, and we wish to track the evolution of the unstable eigenmode. We then march in steps of 0.01, solving for ζ_0, and hence using (4.38), to solve for κ at each step. Figure 4.2 shows this numerical result for $\epsilon^6 = 0, 10^{-6}, 10^{-4}$.

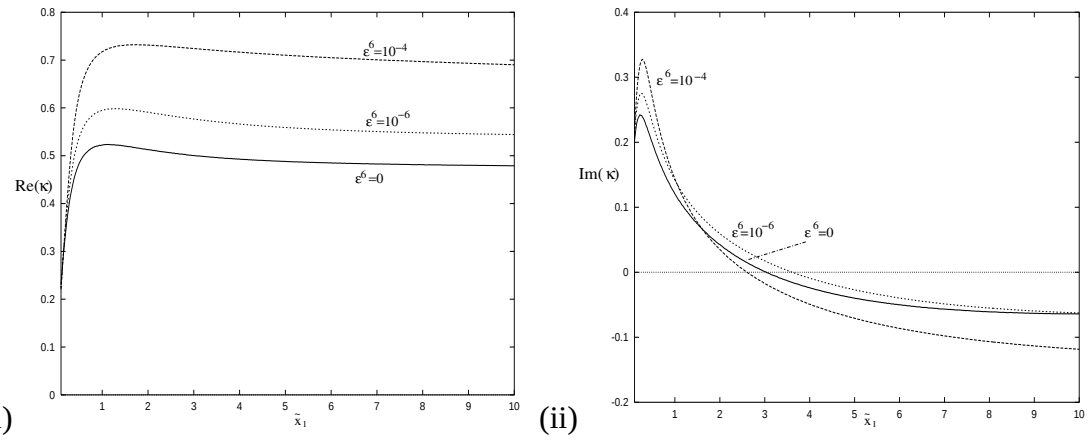

Figure 4.2: Plot of (a) the real part, and (b) the imaginary part of the wavenumber, κ, as a function of the scaled downstream distance variable $\tilde{x}_1$.

The $\epsilon = 0$ case is the solution in the limit $Re \longrightarrow \infty$, and hence corresponds to the

leading order term of the asymptotic expansion given below. Note, that at this order (up to and including terms of $O(\epsilon^3 \ln \epsilon)$) the lower branch neutral stability point ($\mathrm{Im}(\kappa) = 0$) first moves downstream, then upstream for increasing ϵ. However this is not the case if more terms in the small ϵ expansion are retained. As ϵ increases, the missing $O(\epsilon^3)$ term from this result becomes more and more important, and hence contributes more and more to the solution, as we shall see later when we study the full PSE numerics.

We also note that for both the real and imaginary cases, the solution converges to the same solution for different ϵ as $\tilde{x}_1 \longrightarrow 0$. This is the previously discussed 'matching region', where the leading edge solution and the Orr-Sommerfeld solution both become valid.

An alternative approach to solving (4.36) is by asymptotically expanding κ in the form

$$\kappa = \kappa_0 + \epsilon\kappa_1 + \epsilon^2\kappa_2 + \epsilon^3(\ln\epsilon)\kappa_3 + O(\epsilon^3).$$

Substituting this into (4.36) and (4.38), expanding $H(\zeta_0)$ in a Taylors series about

$$\zeta_{00} = e^{-\frac{5}{6}i\pi}\left(\frac{\tilde{x}_1^{\frac{1}{2}}}{\kappa_0}\right)^{\frac{2}{3}}, \tag{4.43}$$

and equating coefficients of like powers of ϵ, leads to

$$\begin{aligned}
H(\zeta_{00}) &= \tilde{x}_1^{\frac{3}{2}}, && (4.44)\\
\frac{\kappa_1}{\kappa_0} &= -\frac{3}{2}e^{\frac{1}{4}i\pi}\zeta_{00}^{\frac{1}{2}}\tilde{x}_1\left(2 - \frac{\tilde{x}_1^{\frac{3}{2}}J_1}{i\zeta_{00}^3}\right)/H'(\zeta_{00}), && (4.45)\\
\frac{\kappa_2}{\kappa_0} &= -\frac{1}{3}\left(\frac{1}{2} - \frac{H''(\zeta_{00})\zeta_{00}}{H'(\zeta_{00})}\right)\left(\frac{\kappa_1}{\kappa_0}\right)^2\\
&+ 3e^{-\frac{1}{4}i\pi}\left(\frac{\tilde{x}_1}{\zeta_{00}}\right)^{\frac{5}{2}}J_1\left(\frac{\kappa_1}{\kappa_0}\right)/H'(\zeta_{00})\\
&- \frac{3}{2}i\zeta_{00}^2\tilde{x}_1^{\frac{1}{2}}\left(1 + \frac{2\tilde{x}_1^{\frac{3}{2}}J_2}{i\zeta_{00}^3} - \frac{\tilde{x}_1^3 J_3}{i\zeta_{00}^6}\right)/H'(\zeta_{00}), && (4.46)\\
\frac{\kappa_3}{\kappa_0} &= \frac{3}{4U_0'^2}e^{\frac{1}{4}i\pi}\zeta_{00}^{\frac{1}{2}}\tilde{x}_1^{\frac{3}{2}}/H'(\zeta_{00}), && (4.47)
\end{aligned}$$

where $H(\zeta_{00})$ is defined by (4.36) and primes on H denote derivatives with respect to ζ_{00}.

The majority of the correction at $O(\epsilon^3)$ comes in via the slowly varying amplitude function $A(x_1)$, which is discussed in §4.3.2. However, a small amount of the $O(\epsilon^3)$

correction comes via (4.36). If we extend the asymptotic analysis to incorporate this term, we find

$$\begin{aligned}\frac{\kappa_4}{\kappa_0} &= \frac{1}{27}\left(47 - 15\frac{\zeta_{00}H''(\zeta_{00})}{H'(\zeta_{00})} - 2\frac{\zeta_{00}^2 H'''(\zeta_{00})}{H'(\zeta_{00})}\right)\left(\frac{\kappa_1}{\kappa_0}\right)^3 + \frac{2}{3}\left(1 + \frac{\zeta_{00}H''(\zeta_{00})}{H'(\zeta_{00})}\right)\frac{\kappa_1\kappa_2}{\kappa_0^2} \\ &- \frac{3}{2}e^{-\frac{1}{4}i\pi}\left(\frac{\tilde{x}_1}{\zeta_{00}}\right)^{\frac{5}{2}} J_1\left(\left(\frac{\kappa_1}{\kappa_0}\right)^2 - 2\frac{\kappa_2}{\kappa_0}\right)/H'(\zeta_{00}) \\ &+ 3i\zeta_{00}^2\tilde{x}_1^{\frac{1}{2}}\left(1 + \frac{\tilde{x}_1^3 J_3}{\zeta_{00}^6}\right)\left(\frac{\kappa_1}{\kappa_0}\right)/H'(\zeta_{00}) + \frac{\kappa_3}{\kappa_0}\ln\left(\frac{e^{\frac{1}{4}i\pi}\zeta_{00}^{\frac{3}{2}}}{\tilde{x}_1^{\frac{1}{2}}U_0'}\right). \end{aligned} \tag{4.48}$$

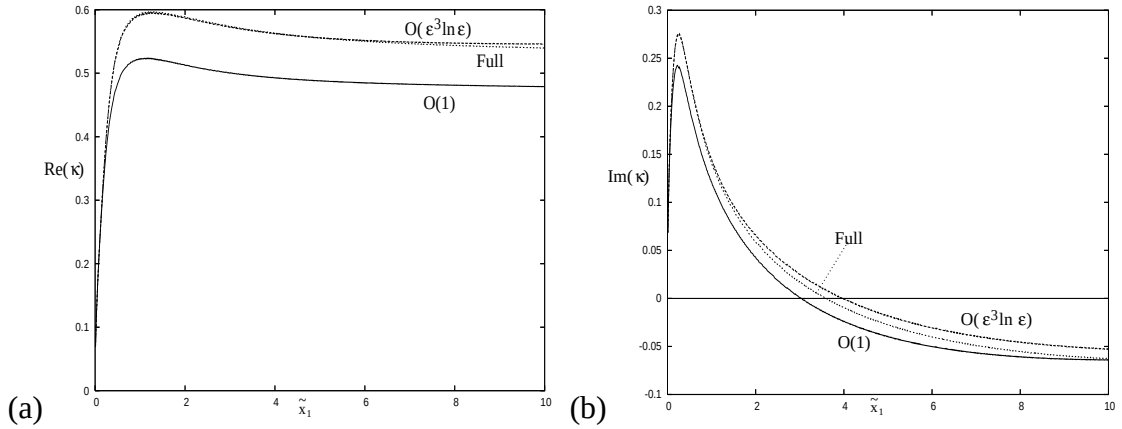

Figure 4.3: Comparison of (a) the real part, and (b) the imaginary part of the asymptotic and numerical value of the wavenumber, κ, for $\epsilon = 0.1$.

Figure 4.3 shows a comparison between the full numerical form of the wavenumber, κ, and its asymptotic form at $O(1)$ and up to and including $O(\epsilon^3 \ln \epsilon)$. We see good agreement between the numerics and the asymptotics over approximately the first half of the region considered, however downstream we have a slight discrepancy between the numerical and asymptotic results which proves to be crucial later when trying to calculate the $O(\epsilon^3)$ term. The $O(1)$ asymptotic expansion, is quite different from the other two results, although to leading order, they are the same, this proves that the correction terms are very important, even for small ϵ.

The mode shape function $\gamma(x_1, \eta)$ has a three layer structure similar to the leading

edge region,

$$\gamma(x_1,\eta) = \begin{cases} \frac{\epsilon\bar{c}\int_{\zeta_0}^{\zeta}(\zeta-\tilde{\zeta})Ai(\tilde{\zeta})d\tilde{\zeta}}{\zeta_0\int_{\infty_1}^{\zeta_0}Ai(\tilde{\zeta})d\tilde{\zeta}} + O(\epsilon^2) & \text{for} \quad \eta = O(\epsilon), \\ U - \epsilon\bar{c} - \epsilon\bar{\alpha}U\left(\int_{\infty}^{\eta}\left(\frac{1}{U^2}-1\right)d\eta + \eta\right) + O(\epsilon^2) & \text{for} \quad \eta = O(1), \\ (1-\epsilon\bar{c})\,e^{-\bar{\alpha}\eta} + O(\epsilon^2) & \text{for} \quad \eta = O(\epsilon^{-1}), \end{cases} \tag{4.49}$$

where $U = f'(\eta)$, $\bar{\alpha} = (2x_1)^{\frac{1}{2}}\kappa$, $\bar{c} = 1/\kappa$ and $\zeta = \zeta_0(1 - U_0'\eta/(\bar{c}\epsilon))$.

4.3.2 Determination of the $O(\epsilon^3)$ term of the wavenumber

The $O(\epsilon^3)$ term in the asymptotic expansion for the wavenumber is not included in Goldstein (1983), however it is included in the NASA report Goldstein (1982). This section looks at the equation from which the $O(\epsilon^3)$ term is determined, and we derived the form of the undetermined constants $\tilde{A}_n$ which appear in this equation so that we can determine the $O(\epsilon^3)$ term. The form of these constants were not given in Goldstein (1982).

To find the $O(\epsilon^3)$ correction term to the wavenumber, κ, we must find the form of $d\ln A/dx_1$, because by considering (4.35), we see that

$$\psi = \epsilon^s\gamma(x_1,\eta,\epsilon)\exp\left(\frac{i}{\epsilon}\int_0^x\left(\kappa(x_1,\epsilon) - i\epsilon^3\frac{d\ln A}{dx_1}\right)dx\right). \tag{4.50}$$

Goldstein (1982) derives the governing equation for $A(x_1)$, and writes it in the form

$$\begin{aligned} 2\bar{\alpha}\frac{d\ln A}{dx_1} &+ \bar{\alpha}_{x_1} - \frac{\bar{\alpha}}{2x_1} + \frac{\bar{\alpha}}{\bar{c}}\sum_{n=0}^{3}\tilde{A}_n\bar{c}^n\bar{\alpha}^{(3-n)} \\ &= \pi U_0'Bi'(\zeta_0)\int_0^{\infty}\left(\bar{H}_1\frac{d\ln A}{dx_1} + \bar{H}_2\right)Ai(\zeta)d\bar{\eta} - \frac{i\bar{\alpha}}{\bar{c}U_0'}\int_0^{\infty}\Gamma^{\dagger}d\bar{\eta}, \end{aligned} \tag{4.51}$$

where $\tilde{A}_n$ are O(1) constants and

$$\bar{H}_1 \equiv \bar{D}(\bar{\gamma}_0 - \bar{\eta}\bar{D}\bar{\gamma}_0), \tag{4.52}$$

$$\bar{H}_2 \equiv \bar{D}\left(\frac{\partial}{\partial x_1}(\bar{\gamma}_0 - \bar{\eta}\bar{D}\bar{\gamma}_0) + \frac{1}{4x_1}\bar{D}(\bar{\eta}^2\bar{D}\bar{\gamma}_0) - \frac{iU_0'}{3!\bar{c}}\bar{\eta}^3(\bar{\gamma}_0 - \frac{1}{4}\bar{\eta}\bar{D}\bar{\gamma}_0)\right). \tag{4.53}$$

In the above equation, $\bar{\eta} = \eta/\epsilon$, $\bar{D} \equiv d/d\bar{\eta}$, and $\bar{\gamma}_0$ is defined by the mode shape in the $\eta = O(\epsilon)$ layer of (4.49). In (4.51),

$$\begin{aligned} \int_0^{\infty}\Gamma^{\dagger}d\bar{\eta} &= -i\zeta_0U_0'\int_0^{\infty}\left(Wi\left(\bar{H}_1\frac{d\ln A}{dx_1} + \bar{H}_2 - \frac{U_0'}{2x_1}\right.\right. \\ &\quad \left.\left. + \frac{iU_0'}{2\bar{c}}\bar{\eta}^2(a_1 + U_0'\bar{\eta}) + \frac{\bar{c}(a_1+\bar{c})}{2iU_0'}\right) + \frac{\bar{c}(a_1+\bar{c})}{2iU_0'\zeta}\right)d\bar{\eta}, \end{aligned} \tag{4.54}$$

where

$$Wi(\zeta) = -\pi \left(Ai(\zeta) \int_{\zeta_0}^{\zeta} Bi(\xi) d\xi - Bi(\zeta) \int_{\infty_1}^{\zeta} Ai(\xi) d\xi \right), \tag{4.55}$$

and

$$\zeta = \zeta_0 \left(1 - \frac{U_0' \bar{\eta}}{\bar{c}} \right). \tag{4.56}$$

Note that (4.54) is not derived completely in Goldstein (1982), but a full derivation for it can be found in Appendix D. The majority of the integrals in (4.51) can actually be evaluated, or simplified, although this was not noted in the preparation of this work (Turner, 2006).

In his appendix B, Goldstein (1982) writes that the solution for γ in the middle deck of the Orr-Sommerfeld region can be expressed as

$$\gamma = \gamma_H + O(\epsilon^4). \tag{4.57}$$

He then states on p40, that it can be shown that

$$\gamma_H = \frac{\bar{\alpha}\bar{c}^3}{2U_0'^3} \ln \eta - \frac{i\bar{\alpha}}{U_0'} \sum_{n=0}^{3} A_n \bar{c}^n \bar{\alpha}^{(3-n)} + O(\eta \ln \eta) \quad \text{as} \quad \eta \longrightarrow 0, \tag{4.58}$$

where the A_n's are $O(1)$ constants related to the $\tilde{A}_n$'s. Hence to find the exact form of the $\tilde{A}_n$'s to be able to solve (4.51), we have to find the asymptotic form of γ_H as $\eta \longrightarrow 0$, and compare it with (4.58). To find γ_H we substitute (4.57) into Goldstein's governing equation (B-1) of Appendix B to show that γ_H satisfies Rayleigh's equation

$$(U(\eta) - \epsilon\bar{c})(D^2 - \epsilon^2\bar{\alpha}^2)\gamma_H - U''(\eta)\gamma_H = 0, \tag{4.59}$$

where $D \equiv d/d\eta$, $\bar{c}$ is the wave speed of the problem, and $\bar{\alpha}$ is the corresponding wave number. We solve this equation by expanding γ_H as an asymptotic expansion for small ϵ, of the form

$$\gamma_H(\eta) = \gamma_0(\eta) + \epsilon\gamma_1(\eta) + \epsilon^2\gamma_2(\eta) + \epsilon^3\gamma_3(\eta) + \epsilon^4\gamma_4(\eta) + O(\epsilon^5). \tag{4.60}$$

This yields the system of equations

$$O(1): \qquad UD^2\gamma_0 - U''\gamma_0 = 0, \tag{4.61}$$

$$O(\epsilon): \qquad UD^2\gamma_1 - U''\gamma_1 = \bar{c}D^2\gamma_0, \tag{4.62}$$

$$O(\epsilon^2): \qquad UD^2\gamma_2 - U''\gamma_2 = \bar{c}D^2\gamma_1 - U\bar{\alpha}^2\gamma_0, \tag{4.63}$$

$$O(\epsilon^3): \qquad UD^2\gamma_3 - U''\gamma_3 = \bar{c}D^2\gamma_2 + U\bar{\alpha}^2\gamma_1 - \bar{c}\bar{\alpha}^2\gamma_0, \tag{4.64}$$

$$O(\epsilon^4): \qquad UD^2\gamma_4 - U''\gamma_4 = \bar{c}D^2\gamma_3 + U\bar{\alpha}^2\gamma_2 - \bar{c}\bar{\alpha}^2\gamma_1. \tag{4.65}$$

Each of these equations has to be solved with the conditions that they match to the outer and inner layers.

The first two equations (4.61) and (4.62) can be solved quite easily, and have the solutions

$$\gamma_0 = U(\eta), \tag{4.66}$$

$$\gamma_1 = -\bar{c} - \bar{\alpha}U(\eta)\left(\int_\infty^\eta \left(\frac{1}{U^2} - 1\right) d\eta + \eta\right). \tag{4.67}$$

Equation (4.61) has to be solved with the condition that the lowest order normal velocity component of this solution has to vanish at the wall, i.e.

$$\gamma_0(0, x_1) = 0.$$

This is why we take (4.66) as our solution and we ignore the unimportant normalization constant.

As $\eta \longrightarrow 0$ we can write each solution as an asymptotic series in powers of η. Therefore,

$$\gamma_0 \sim U_0'\eta - \frac{U_0'^2\eta^4}{24} + \frac{11U_0'^3\eta^7}{5040} - \frac{5U_0'^4\eta^{10}}{48384} + o(\eta^{11}), \tag{4.68}$$

$$\gamma_1 \sim \left(\bar{c} + \frac{\bar{\alpha}}{U_0'}\right) - \bar{\alpha}U_0'J_0\eta - \frac{\bar{\alpha}\eta^3}{12} + \frac{\bar{\alpha}U_0'^2J_0\eta^4}{24} + \frac{3\bar{\alpha}U_0'\eta^6}{800} + O(\eta^7), \tag{4.69}$$

where $J_0 = \int_\infty^0 \left(\frac{1}{U^2} - \frac{1}{(U_0'\eta)^2} - 1\right) d\eta$. We can also solve (4.63) exactly, but writing down the solution is very complicated, and as we only need the solution in the limit $\eta \longrightarrow 0$, we find it beneficial to guess a small η expansion for γ_2, substitute it into (4.63) with $U(\eta)$ expanded for small η, and equate powers of η.

Therefore for each of the remaining equations (4.63), (4.64) and (4.65), we assume a general asymptotic expansion of the form

$$\gamma_n = \sum_{i=0}^{6} \gamma_{ni}\eta^i + \ln\eta \sum_{i=0}^{6} \hat{\gamma}_{ni}\eta^i + O\left(\eta^7\right), \tag{4.70}$$

for $n = 2, 3, 4$, where for each solution the constants, γ_{n0} and γ_{n1}, are determined by matching to the inner and outer expansions. Thus although this method won't determine the full form of γ_H, it will help us to determine the higher order γ_{ni} in terms of these constants.

Substituting (4.70) into (4.63), (4.64) and (4.65) and equating powers of η we get the following expansions for γ_2, γ_3 and γ_4,

$$\begin{aligned}
\gamma_2 &= \gamma_{20} + \gamma_{21}\eta - \frac{\bar{c}\bar{\alpha}\eta^2}{4U_0'} + \left(\frac{U_0'\bar{\alpha}^2}{6} - \frac{U_0'\gamma_{20}}{12} + \frac{U_0'\bar{c}\bar{\alpha}J_0}{12}\right)\eta^3 \\
&- \frac{U_0'\gamma_{21}\eta^4}{24} + \frac{13\bar{c}\bar{\alpha}\eta^5}{1200} + O(\eta^6), \qquad (4.71) \\
\gamma_3 &= \gamma_{30} + \gamma_{31}\eta - \frac{\bar{c}^2\bar{\alpha}}{2U_0'^2}\eta\ln(\eta) + \left(-\frac{\bar{c}\bar{\alpha}^2}{2} + \frac{\bar{\alpha}^3}{2U_0'} + \frac{\bar{c}^2\bar{\alpha}J_0}{4} - \frac{\bar{c}\gamma_{20}}{4}\right)\eta^2 \\
&+ \left(-\frac{U_0'\bar{\alpha}^3J_0}{6} - \frac{U_0'\gamma_{30}}{12} - \frac{\bar{c}\gamma_{21}}{12}\right)\eta^3 \\
&+ \left(\frac{\bar{c}^2\bar{\alpha}}{240U_0'} - \frac{U_0'\gamma_{31}}{24}\right)\eta^4 + \frac{\bar{c}^2\bar{\alpha}}{48U_0}\eta^4\ln(\eta) + O(\eta^5), \qquad (4.72) \\
\gamma_4 &= \gamma_{40} + \frac{\bar{c}^3\bar{\alpha}}{2U_0'^3}\ln(\eta) + \gamma_{41}\eta + \left(-\frac{\bar{c}\gamma_{20}}{2U_0'} + \frac{\bar{c}^3\bar{\alpha}J_0}{2U_0'}\right)\eta\ln(\eta) + O(\eta^2). \qquad (4.73)
\end{aligned}$$

Now that we have determined the higher order terms in terms of the matching constants, we can use another form of the Rayleigh equation given by Miles (1962), which is the inviscid Rayleigh equation transformed into a Riccati equation, to determine these matching constants. His result can be written as

$$\begin{aligned}
\frac{D\gamma_H}{\gamma_H} &= \frac{U'}{U-\epsilon\bar{c}} - \frac{1}{(U-\epsilon\bar{c})^2\Omega} + O(\epsilon^5), \qquad (4.74) \\
\Omega &= \frac{1}{\epsilon\bar{\alpha}(1-\epsilon\bar{c})^2} + \Omega_0 + \epsilon\bar{\alpha}\Omega_1 + \epsilon^2\bar{\alpha}^2\Omega_2, \qquad (4.75)
\end{aligned}$$

where

$$\Omega_0 = -\frac{1}{(1-\epsilon\bar{c})^2}\int_\eta^\infty \left(\frac{(U-\epsilon\bar{c})^2}{(1-\epsilon\bar{c})^2} - \frac{(1-\epsilon\bar{c})^2}{(U-\epsilon\bar{c})^2}\right) d\eta, \tag{4.76}$$

$$\Omega_1 = -\frac{2}{(1-\epsilon\bar{c})^2}\int_\eta^\infty (U-\epsilon\bar{c})^2\Omega_0 d\eta, \tag{4.77}$$

$$\Omega_2 = -\int_\eta^\infty (U-\epsilon\bar{c})^2\left(\frac{2\Omega_1}{(1-\epsilon\bar{c})^2} + \Omega_0^2\right) d\eta, \tag{4.78}$$

and the dash denotes derivative with respect to η.

To solve this equation, we expand γ_H as in (4.60), expand the right hand side and left hand side for small ϵ, and equate powers of ϵ. Each equation can then be solved fully, if possible, or we can let $\eta \longrightarrow 0$ and expand for small η to pick out the leading order term. The reason we only want the leading order term, is because that's what we require to substitute into (4.51). Doing this we find

$$\gamma_0 = U(\eta), \tag{4.79}$$

$$\gamma_1 = \left(-\bar{c} + \frac{\bar{\alpha}}{U_0'}\right) + \gamma_{11}\eta + O(\eta^2), \tag{4.80}$$

both as we found earlier. The constant γ_{11} can be written down as $-\bar{\alpha}U_0'J_0$ as before, but we decide to leave it in this form to make the analysis easier. Similarly in the next set of equations, γ_{21} etc. can be determined, although their explicit form is not important here. We find the solutions for γ_2, γ_3 and γ_4 to be

$$\gamma_2 = -\frac{\bar{\alpha}\left(2\bar{c} - \frac{\bar{\alpha}J_1}{U_0'}\right)}{U_0'} + \frac{\gamma_{11}\left(-\bar{c} + \frac{\bar{\alpha}}{U_0'}\right)}{U_0'} + \gamma_{21}\eta + O(\eta^2), \tag{4.81}$$

$$\begin{aligned}\gamma_3 &= \frac{\bar{\alpha}\left(\bar{c}^2 + \frac{2\bar{\alpha}\bar{c}J_2}{U_0'} + \frac{\bar{\alpha}^2J_3}{U_0'^2}\right)}{U_0} + \frac{\gamma_{21}\left(-\bar{c} + \frac{\bar{\alpha}}{U_0'}\right)}{U_0'} \\ &- \frac{\gamma_{11}\bar{\alpha}\left(2\bar{c} - \frac{\bar{\alpha}J_1}{U_0'}\right)}{U_0'^2} + \gamma_{31}\eta + O(\eta^2),\end{aligned} \tag{4.82}$$

$$\begin{aligned}\gamma_4 &= \gamma_{400} + \frac{\gamma_{31}\left(-\bar{c} + \frac{\bar{\alpha}}{U_0'}\right)}{U_0'} - \frac{\gamma_{21}\bar{\alpha}\left(2\bar{c} - \frac{\bar{\alpha}J_1}{U_0'}\right)}{U_0'^2} \\ &+ \frac{\gamma_{11}\bar{\alpha}\left(\bar{c}^2 + \frac{2\bar{\alpha}\bar{c}J_2}{U_0'} + \frac{\bar{\alpha}^2J_3}{U_0'^2}\right)}{U_0'^2} + \frac{\bar{\alpha}\bar{c}^3}{2U_0'^3}\ln(\eta) + O(\eta),\end{aligned} \tag{4.83}$$

where

$$\begin{aligned}\gamma_{400} &= \bar{\alpha}^4\left(\frac{2J_1J_3}{U_0'^4}-\frac{J_1^3}{U_0'^4}+J_6\right)+\bar{\alpha}^3\bar{c}\left(\frac{4J_1J_2}{U_0'^3}+\frac{6J_1^2}{U_0'^3}-J_5-\frac{4J_3}{U_0'^3}\right)\\ &+ \bar{\alpha}^2\bar{c}^2\left(J_4-\frac{8J_2}{U_0'^2}-\frac{10J_1}{U_0'^2}-\frac{5}{24U_0'^4}\right)+\frac{\bar{\alpha}\bar{c}^3}{U_0'^3},\end{aligned} \tag{4.84}$$

and J_1 to J_6 are defined as

$$J_1 = U_0'\int_0^\infty\left(U^2-\frac{1}{U^2}+\frac{1}{(U_0'\eta)^2}\right)d\eta, \tag{4.85}$$

$$J_2 = -U_0'\int_0^\infty\left(\frac{1}{U^3}-\frac{2}{U^2}+U-\frac{1}{(U_0'\eta)^3}+\frac{2}{(U_0'\eta)^2}\right)d\eta, \tag{4.86}$$

$$J_3 = J_1^2-2U_0'^2\int_0^\infty U^2\int_\eta^\infty\left(U^2-\frac{1}{U^2}\right)d\eta d\eta, \tag{4.87}$$

$$J_4 = -\frac{1}{U_0'}\int_0^\infty\left(\frac{3}{U^4}-1+8U-10U^2-\frac{3}{(U_0'\eta)^4}-\frac{1}{2U_0'^3\eta}\right)d\eta, \tag{4.88}$$

$$\begin{aligned}J_5 &= \frac{4}{U_0'}\left(\int_0^\infty(U^2-U)\int_\eta^\infty\left(U^2-\frac{1}{U^2}\right)d\eta d\eta\right.\\ &+ \left.\int_0^\infty U^2\int_\eta^\infty\left(2U^2-\frac{1}{U^3}-U\right)d\eta d\eta\right),\end{aligned} \tag{4.89}$$

$$\begin{aligned}J_6 &= \frac{1}{U_0'}\left(\int_0^\infty U^2\left(4\int_\eta^\infty U^2\int_\eta^\infty\left(U^2-\frac{1}{U^2}\right)d\eta d\eta\right.\right.\\ &\left.\left.+\left(\int_\eta^\infty\left(U^2-\frac{1}{U^2}\right)d\eta\right)^2 d\eta\right)\right).\end{aligned} \tag{4.90}$$

Thus with a little bit of rearranging and manipulation we find

$$\tilde{A}_0 = iU_0'\left(\frac{2J_1J_3}{U_0'^4}-\frac{J_1^3}{U_0'^4}+J_6\right), \tag{4.91}$$

$$\tilde{A}_1 = iU_0'\left(\frac{4J_1J_2}{U_0'^3}+\frac{6J_1^2}{U_0^3}-J_5-\frac{4J_3}{U_0'^3}\right), \tag{4.92}$$

$$\tilde{A}_2 = iU_0'\left(J_4-\frac{8J_2}{U_0'^2}-\frac{10J_1}{U_0'^2}-\frac{5}{24U_0'^4}\right), \tag{4.93}$$

$$\tilde{A}_3 = \frac{i}{2U_0'^2}, \tag{4.94}$$

These are then used in (4.51) which can now be solved to find $d\ln A/dx_1$.

4.3.3 Matching of the leading edge and the Orr-Sommerfeld asymptotics

We stated, without proof in §4.3.1, that the Orr-Sommerfeld solution matches onto the leading edge solution as $x_1 \longrightarrow 0$. We now formally prove this statement by considering

the asymptotic solutions in both regions. If we consider the form of the solution in the Orr-Sommerfeld region as $x_1 \longrightarrow 0$, it follows from (4.43) that

$$\kappa_0 \longrightarrow \frac{i(2x_1)^{\frac{1}{2}}\lambda_j}{U_0'} = \frac{i\epsilon(2x)^{\frac{1}{2}}\lambda_j}{U_0'}, \tag{4.95}$$

and λ_j is given by $e^{\frac{i\pi}{4}}/\rho_j^{\frac{3}{2}}$. More precisely it can be shown that

$$\kappa_0 = \frac{i\epsilon(2x)^{\frac{1}{2}}\lambda_j}{U_0'} + 3C_0x_1^2 + o(x_1^2),$$

as $x_1 \longrightarrow 0$, where C_0 is an $O(1)$ constant. Also it follows that $H'(\zeta_{00})$ and $H'(\zeta_{00})/H''(\zeta_{00})$ are non-zero constants as $x_1 \longrightarrow 0$ (Abramowitz, 1964). Hence (4.45), (4.46) and (4.47) imply

$$\kappa_1 \longrightarrow \frac{5}{2}C_1x_1^{\frac{3}{2}}, \quad \kappa_2 \longrightarrow 2C_2x_1, \quad \kappa_3 \longrightarrow 3C_3x_1^2,$$

as $x_1 \longrightarrow 0$, where C_1, C_2 and C_3 are $O(1)$ constants. We can therefore conclude from (4.35) that

$$\begin{aligned}\exp\left\{\frac{i}{\epsilon}\int_0^x \kappa(x_1,\epsilon)dx\right\} &= \exp\left\{-\frac{\lambda_j(2x)^{\frac{3}{2}}}{3U_0'} + i\epsilon^3x^2\left(C_0x + C_1x^{\frac{1}{2}} + C_2\right) + iC_3\epsilon^6\ln\epsilon\, x^3 + O(\epsilon^4)\right\},\\ &= \exp\left[\frac{-\lambda_j(2x)^{\frac{3}{2}}}{3U_0'}\right]\left(1 + i\epsilon^3x^2\left(C_0x + C_1x^{\frac{1}{2}} + C_2\right) + O(\epsilon^4)\right).\end{aligned}$$

Hence this exponential term matches with the exponential term from (4.28) when the subscript 1 is replaced by j for the more general case.

Now by considering (4.95), we can see that

$$\bar{c} \longrightarrow \frac{U_0'}{i\epsilon(2x)^{\frac{1}{2}}\lambda_j} \quad \text{and} \quad \bar{\alpha} \longrightarrow \frac{i\epsilon^2(2x)\lambda_j}{U_0'},$$

as $x_1 \longrightarrow 0$. Hence it is straightforward to prove that

$$\gamma \longrightarrow \frac{g_0}{(2x)^{\frac{1}{2}}} \quad \text{as} \quad x_1 \longrightarrow 0,$$

in every layer, using the fact that $\zeta_0 \longrightarrow \zeta_j$ in the inner deck. So the amplitude functions will match completely if

$$A(x_1) \longrightarrow x_1^{\tau_j}(2x_1)^{\frac{1}{2}},$$

as $x_1 \longrightarrow 0$. This can be proved by replacing $\zeta_0, \bar{c}$ and $\bar{\alpha}$ in (4.51) by their first-order approximations $\zeta_{00}, \kappa_0^{-1}$ and $(2x_1)^{\frac{1}{2}}\kappa_0$ respectively. We also note that as $Wi(\zeta)$ and

$Bi'(\zeta_0)Ai(\zeta)$ are both $O(1)$ as $\zeta_0 \longrightarrow \zeta_j$, we see that the second term on the right-hand side of (4.51) will be negligible compared to the first. Expanding ζ_{00}, for small x_1, shows that $\partial\zeta_{00}/\partial x_1$ is bounded for small x_1, but

$$\frac{\partial \bar{c}}{\partial x_1} \longrightarrow -\frac{1}{2x_1}\bar{c},$$

as $x_1 \longrightarrow 0$. Hence it follows by using the chain rule that as $x_1 \longrightarrow 0$

$$\frac{\partial \bar{\gamma}_0}{\partial x_1} \longrightarrow -\frac{1}{2x_1}\bar{\gamma}_0 + \frac{\partial \bar{\gamma}_0}{\partial \zeta}\frac{\partial \zeta}{\partial x_1} = -\frac{1}{2x_1}\bar{\gamma}_0 + \bar{D}\bar{\gamma}_0\frac{\partial \zeta}{\partial x_1}\frac{\partial \bar{\eta}}{\partial \zeta},$$

where on inserting $\bar{c} = \kappa_0^{-1}$ into (4.56) and using (4.95) to eliminate ζ gives

$$\frac{\partial \bar{\gamma}_0}{\partial x_1} \longrightarrow -\frac{1}{2x_1}\left(\bar{\gamma}_0 - \bar{\eta}\bar{D}\bar{\gamma}_0\right).$$

Inserting this along with $\bar{c} = \kappa_0^{-1}$ into (4.53) gives

$$\bar{H}_2 \longrightarrow \bar{D}\left[-\frac{1}{2x_1}\left(\left(\bar{\gamma}_0 - \bar{\eta}\bar{D}\bar{\gamma}_0\right) + \frac{1}{2}\left(\bar{\eta}\bar{D}^2\bar{\gamma}_0 - 2\bar{\eta}\bar{D}\bar{\gamma}_0\right) - \frac{1}{6}\sigma^3\lambda_j\left(\bar{\gamma}_0 - \frac{\bar{\eta}}{4}\bar{D}\bar{\gamma}_0\right)\right)\right], \tag{4.96}$$

as $x_1 \longrightarrow 0$, where $\sigma = (2x)^{\frac{1}{2}}\eta = \epsilon^{-1}(2x_1)^{\frac{1}{2}}\eta$.

It also follows that in equation (4.51)

$$U_0'\pi Bi(\zeta_0)\int_0^\infty \bar{H}_1 Ai\; d\bar{\eta},$$

is $O(1)$ and will not go to zero as $x_1 \longrightarrow 0$, whereas $\bar{\alpha}$ does go to zero. Therefore the first term on the left-hand side of (4.51) goes to zero, and the remaining terms tend to a constant as $x_1 \longrightarrow 0$, hence we can neglect them, as our leading order term on the right hand side increases like $1/x_1$ as $x_1 \longrightarrow 0$.

Therefore (4.51) can be approximated by the first term on the right hand side. Thus inserting (4.96) into this result, and using $\gamma_0 = g_0/2x_1$ to eliminate $\bar{\gamma}_0$ in terms of g_0, and introducing σ, defined above, as the new variable of integration, leads to

$$\frac{d\ln A}{dx_1} \longrightarrow \frac{2\tau_j + 1}{2x_1} \quad \text{as} \quad x_1 \longrightarrow 0,$$

where τ_j is defined in equation (3.16) of Goldstein (1983). Hence integrating with respect to x_1 and making the appropriate choice for the integration constant leads to the required

result, showing that the amplitude functions do indeed match as $x_1 \longrightarrow 0$. This is demonstrated numerically in figure 4.4, which plots $d\ln A/dx_1$ and $(2\tau_1+1)/2x_1$ to show that we have good agreement as $x_1 \longrightarrow 0$, and in fact we have good agreement for $\tilde{x}_1 < 0.08$. The imaginary part of $d\ln A/dx_1$ tends to zero as $x_1 \longrightarrow 0$.

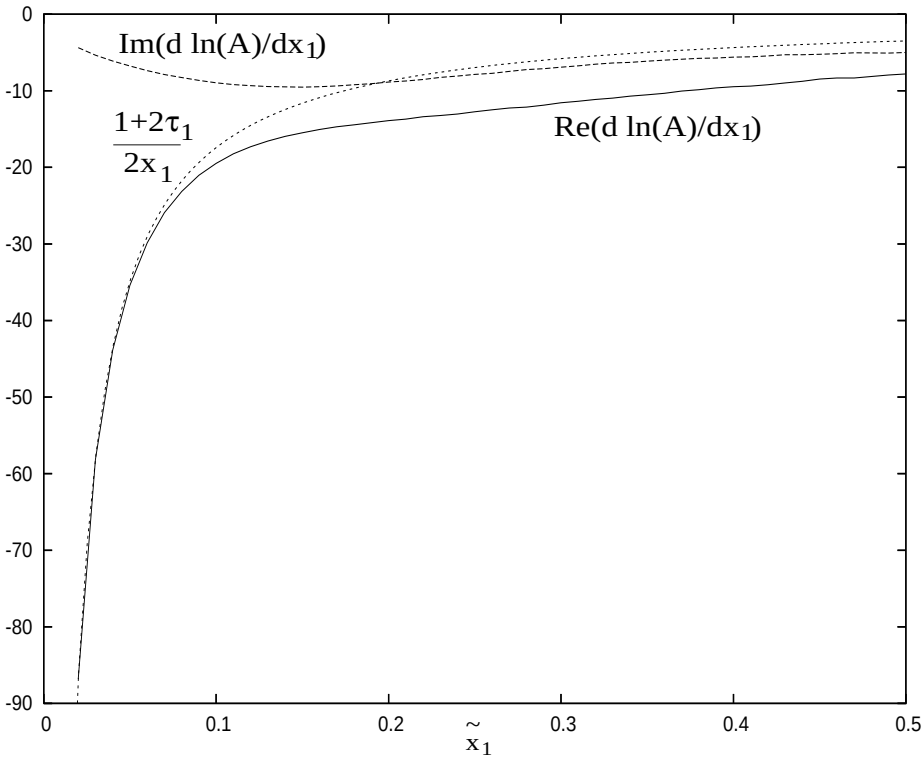

Figure 4.4: Plot of $d\ln A/dx_1$ as a function of $\tilde{x}_1$ plotted with $(2\tau_1+1)/2x_1$, to emphasise the matching of these results as $\tilde{x}_1 \longrightarrow 0$.

4.3.4 Re-normalization

For a semi-infinite flat plate, the PSE normalization condition simplifies to

$$\int_0^\infty \phi_{x_P}\phi^\dagger d\eta = 0,$$

where we now use $N = \eta$ to be consistent with Goldstein's asymptotics. However the normalization conditions used for the local PSE and Goldstein's Orr-Sommerfeld region asymptotics, were both different. The local PSE was normalized by setting $\alpha_1 = 0$, and Goldstein (1982) chose to let his middle deck solution be of the form

$$\gamma = U - \bar{c} - \epsilon\bar{\alpha}U\left(\int_\infty^\eta \left(\frac{1}{U^2}-1\right)d\eta + \eta\right) + O(\epsilon^2),$$

where he sets the constant multiplying the $O(1)$ term, $U(\eta)$, equal to 1, thus forcing a split between the amplitude function and the wavenumber. The fact that more than one normalization condition has been used means that, as they are, the different methods cannot be easily compared. To overcome this, we re-normalize all of the solutions, by factorizing the amplitude function $\phi(x_P, \eta)$ such that

$$\phi(x_P, \eta) = \phi_{max}(x_P)\bar{\phi}(x_P, \eta),$$

where the maximum value of $\bar{\phi}$ is 1. The stream function, ψ, for this problem is then given by

$$\psi = \bar{\phi}(x_p, \eta) \exp\left(i\tilde{\theta}(x_P) - \omega t\right) + \text{complex conjugate}, \tag{4.97}$$

with

$$\frac{d\tilde{\theta}}{dx_P} = G(x_P),$$

where $G(x_P)$ is the wave amplitude growth rate, and is given by

$$G(x_P) = \frac{Re}{R_0}\left(i\alpha + \frac{1}{\phi_{max}}\frac{\partial \phi_{max}}{\partial x_P}\right). \tag{4.98}$$

We use a similar re-normalization on $\gamma(x, \eta)$, and define $\hat{\gamma} = (2x)^{\frac{1}{2}}\gamma$, and $\bar{A}(x_1) = A(x_1)/(2x)^{\frac{1}{2}}$, thus producing the growth rate

$$G = \frac{i}{\epsilon}\left(\kappa - \epsilon^3 i\frac{d\ln(\bar{A})}{dx_1}\right) + \frac{2\epsilon^2}{U_0'^2}\frac{1}{\hat{\gamma}_{max}}\frac{\partial \hat{\gamma}_{max}}{\partial \tilde{x}_1}, \tag{4.99}$$

for Goldstein's asymptotics in the Orr-Sommerfeld region, where $\tilde{x}_1 = 2x_1/U_0'^2$.

4.4 Asymptotic results in the Orr-Sommerfeld region

4.4.1 Matching region

The PSE has three possible initial conditions which are the parallel Orr-Sommerfeld solution, the local PSE and the leading edge receptivity analysis. Figures 4.5 and 4.6 show a comparison between the initial mode shapes of the three upstream boundary conditions at two different starting positions, $\tilde{x}_1^{(0)} = 0.3$ and $\tilde{x}_1^{(0)} = 1.0$ when $\epsilon = Re^{-\frac{1}{6}} = 0.1$ and where the superscript (0) signifies that this is a starting position. The real parts, figure

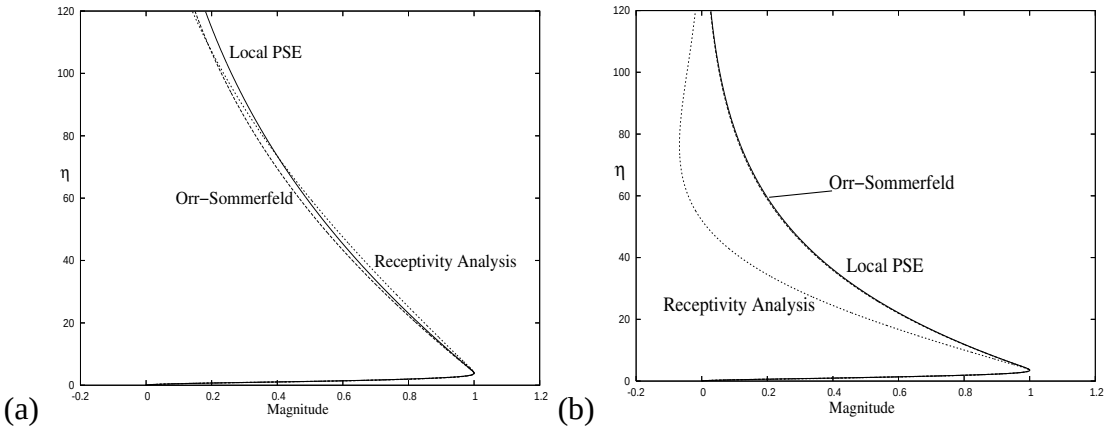

Figure 4.5: Comparison of the real part of the initial mode shapes of the three regimes at streamwise locations (a) $\tilde{x}_1^{(0)} = 0.3$, and (b) $\tilde{x}_1^{(0)} = 1.0$, for $\epsilon = 0.1$.

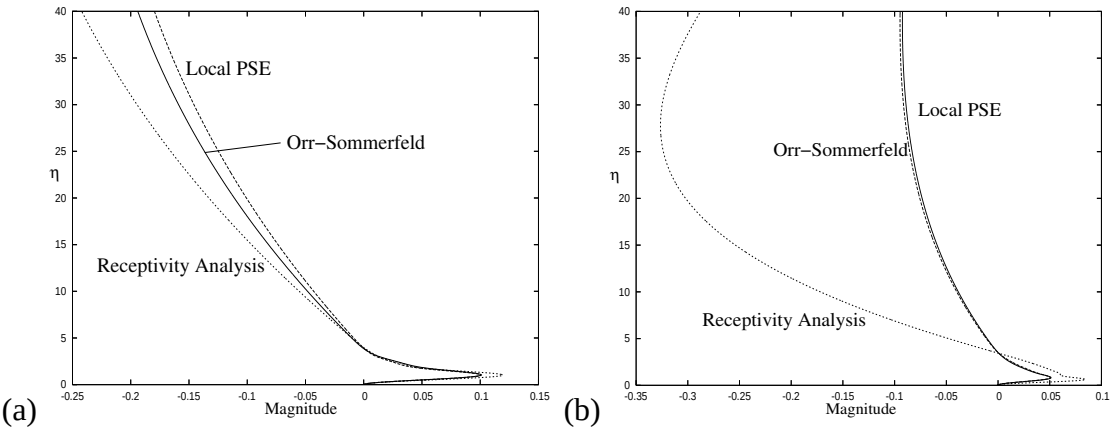

Figure 4.6: Comparison of the imaginary part of the initial mode shapes of the three regimes at streamwise locations (a) $\tilde{x}_1^{(0)} = 0.3$, and (b) $\tilde{x}_1^{(0)} = 1.0$, for $\epsilon = 0.1$.

4.5, and imaginary parts, figure 4.6, compare very well close to the wall for both starting points, but as we move away from the wall, they all decay to zero at slightly different rates, and at $\tilde{x}_1^{(0)} = 1.0$ the parallel Orr-Sommerfeld and local PSE mode shapes vary more from the receptivity mode shape than they do at $\tilde{x}_1^{(0)} = 0.3$. This suggests that $\tilde{x}_1^{(0)} = 0.3$ lies closer to the overlap region, between the leading edge and Orr-Sommerfeld regions, than $\tilde{x}_1^{(0)} = 1.0$. Considering smaller values of $\tilde{x}_1^{(0)}$ for this value of ϵ does not improve the agreement between the three mode shapes since the parallel Orr-Sommerfeld equation and the local PSE become invalid as $\tilde{x}_1^{(0)} \longrightarrow 0$ due to non-parallel effects entering at leading order. Also as we let $\tilde{x}_1^{(0)} \longrightarrow 0$, we encounter problems identifying the most unstable eigenvalue for both the parallel Orr-Sommerfeld and local PSE calculations as

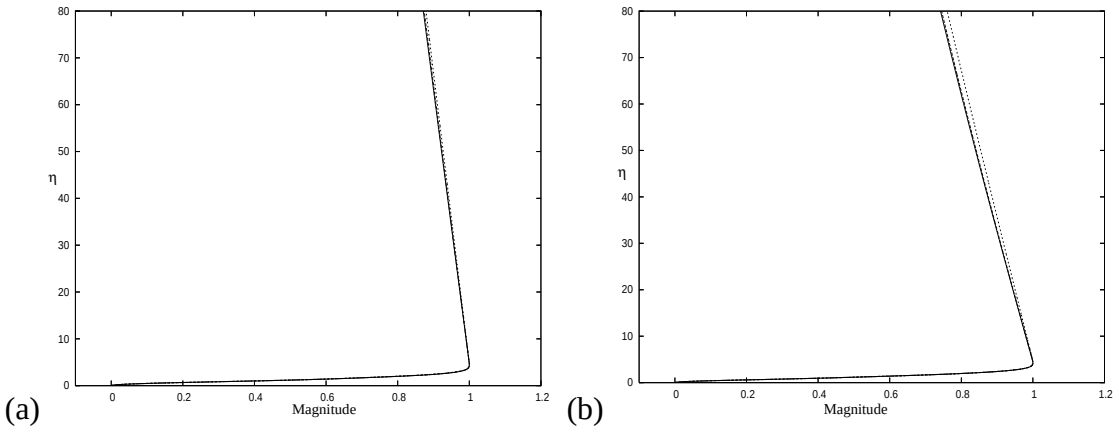

Figure 4.7: Comparison of the real part of the initial mode shapes for the leading edge receptivity, parallel Orr-Sommerfeld and local PSE analysis, where the line styles correspond to those in figures 4.5 and 4.6. With (a) $\epsilon = 0.05$ and $\tilde{x}_1^{(0)} = 0.1$, where the 3 mode shapes lie over each other, and (b) $\epsilon = 0.05$ and $\tilde{x}_1^{(0)} = 0.2$, where only the leading edge mode shape is distinguishable from the other two.

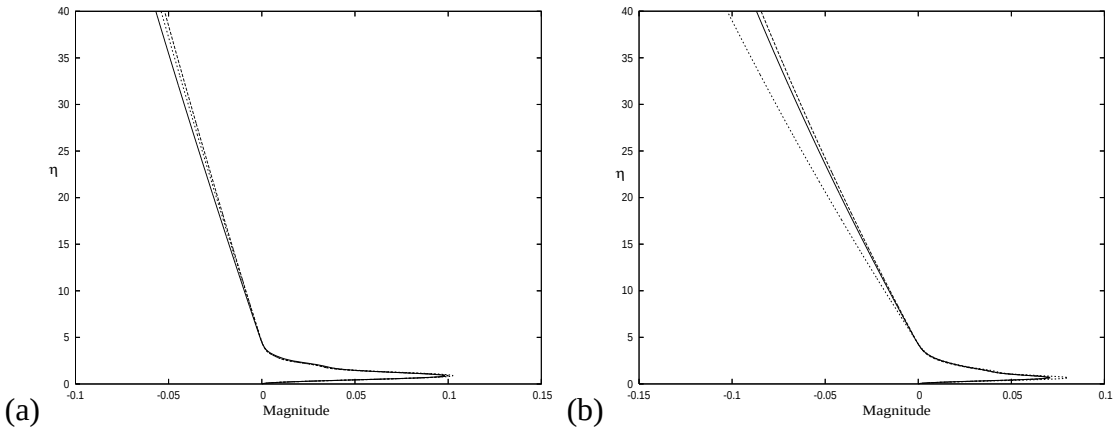

Figure 4.8: Comparison of the imaginary part of the initial mode shapes for the leading edge receptivity, parallel Orr-Sommerfeld and local PSE analysis, where the line styles correspond to those in figures 4.5 and 4.6. With (a) $\epsilon = 0.05$ and $\tilde{x}_1^{(0)} = 0.1$, where the solutions are the same for small η, and (b) $\epsilon = 0.05$ and $\tilde{x}_1^{(0)} = 0.2$, where the leading edge mode shape is more distinguishable.

discussed in §2.2.1. It is found that the unstable eigenvalue becomes indistinguishable from the discrete approximation to the continuous spectrum of eigenvalues in each case.

In order to illustrate the existence of a matching region more clearly, we consider corresponding results for a smaller value of ϵ. With $\epsilon = 0.05$, we can solve the parallel Orr-Sommerfeld and local PSE equations closer to $\tilde{x}_1^{(0)} = 0$ due to the unstable eigenmode being distinguishable from the continuous spectrum closer to the leading edge, as

discussed in §2.2.1. Figures 4.7 and 4.8 compare the real and imaginary parts of the mode shapes respectively at $\tilde{x}_1^{(0)} = 0.1$ and $\tilde{x}_1^{(0)} = 0.2$. For this smaller value of ϵ, figure 4.7(a) shows that the real part of the three solutions at $\tilde{x}_1^{(0)} = 0.1$ overlap each other while figure 4.8(a) shows that for the imaginary part of the solution at this point, the local PSE is in fact in slightly better agreement with the receptivity solution than the parallel Orr-Sommerfeld solution. From these figures it is clear that $\tilde{x}_1^{(0)} = 0.1$ lies within an overlap region between the leading edge region and the Orr-Sommerfeld region.

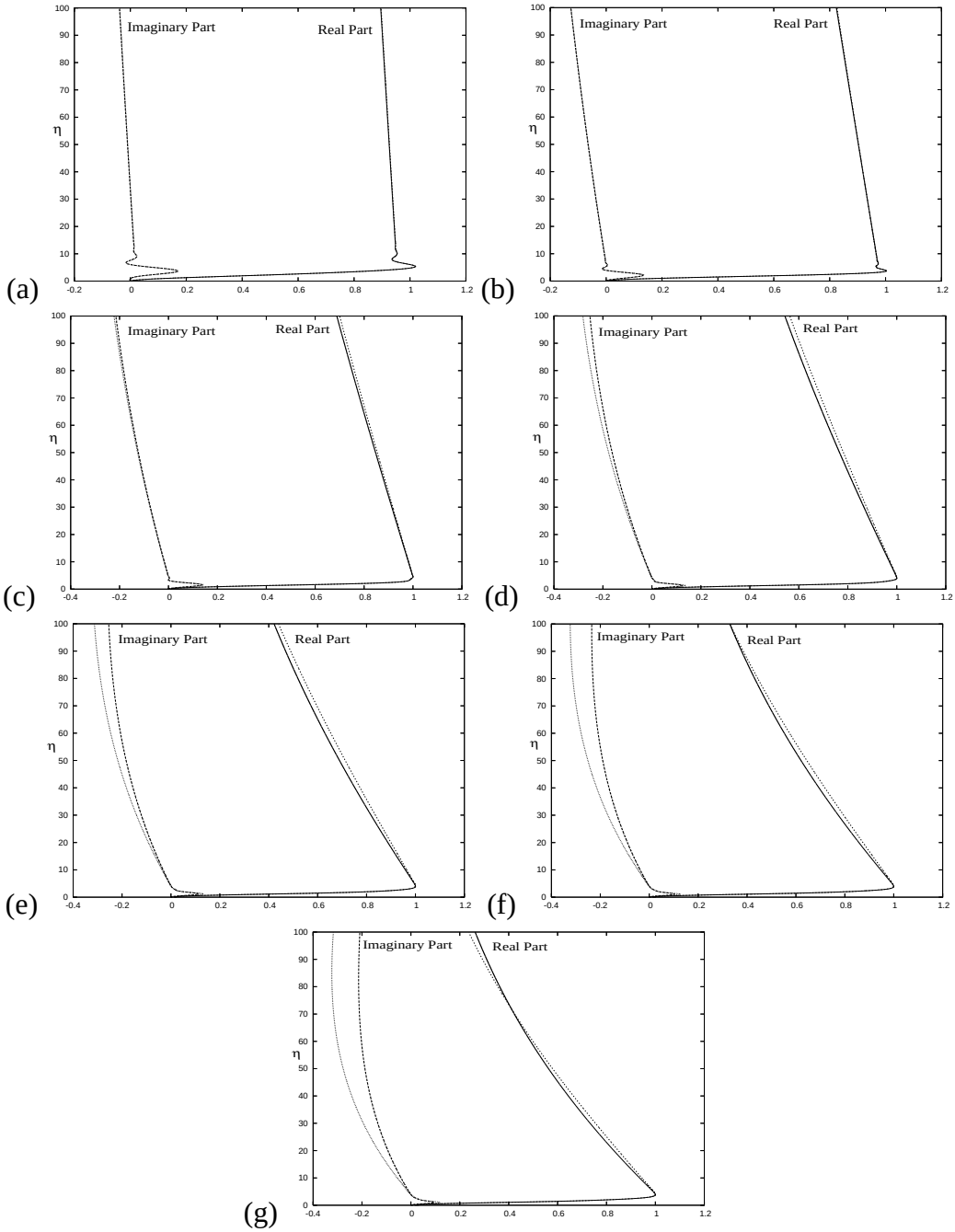

Figure 4.9: Plot of the mode shapes for Goldstein's Orr-Sommerfeld solution (dashed lines), and the leading edge solution (solid line and dotted line) for $\tilde{x}_1 =$ (a) 0.02, (b) 0.05, (c) 0.1, (d) 0.15, (e) 0.2, (f) 0.25 and (g) 0.3, with $\epsilon = 0.1$. Note that in figures (a) and (b), the 2 solutions are indistinguishable.

The existence of this matching region can be seen more clearly in figure 4.9. This figure shows an evolution plot of both the leading edge and asymptotic Orr-Sommerfeld mode shapes close to the leading edge, for $\epsilon = 0.1$. Note that from $\tilde{x}_1 = 0.02$ to $\tilde{x}_1 = 0.1$, the mode shapes for both schemes are almost identical, suggesting that this region is the matching region. As we go further out of this region, we see that the imaginary parts seem to differ more from each other than the real parts, although there is no specific reason for this.

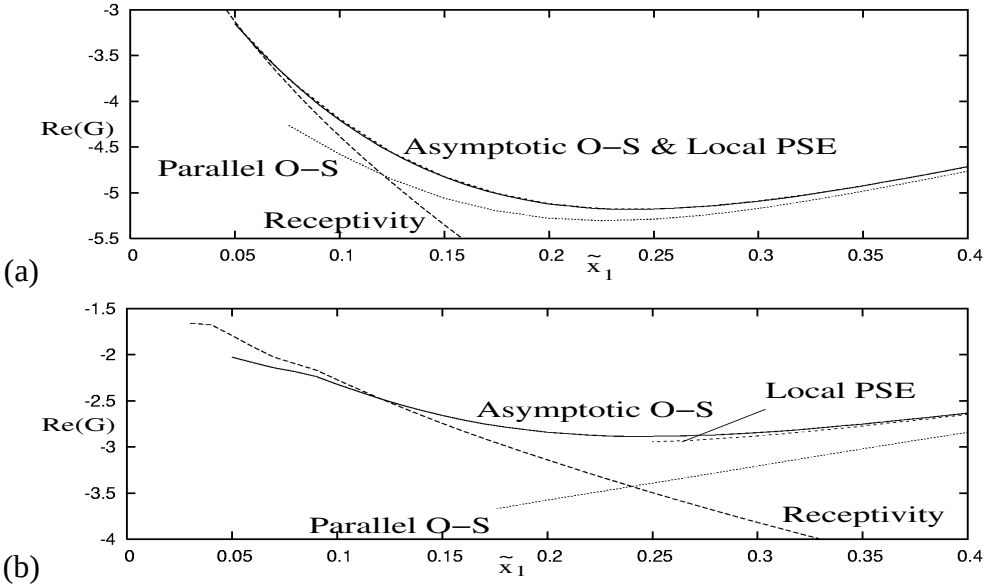

Figure 4.10: Plot of the real part of the growth rate G as a function of downstream distance, calculated by leading edge receptivity analysis, parallel Orr-Sommerfeld theory, local PSE theory, and asymptotic Orr-Sommerfeld theory for the cases (a) $\epsilon = 0.05$ and (b) $\epsilon = 0.1$.

Figure 4.10 shows a comparison of the real part of the growth rate, G, calculated using the different methods described in the previous sections for two different values of ϵ. The solid line shows the results for Goldstein's asymptotic results in the Orr-Sommerfeld region given by (4.99), up to and including the $O(\epsilon^3)$ term. This can be compared with results from parallel Orr-Sommerfeld theory, (4.19) and from the local PSE (4.26) which takes some account of non-parallel effects. For $\epsilon = 0.05$ (figure 4.10(a)) results from asymptotic analysis and the local PSE are indistinguishable, while the parallel flow results start to differ as the leading edge is approached, which is to be expected as non-parallel

effects begin to dominate. As ϵ is increased to $\epsilon = 0.1$ (figure 4.10(b)), the difference between the different solutions in the Orr-Sommerfeld region are larger. In addition, the local PSE solution can only be calculated for $\tilde{x}_1 \gtrapprox 0.25$ due to the first eigenvalue of (4.26) becoming indistinguishable from the other eigenvalues, as described earlier.

Figure 4.10 also shows the existence of a matching region between the receptivity region close to the leading edge and the Orr-Sommerfeld region further downstream. The dashed line marks the asymptotic growth rate of the first Lam-Rott mode given by (4.28). For the case $\epsilon = 0.05$ (figure 4.10(a)), the receptivity results overlap the results from the asymptotic Orr-Sommerfeld and the local PSE in the range $0.05 < \tilde{x}_1 < 0.1$ and so a matching region clearly exists. For the larger value of ϵ (figure 4.10(b)), a reasonable match between the receptivity and asymptotic Orr-Sommerfeld results is seen at $\tilde{x}_1 \approx 0.1$, but there is no matching region between the receptivity results and local PSE results due to the problem obtaining PSE results close enough to the leading edge.

4.4.2 Importance of $O(\epsilon^3)$ term

The $O(\epsilon^3)$ term in the asymptotic expansion of κ is calculated from (4.51), and in this section we illustrate its importance in the overall form of the wavenumber.

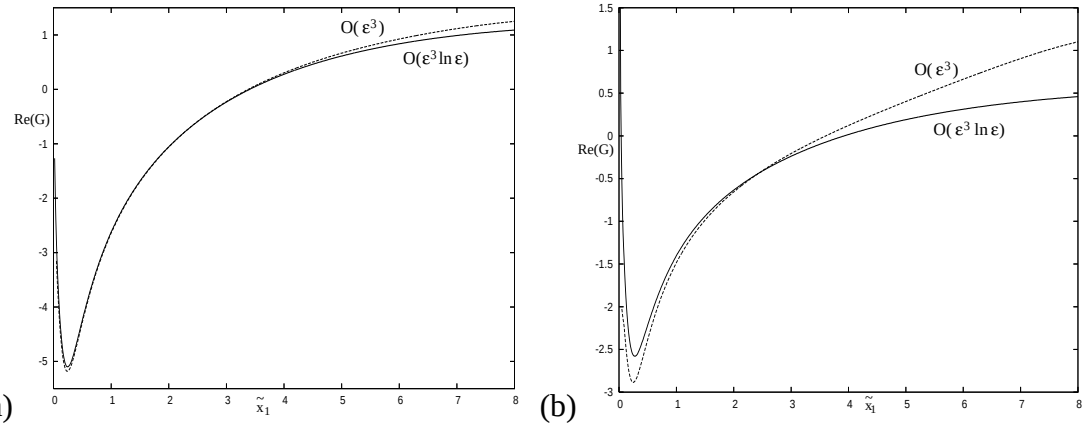

Figure 4.11: Plot of the real part of G as a function of downstream distance, comparing the asymptotic Orr-Sommerfeld results up to $O(\epsilon^3 \ln \epsilon)$, and when the $O(\epsilon^3)$ term is included for (a) $\epsilon = 0.05$ and (b) $\epsilon = 0.1$

Figure 4.11 shows the real part of G, for the asymptotic Orr-Sommerfeld regime, when

we include only terms up to $O(\epsilon^3 \ln \epsilon)$ and up to $O(\epsilon^3)$. When $\epsilon = 0.05$, figure 4.11(a) shows that the overall effect of having the extra term seems small. However when $\epsilon = 0.1$, figure 4.11(b) shows that after $\tilde{x}_1 = 4.0$, the effect of this extra term becomes significant. There is also a reasonable difference close to the leading edge, but figure 4.10(a) shows that this difference may be necessary to match with the leading edge result. Therefore we can conclude that the $O(\epsilon^3)$ term is important to the overall result, as it is significant close to the leading edge in the matching region. However this $O(\epsilon^3)$ term appears to become non-uniform downstream, thus will introduce errors into our calculation of disturbance amplitudes.

The $O(\epsilon^3)$ term in the asymptotic expansion for κ, plotted in figure 4.11, is constructed by only retaining the $O(1)$ terms from (4.51). This was done by using κ_0 everywhere that κ appeared. However, if we use κ calculated up to and including $O(\epsilon^3 \ln \epsilon)$ in (4.51) instead, we expect this solution to be a small perturbation from the previous one, because we have included some $O(\epsilon^4)$, $O(\epsilon^5)$ and higher correction terms, although we haven't included all the correction terms at these orders. The resulting solutions are shown in figure 4.12.

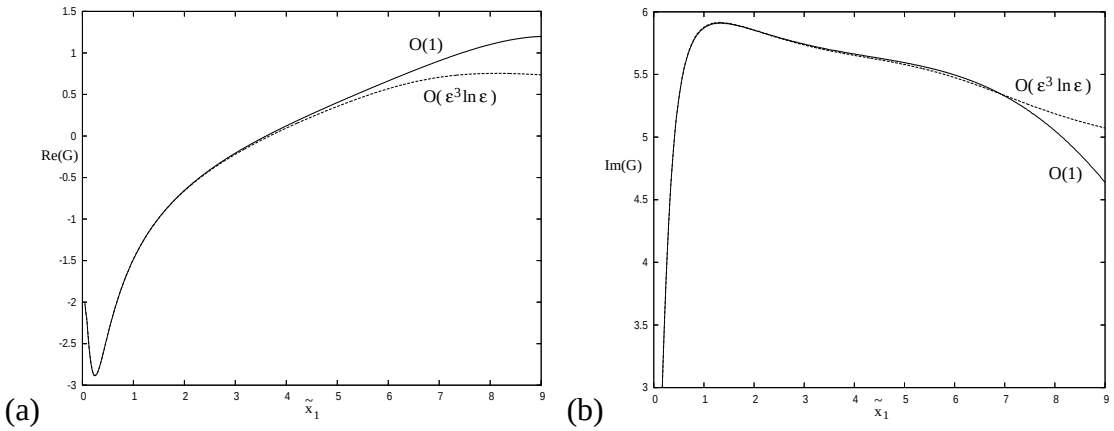

Figure 4.12: Comparison of (a) the real part, and (b) the imaginary part of G as a function of downstream distance, when the $O(\epsilon^3)$ term is calculated with κ of both $O(1)$, and $O(\epsilon^3 \ln \epsilon)$, for $\epsilon = 0.1$.

We see that both solutions are in good agreement up to $\tilde{x}_1 = 5$, but beyond this point, there is a considerable difference between the two solutions. It's relatively straightforward

to show that this difference is due to the second term on the right-hand side of (4.51). The function $Wi(\zeta)$ is very sensitive to small changes in ζ, and hence κ, as this moves the integration contour along which $Wi(\zeta)$ is evaluated. Figure 4.3 shows that there is a small variation in κ as we add more terms to the asymptotic expansion, and it's this variation which is translated into the difference shown in figure 4.12. These growth rates will be compared with our PSE calculations in the next section.

Another subtle, but equally important problem that arises when calculating the solution for $A(x_1)$, is that, in the derivation of (4.51), the asymptotic approximation $a_1 = \bar{\alpha}/U_0' - \bar{c} + O(\epsilon)$ is used to simplify the equation, where

$$a_1 = \lim_{\bar{\eta}\longrightarrow\infty}\left(\bar{\gamma}_0 - \bar{\eta}\frac{\partial\bar{\gamma}_0}{\partial\bar{\eta}}\right).$$

However if we don't make this approximation, and keep the higher order terms, the governing equation for $A(x_1)$ becomes

$$\begin{aligned} U_0' & \left(a_1 + \bar{c} + \frac{\bar{\alpha}}{U_0'}\right)\frac{d\ln A}{dx_1} + U_0' a_{1x_1} + U_0'\bar{c}_{x_1} - U_0'\frac{a_1 + \bar{c} + \frac{\bar{\alpha}}{U_0'}}{4x_1} + \frac{\bar{\alpha}}{\bar{c}}\sum_{n=0}^{3}\tilde{A}_n\bar{c}^n\bar{\alpha}^{(3-n)} \\ = \quad & \pi U_0' Bi'(\zeta_0)\int_0^\infty\left(\bar{H}_1\frac{d\ln A}{dx_1} + \bar{H}_2\right)Ai(\zeta)d\bar{\eta} - \frac{i(a_1+\bar{c})}{\bar{c}}\int_0^\infty\Gamma^\dagger d\bar{\eta}, \end{aligned} \tag{4.100}$$

rather than (4.51). In figure 4.12, we showed that (4.51) can be solved using $\kappa = \kappa_0$, or the expansion of κ up to $O(\epsilon^3\ln\epsilon)$. The results for $A(x_1)$ obtained using (4.51) and (4.100) with $\kappa = \kappa_0$ are in close agreement except close to the leading edge. Similarly if κ is taken up to $O(\epsilon^3\ln\epsilon)$, good agreement is found downstream. However when we consider the growth rate curves with (4.51) and (4.100) solved with $\kappa = \kappa_0$ close to $\tilde{x}_1 = 0$, we see a slight difference between the two curves. Figure 4.13 shows that the solution to (4.100) actually gives a better match with the leading edge asymptotics, when compared to the solution (4.51). Therefore this, along with figure 4.12, shows that the higher order terms in the expansion for κ are very important, but they become very difficult to formulate. Thus extending these asymptotics to bodies other than the flat plate would be extremely tedious and we expect to find that, as for the flat plate, the $O(\epsilon^3)$ term is significant close to the leading edge, but that it has an apparent non-uniformity, due to numerical evidence, downstream (Turner, 2006). Thus we use our PSE to march through the Orr-Sommerfeld

region to eliminate the difficulty of deriving general asymptotics in the Orr-Sommerfeld region.

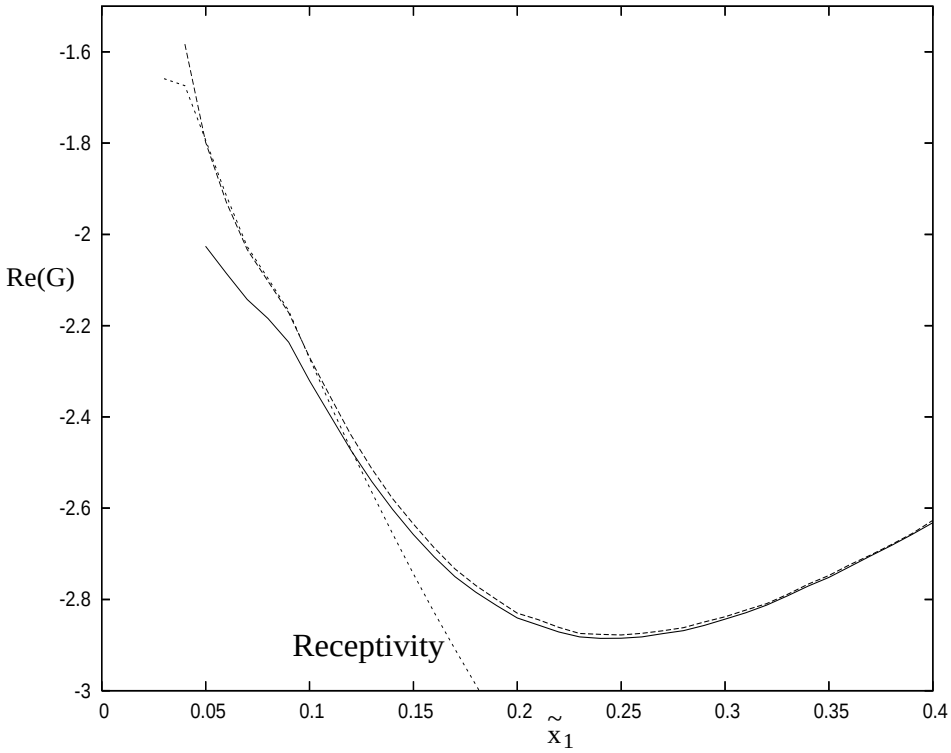

Figure 4.13: Plot of $Re(G)$ as a function of downstream distance for the Asymptotic Orr-Sommerfeld problem, with the $O(\epsilon^3)$ term calculated from (4.100) (dashed line) with $\kappa = \kappa_0$. The solid line represents the same solution, except with the $O(\epsilon^3)$ term calculated using (4.51), and the dotted line represents the leading edge growth rate.

4.5 PSE results in the Orr-Sommerfeld region

In this section, we consider results from PSE calculations. We compare results from the three upstream boundary conditions discussed, and see how different starting positions affect the downstream amplitude. We discuss some problems which occur when using PSE, and in particular, we discuss the problem of initial transients from the initial data. We go on to compare the results with the asymptotic results given by Goldstein (1982), in order to justify the use of the PSE method.

4.5.1 Comparison of different upstream boundary conditions

Previous studies of the PSE have either used the parallel Orr-Sommerfeld approximation, or the local PSE analysis as their upstream boundary condition. We hope to justify the use of the leading edge analysis as a suitable upstream boundary condition, and show that the PSE results are in good agreement with the Orr-Sommerfeld asymptotics.

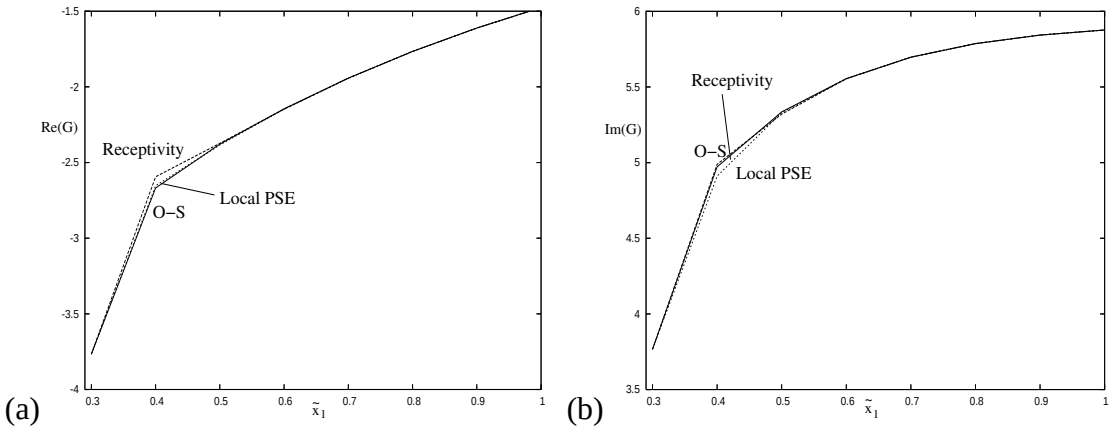

Figure 4.14: Comparison of (a) the real part, and (b) the imaginary part of G as a function of downstream distance for the three different initial conditions for the case $\epsilon = 0.1$ and with the initial conditions given at $\tilde{x}_1^{(0)} = 0.3$.

Figure 4.14 compares the initial steps of the PSE for the initial conditions of the leading edge asymptotics, the local PSE and the parallel Orr-Sommerfeld analysis, given at $\tilde{x}_1^{(0)} = 0.3$. The initial mode shapes are given in figures 4.5(a) and 4.6(a), and the initial PSE wavenumbers, α_0, are given in table 4.1. We see that the three solutions iterate to the same solution after about 2 or 3 streamwise steps, where in this case the streamwise step size is $\Delta\tilde{x}_1 = 0.1$. The local PSE and parallel Orr-Sommerfeld solutions are practically identical, but the receptivity solution is slightly different, although after $\tilde{x}_1 = 0.5$ all three

Regime	α_0
Receptivity Analysis	$0.006849 + 0.006849i$
O-S Theory	$0.008236 + 0.005829i$
Local PSE	$0.006833 + 0.004813i$

Table 4.1: Initial PSE eigenvalues for the three different regimes for the starting position $\tilde{x}_1 = 0.3$.

are indistinguishable from the others. This justifies our choice of receptivity boundary condition, although the solution requires two or three streamwise steps to iterate onto the correct solution.

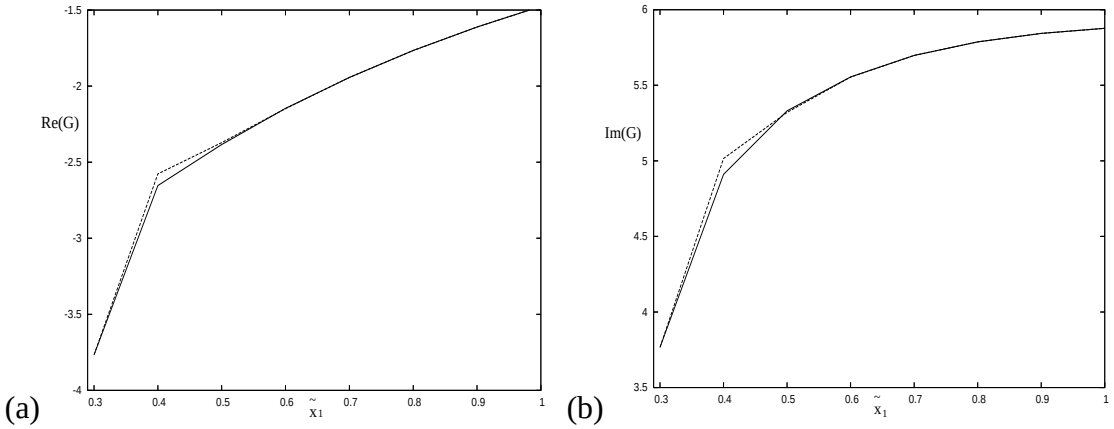

Figure 4.15: Comparison of (a) the real part, and (b) the imaginary part of G as a function of downstream distance for both the possible local PSE conditions, for the case $\epsilon = 0.1$ and $\tilde{x}_1^{(0)} = 0.3$.

We discussed in §4.1.3 that there is ambiguity over which eigenvalue and eigenmode to choose for the local PSE problem, and at $\tilde{x}_1^{(0)} = 0.3$, the local PSE problem has eigenvalues $\alpha_{01} = 0.006833 + 0.004813i$ and $\alpha_{02} = 0.009533 + 0.006518i$. However figure 4.15 shows that either pair is acceptable, as they both iterate to the same solution, again after only 2 or 3 streamwise steps, as expected, because Bertolotti *et al.* (1992) proved that the difference in the eigenvalues does not carry over to the growth rate.

We have now established that the leading edge asymptotics is a suitable upstream boundary condition for the PSE, however we need to be confident that starting the analysis at different starting points is consistent and leads to the same solution downstream.

4.5.2 Matching between the PSE and the leading edge region

For sufficiently small ϵ, we demonstrated in §4.4.1 that a matching region between the leading edge and Orr-Sommerfeld regions exists, hence we can utilise this result by starting our PSE analysis from inside or close to this region using (4.29) and (4.30) as the initial conditions. Figure 4.16 shows the real part of the growth rate G, defined in (4.98),

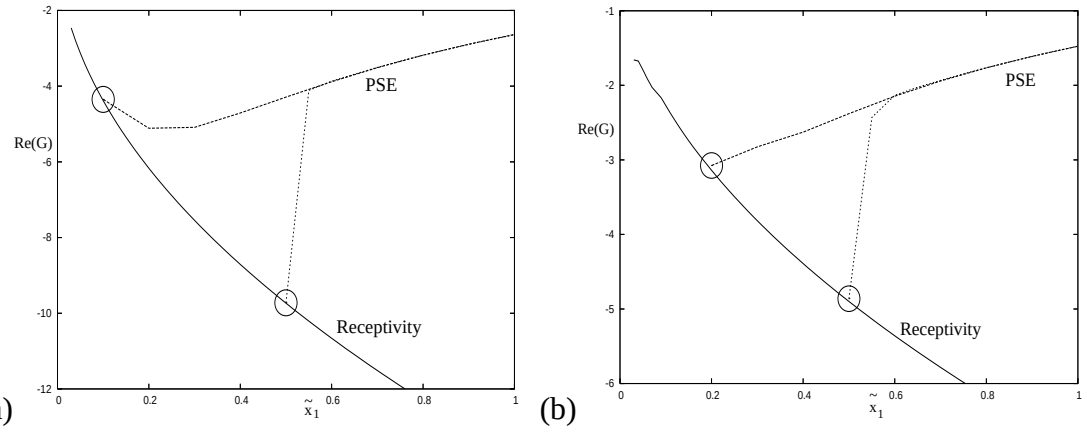

Figure 4.16: Plot of the real part of the growth rate G, given by the PSE, started at two different positions (ringed) for (a) $\epsilon = 0.05$ and (b) $\epsilon = 0.1$.

calculated using the PSE at different starting points, with the initial condition given by the receptivity analysis. Two starting positions were chosen, one lying within the matching region discussed above, and one further downstream where the LUBLE has become invalid. The results in figure 4.16 illustrate the smallest possible value of $\tilde{x}_1^{(0)}$ that the PSE was able to be started at in each case, together with a sample calculation starting the PSE marching solution further downstream. When we attempted to use an initial condition further upstream of these smallest values, we found that the PSE would not iterate to the correct solution. This is due to the unstable eigenvalue being close to the continuous spectrum of eigenvalues, and hence the numerical scheme has difficulties picking out this eigenvalue. We note that the minimum value of $\tilde{x}_1$ at which PSE marching solutions can be initiated increases as ϵ increases. The use of the initial condition further downstream highlights the fact that the PSE will iterate to the correct solution, even if an incorrect initial condition is imposed, as long as the point chosen is not so far downstream that the numerical scheme does not converge. This failure to converge to the correct solution is due to the first initial jump in the eigenvalue being too large. However if at this point we use the same mode shape as before, but instead use an initial eigenvalue taken from a previous calculation which passes through this point, we find that the solution does indeed match onto the previous runs. This appears to suggest that the numerical scheme involved in solving the PSE needs a good initial approximation for the eigenvalue, but is

more flexible in responding to the initial mode shape.

There are still two questions relating to the PSE which need addressing. Specifically, how is the disturbance amplitude downstream affected by changing the starting position of the PSE and by varying the step size? To address this, we define

$$\hat{A}(\tilde{x}_1^{(0)}, \tilde{x}_1) = \left| C_1 \psi_{LR}(\tilde{x}_1^{(0)}) \exp\left(\frac{U_0'^2}{2\epsilon^2} \int_{\tilde{x}_1^{(0)}}^{\tilde{x}_1} G(s) ds \right) \right|,$$

to be the disturbance amplitude at $\tilde{x}_1$, starting the PSE calculation at $\tilde{x}_1^{(0)}$, with the initial condition given by the receptivity result (4.29) and (4.30). The function $C_1\psi_{LR}(\tilde{x}_1^{(0)})$ is the amplitude of the Lam-Rott eigenmode from the leading edge region evaluated at the point $\tilde{x}_1^{(0)}$, and at the η value where $|\psi_{LR}|$ is at its maximum. This value of $C_1\psi_{LR}(\tilde{x}_1^{(0)})$ is calculated from the composite solution of (2.70) and (2.87). Using this, the existence of a matching region between the receptivity results and the region over which PSE calculations are possible corresponds to the range of values of $\tilde{x}_1^{(0)}$ over which $\hat{A}$ is independent of $\tilde{x}_1^{(0)}$. Taking $\epsilon = 0.05$ and a step size $\Delta\tilde{x}_1 = 0.05$, PSE calculations can not be started closer to the leading edge than $\tilde{x}_1^{(0)} = 0.05$, for reasons explained earlier. Thus in figure 4.17 we plot the amplitude at $\tilde{x}_1 = 0.5$ as a function of starting position, but normalized by the value when $\tilde{x}_1^{(0)} = 0.05$

$$\tilde{A}(\tilde{x}_1^{(0)}) = \frac{\hat{A}(\tilde{x}_1^{(0)}, 0.5)}{\hat{A}(0.05, 0.5)}.$$

The position $\tilde{x}_1 = 0.5$ is chosen as the point of comparison of the amplitudes because it is far enough from the turning point in $Re(G)$, that the change in growth rate is much smoother (see figure 4.16(a)), thus not affecting any interpolation of the final point in the growth rate, which may introduce a small error. Taking larger values of $\tilde{x}_1$ at which to calculate the amplitude increases the computation time but does not affect the results. For a PSE step size of $\Delta\tilde{x}_1 = 0.05$, it is seen that for $0.05 < \tilde{x}_1^{(0)} < 0.1$ there is a 26 % change in amplitude. This reinforces the earlier conclusion that a well defined matching region exists, at least for sufficiently small ϵ. It is also apparent that changing the step size makes about a 4% change in the amplitude. Comparisons over a wider range of step sizes is not possible due to the appearence of initial transients which are discussed in the next section.

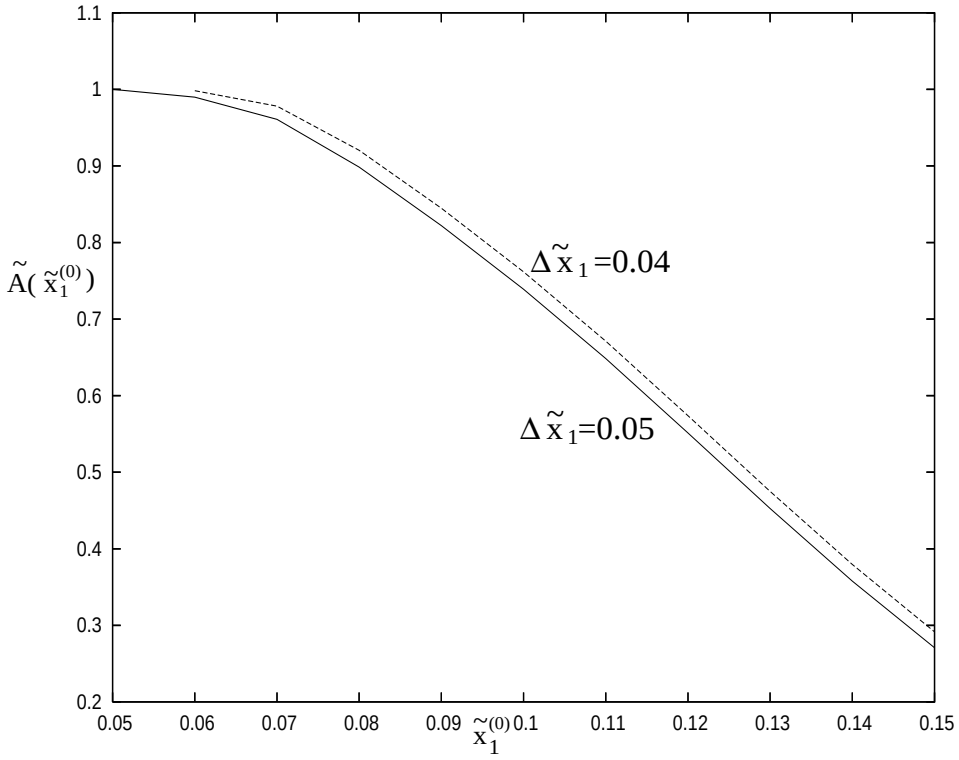

Figure 4.17: Plot of eigensolution amplitude at $\tilde{x}_1 = 0.5$ as a function of the starting point $\tilde{x}_1^{(0)}$ for $\epsilon = 0.05$. The downstream amplitude is normalized with respect to the value given when $\tilde{x}_1^{(0)} = 0.05$.

In general, we define the disturbance amplitude to be the absolute value of ψ at the point where the real part of ψ attains its maximum value, i.e where $Re(\bar{\phi}) = 1$. We must take great care when evaluating the disturbance amplitude downstream, because of the

$$\exp\left(\int^x G(x)dx\right),$$

term in (4.97), which when we change variables to $\tilde{x}_1$ becomes

$$\exp\left(\frac{U_0'^2}{2\epsilon^2}\int^{\tilde{x}_1} G(\tilde{x}_1)d\tilde{x}_1\right),$$

as seen above. Thus any errors in the evaluation of the integral due to the step size $\Delta\tilde{x}_1$ are magnified for very small ϵ. Thus we use Bode's rule for equally spaced mesh points, which has an error term of $O((\Delta\tilde{x}_1)^7)$. This is applied to all the amplitude calculations above and in future sections.

4.5.3 Initial transients

In the previous section we encountered the problem that the PSE does not converge when the initial condition, taken via the leading edge receptivity result, is too far downstream. However, there is also a minimum $\tilde{x}_1$, for each value of ϵ, before which the PSE will not converge. Figure 4.16 shows this minimum value for the cases $\epsilon = 0.05$ and 0.1. For smaller ϵ, we can start the PSE closer to $\tilde{x}_1 = 0$, however we have to increase the streamwise step size to achieve this. We believe this is related to the problem experienced by Bertolotti *et al.* (1992), where they see initial transients when they ran their PSE code for large frequencies (large ϵ). An example of these initial transients is shown in figure 4.18. Figure 4.18 shows two PSE calculations for $\epsilon = 0.175$, one with a step

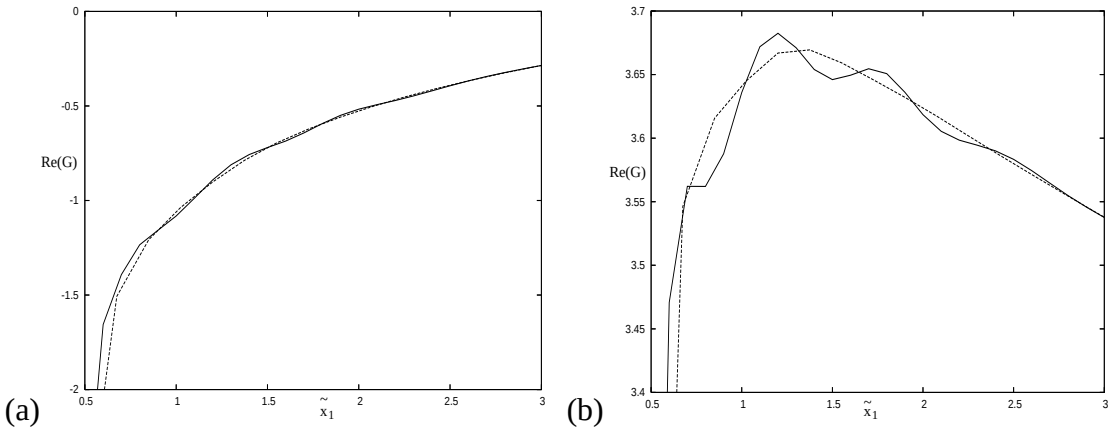

Figure 4.18: Plot of (a) the real part and (b) the imaginary part of G as a function of downstream distance for $\epsilon = 0.175$, showing the effects of transients from the initial conditions for the step sizes $\Delta\tilde{x}_1 = 0.15$ and 0.175

size of $\Delta\tilde{x}_1 = 0.15$ which has these initial transients present, and one with a step size of $\Delta\tilde{x}_1 = 0.175$, without the transients. As the step size is made smaller and smaller, we find that these transients become larger and larger, until eventually they become so large that the numerical scheme fails to converge. This step size restriction is not the same as the step size restriction encountered in the primitive variable formulation (Andersson *et al.*, 1998), because our PSE is formulated in terms of the stream function, ψ, which has a less severe step size problem than the primitive variable formulation. We believe that the minimum starting point problem may be related to this initial transient problem. This

is because as we move closer to the leading edge, we are forced to increase the step size to make the PSE converge, which could be conceived as increasing the step size to overcome these transients. Although these transients have been noted in previous studies, no systematic study has been conducted. However some general observations can be made about the appearance of such transients. In figure 4.19 we see a more detailed plot of the transients on the real part of G for the case $\epsilon = 0.15$. We note that for the two largest step sizes, $\Delta\tilde{x}_1 = 0.2$ and 0.1 there are no oscillations, and the difference between these solutions is small. As we decrease the step size to $\Delta\tilde{x}_1 = 0.06$, we see these transients beginning to appear and as we decrease the step size further, the amplitude of these oscillations increases, while the wavelength remains approximately constant, $\lambda_{\tilde{x}_1} \approx 0.39$. One possible explanation for the appearance of these transients is that since the initial condition is only a numerical approximation to the first eigenmode, the initial waveform is likely to contain small contributions from higher eigenmodes. Thus our initial condition

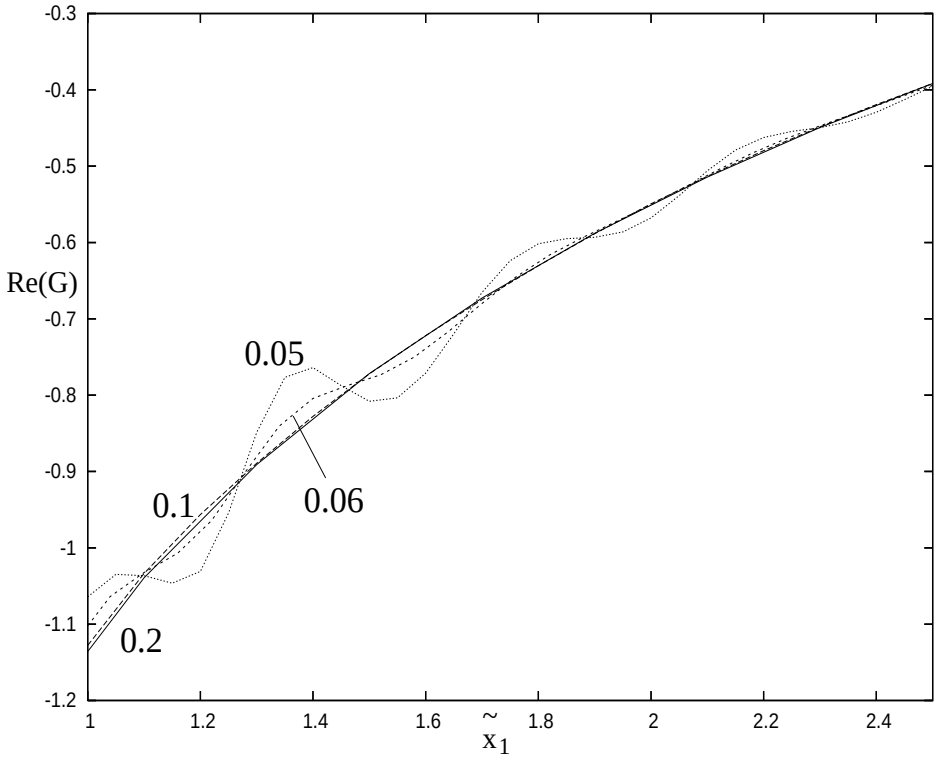

Figure 4.19: Plot of the initial transients on $Re(G)$ for $\epsilon = 0.15$ for 4 different step sizes, $\Delta\tilde{x}_1 = 0.05, 0.06, 0.1, 0.2$, showing the occurrence of these transients as the step size reduces.

is in fact a sum of these eigenmodes of the form

$$\psi_{IC} = \sum_{i=1}^{\infty} A_i \psi_i,$$

where the A_i's are constants. For small values of ϵ, where we can start the PSE from within the matching region and where the composite solution of (2.70) and (2.87) is an accurate representation of the first Lam-Rott eigenmode, the A_i's for $i \geq 2$ should be small. However if we have to take our initial condition outside the matching region, then the A_i's for $i \geq 2$ will be larger because of the inaccuracy of the composite solution. Initially the higher eigenmodes decay more slowly than the first eigenmode and hence these contributions may become significant if the A_i's are large enough.

We can investigate the significance of the higher eigenmodes, by considering Goldstein's asymptotic form of the wavenumber, as given in §4.3.1, up to $O(\epsilon^3 \ln \epsilon)$. We define the function $\hat{\Psi}$ as

$$\hat{\Psi} = \psi_1 + \hat{\epsilon}\psi_2,$$

where ψ_n given by

$$\psi_n = \epsilon^{-(2\tau_n+1)} \gamma_n(x_1, \eta) A(x_1) \exp\left(\frac{i}{\epsilon}\int_0^x \kappa_n(x_1, \epsilon) dx\right),$$

for $n = 1, 2$, is the n^{th} T-S mode, and $\hat{\epsilon}$ is a small constant. We then define

$$\Psi = \frac{\hat{\Psi}}{\psi_1} = 1 + \hat{\epsilon}\frac{\psi_2}{\psi_1}, \tag{4.101}$$

which we evaluate at the value of η where the value of $|\psi_1|$ reaches its maximum. The results we expect to see, when we plot Ψ as a function of $\tilde{x}_1$, is a region close to the leading edge where $\Psi = 1$, i.e. where ψ_1 dominates the solution, then a region of oscillation, where ψ_2 dominates, and finally another region where ψ_1 dominates again. This behaviour is clearly seen in figure 4.20(a), which shows the real part of Ψ as a function of $\tilde{x}_1$ for $\epsilon = 0.05$, and $\hat{\epsilon} = 1 \times 10^{-41}$. The reason $\hat{\epsilon}$ was chosen so small in this case, is just to make the oscillations the same order of magnitude as those in the numerical solution for $\epsilon = 0.15$ illustrated in figure 4.20(b). Hence for $\epsilon = 0.05$ the oscillations would be very large, if we had a large component of ψ_2 in our initial condition to the PSE. However, as we are able to start the PSE right back into the matching region for this value of ϵ,

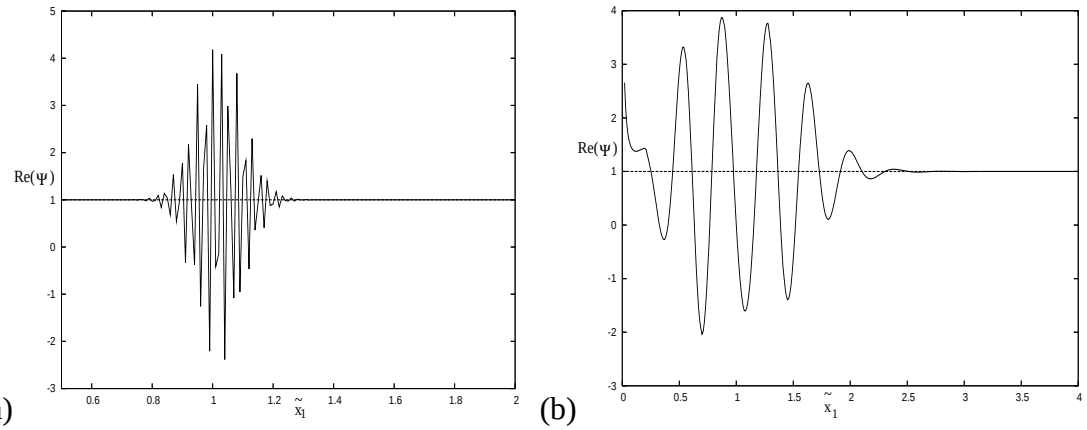

Figure 4.20: Figure of the real part of Ψ as a function of $\tilde{x}_1$ for (a) $\epsilon = 0.05$ and $\hat{\epsilon} = 1 \times 10^{-41}$ and (b) $\epsilon = 0.15$ and $\hat{\epsilon} = 0.1$.

we find the constant multiplying the second eigenmode is small. Also for this value of ϵ, the wavelength of this oscillation, $\lambda_{\tilde{x}_1}$ is very small, and in fact $\lambda_{\tilde{x}_1} \approx 0.025$. If we now consider the case $\epsilon = 0.15$, in figure 4.20(b), which was the value for which we saw the transients in figure 4.19, we see that the region close to the leading edge where ψ_1 dominates has now disappeared. The reason that $Re(\Psi)$ does not go to 1 as $\tilde{x}_1 \longrightarrow 0$, is due to the neglected $O(\epsilon^3)$ term being important in the asymptotics. Despite this, we still obtain the region where ψ_1 dominates downstream, but the region over which ψ_2 dominates is now larger. We note that for this value of ϵ, we chose $\hat{\epsilon} = 0.1$, and we can see that the magnitude of the oscillations appears to be smaller than for the $\epsilon = 0.05$ case. The wavelength of the oscillations is also larger for this case, $\lambda_{\tilde{x}_1} \approx 0.36$, however we note that this wavelength is of a similar size to the one seen in figure 4.19. The reason we don't notice these transients for the $\epsilon = 0.05$ case, as we do for the $\epsilon = 0.15$ case, is possibly due to the wavelength of the oscillations seen in figure 4.20. The wavelength for $\epsilon = 0.05$ is very small, and generally we use a step size of about twice this wavelength. However for $\epsilon = 0.15$, a step size of $\Delta\tilde{x}_1 = 0.05$ is smaller than the wavelength of the second eigenmode oscillations, and hence the PSE will pick up this behaviour. We saw no transients for $\Delta\tilde{x}_1 = 0.1$, and this step size is just larger than a quarter of the wavelength of the oscillations.

While this is not conclusive evidence of the origin of transients in PSE solutions, it

seems to suggest a connection between these transients and the higher eigenmodes. However further investigation is needed to find a step size limit in terms of this wavelength. We believe it is a combination of these transients, which are related to the streamwise step size, as well as the difficulty finding the eigenvalue which leads to the failure of PSE convergence starting the calculation too close to the leading edge. The magnitude of the initial transient oscillations become increasingly large for smaller ϵ or smaller $\tilde{x}_1^{(0)}$, and in most cases become so large so quickly, that the PSE code fails to converge.

The comparisons described in the above sections show that the PSE scheme proposed gives consistent results, independent of initial position and step size. We now compare these numerical results with the Orr-Sommerfeld asymptotic results defined earlier in this section.

4.5.4 Comparison of PSE and asymptotics in the Orr-Sommerfeld region

Having established that the leading edge receptivity analysis is a suitable upstream boundary condition for the PSE, we compare the PSE results with Goldstein's established asymptotic results in the Orr-Sommerfeld region. In the following results, the upstream boundary condition was given by the leading edge asymptotic analysis.

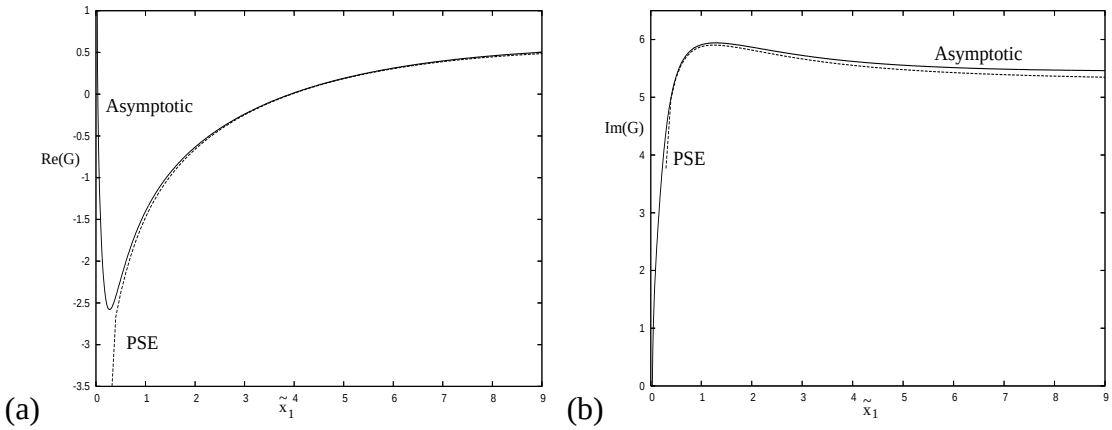

Figure 4.21: Comparison of (a) the real parts and (b) the imaginary parts of G, calculated using the asymptotics and PSE, as a function of downstream distance, for $\epsilon = 0.1$.

Figures 4.21 and 4.22 show a comparison of the PSE and asymptotic forms of G, for

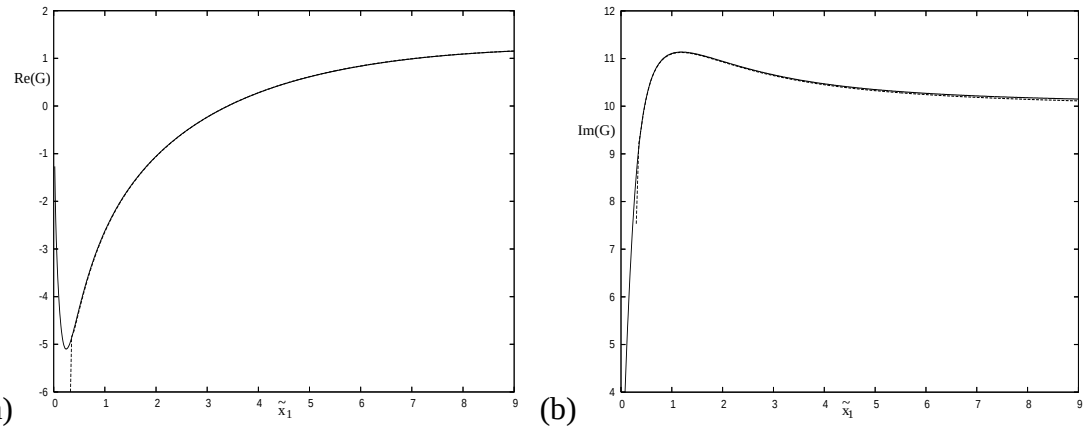

Figure 4.22: Comparison of (a) the real parts and (b) the imaginary parts of G, calculated using the asymptotics and PSE, as a function of downstream distance, for $\epsilon = 0.05$. For this value of ϵ, the two solutions are almost indistinguishable from one another.

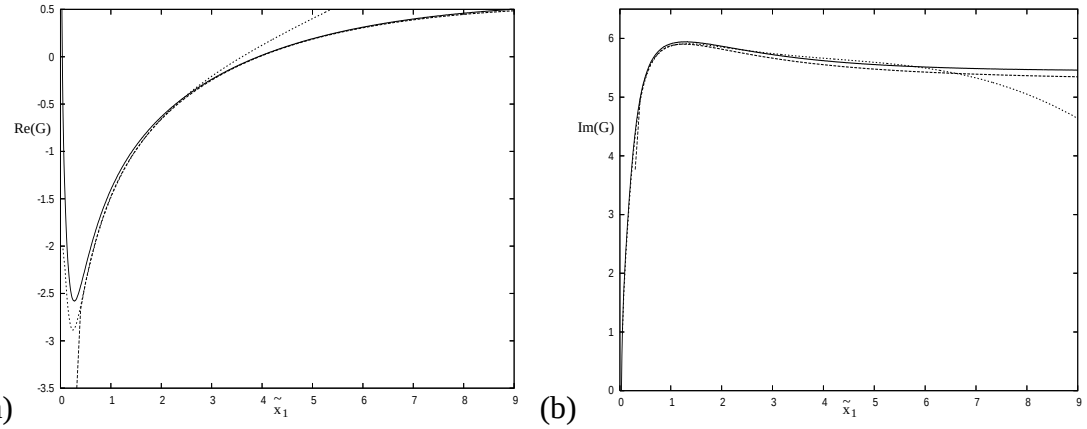

Figure 4.23: Comparison of (a) the real parts and (b) the imaginary parts of G, calculated using the asymptotics and PSE, as a function of downstream distance, for $\epsilon = 0.1$, including the asymptotics up $O(\epsilon^3)$, denoted by the dotted line.

$\epsilon = 0.1$ and $\epsilon = 0.05$, where the asymptotics are given up to and including $O(\epsilon^3 \ln \epsilon)$ terms. For the $\epsilon = 0.1$ case in figure 4.21, we see that there is a small difference between the real part of the two solutions near to the turning point, but as we discussed in the previous section, this is due to the $O(\epsilon^3)$ term being significant here. If we add this extra term onto the asymptotics, figure 4.23, then we see we have a much better agreement up to $\tilde{x}_1 = 3.0$, but due to the likely non-uniformity of the asymptotics, we have poor agreement downstream of this point. Other than that, the real parts agree very well over the range of

values shown in figure 4.21. The imaginary parts show more of a difference between the solutions, and this difference increases as we move downstream. This slight difference isn't too significant, as this gives just a slight shift in the phase of the eigenmode, rather than any difference to the amplitude. If we now compare the growth rates for $\epsilon = 0.05$ in figure 4.22, we see that in this case both solutions are almost indistinguishable for both the real and imaginary parts. This definitely shows that our PSE method is working and is a very effective way to calculate the growth rate on a body.

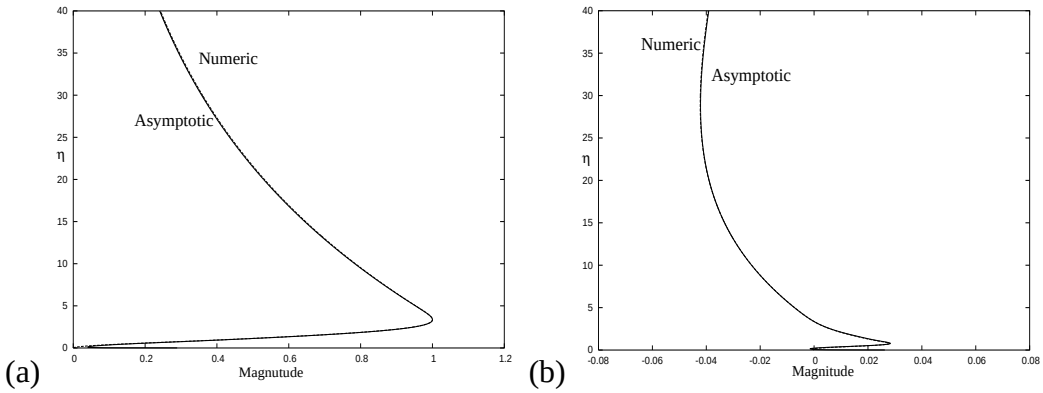

Figure 4.24: Plot of (a) the real parts and (b) the imaginary parts of the mode shape at $\tilde{x}_1 = 2.0$ with $\epsilon = 0.1$.

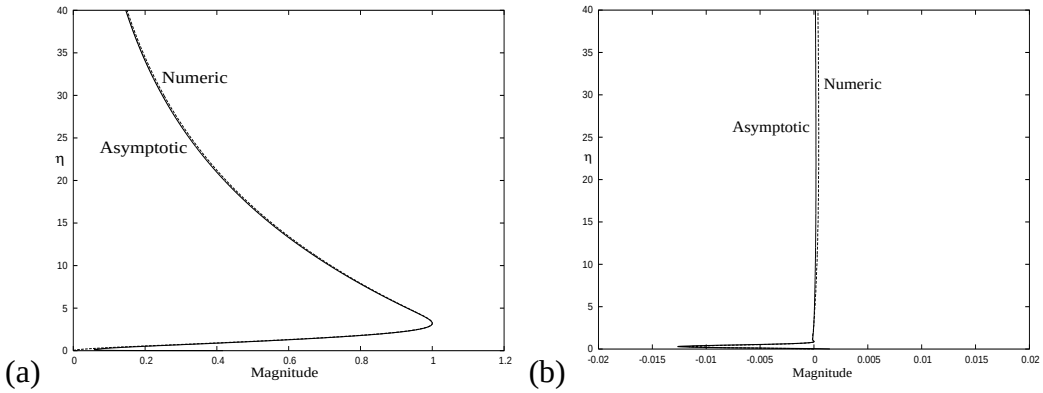

Figure 4.25: Plot of (a) the real parts and (b) the imaginary parts of the mode shape at $\tilde{x}_1 = 4.0$ with $\epsilon = 0.1$.

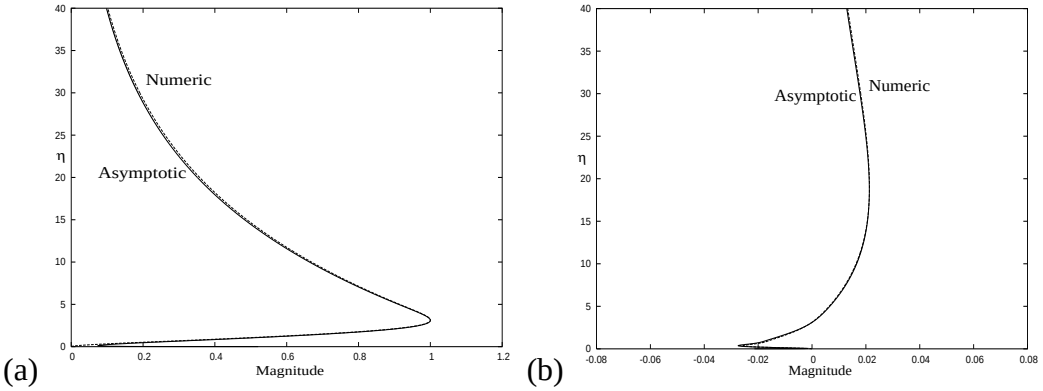

Figure 4.26: Plot of (a) the real parts and (b) the imaginary parts of the mode shape at $\tilde{x}_1 = 6.0$ with $\epsilon = 0.1$.

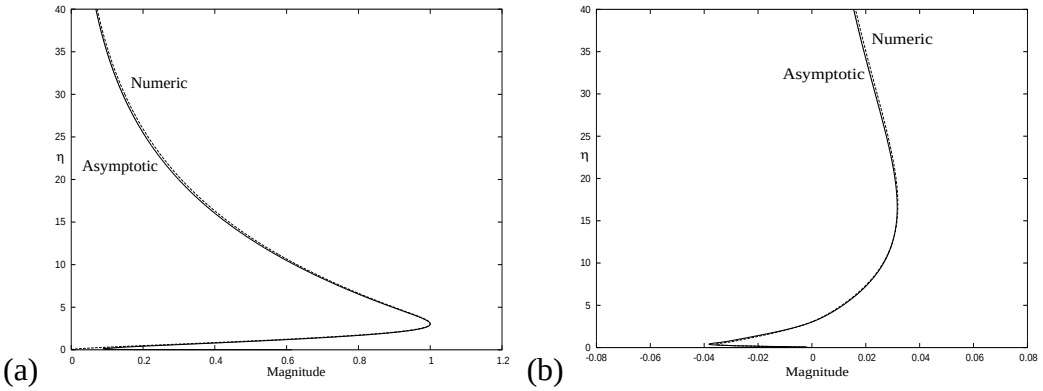

Figure 4.27: Plot of (a) the real parts and (b) the imaginary parts of the mode shape at $\tilde{x}_1 = 8.0$ with $\epsilon = 0.1$.

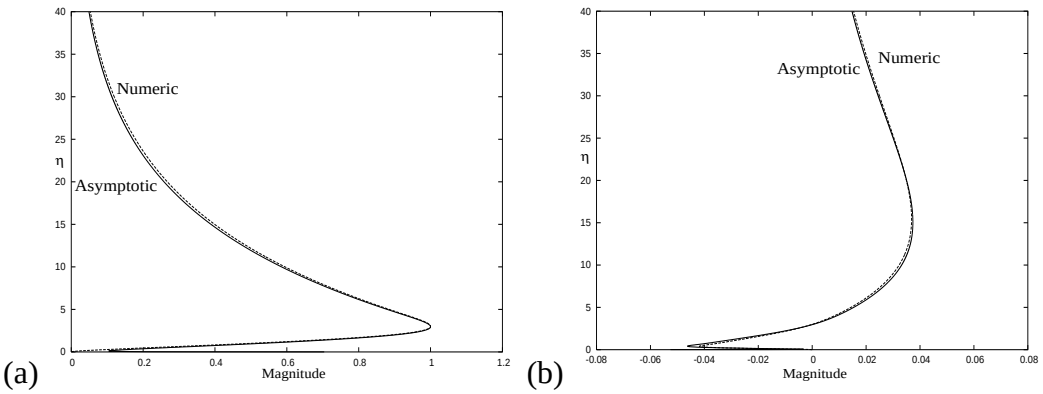

Figure 4.28: Plot of (a) the real parts and (b) the imaginary parts of the mode shape at $\tilde{x}_1 = 10.0$ with $\epsilon = 0.1$.

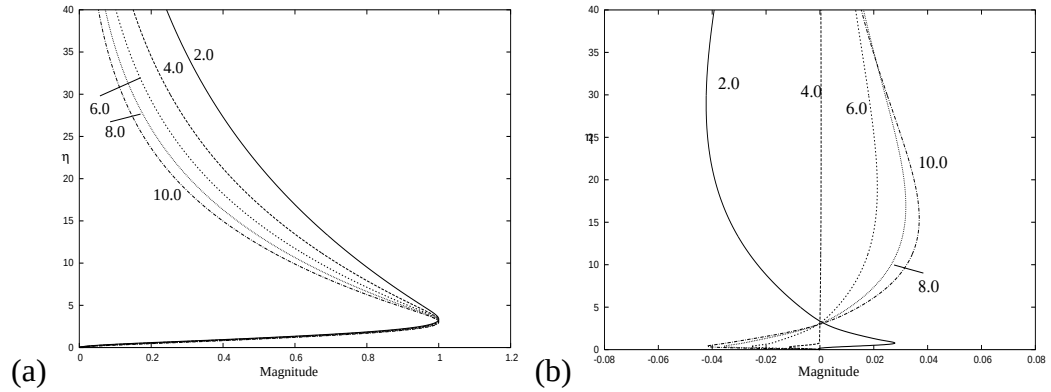

Figure 4.29: An evolution plot of (a) the real parts and (b) the imaginary parts of the mode shape at $\tilde{x}_1 = 2.0, 4.0, 6.0, 8.0, 10.0$.

The good agreement between the PSE and the asymptotics can also be seen in figures 4.24, 4.25, 4.26, 4.27 and 4.28, which show a comparison of the PSE and asymptotic mode shapes at 5 downstream positions for $\epsilon = 0.1$. In each case there is almost no visible difference between the two solutions, further reinforcing the validity of our PSE method.

Figure 4.29 shows an evolution plot of the mode shapes for $\epsilon = 0.1$, calculated using the PSE. Figure 4.29(a) shows that the real parts are all of a similar shape, but the maximum point moves slowly towards the wall as we move downstream. Also as we move downstream, the real parts decay to zero faster as $\eta \longrightarrow \infty$, so the main part of the mode shape becomes more concentrated closer to the wall. The imaginary part on the other hand, figure 4.29(b), shows that as the disturbance moves through the neutral stability point, $\tilde{x}_1 = 3.946$, the mode shape becomes purely real, and downstream of this point, we find that the imaginary part has the opposite sign to that which it had upstream of the neutral stability point, with the imaginary part slowly becoming more concentrated at the wall.

The above figures show good visible agreement between the asymptotic and numerical values of G, and the mode shape, but we also compare some numerical properties of the solutions to see if the two methods agree. Table 4.2 shows the neutral stability point, where $Im(G) = 0$, as a function of ϵ for both methods, with the asymptotics up to and

including the $O(\epsilon^3 \ln \epsilon)$ terms. The values in this table are also plotted in figure 4.30.

ϵ	Asymptotic NS point $\tilde{x}_1$	PSE NS point $\tilde{x}_1$
0.035	3.282	3.278
0.05	3.402	3.405
0.075	3.643	3.647
0.1	3.928	3.946
0.125	4.267	4.328
0.15	4.689	4.818
0.175	5.187	5.456
0.2	5.774	6.359

Table 4.2: Neutral stability points for the PSE and asymptotics.

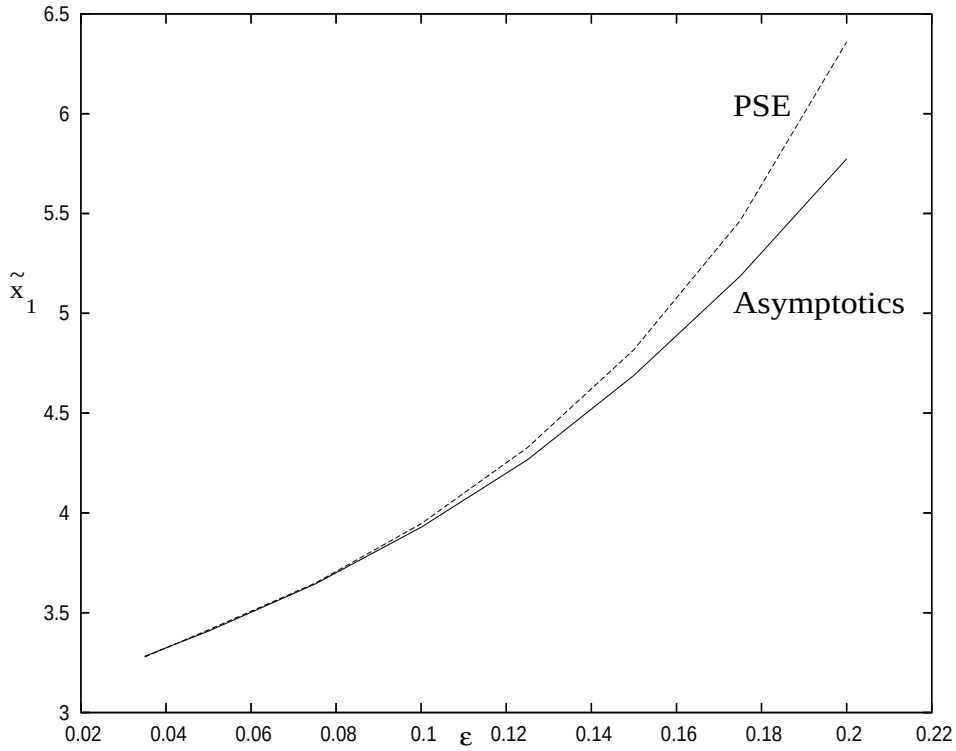

Figure 4.30: Plot of the position of the neutral stability point as a function of ϵ comparing the PSE and the asymptotics.

The results in table 4.2 are as expected, in that the difference between the two methods increases as ϵ increases. However, it also helps to confirm the importance of the $O(\epsilon^3)$ term in the asymptotics, although adding this term into the asymptotic expansion does not

improve the results for large ϵ, due to the apparent non-uniformity seen in figure 4.11. We note that for the case of $\epsilon = 0.05$, for example, the error between the numerics and asymptotics is $0.007 \approx 50\epsilon$. This sizable difference shows that the higher order terms of the asymptotic expansion appear to be very significant.

The main reason for developing this PSE theory, is so that we can use it to calculate the amplitude of the eigenmodes at different positions along the body. The amplitude of the 1^{st} T-S mode, $\psi_1(x,\eta)$, given at a point x, and at the η value where $|\psi_1|$ is at its maximum, is

$$|\psi_1| = \left| C_1 \psi_{LR}(x_{LE}) \exp\left(\int_{x_{LE}}^{x} G(s)\, ds \right) \right|, \tag{4.102}$$

where $\psi_{LR}(x_{LE})$ is the amplitude of the Lam-Rott eigenmode evaluated at the point x_{LE} and at the position where $|\psi_{LR}|$ is at its maximum. Also, $C_1 = -0.45 + 0.855i$ is the receptivity coefficient for acoustic wave propagating parallel to the mean flow (Goldstein *et al.*, 1983), and x_{LE} is a streamwise position in the matching region where the Lam-Rott eigenmodes are valid. However at the moment, we are only interested in comparing the relative accuracies of the PSE and the asymptotics, so rather than having the lower limit of integration as x_{LE}, which is not possible for large ϵ, we start our analysis at some given point along the body. We also ignore C_1, as it's the same for both methods. For this analysis we chose our starting point to be $\tilde{x}_1 = 1.0$, and our end point to be the lower branch neutral stability point. Although this point is different for the PSE and asymptotic methods, it still gives a very good comparison between the two methods. Hence in our case we define

$$|\check{\psi}| = \left| \exp\left(\frac{U_0'^2}{2\epsilon^2} \int_{1.0}^{\tilde{x}_{1_{NS}}} G(s) ds \right) \right|, \tag{4.103}$$

as the amplitude we compare, where the $U_0'^2/(2\epsilon^2)$ term comes from changing variables from x to $\tilde{x}_1 = 2\epsilon^2 x / U_0'^2$.

Table 4.3 shows a comparison between the asymptotic and numerical values of (4.103), and because the amplitudes at each value of ϵ are of the same order of magnitude the results appear to be satisfactory. We can compare the accuracy of the numerical method better, if we consider table 4.4, which is $\epsilon^2 \ln(\check{\psi})$ of the values in table 4.3. This then gives a comparison of the values of the integrals in the exponentials, which is a much bet-

ϵ	$\lvert\check{\psi}_{\mathrm{ASY}}\rvert$	$\lvert\check{\psi}_{\mathrm{PSE}}\rvert$
0.035	4.783×10^{-126}	4.872×10^{-126}
0.05	1.275×10^{-46}	8.616×10^{-47}
0.075	6.771×10^{-16}	3.618×10^{-16}
0.1	7.191×10^{-8}	3.556×10^{-8}
0.125	8.130×10^{-5}	3.801×10^{-5}
0.15	2.207×10^{-3}	9.564×10^{-4}
0.175	1.297×10^{-2}	5.105×10^{-3}
0.2	3.663×10^{-2}	1.314×10^{-2}

Table 4.3: Table of $|\check{\psi}|$ at the neutral stability point, for the PSE and the asymptotics.

ter comparison, as any errors in the integral is magnified by the ϵ^{-2} term in the exponential in table 4.3, as discussed earlier.

ϵ	$\epsilon^2 \ln(\check{\psi}_{\mathrm{ASY}})$	$\epsilon^2 \ln(\check{\psi}_{\mathrm{PSE}})$
0.035	$-0.353 + 3.840i$	$-0.353 + 3.832i$
0.05	$-0.264 + 2.882i$	$-0.265 + 2.880i$
0.075	$-0.196 + 2.181i$	$-0.200 + 2.175i$
0.1	$-0.164 + 1.872i$	$-0.172 + 1.866i$
0.125	$-0.147 + 1.729i$	$-0.159 + 1.699i$
0.15	$-0.138 + 1.686i$	$-0.156 + 1.696i$
0.175	$-0.133 + 1.703i$	$-0.162 + 1.734i$
0.2	$-0.132 + 1.767i$	$-0.173 + 1.865i$

Table 4.4: Table of $\epsilon^2 \ln(\check{\psi})$ at the neutral stability point for the PSE and the asymptotics.

Table 4.4 shows excellent agreement between the amplitudes as $\epsilon \longrightarrow 0$, and we can see this in figure 4.31, which shows the real part of $\epsilon^2 \ln(\check{\psi})$. The difference between the imaginary parts is almost constant as ϵ varies, so we don't get their values tending to the same value quite as rapidly as we do for the real part as $\epsilon \longrightarrow 0$. This is possibly due to the missing $O(\epsilon^3)$ term in the asymptotics, which is very significant for the $Im(G)$.

This section has proved that for sufficiently small ϵ, the numerical PSE results agree very well with Goldstein's asymptotics, and for larger values of ϵ, the PSE appears to be a suitable way to calculate the growth rate. Thus, now we are satisfied that our PSE method is valid, we can use it to calculate T-S wave amplitudes to compare with experimental studies, and full numerical simulations.

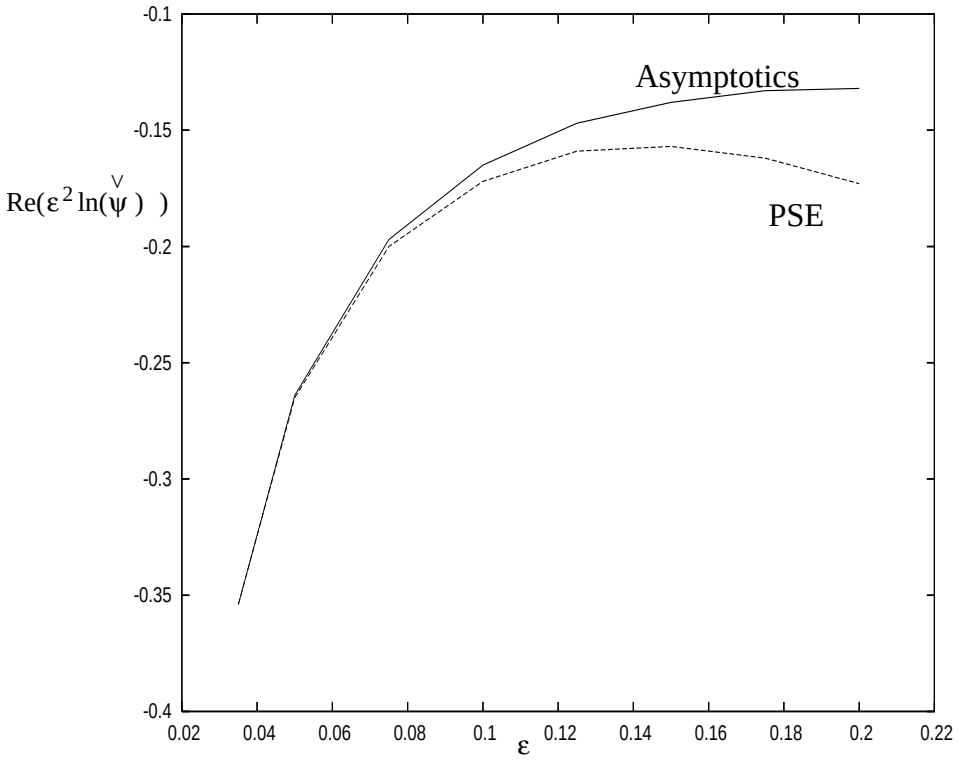

Figure 4.31: Plot of the real part of $\epsilon^2 \ln(\check{\psi})$ as a function of ϵ comparing the PSE and the asymptotics

4.6 Experimental comparisons

We have now established that the PSE is a good method for calculating the solution to the stability problem in the Orr-Sommerfeld region, we therefore now use this method to calculate the amplitude of the eigenmode as a function of downstream position via (4.102):

$$|\psi_1| = \left| C_1 \psi_{LR}(x_{LE}) \exp\left(\int_{x_{LE}}^{x} G(s) ds \right) \right|,$$

where C_1 is the receptivity coefficient. To calculate this amplitude we need to be able to integrate over the growth rate from some point in the receptivity region which we believe to be in the matching region, x_{LE}, and where the amplitude is known from (4.28), downstream to the point at which the amplitude is to be calculated. This is straightforward for small values of ϵ, as we can take the PSE right back to this matching region. However, for larger ϵ, we have to 'patch' this region using a curve fitting technique.

4.6.1 Patching

For moderately small values of ϵ, the need to patch the solutions valid in different downstream regions can be seen in figure 4.16(b), where $\epsilon = 0.1$. The PSE result has to be taken from $\tilde{x}_1 \approx 0.5$, and matched with the leading edge asymptotics at $\tilde{x}_1 \approx 0.09$, as this appears to be a point in the matching region for $\epsilon = 0.1$. The difficulty in patching this region is that the real part of G has a turning point between these two points. Determining exactly where this turning point lies, and the minimum value of $Re(G)$ are not straightforward. We can overcome this problem slightly by using the solution to the local PSE problem from a point at which the PSE result has settled onto a solution, backwards towards the leading edge. By doing this we decrease the size of the patch needed, and hence hope to increase the accuracy of the result.

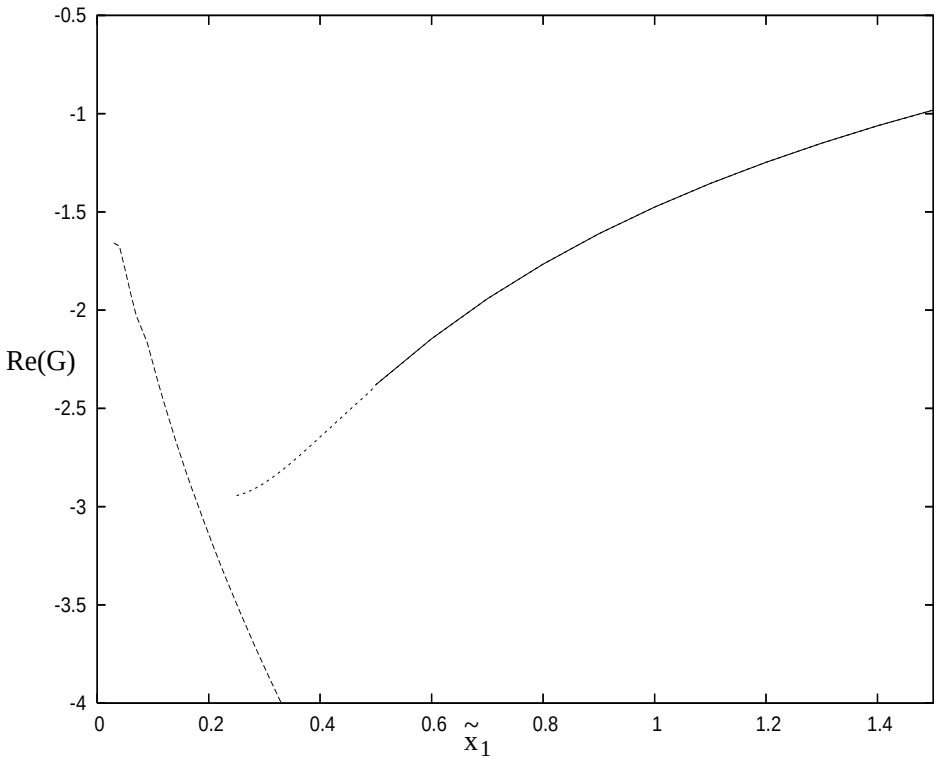

Figure 4.32: Plot of the real part of G as a function of $\tilde{x}_1$ showing the local PSE patching (dotted line) over the gap between the PSE (solid line) and leading edge solutions (dashed line) for $\epsilon = 0.1$.

Figure 4.32 shows that the PSE and local PSE lie over one another from about $\tilde{x}_1 =$

0.45, and the local PSE patches back to approximately $\tilde{x}_1 = 0.3$, for the case $\epsilon = 0.1$. Hence we now only have to patch from about $\tilde{x}_1 = 0.3$ back to the leading edge. For the case $\epsilon = 0.1$, the local PSE brings the PSE solution just back far enough so that we have an idea where the turning point is, and how large it is, see figure 4.32. For larger values of ϵ we are not so lucky, and some element of guess work is required. We patch the growth rate, G, in the range $\tilde{x}_\alpha < \tilde{x}_1 < \tilde{x}_\beta$, where $\tilde{x}_\alpha$ is a point in the receptivity region that we believe to be in the matching region, and $\tilde{x}_\beta$ is the closest point to the leading edge that we could calculate the result in the Orr-Sommerfeld region. We require that

$$G(\tilde{x}_1) \approx \begin{cases} f_1(\tilde{x}_1) & \tilde{x}_1 < \tilde{x}_\alpha \\ f_2(\tilde{x}_1) & \tilde{x}_1 > \tilde{x}_\beta \end{cases},$$

or better still we require equality, where the function f_1 is the asymptotic receptivity result and f_2 is the PSE/local PSE result.

There are various patching methods available, and we only consider two of them here.

Patching method 1

The first method introduces the function defined on $\tilde{x}_\alpha < \tilde{x}_1 < \tilde{x}_\beta$ as,

$$G_1(\tilde{x}_1) = \lambda_1(\tilde{x}_1)\tilde{f}_1(\tilde{x}_1) + \lambda_2(\tilde{x}_1)\tilde{f}_2(\tilde{x}_1),$$

where

$$\lambda_1 = \frac{1}{2}(1 - \tanh\theta) \quad \text{and} \quad \lambda_2 = \frac{1}{2}(1 + \tanh\theta),$$

and

$$\theta = \frac{5\left(\tilde{x}_1 - \frac{1}{2}(\tilde{x}_\alpha + \tilde{x}_\beta)\right)}{\tilde{x}_\beta - \tilde{x}_\alpha}.$$

The function $\tilde{f}_1$ is taken to be the straight line extension of f_1 from $\tilde{x}_\alpha$ to $\tilde{x}_\beta$, and $\tilde{f}_2$ is taken to be the straight line extension of f_2 from $\tilde{x}_\beta$ to $\tilde{x}_\alpha$.

Patching method 2

For the second patching method, we define G_2 to be

$$G_2(\tilde{x}_1) = \begin{cases} f_1(\tilde{x}_1) & \tilde{x}_1 < \tilde{x}_\alpha \\ A\tilde{x}_1^3 + B\tilde{x}_1^2 + C\tilde{x}_1 + D & \tilde{x}_\alpha < \tilde{x}_1 < \tilde{x}_\beta \\ f_2(\tilde{x}_1) & \tilde{x}_1 > \tilde{x}_\beta \end{cases},$$

where A, B, C and D are constants found by ensuring that $G(\tilde{x}_1)$ is continuous and has continuous slope at $\tilde{x}_\alpha$ and $\tilde{x}_\beta$. Hence we require

$$\begin{aligned} G_2(\tilde{x}_\alpha) &= f_1(\tilde{x}_\alpha), \\ G_2'(\tilde{x}_\alpha) &= f_1'(\tilde{x}_\alpha), \\ G_2(\tilde{x}_\beta) &= f_2(\tilde{x}_\beta), \\ G_2'(\tilde{x}_\beta) &= f_2'(\tilde{x}_\beta), \end{aligned}$$

where the dash denotes differentiation with respect to $\tilde{x}_1$.

The results of patching the growth rates, $Re(G_1)$ and $Re(G_2)$, can be seen for two values of ϵ in figure 4.33. For the case $\epsilon = 0.075$, only a small amount of patching was required around $\tilde{x}_1 = 0.1$ and both methods gave similar results. However when $\epsilon = 0.2$, we had to patch a much larger region between $0.25 < \tilde{x}_1 < 1.0$, which leads to the growth rate curve of G_1 possibly dropping more rapidly between $0.5 < \tilde{x}_1 < 1.0$ than expected when we compare its shape to the $\epsilon = 0.075$ curve. However the G_2 curve appears to give a shape similar to the $\epsilon = 0.075$ curve, and this curve also has the correct values at $\tilde{x}_\alpha$ and $\tilde{x}_\beta$, rather than approximations using the first patching method. It is because of these reasons that we choose to use the second patching technique for the remainder of this work.

Figure 4.34 shows the imaginary part of the growth rate corresponding to the real part in figure 4.33. We notice that the G_1 curve for $\epsilon = 0.2$ doesn't have quite as smooth an arc as the G_2 curve has, and in fact the G_1 curve has a slight rise in value at $\tilde{x}_1 \approx 0.55$. This rise is completely due to the choice of patching method. However, this is not too significant in our work, because when we integrate G, the imaginary part just gives us

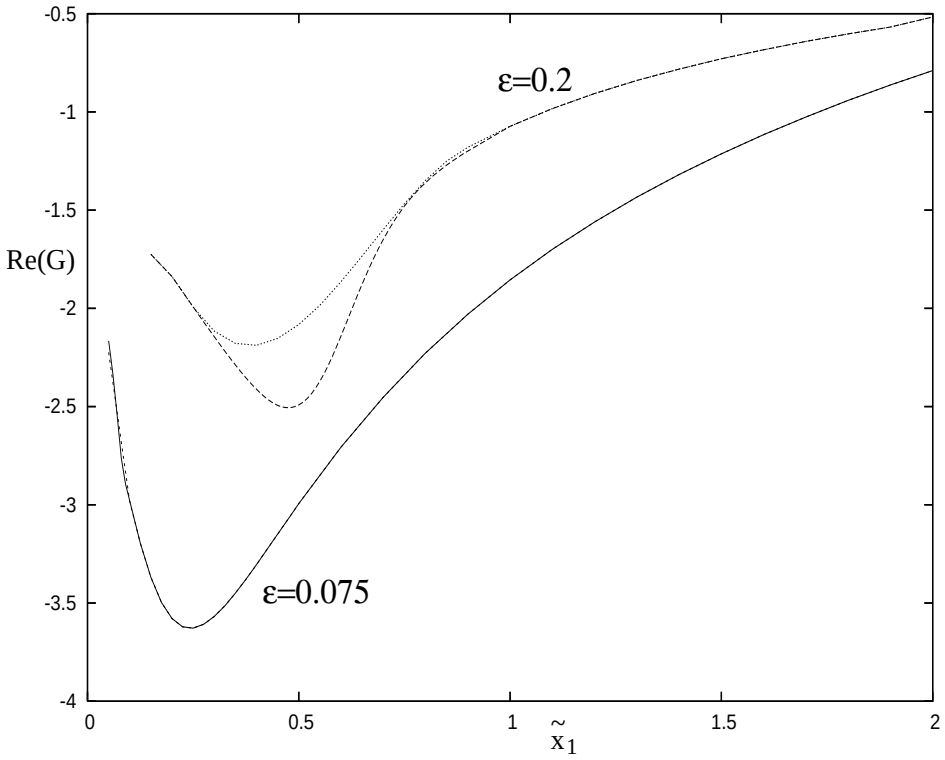

Figure 4.33: Plot of growth rates, $Re(G_1)$ and $Re(G_2)$, for $\epsilon = 0.075$ which requires very minimal patching, and $\epsilon = 0.2$ which requires much more patching. The lower of the two curves for the $\epsilon = 0.2$ case corresponds to $Re(G_1)$.

the phase of the eigenmode at that point. Hence this slight rise will only cause a slight change of phase rather than any change of amplitude. We found that with the first patching method, this rise in $Im(G_1)$ increase slightly as ϵ increases.

Based on the results shown in figures 4.33 and 4.34, we chose to use the second patching method. Table 4.5 shows the values of $\tilde{x}_\alpha$ that we thought were appropriate, along with the values of $\tilde{x}_\beta$ which are the closest positions to the leading edge that the local PSE could be solved. Note that both values increase as ϵ increases.

Now that we can successfully patch the solution data to give a continuous complex growth rate, G, we can now consider amplitudes of the eigenmodes at various places downstream.

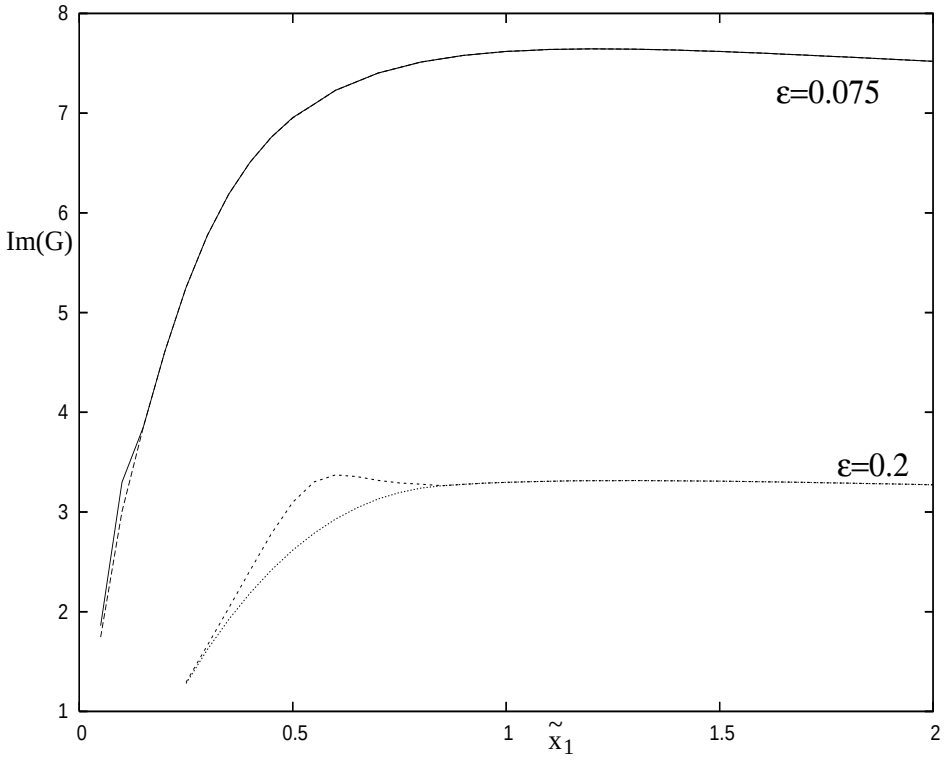

Figure 4.34: Plot of the imaginary parts of the growth rates, $Im(G_1)$ and $Im(G_2)$, for $\epsilon = 0.075$ which requires very minimal patching, and $\epsilon = 0.2$ which requires much more patching. The lower of the two curves for the $\epsilon = 0.2$ case corresponds to $Im(G_2)$.

ϵ	$\tilde{x}_\alpha$	$\tilde{x}_\beta$
0.035	0.05	0.05
0.05	0.05	0.05
0.075	0.05	0.10
0.1	0.09	0.14
0.125	0.15	0.30
0.15	0.22	0.40
0.175	0.25	0.50
0.2	0.25	0.90
0.225	0.25	1.00

Table 4.5: Table of values of $\tilde{x}_\alpha$ and $\tilde{x}_\beta$ that we found appropriate for the present work.

4.6.2 Eigenmode amplitudes at lower branch

The position commonly used in numerical and experimental work to calculate T-S wave amplitudes is at the branch I (lower branch) neutral stability point. Thus to calculate these

values, we use the asymptotic form of the leading edge solution as our initial condition to the PSE, calculate the form of the growth rate $G(x)$, patch it where necessary and integrate it to the lower branch point. If we assume the free-stream disturbance to be an acoustic wave propagating parallel to the mean flow, then the receptivity coefficient C_1 is then given by Goldstein *et al.* (1983) as $|C_1| = 0.9662$, and hence the amplitude of ψ_1 at lower branch is given by

$$|\psi_1^I| = \left| C_1 \psi_{LR}(x_{LE}) \exp\left(\int_{x_{LE}}^{x_{NS}} G(x) dx \right) \right|,$$

where x_{LE} is a position in the matching region and x_{NS} is the position of the neutral stability point. The values of $|\psi_1^I|$ are displayed in table 4.6 for the two patching methods.

ϵ	$\lvert\psi_1^I\rvert$ Patching 1	$\lvert\psi_1^I\rvert$ Patching 2	$\%$ difference
0.05	1.068×10^{-121}	1.068×10^{-121}	0
0.075	1.769×10^{-39}	1.915×10^{-39}	7.62
0.1	1.488×10^{-18}	1.670×10^{-18}	10.90
0.125	7.154×10^{-11}	7.887×10^{-11}	9.29
0.15	2.471×10^{-7}	2.605×10^{-7}	5.14
0.175	1.143×10^{-5}	1.486×10^{-5}	23.08
0.2	1.502×10^{-4}	1.922×10^{-4}	21.85
0.225	7.493×10^{-4}	9.324×10^{-4}	19.63

Table 4.6: Table of T-S wave amplitudes at the lower branch neutral stability point, using both patching methods. The two methods are compared using the $\%$ difference between them, $100 \times \left| |\psi_1^I|_2 - |\psi_1^I|_1 \right| / |\psi_1^I|_2$.

Table 4.6 shows a rapid increase in the size of the T-S wave at lower branch as we move from $\epsilon = 0.05$ through to $\epsilon = 0.15$, but we see a much slower increase after $\epsilon = 0.15$. This slowdown in growth can be seen much more clearly in figure 4.35, which shows a plot of $|\psi_1^I|$, using the second patching method, from table 4.6, as a function of ϵ, plotted on a log scale. We only plot the amplitudes from $\epsilon = 0.075$, in order to emphasise the slowing down of the amplitude growth as ϵ gets larger. Results for very small ϵ are asymptotically valid due to the well-defined matching region, but are perhaps of limited physical relevance, while results for larger values of ϵ involve numerical patching but do allow comparison with experimental and numerical results such as Haddad and Corke

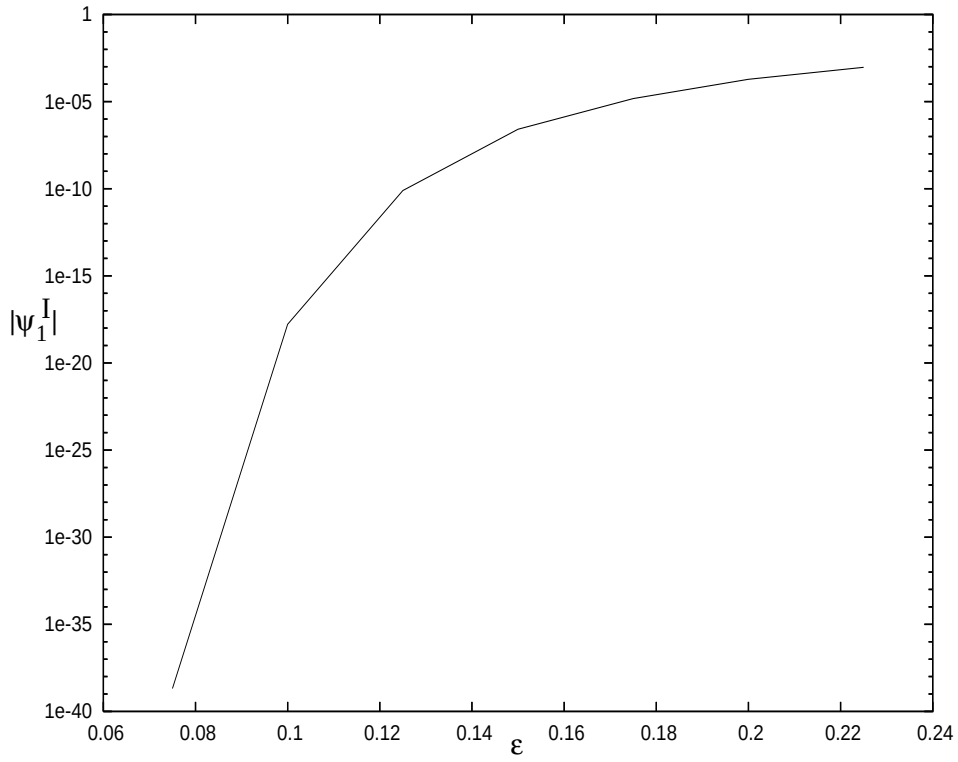

Figure 4.35: Plot of $|\psi_1^I|$ at the lower branch neutral stability point as a function of ϵ for the second patching method.

(1998) and Wanderley and Corke (2001).

Haddad and Corke (1998) consider a parabola at zero angle of incidence to a uniform flow with a small amplitude acoustic disturbance propagating parallel to the mean flow. The steady flow around the body is solved numerically and the unsteady disturbance obtained by solving as a linear perturbation. Downstream, the unsteady disturbance consists of a Stokes-wave determined by the local forcing at that location, together with a sum of Tollmien-Schlichting waves. Upstream of the first neutral stability point, the T-S waves are small compared with the Stokes wave. The asymptotic form of the Stokes wave far downstream at leading order is given by

$$\psi_{ST}(x,\eta) = (2x)^{\frac{1}{2}}\left(\eta - \frac{1+i}{2}\frac{1}{x^{\frac{1}{2}}} + \frac{i\beta}{2}\frac{1}{x} + \frac{13U_0'}{32}\frac{1}{x^2} - \frac{39iU_0'}{64}\frac{1}{x^3} - \frac{4051(1-i)U_0'^2}{2048}\frac{1}{x^{\frac{7}{2}}}\right) + O(Re^{-1}).$$

But rather than use this form, Haddad and Corke obtain a numerical approximation to the Stokes solution by solving the unsteady equation with convective-inertia terms dropped. If we calculate the leading order term of the large x asymptotic solution using the equations

used by Haddad and Corke, we find that

$$\psi_{ST} = (2x)^{\frac{1}{2}}\eta + O(Re^{-1}).$$

Therefore Haddad and Corke's Stokes solution is the same as (2.66) except without the $O(1)$ correction terms. Having obtained an expression for the Stokes solution, this is subtracted from the unsteady solution in order to provide an approximation to the magnitude of the T-S waves, after a filtering process in which any waves of wavelength greater than $2\lambda_{TS}$ are removed, where λ_{TS} is the wavelength of the unstable T-S wave. As well as removing the higher T-S modes, this filtering process should also remove any remaining contribution from the Stokes solution. Haddad and Corke checked their method against the asymptotics of Ackerberg and Phillips (1972) for a flat plate by considering the limit as the nose radius goes to zero. We illustrate the results from our numerical scheme by comparing them to the numerical results of Haddad and Corke, in the limit as the nose radius goes to zero.

Figure 4.36 shows a plot of the streamwise velocity, u_{TS}, at $\eta = 0.033$ as a function of $R_x = U_\infty x^*/\nu$, where x^* is a dimensional distance from the leading edge. The streamwise velocity, u_{TS} is defined as $u_{TS} = \partial\psi_{TS}/\partial y$, where

$$\psi_{TS} = \psi_1 = C_1\phi(x,\eta)\exp\left(\int^x G(x')dx'\right),$$

therefore

$$u_{TS} = \frac{\partial\psi_{TS}}{\partial y} = C_1\frac{1}{(2x)^{\frac{1}{2}}}\frac{\partial\phi}{\partial\eta}\exp\left(\int^x G(x')dx'\right),$$

after the filtering process. The results of the present work (solid line) agree well with the results of Haddad and Corke (dotted line) (cf figure 13(b) from Haddad and Corke (1998), after the data has been filtered), downstream of the lower branch point and in particular around the upper branch of the neutral stability curve. The discrepancy between the two sets of results around the lower branch point could be due to two factors. Firstly, the value of $\epsilon = 0.248$ is relatively large and hence we are considering points close to the turning point of the neutral stability curve, where all numerical methods are very sensitive (see Schmid and Henningson (2001), figure 7.30). Secondly, any numerical errors associated with the subtraction of the Stokes wave and the filtering of higher modes in Haddad and

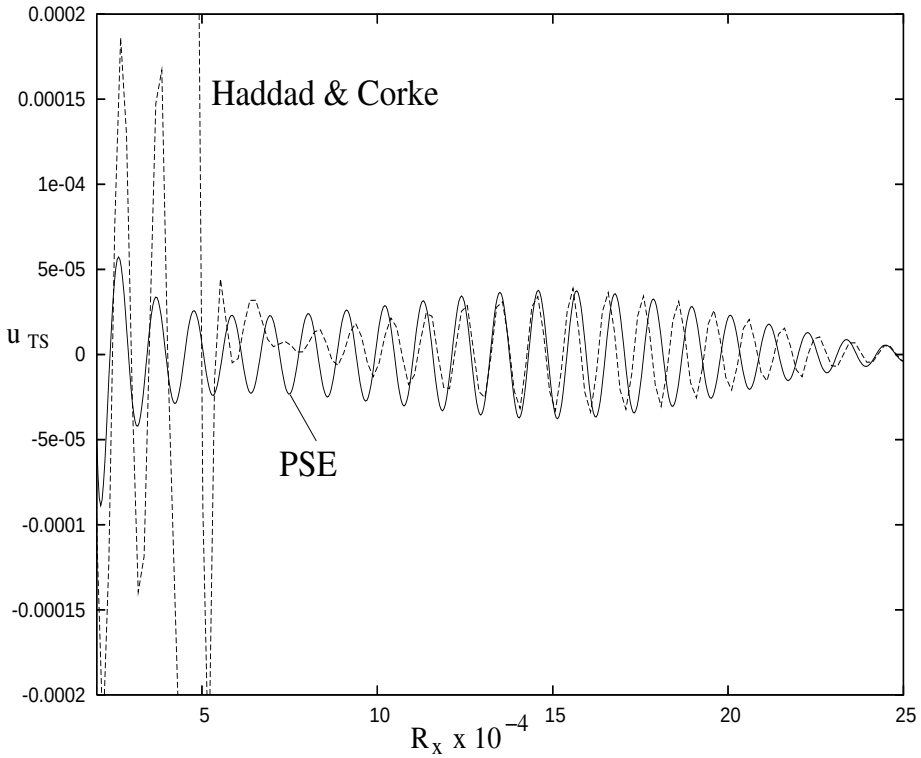

Figure 4.36: Plot of the T-S wave velocity, u_{TS}, as a function of $R_x = U_\infty x^*/\nu$ at the level $\eta = 0.033$, for both Haddad and Corke's method, and our PSE method, for $\epsilon = 0.248$.

Corke (1998) are likely to be most significant at this point since the unstable T-S wave has its lowest amplitude there. This comparison strongly suggests that our receptivity/PSE method is valid.

4.6.3 Leading edge receptivity coefficient

As well as producing amplitude results at lower branch to compare with experimental measurements, the numerical methods of Corke and co-workers were used to compare with leading edge receptivity results. Wanderley and Corke (2001) define a general form of the receptivity coefficient as the ratio of the maximum T-S wave amplitude at an x-location to the amplitude of the free-stream disturbance, and denote it by $K_x = |(u_{TS})|/|(u_\infty)|$, where u_{TS} is the streamwise velocity and u_∞ is the free-stream disturbance. This definition of the receptivity coefficient depends on downstream distance and has a very different meaning from the receptivity coefficient defined in the asymptotic

analysis.

Wanderley and Corke (2001) consider flow over a Modified Super Ellipse (MSE) at a zero angle of incidence to the free-stream. A MSE is half an ellipse stuck onto a flat plate with the discontinuity in curvature at the join removed. This body is of great importance to experimentalists, and we discuss its properties in more detail in chapter 6. Wanderley and Corke solve the flow around a MSE in an identical fashion to Haddad and Corke. The steady flow is solved numerically and the unsteady disturbance is obtained by solving a linear perturbation problem.

Wanderley and Corke calculate the value of K_{LE}, which is K_x evaluated at the leading edge, by considering results close to the neutral stability point. Corke and co-workers assumed that the 1^{st} T-S wave dominates the solution at this point, and they extrapolate the amplitude of this wave back to the leading edge in order to compare their numerical results with the receptivity results of Goldstein (1983) and Hammerton and Kerschen (1996). For the MSE, Wanderley and Corke considered the disturbance amplitude in a region just upstream of the lower branch neutral stability point believing that in this region the first T-S mode dominates. We are able to investigate this assumption for a flat plate in figure 4.37, which shows the log of the amplitudes ($\ln(\psi_1) = \int Re(G)dx$) of the first 5 eigenfunctions calculated using Goldstein's asymptotic method as a function of the streamwise variable, R_x. The value of $F = \nu\omega/U_\infty^2 = 54 \times 10^{-6}$ used in Wanderley and Corke (2001) corresponds to $\epsilon^6 = 54 \times 10^{-6}$, and hence $\epsilon = 0.194$. For this value of ϵ the neutral stability point occurs at $R_x \approx 3.1 \times 10^5$, where $R_x = U_\infty x^*/\nu$ and x^* is the dimensional distance from the leading edge. In the region $2 \times 10^5 < R_x < 3 \times 10^5$ considered by Wanderley and Corke it does not appear that the $1^{\rm st}$ T-S mode dominates the $3^{\rm rd}$, $4^{\rm th}$ and $5^{\rm th}$ T-S modes, although it does dominate the $2^{\rm nd}$. However, Goldstein *et al.* (1983) showed that for a flat plate the receptivity coefficients multiplying the $3^{\rm rd}$, $4^{\rm th}$ and $5^{\rm th}$ T-S modes, are at least 5 times smaller than the coefficient multiplying $1^{\rm st}$ T-S mode. Hence if similar results hold for the rounded leading edge geometry considered, then the assumption that the first T-S mode dominates all other T-S modes may indeed be valid.

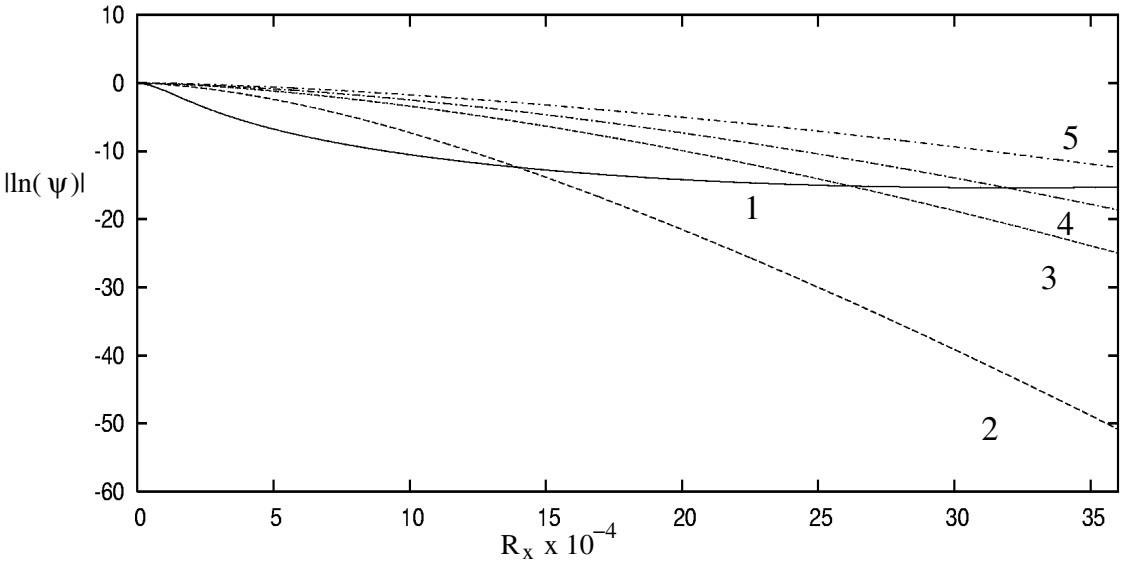

Figure 4.37: Plot of the log of the amplitudes ($\int Re(G)dx$) of the first 5 T-S modes (numbered) as a function of R_x, with $\epsilon = 0.194$. The neutral stability point occurs at $R_x \approx 35 \times 10^{-4}$.

Wanderley and Corke (2001) then assume that this T-S mode has constant decay rate at all locations back to the leading edge and thus they obtain an amplitude for the unsteady disturbance at the leading edge, though the physical interpretation of such a quantity is unclear. This extrapolation is marked as the dotted line in figure 4.38 (cf figure 10 of Wanderley and Corke (2001)) for $\epsilon = 0.194$. However this analysis does have some possible flaws. The most important of these is the assumption of constant decay rate between the leading edge and the lower branch neutral stability point. If the extrapolation was performed on results closer to the neutral stability point the measured decay rate would be much less and the value of K_x extrapolated to the leading edge would be much smaller. In figure 4.38 the results from this thesis for a flat plate are compared with the numerical results, on a MSE, of Wanderley and Corke (2001). This shows that the assumption of constant growth rate is not valid in this case. It is possible that the points calculated by Wanderley and Corke in figure 4.38 could be solely that of the 1^{st} T-S mode, however a better comparison between leading edge receptivity analysis and the numerical analysis of Wanderley and Corke would be possible if T-S amplitudes slightly downstream

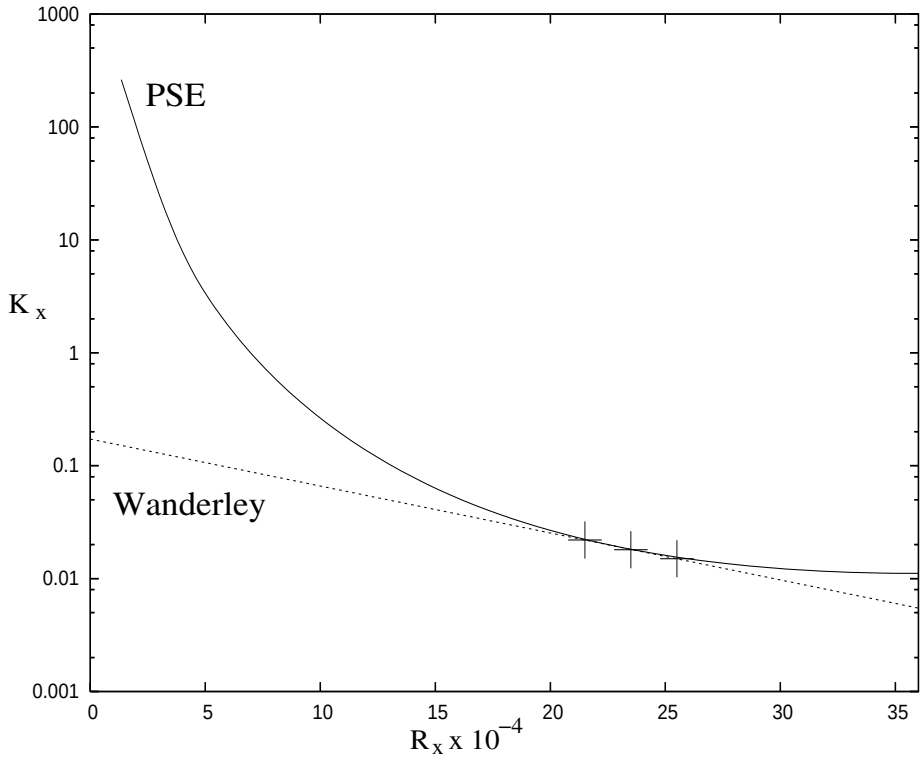

Figure 4.38: Plot of figure 10 from Wanderley and Corke (2001) for a 20:1 MSE with the results from PSE calculations for $\epsilon = 0.194$.

of the lower branch neutral stability point were available, since then there would be no question that the unstable T-S mode dominated the solution as seen in figure 4.36. Also when we compare the value of K_x, evaluated at the lower branch point, for a MSE from Wanderley and Corke with the corresponding value for a flat plate calculated using the PSE, we find that these values differ by three orders of magnitude. Hence, leading edge curvature is very important in calculating T-S wave amplitudes. Using results from PSE calculations for the particular geometry would then allow the extrapolation of the T-S amplitude to positions closer to the leading edge. This would then allow comparison with the receptivity coefficients used in asymptotic investigations which have more physical relevance in this leading edge region than the K_{LE} calculated by Wanderley and Corke.

4.7 Summary

In this chapter we consided the Orr-Sommerfeld region asymptotics, derived for a flat plate by Goldstein (1983), and numerical results in this region via the PSE. We found that the $O(\epsilon^3)$ term of the asymptotics given in Goldstein (1982) is very complicated and, due to terms which contain integrals of Airy functions, appears to be non-uniform as we move downstream. However this term is important near the leading edge as shown by comparing the asymptotic and the numerical growth rates. Thus the conclusion is that the $O(\epsilon^3)$ term is very important for the accurate calculation of T-S wave amplitudes. However because of the complexity of its derivation, and the apparent non-uniform behaviour, it is not feasible to extend this method to general bodies.

The asymptotics and the local PSE calculations proved the existence of a matching region between the leading edge region and the Orr-Sommerfeld region, for sufficiently small ϵ. This result was confirmed by the PSE, when a region was found for $\epsilon = 0.05$ where the amplitude at a point downstream was almost independent of the starting position of the PSE within that region. The PSE results also proved to be in excellent agreement with Goldstein's asymptotics, up to $O(\epsilon^3 \ln \epsilon)$, away from the leading edge region, in the limit as $\epsilon \longrightarrow 0$. As ϵ gets larger, the asymptotics become more dependent on the missing $O(\epsilon^3)$ term, but the PSE appear to be a good alternative to the asymptotics.

PSE calculations for larger ϵ suffer from numerical problems in the form of initial transients, which come from a poor guess for the first Lam-Rott eigenmode for the initial upstream boundary condition. Although no definite mechanism was found to be responsible for these transients, it was shown that higher T-S wave eigenmodes are the likely cause. These modes enter the problem through the initial condition, and propagate with the T-S wave via the PSE, and these higher modes have a region where they dominate over the primary T-S wave. Hence the growth rate will contain contributions to these waves in the form of transients.

A patching method was developed in order to calculate successfully T-S wave amplitudes in the Orr-Sommerfeld region for values of ϵ for which a matching region appears not to exist. In these cases we were not able to start our PSE calculation right back at the

leading edge receptivity result, because of the non-convergence of the PSE. We decided on a patching method based on a cubic curve fitting technique, however an extensive study of this, and the convergence of the PSE are left as areas of future study.

The results for the semi-infinite flat plate were in good agreement with those of Haddad and Corke (1998) in the limit as the nose radius of the parabola goes to zero. At this stage we weren't able to make comparisons with more realistic geometries, because it appears, from numerical studies, that the introduction of a non-zero nose radius can make lower branch amplitude values increase by as much as three orders of magnitude. Thus we next consider the effect of non-zero mean pressure gradients and a rounded leading edge.

The next chapter extends the PSE method to the case of a parabola, to examine how a favourable pressure gradient affects the propagation of the T-S wave.

Chapter 5

A parabolic body

In chapter 4, we were able to validate our numerical stability method on a semi-infinite flat plate, where asymptotics were available in the Orr-Sommerfeld region, with which to compare our results. However we are interested in performing stability calculations on more realistic bodies which have a non-zero nose radius. In this chapter we look at a parabolic body, which was considered by Hammerton and Kerschen (1996). We will show how the favourable pressure gradient on the body pushes the neutral stability point downstream compared to the flat plate value, and show that as the leading edge curvature increases, the value of the T-S wave amplitude evaluated at the lower branch neutral stability point reduces. In chapter 4, we considered only acoustic incident waves parallel to the flat plate, but in this chapter, we consider how the receptivity coefficient, and hence the disturbance amplitude, varies as a function of the incident wave angle. This is important for experimentalists, because it allows comparisons with wind tunnel experiments, where reflected sound waves from the walls are incident to the airfoil.

5.1 The governing equations

Hammerton and Kerschen (1996) considered flow past a parabola at zero angle-of-attack to the mean flow. A schematic illustration of the boundary-layer structure can be seen in figure 5.1.

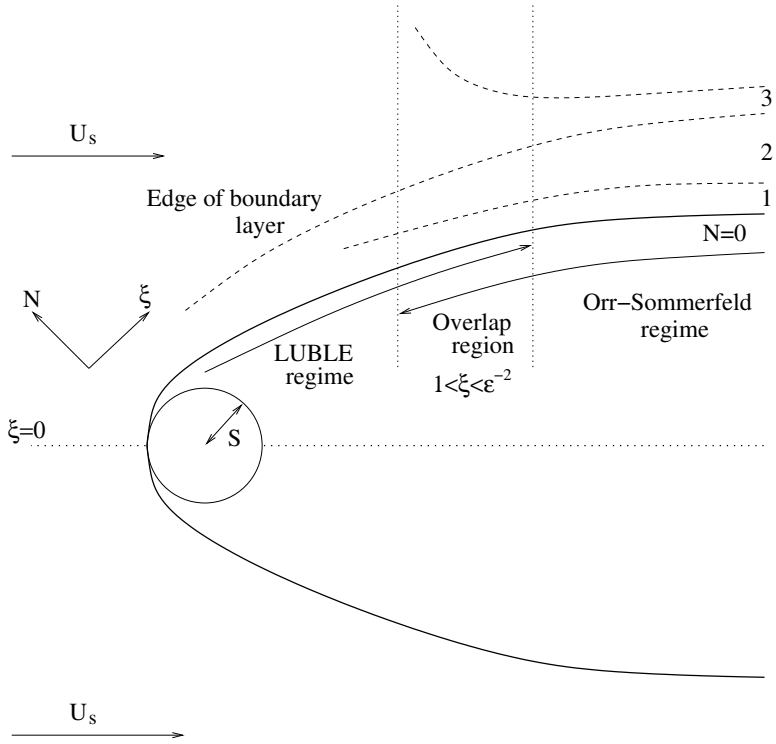

Figure 5.1: A schematic illustration of the boundary-layer structure for a body with a parabolic leading edge at zero angle of attack. The three decks in the Orr-Sommerfeld region are 1- the viscous wall layer; 2- the main inviscid layer; 3- the outer irrotational layer. Again $\epsilon^6 = Re^{-1}$.

The non-dimensional quantity S is called the Strouhal number and is defined as

$$S = \frac{\omega r_n}{U_\infty}, \tag{5.1}$$

where r_n is the dimensional nose radius of the airfoil. The Strouhal number is the non-dimensional form of the nose-radius. The inviscid flow around the airfoil can be calculated using slender wing theory, and around the nose by local complex potential methods. Hammerton and Kerschen (1996) formulated their work in terms of parabolic coordinates (ξ_H, η_H), where ξ_H is the coordinate along the body, and η_H is the coordinate normal to the body, and the subscript H distinguishes between their variables and ours. In terms of the streamwise variable, ξ_H, it can be shown that the slip velocity, U_f, at the outer edge of the boundary-layer due to the free-stream is

$$U_f(\xi_H) = \frac{\xi_H}{(\xi_H^2 + S)^{\frac{1}{2}}}. \tag{5.2}$$

The derivation of equation (5.2) will be given in §5.3.

In order to obtain the corresponding form of $U_f(\xi)$ to use in the governing equations defined in chapter 2, we need to find the relationship $\xi = \xi(\xi_H)$. From equation (2.33) we know $\xi = \xi(x)$ where x is the distance measured along the body from the leading edge, hence we can find the relationship $\xi = \xi(\xi_H)$ by

$$\xi = \int_0^x U_f(x')dx' = \int_0^{\xi_H} U_f(\xi'_H)\frac{dx}{d\xi_H}(\xi'_H)d\xi'_H, \tag{5.3}$$

where

$$\frac{dx}{d\xi_H} = \left(\left(\frac{dx_H}{d\xi_H}\right)^2 + \left(\frac{dy_H}{d\xi_H}\right)^2\right)^{\frac{1}{2}}, \tag{5.4}$$

is evaluated on the surface of the parabola ($N = \eta_H = 0$). The coordinates (x_H, y_H) are Cartesian coordinates related to the parabolic coordinates by

$$x_H + iy_H = \frac{1}{2}\left(\left(\xi_H + i\epsilon^3\eta_H + iS^{\frac{1}{2}}\right)^2 + S\right), \tag{5.5}$$

and η_H is measured normal to the body with $\eta_H = 0$ corresponding to the parabola's surface. So far we have used N and η_H interchangeably, but we shall see later that there is no problem doing this, as they are the same to leading order. Thus the relation between the ξ_H variable used by Hammerton and Kerschen (1996) and the one, ξ, in the present study is $\xi = \xi_H^2/2$. Using this transformation, the slip velocity due to the free-stream, the mean pressure gradient, $\beta(\xi)$, and the function $\Omega(\xi)$ are given by

$$U_f(\xi) = \frac{(2\xi)^{\frac{1}{2}}}{(2\xi + S)^{\frac{1}{2}}}, \quad \beta(\xi) = \frac{S}{2\xi + S}, \quad \text{and} \quad \Omega(\xi) = 2\xi + S. \tag{5.6}$$

Similarly it is found that to leading order $N = \eta_H$, as

$$\frac{d\bar{y}}{d\eta_H} = \left(\left(\frac{dx_H}{d\eta_H}\right)^2 + \left(\frac{dy_H}{d\eta_H}\right)^2\right)^{\frac{1}{2}} = \epsilon^3(\xi_H^2 + S)^{\frac{1}{2}} + O(\epsilon^6\eta_H),$$

where $\bar{y}$ is the non-dimensional normal coordinate of the Navier-Stokes equation introduced in (2.6) and

$$N = g(\xi)y = \frac{\epsilon^{-3}\bar{y}}{(\xi_H^2 + S)^{\frac{1}{2}}} = \eta_H + O\left(\epsilon^3\eta_H^2\right) \quad \text{where} \quad \epsilon^6 = Re^{-1} \ll 1.$$

Under this change of variables, it has been shown by Nichols (2001) that both the steady equation (2.32) and the LUBLE (2.37) are identical to those found by Hammerton and Kerschen (1996).

If we consider the form of the inviscid slip velocity as $\xi \longrightarrow \infty$, we find

$$U_f(\xi) \sim 1 - \frac{S}{4\xi} + \frac{3S^2}{32\xi^2} + O\left(\xi^{-3}\right). \tag{5.7}$$

Thus when we compare this with (2.41), we see that $\alpha = -S/4$. We can now use this to determine the large ξ asymptotic form of the solution in the leading edge region, and also obtain the governing equation in the Orr-Sommerfeld region.

5.1.1 Leading edge asymptotic solution

In the leading edge region, (2.59) gives the asymptotic form of the steady solution for flow past a parabola as

$$\phi_1(\xi, N) \sim f(N) + 0.300575\frac{S}{\xi}\ln(\xi) + \left(D\left(Nf' - f\right) + E(N)\right)\frac{1}{\xi} + O(\xi^{-1.887}), \tag{5.8}$$

where the constant D can be calculated by comparison with the numerical solution (Nichols, 2001), and is found to be $D \approx 0.0263$ for the case $S = 0.01$. We can remove the dependency on the value S from the steady flow equation (2.34), and hence the above equation, by introducing the new variable $\hat{\xi} = 2\xi/S$. With respect to $\hat{\xi}$, the asymptotic form of the steady solution becomes

$$\phi_1(\hat{\xi}, N) \sim f + 0.60115(Nf' - f)\frac{\ln(\hat{\xi})}{\hat{\xi}} + \frac{B_1(Nf' - f) + \hat{E}}{\hat{\xi}} + O(\hat{\xi}^{-1.887}), \tag{5.9}$$

where

$$B_1 = \frac{2D}{S} + 0.60115\ln\left(\frac{S}{2}\right), \quad \text{and} \quad \hat{E}(N) = \frac{2E(N)}{S}. \tag{5.10}$$

Nichols (2001) calculates the value of $B_1 \approx 2.075$, which agrees with the approximate value $B_1 \approx 2.08$ given by Hammerton and Kerschen (1996). The convenience of this formulation is now apparent, because the constant D can now be calculated for different values of S, without the need for the numerical solution of the steady flow equation (2.34) to be calculated each time.

In the new variable, $\hat{\xi}$, both the steady slip velocity, U_f, and the mean pressure gradient, β, become

$$U_f(\hat{\xi}) = \frac{\hat{\xi}^{\frac{1}{2}}}{(1+\hat{\xi})^{\frac{1}{2}}} \quad \text{and} \quad \beta(\hat{\xi}) = \frac{1}{1+\hat{\xi}},$$

which have been plotted in figure 5.2. Note from figure 5.2(b) that the pressure gradient is everywhere positive along the body, hence we say that this is a favourable pressure gradient, as it helps to keep the boundary-layer attached to the body. A negative pressure gradient is said to be adverse, and this then encourages the boundary-layer to become detached from the body, and we get boundary-layer separation.

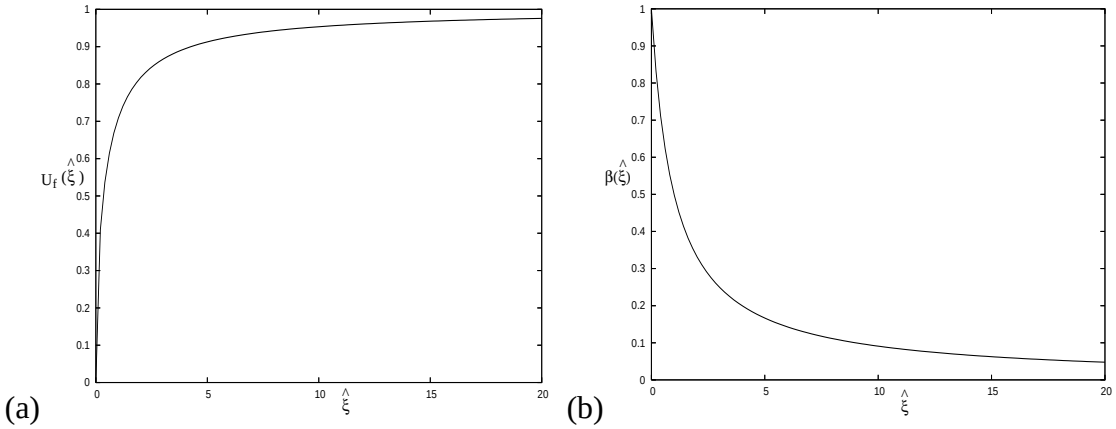

Figure 5.2: Plot of (a) $U_f(\hat{\xi})$ and (b) $\beta(\hat{\xi})$ for a parabolic body.

Equations (2.74) and (2.75) give

$$\tau_1 = -0.9621 - 1.9878Si, \tag{5.11}$$

$$T_1(\xi) = \frac{-\lambda_1(2\xi)^{\frac{3}{2}}}{U_0'}\left(\frac{1}{3} - 0.300575S\frac{\ln(\xi)}{\xi} + (1.35115S - D)\frac{1}{\xi}\right), \tag{5.12}$$

which are precisely the solutions given by Hammerton and Kerschen (1996) when ξ is replaced by $\xi_H^2/2$ in (5.12). Equation (5.12) gives the asymptotic evolution of the wavenumber for this flow over a parabola.

5.1.2 Upstream boundary conditions to the PSE

Equations (5.11) and (5.12) along with (2.129) produce the initial conditions for the PSE. The initial value of the wavenumber for the lowest order Lam-Rott eigenmode is given by

$$\alpha_0 = \frac{R_0}{Re}\frac{i\lambda_1(2\xi)^{\frac{1}{2}}}{U_0'}\left(1 - 0.300575S\frac{\ln(\xi)}{\xi} + \frac{(0.75S - D)}{\xi}\right), \tag{5.13}$$

and the initial mode shape given by (2.70) and (2.87) is found by the composite solution of

$$\phi(\xi_0, N) = \begin{cases} \xi_0^{\tau_1}\left(U_0' \frac{\int_0^{M_0}(M_0-\widetilde{M})Ai(\tilde{z})d\widetilde{M}}{\int_0^{\infty}Ai(\tilde{z})d\widetilde{M}}\right) & N = O(\xi^{-\frac{1}{2}}), \\ \xi_0^{\tau_1}\left((2\xi_0)^{\frac{1}{2}}f'(N) + \frac{U_0'i}{\lambda_1}\right) & N = O(1), \\ \xi_0^{\tau_1}\left((2\xi_0)^{\frac{1}{2}} + \frac{U_0'i}{\lambda_1}\right)\exp\left(-\frac{\epsilon^3\sqrt{2}(1+i)\xi_0 N}{U_0'\hat{\gamma}(\xi_0)\rho_1^{\frac{3}{2}}}\right) & N = O(\epsilon^{-3}\xi^{-1}), \end{cases} \tag{5.14}$$

where for the parabola

$$M = (2\xi)^{\frac{1}{2}}\left(1 + \frac{S}{4\xi}\right)N, \tag{5.15}$$

$$\hat{\gamma}(\xi) = 1 + 0.300575S\frac{\ln(\xi)}{\xi} + \left(D - \frac{3S}{4}\right)\frac{1}{\xi}. \tag{5.16}$$

Hence for given ϵ, S and starting position ξ_0, we can march downstream via the PSE to calculate the growth rate of the T-S wave as a function of ξ and hence x.

5.2 Results for the parabola

In this section we consider the matching region. How does the nose radius affect this region? Does the region remain well-defined as ϵ varies. We also look at how the non-zero pressure gradient on the body affects the position of the neutral stability point and we again calculate the T-S wave amplitude at this point.

In figure 5.3 we show how a non-zero nose radius affects the matching region we found in chapter 4 for a flat plate, using the local PSE and the leading edge asymptotics (see figure 4.10 for flat plate case, $S = 0$). Just as for the flat plate, we see that the $\epsilon = 0.05$ case, in figure 5.3(a), has a clearly defined matching region for both values of S considered. We were unable to extrapolate the solution back toward the leading edge quite as far as for the flat plate, however the appearance of this overlap region from $\tilde{\xi}_1 = 2\epsilon^2\xi/U_0'^2 \approx 0.075$ is very satisfactory. Not being able to extrapolate solutions as close to the leading edge as we did for the flat plate may be expected, because the favourable pressure gradient acts so to shift the whole growth rate curve downstream by an amount proportional to a function of S, which will be discussed later. Figure 5.3(b) shows the same as in figure 5.3(a), except with $\epsilon = 0.1$. In this case we see that we cannot

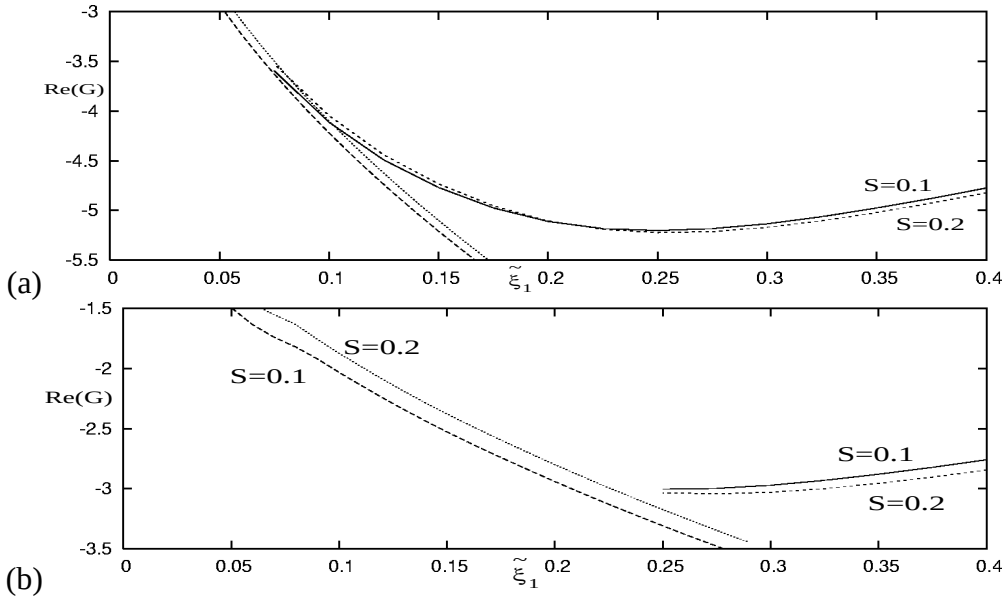

Figure 5.3: Plot of the real part of the growth rate G as a function of downstream distance, calculated by leading edge receptivity analysis and local PSE theory, for $S = 0.1$ and $S = 0.2$ for the cases (a) $\epsilon = 0.05$ and (b) $\epsilon = 0.1$. See figure 4.10 for the $S = 0$ case.

solve the local PSE right back to the leading edge receptivity asymptotics, as we found for the flat plate case, hence we will again patch the two curves so that we can extract amplitude calculations.

The shift in the real part of the growth rate curve due to the Strouhal number is shown in figure 5.4 which plots $Re(G)$ for $\epsilon = 0.05$ and $S = 0, 0.15$ and 0.3. From figure 5.4 we note that the $S = 0.15$ curve always lies to the right of the $S = 0$ curve and similarly the $S = 0.3$ curve lies to the right of both curves.

Table 5.1 and figure 5.5 show the variation in the position of the lower branch neutral stability point as a function of S. The neutral stability point was calculated both in terms of the scaled variable $\tilde{\xi}_1$ and the variable $\tilde{x}_1 = 2\epsilon^2 x/U_0'^2$, which is the scaled variable along the body which does not contain any geometry effects. For all three cases we see an increase in the position of both forms of the neutral stability point due to the favourable pressure gradient. We also note that this increase appears to be almost linear in S, but this is possibly due to the small range of S chosen rather than a linear relation actually being the case. We decided against checking this relation by increasing S further, because $S = 0.2$ is a typical Strouhal number for an airfoil (Hammerton and Kerschen, 1996),

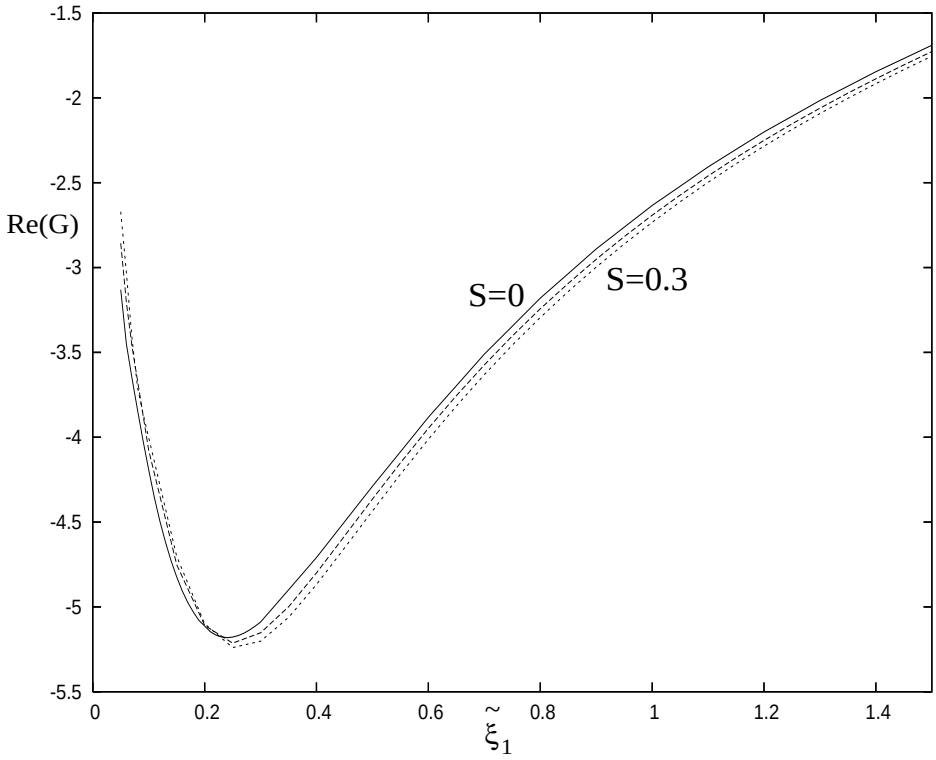

Figure 5.4: Plot of the growth rate, $Re(G)$, for $\epsilon = 0.5$ for $S = 0$ (solid line), 0.15 (dashed line) and 0.3 (dotted line), showing the downstream shift in the curves as S increases.

	$\tilde{\xi}_1$	$\tilde{\xi}_1$	$\tilde{\xi}_1$	$\tilde{x}_1$	$\tilde{x}_1$	$\tilde{x}_1$
S	$\epsilon = 0.05$	$\epsilon = 0.1$	$\epsilon = 0.2$	$\epsilon = 0.05$	$\epsilon = 0.1$	$\epsilon = 0.2$
0.0	3.402	3.946	6.359	3.402	3.946	6.359
0.025	3.406	3.962	6.432	3.408	3.968	6.454
0.05	3.410	3.977	6.492	3.413	3.988	6.533
0.1	3.417	4.003	6.601	3.423	4.024	6.676
0.15	3.424	4.028	6.706	3.432	4.058	6.813
0.2	3.430	4.052	6.809	3.441	4.090	6.947
0.25	3.437	4.074	6.906	3.450	4.121	7.074
0.3	3.443	4.096	6.994	3.459	4.151	7.191

Table 5.1: Neutral stability points for the parabola, $\epsilon = 0.05, 0.1$ and 0.2 for various S.

hence $S > 0.3$ gives nose radii which are not typical of airfoils. However this does suggest that in the vicinity of the neutral stability point, the form of the neutral stability point is

$$\tilde{\xi}_{1NS} = \tilde{\xi}^{FP}_{1NS} + Sf(\epsilon),$$

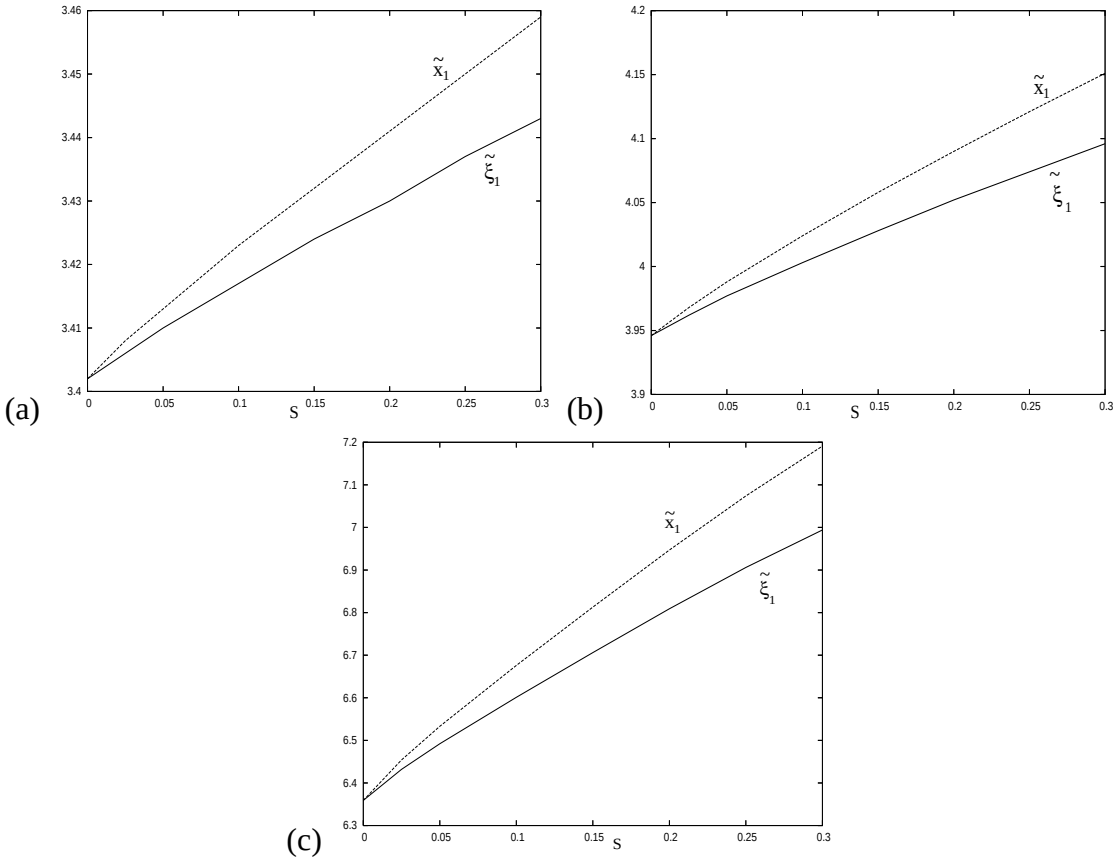

Figure 5.5: Plot of the neutral stability point on a parabola as a function of S for both $\tilde{\xi}_1$ and $\tilde{x}_1$ for (a) $\epsilon = 0.05$, (b) $\epsilon = 0.1$ and (c) $\epsilon = 0.2$.

where $\tilde{\xi}_{1NS}^{FP}$ is the neutral stability point for the flat plate case, and $f(\epsilon)$ is a function which solely depends on ϵ.

S	$\lvert C_1^{-1}\psi_1^I\rvert \times 10^{121}$	$\lvert C_1\rvert$	$\lvert\psi_1^I\rvert \times 10^{121}$
0.0	1.105	0.9662	1.068
0.025	0.6010	0.98	0.5890
0.05	0.3401	0.95	0.3231
0.1	0.1104	0.78	0.08611
0.15	0.03630	0.57	0.02069
0.2	0.01206	0.37	0.004463
0.25	0.004040	0.19	0.0007676
0.3	0.001365	0.10	0.0001365

Table 5.2: Eigenfunction, $|C_1^{-1}\psi_1^I|$, and T-S mode, $|\psi_1^I|$, amplitudes on a parabola at lower branch for varying S with $\epsilon = 0.05$. The values of the receptivity coefficient, $|C_1|$ are taken from Nichols (2001).

S	$\lvert C_1^{-1}\psi_1^I\rvert \times 10^{18}$	$\lvert C_1\rvert$	$\lvert\psi_1^I\rvert \times 10^{18}$
0.0	1.728	0.9662	1.670
0.025	1.247	0.98	1.222
0.05	0.9120	0.95	0.8664
0.1	0.4893	0.78	0.3817
0.15	0.2698	0.57	0.1538
0.2	0.1434	0.37	0.05528
0.25	0.08705	0.19	0.01654
0.3	0.05042	0.10	0.005042

Table 5.3: Eigenfunction, $|C_1^{-1}\psi_1^I|$, and T-S mode, $|\psi_1^I|$, amplitudes on a parabola at lower branch for varying S with $\epsilon = 0.1$. The values of the receptivity coefficient, $|C_1|$ are taken from Nichols (2001).

S	$\lvert C_1^{-1}\psi_1^I\rvert \times 10^{4}$	$\lvert C_1\rvert$	$\lvert\psi_1^I\rvert \times 10^{4}$
0.0	1.989	0.9662	1.922
0.025	1.805	0.98	1.769
0.05	1.636	0.95	1.545
0.1	1.337	0.78	1.043
0.15	1.057	0.57	0.6023
0.2	0.8062	0.37	0.2983
0.25	0.6382	0.19	0.1213
0.3	0.4940	0.10	0.04940

Table 5.4: Eigenfunction, $|C_1^{-1}\psi_1^I|$, and T-S mode, $|\psi_1^I|$, amplitudes on a parabola at lower branch for varying S with $\epsilon = 0.2$. The values of the receptivity coefficient, $|C_1|$ are taken from Nichols (2001).

As for the flat plate case, we choose to calculate the amplitude of the T-S wave

$$|\psi_1^I| = \left| C_1 \psi_{LR}(\xi_{LE}) \exp\left(\int_{\xi_{LE}}^{\xi_{NS}} G(x)dx \right) \right|,$$

at the neutral stability point. Tables 5.2, 5.3 and 5.4 along with figure 5.6 show how the amplitude of the unstable eigenmode varies as a function of S. In figure 5.6, we see that for all three cases the amplitude of the eigenmode at lower branch decreases as S increases. Although the amplitude of the eigenmode itself, $|C_1^{-1}\psi_1|$, decays, we see that when we include the effect of the receptivity coefficient, C_1, the overall amplitude of the T-S mode, $|\psi_1^I|$, decays faster.

The reason why we included the value $S = 0.025$ in these calculations is because

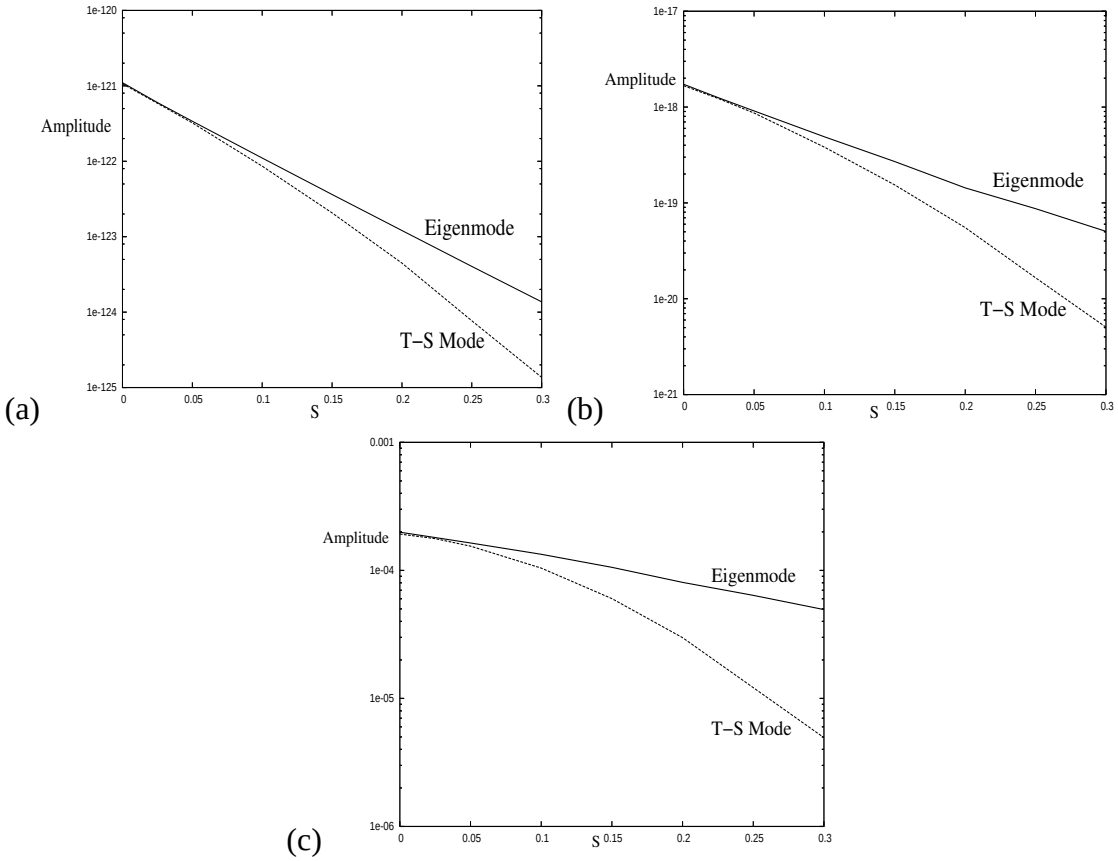

Figure 5.6: Plot on a log scale for the eigensolution, $|C_1^{-1}\psi_1^I|$, and the T-S mode, $|\psi_1^I|$, amplitudes on a parabola at lower branch, as a function of S for (a) $\epsilon = 0.05$, (b) $\epsilon = 0.1$ and (c) $\epsilon = 0.2$.

Hammerton and Kerschen (1996) showed that at $S = 0.025$, the receptivity coefficient $|C_1|$ rises from the flat plate value. However, even though the receptivity coefficient increases, the decay in the eigenmode was great enough that the T-S mode amplitude decreased from the flat plate value for $S = 0.025$, at least for the values of ϵ chosen.

5.3 Free-stream disturbances at an incident angle

Up to this point we have only considered a free-stream acoustic wave traveling at a zero incidence angle with the chord of the body. We now consider what happens if we have a free-stream acoustic wave interacting at an angle θ to the chord of the airfoil as shown in figure 5.7.

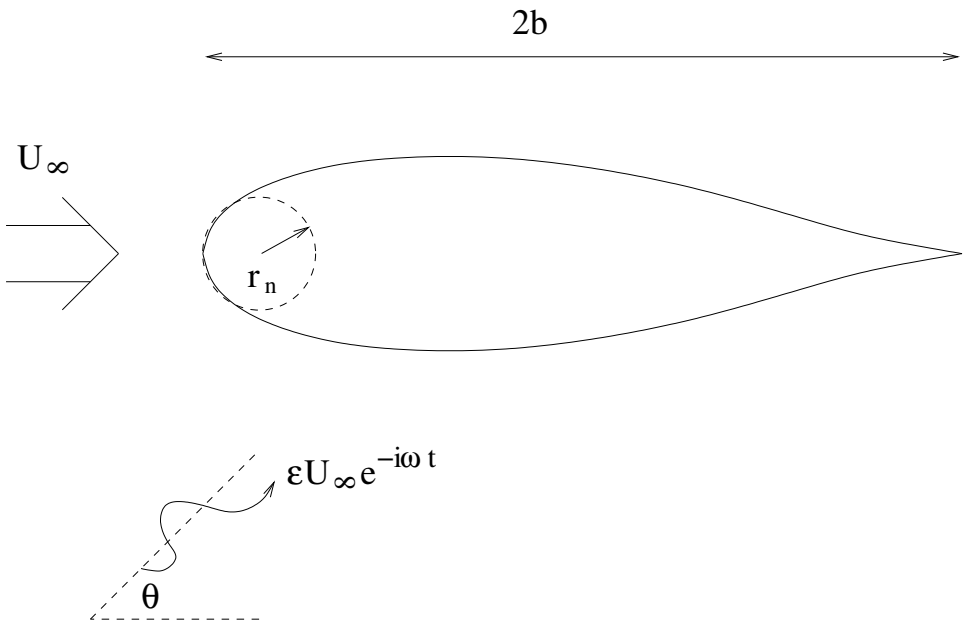

Figure 5.7: Sketch of a thin symmetric airfoil of chord length $2b$ and nose radius r_n in a uniform stream, U_∞, at zero angle of attack with a plane wave incident at an angle θ to the downstream direction of the airfoil chord.

Having the acoustic wave at a non-zero angle of incidence affects the flow solution around the parabola directly through the receptivity coefficient C_1, see appendix E. Hammerton and Kerschen (1996) discuss how this incident angle affects the receptivity coefficient for the two particular cases of very small Mach numbers, and the case when the acoustic wavelength is long compared to the hydrodynamic length scale, U_∞/ω, but shorter than the airfoil itself. These two cases can be described in terms of the reduced acoustic frequency $k = \omega b/c$, where c is the speed of sound in the undisturbed fluid, as $k \ll 1$ and $k \gg 1$ respectively. As the amplitude of the T-S wave is just the receptivity coefficient multiplied by the amplitude of the eigenmode, the results for the receptivity coefficient are analogous to the results for the T-S wave amplitude at lower branch. Hence we briefly describe the results here.

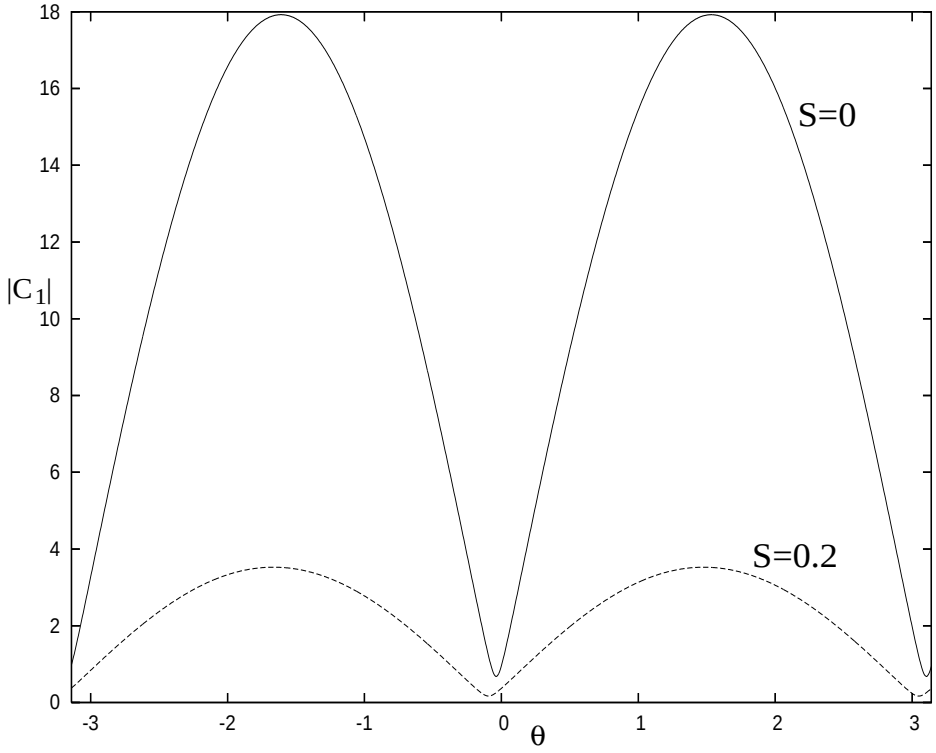

Figure 5.8: Variation of $|C_1|$ with the acoustic incident angle θ, for $k \ll 1$ and with a non-dimensional airfoil chord length $a = 10$, for $S = 0$ and $S = 0.2$.

5.3.1 Small Mach numbers ($k \ll 1$)

In equation (E.6), we show that the receptivity coefficient, C_1, can be decomposed into a symmetric, C_s, and an antisymmetric, C_a, part as follows,

$$C_1(S, \theta) = \kappa_s(\theta) C_s(S) + \kappa_a(\theta) C_a(S),$$

where the symmetric coefficient, $\kappa_s(\theta)$, and the antisymmetric coefficient, $\kappa_a(\theta)$, are calculated in appendix E.

For the case of very small Mach numbers $k \ll 1$, figure 5.8 shows the variation of $|C_1|$ as a function of acoustic incident angle θ, where the value of $a = 10$ was chosen, to coincide with a typical value for an airfoil. For the case $S = 0$, which corresponds to a flat plate, we see that the receptivity is dominated by the antisymmetric part, and the curve resembles that of the $\sin(\theta)$ curve, except near $\theta = 0$ and π, where the flow is dominated by the symmetric part. The values $S = 0.2$, $a = 10$ correspond to typical

airfoil values, and for these values we see that the antisymmetric part still dominates, but not as much. This is due to the fact that as S increases, the value of $|C_s|$ decreases more than the value of $|C_a|$ (Hammerton and Kerschen, 1996). The peak receptivity value for $S = 0.2$ is approximately one fifth of that for the flat plate.

As the amplitude of the T-S wave is directly proportional to the value of $|C_1|$, we note that the amplitude at lower branch has its maximum value around $\theta = \pm\pi/2$, and has its minimum value close to $\theta = 0$. The angle θ has a strong physical effect on the amplitude of the T-S wave at the lower branch neutral stability point.

5.3.2 Case where $k \gg 1$

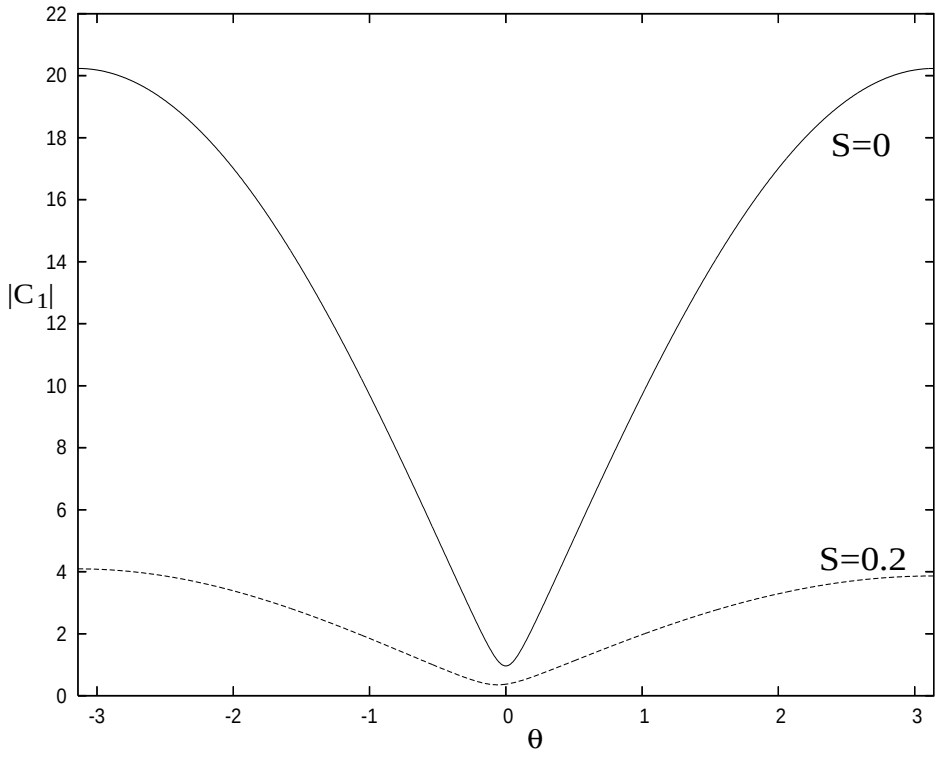

Figure 5.9: Variation of $|C_1|$ with the acoustic incident angle θ, for $k \gg 1$ and with a Mach number $M_\infty = 0.1$, for $S = 0$ and $S = 0.2$.

For the case $k \gg 1$, the variation of $|C_1|$ as a function of θ for a Mach number of 0.1 is shown in figure 5.9 (The large k case is very different from the case $k \ll 1$ already considered in figure 5.8). The $S = 0$ case is dominated by the antisymmetric part of the

flow, and the curve resembles that of the $\sin\left(\frac{\theta}{2}\right)$ graph, except near $\theta = 0$, where the symmetric part dominates. As for the case $k \ll 1$, the overall receptivity for $S = 0.2$ is reduced, but again the symmetric component is becoming more important. We note that this effect means that the amplitude of the T-S mode at lower branch reaches its maximum value at approximately $\theta = \pm\pi$, hence we again see that the value of θ can have a huge influence on the value of the T-S wave amplitude.

The main reason for considering the free-stream disturbance at an incident angle is because in experiments, the results are sometimes contaminated by waves reflecting from the walls of the wind tunnel, and interfering with the airfoil. Thus the results from this section can be used by experimentalists to see how much of an effect these stray disturbances have on their measured results.

5.4 Summary

As for the flat plate, the numerical solution to the local PSE shows that a matching region exists between the leading edge, and Orr-Sommerfeld regions, for sufficiently small ϵ. Thus we can use the PSE as we did for the flat plate, to calculate T-S wave amplitudes at the lower branch point.

The parabolic body has a monotonically decreasing, favourable pressure gradient along its surface, and this moves the neutral stability point downstream of its flat plate value, with increasing Strouhal number, in line with experimental observations. The favourable pressure gradient also produces a decrease in both the eigenmode and T-S wave amplitudes at the lower branch point, as the Strouhal number increases, when compared to the flat plate value. This is consistent with experimental observations, and the numerical work of Haddad and Corke (1998).

The effect of the disturbance wave's incident angle, θ, is also considered to try and answer contamination observations in wind tunnel experiments. When the acoustic wavelength is long compared to the hydrodynamic length scale and airfoil chord, the T-S waves display maximum amplitudes when $\theta \approx \pm\frac{\pi}{2}$. However, when the acoustic wavelength is long compared the the hydrodynamic length scale but shorter than the length of the airfoil

itself, the T-S wave has its maximum when $\theta \approx \pm\pi$.

Although the parabola satisfies the condition that the inviscid slip velocity $U_f \longrightarrow 1$ far downstream, it actually has an infinite thickness which is not realistic. Hence in the next chapter we apply the same ideas from this chapter to a Rankine body.

Chapter 6

Realistic experimental bodies - The Rankine body

In the previous two chapters, we considered two simple body geometries, the flat plate and the parabola. The flat plate was useful because its geometry lead to simple equations, and we also had the advantage that we have asymptotic results in the Orr-Sommerfeld region (Goldstein, 1983), with which to check our PSE code. The flat plate asymptotics also give us insight into what happens as the T-S wave disturbance, generated at the leading edge, moves into the Orr-Sommerfeld region. Next we considered a parabolic body, which had the advantage of being slightly more realistic, in that, it had a non-zero thickness, and the curved leading edge is more like that of a typical airfoil. However a parabola isn't very widely used in experiments, because although its inviscid slip velocity tends to a constant far downstream, the body there has an infinite thickness. This makes wind tunnel experiments difficult, as the body would increase in thickness and block the tunnel, producing interactions between the flow and the wall of the wind tunnel. Thus there exists very little experimental data with which to compare our results in the last section, and only the numerics of Haddad and Corke (1998) give any meaningful insight. However, they do not calculate the T-S wave amplitude at lower branch as we did in the previous section.

Most experimental and numerical studies on receptivity and stability are carried out on flat plates with an elliptical leading edge, whether that be an ellipse stuck on to a flat plate

(Saric and Rasmussen, 1992), or a specially machined Modified Super Ellipse (MSE) (Saric *et al.*, 1995). The geometry of a MSE is reasonably complicated, and obtaining the slip velocity on the surface is difficult even before we could begin to use the methods described in this thesis. However an approach which leads us to a body which is more like a MSE than a parabola, is to consider a line source in a uniform flow, one of whose streamlines has a shape known as a Rankine body. Although the analysis for a Rankine body is not trivial, it's more straightforward than the MSE, so we use it as a stepping stone to a further method described later.

We will show that the analysis for the Rankine body is dependent on one real dimensionless parameter, A, which is directly related to the dimensional nose radius, r_n. We will then use this information to calculate results similar in kind to those we obtained for the parabola. We then discuss how we could calculate similar results for a MSE by using slender body theory to calculate the inviscid slip velocity, U_f.

6.1 The Rankine body

The formulation for the inviscid flow around a Rankine body was studied by Nichols (2001), and the formulation for the inviscid pressure gradient and the slip velocity can be found in appendix F.

We introduce the scaled variables $\hat{z} = z/A$, where $z = x_c + iy_c$ is a complex variable, and the subscript c denotes that these are the usual real Cartesian coordinates. Under this change of variables, the slip velocity, U_f, and pressure gradient, β, can be written as

$$U_f(\hat{y}_c) = \left(1 + \frac{\sin^2(\hat{y}_c)}{\hat{y}_c^2} - \frac{\sin(2\hat{y}_c)}{\hat{y}_c}\right)^{\frac{1}{2}}, \tag{6.1}$$

$$\beta(\hat{y}_c) = \frac{2\hat{\xi}}{U_f^3}\frac{d\hat{y}_c}{dx}\left(\frac{\sin(2\hat{y}_c)}{\hat{y}_c^2} - \frac{\sin^2(\hat{y}_c)}{\hat{y}_c^3} - \frac{\cos(2\hat{y}_c)}{\hat{y}_c}\right), \tag{6.2}$$

where $\hat{\xi}$ is defined by (F.17), and x is a curvilinear coordinate measured parallel to the body from the leading edge.

The plots of $U_f(\hat{\xi})$ and $\beta(\hat{\xi})$ are shown in figure 6.1 and these hold for all A. We see that the slip velocity reaches a maximum of $U_{fmax} = 1.260$, and this occurs at $\hat{y}_c = 2.043$

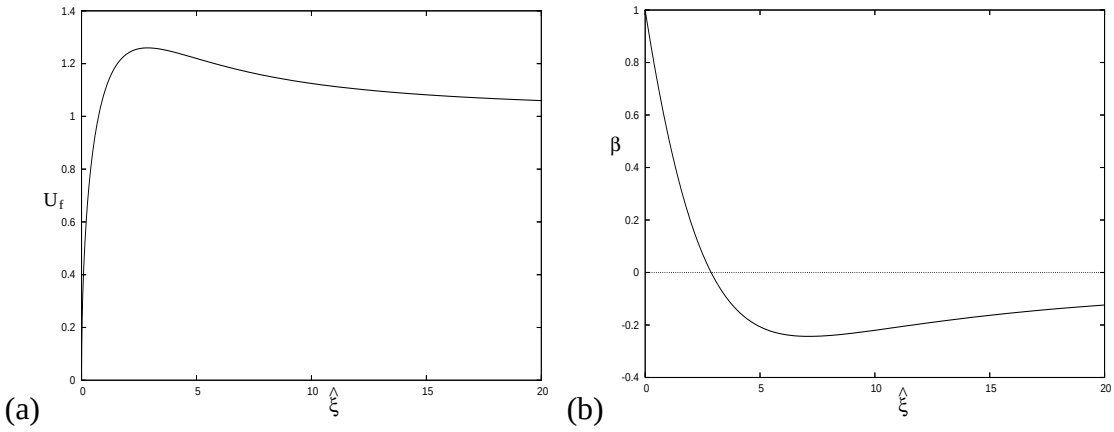

Figure 6.1: Plot of (a) $U_f(\hat{\xi})$ and (b) $\beta(\hat{\xi})$ for a Rankine body.

which correspond to $\hat{\xi} = 2.873$. This leads to the pressure gradient $\beta(\hat{\xi})$ starting off favourable for $\hat{\xi} < 2.873$, but becoming adverse, and slowly tending to zero far downstream. The minimum value for the pressure gradient is $\beta_{min} = -0.2434$ and occurs at $\hat{y}_c = 2.614$, which corresponds to $\hat{\xi} = 7.130$. The position of the neutral stability point on a body depends on the pressure gradient along the body, and hence because the favourable pressure gradient on the parabola moves the neutral stability point downstream of the position for a zero pressure gradient, we expect an adverse pressure gradient to move it upstream of the position for a zero pressure gradient.

6.1.1 Large ξ asymptotics, in the leading edge receptivity region, for a Rankine body

To be able to construct all the leading edge asymptotics formulated in chapter 2, we first need to find the large x asymptotic form of $U_f(x)$. To do this, we first note that as $x \longrightarrow \infty$, $y_c \longrightarrow A\pi$. Hence to construct the asymptotics for the Rankine body, we introduce the new variable $p = A\pi - y_c$, and find the solution about $p = 0$. In this new variable, the asymptotic form of the slip velocity, U_f, and dx/dy_c are

$$U_f \sim 1 + \frac{p}{A\pi} + \frac{p^2}{A^2\pi^2} + \frac{(3-2\pi^2)}{3}\frac{p^3}{A^3\pi^3} + \frac{(6-\pi^2)}{6}\frac{p^4}{A^4\pi^4} + O(p^5), \quad (6.3)$$

$$\frac{dx}{dy_c} \sim \frac{A^2\pi}{p^2} + \frac{\pi}{3} - \frac{2}{3A}p + \frac{(15+2\pi^2)}{30\pi}\frac{p^2}{A^2} - \frac{4}{45A^3}p^3 + O(p^4). \quad (6.4)$$

Hence we can integrate (6.4) with respect to y_c and get

$$x \sim \frac{A^2\pi}{p} - \frac{\pi}{3}p + \frac{1}{3A}p^2 - \frac{(15+2\pi^2)}{90\pi}\frac{p^3}{A^2} + \frac{1}{45A^3}p^4 + O(p^5). \tag{6.5}$$

Inverting (6.5) to find p in terms of x gives

$$p \sim \frac{A^2\pi}{x} - \frac{A^4\pi^3}{3x^3} + O(x^{-4}), \tag{6.6}$$

which on insertion into (6.3) gives

$$U_f(x) \sim 1 + \frac{A}{x} + \frac{A^2}{x^2} + (1-\pi^2)\frac{A}{x^3} + O(x^{-4}). \tag{6.7}$$

From equation (2.33) we can then write the large x asymptotic form of ξ as

$$\xi(x) \sim x + A\ln(x) - \frac{A^2}{x} - \frac{(1-\pi^2)}{2}\frac{A^3}{x^2} + O(x^{-3}), \tag{6.8}$$

hence comparing (6.7) with (2.41) we note that for a Rankine body

$$\alpha = A \quad \text{and} \quad \gamma = A^2.$$

Using these in comparison with (2.45) and (2.46), we can write the large ξ asymptotic form for $\beta(\xi)$ and $\Omega(\xi)$ as

$$\beta(\xi) \sim -\frac{2A}{\xi} - 4A^2\frac{\ln\xi}{\xi^2} + O(\xi^{-3}\ln^2(\xi)), \tag{6.9}$$

$$\Omega(\xi) \sim 2\xi - 4A - 4A^2\frac{\ln\xi}{\xi} + \frac{2A^2}{\xi} + O(\xi^{-2}\ln^2(\xi)). \tag{6.10}$$

From (2.59) we can now see that the asymptotic form of the steady flow past a Rankine body is

$$\phi_1(\xi, N) \sim f - 1.2023A(Nf' - f)\frac{\ln\xi}{\xi} + \frac{D(Nf'-f)+E(N)}{\xi} + O(\xi^{-1.887}), \tag{6.11}$$

where the constant D is given by Nichols (2001) in terms of A as

$$D = A(-4.71125 + 1.2023\ln(A)). \tag{6.12}$$

The corresponding forms of (5.11) and (5.12) for the Rankine body, from (2.74) and (2.75) respectively are

$$\tau_1 = -0.6921 + 7.9508A\,i, \tag{6.13}$$

$$T_1 = -\frac{\lambda_1(2\xi)^{\frac{3}{2}}}{U_0'}\left(\frac{1}{3} + 1.2023A\frac{\ln\xi}{\xi} - (5.4046A + D)\frac{1}{\xi}\right) + O(\xi^{-0.387}). \tag{6.14}$$

From (2.129) the initial form of the wavenumber for the PSE code is

$$\alpha_0 = \frac{R_0}{Re}\frac{i\lambda_1(2\xi)^{\frac{1}{2}}}{U_0'}\left(1 - 1.2023A\frac{\ln\xi}{\xi} - (3A+D)\,\frac{1}{\xi}\right) \tag{6.15}$$

and again the initial mode shape is given by the composite solution of

$$\phi(\xi_0, N) = \begin{cases} \xi_0^{\tau_1}\left(U_0'\frac{\int_0^{M_0}(M_0-\widetilde{M})Ai(\tilde{z})d\widetilde{M}}{\int_0^{\infty}Ai(\tilde{z})d\widetilde{M}}\right) & N = O(\xi^{-\frac{1}{2}}), \\ \xi_0^{\tau_1}\left((2\xi_0)^{\frac{1}{2}}f'(N) + \frac{U_0'i}{\lambda_1}\right) & N = O(1), \\ \xi_0^{\tau_1}\left((2\xi_0)^{\frac{1}{2}} + \frac{U_0'i}{\lambda_1}\right)\exp\left(-\frac{\epsilon^3\sqrt{2}(1+i)\xi_0 N}{U_0'\hat{\gamma}(\xi_0)\rho_1^{\frac{3}{2}}}\right) & N = O(\epsilon^{-3}\xi^{-1}), \end{cases} \tag{6.16}$$

where for the Rankine body

$$M = (2\xi)^{\frac{1}{2}}\left(1 - \frac{A}{\xi}\right)N, \tag{6.17}$$

$$\hat{\gamma}(\xi) = 1 - 1.2023A\frac{\ln(\xi)}{\xi} + (D+3A)\,\frac{1}{\xi}. \tag{6.18}$$

6.1.2 Stability results for a Rankine body

In this section we shall compare results for the position of the lower branch neutral stability point on a Rankine body, along with T-S wave amplitude calculations at the lower branch point.

Position of the neutral stability point

In chapter 5, we compared the position of the neutral stability point, for a parabolic body in terms of $\tilde{\xi}_1 = 2\epsilon^2\xi/U_0'^2$ and $\tilde{x}_1 = 2\epsilon^2 x/U_0'^2$, and also the eigenmode amplitudes at lower branch for a range of values for S. In this section, we will do similar calculations for a range of values of A.

Tables 6.1 and 6.2 together with figure 6.2 show how the position of the lower branch neutral stability point varies with increasing A, for $\epsilon = 0.05$, 0.1 and 0.2. The adverse pressure gradient along the Rankine body forces the neutral stability point to move upstream as A increases, in contrast to the parabola, where the favourable pressure gradient moves it downstream. Also we note that, as ϵ increases, the percentage change in the position of the lower branch point for $\tilde{\xi}_1$, at $A = 0.7$ compared to $A = 0.0$ increases from 1.5% for $\epsilon = 0.05$, to 4.5% for $\epsilon = 0.1$, to 14% for $\epsilon = 0.2$.

A	$\tilde{\xi}_1$	$\tilde{x}_1$
0.0	3.402	3.402
0.005	3.398	3.397
0.01	3.395	3.393
0.015	3.391	3.388
0.02	3.388	3.384
0.025	3.385	3.381
0.0275	3.384	3.379
0.033	3.380	3.374
0.04	3.376	3.370
0.05	3.370	3.362
0.055	3.367	3.359
0.06	3.364	3.355
0.067	3.360	3.350
0.07	3.358	3.348

Table 6.1: Neutral stability points for the Rankine body, for $\epsilon = 0.05$ for various A.

	$\tilde{\xi}_1$	$\tilde{\xi}_1$	$\tilde{x}_1$	$\tilde{x}_1$
A	$\epsilon = 0.1$	$\epsilon = 0.2$	$\epsilon = 0.1$	$\epsilon = 0.2$
0.0	3.946	6.359	3.946	6.359
0.005	3.932	6.297	3.928	6.284
0.01	3.918	6.237	3.911	6.214
0.015	3.906	6.179	3.897	6.147
0.02	3.893	6.126	3.881	6.085
0.025	3.881	6.072	3.867	6.023
0.03	3.870	6.017	3.853	5.961
0.04	3.846	5.905	3.825	5.834
0.05	3.823	5.788	3.798	5.704
0.055	3.811	5.735	3.783	5.645
0.06	3.800	5.680	3.770	5.584
0.07	3.777	5.565	3.748	5.475

Table 6.2: Neutral stability points for the Rankine body, for $\epsilon = 0.1$ and $\epsilon = 0.2$ for various A.

Comparison of favourable and adverse pressure gradients

Before we go on to calculate T-S wave amplitudes at the lower branch point, we first make a comparison of how the position of the neutral stability point is affected by a favourable or adverse pressure gradient.

For the $\epsilon = 0.05$ case in table 6.1, we note that we have included the values of $A =$

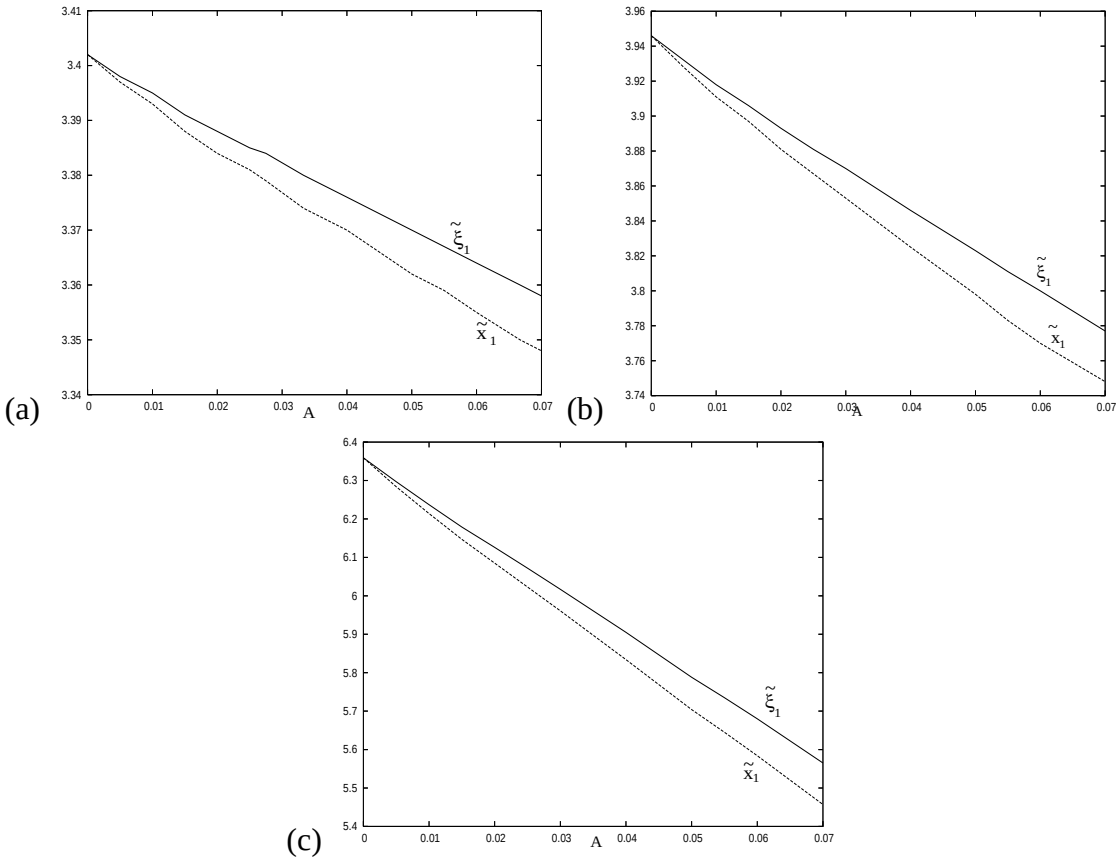

Figure 6.2: Plot of the neutral stability point for the Rankine body, as a function of A for both $\tilde{\xi}_1$ and $\tilde{x}_1$ for (a) $\epsilon = 0.05$, (b) $\epsilon = 0.1$ and (c) $\epsilon = 0.2$.

$A:S$	$\tilde{\xi}_1$ parabola	$\tilde{x}_1$ parabola	$\tilde{\xi}_1$ Rankine body	$\tilde{x}_1$ Rankine Body
0.033 : 0.05	3.410	3.413	3.380	3.374
0.067 : 0.1	3.417	3.423	3.360	3.350
$A:S$	$\lvert\tilde{\xi}_1 - \tilde{\xi}_{1NS}\rvert$ parabola	$\lvert\tilde{x}_1 - \tilde{x}_{1NS}\rvert$ parabola	$\lvert\tilde{\xi}_1 - \tilde{\xi}_{1NS}\rvert$ Rankine body	$\lvert\tilde{x}_1 - \tilde{x}_{1NS}\rvert$ Rankine body
0.033 : 0.05	0.008	0.011	0.022	0.028
0.067 : 0.1	0.015	0.021	0.042	0.052

Table 6.3: Table showing the position of the neutral stability points, $\tilde{\xi}_1$ and $\tilde{x}_1$, for the parabola and Rankine body for $\epsilon = 0.05$ (top two rows), and their relative shift from the flat plate value $\tilde{\xi}_{1NS} = \tilde{x}_{1NS} = 3.402$ (bottom two rows).

0.033 and 0.067. We considered these values, because by using (6.23) and (6.24), we see that these correspond to the Strouhal number values $S = 0.05$ and 0.1 respectively. Table 6.3 shows the position of the lower branch neutral stability point for both the parabola and

the Rankine body, when $\epsilon = 0.05$, along with the size difference between these values and the position of the neutral stability point on a flat plate ($A = S = 0$). We see that although the neutral stability points are moving in opposite directions, the relative change in the $\tilde{\xi}_1$ position for the Rankine body is about 2.8 times that of the parabola, and the $\tilde{x}_1$ change is about 2.5 times that of the parabola. The absolute value of the pressure gradient, β, for the parabola at these neutral stability points is 1.7×10^{-4} for $S = 0.05$ and 3.3×10^{-4} for $S = 0.1$. These values are about 2.5 times smaller than the corresponding values on the Rankine body, which are 4.4×10^{-4} for $A = 0.033$ and 9.0×10^{-4} for $A = 0.067$. This suggests that at least for these bodies an adverse pressure gradient is more significant on the position of the neutral stability point than a favourable one, although it is unclear how much difference the size of the pressure gradient at the neutral stability point makes.

T-S wave amplitudes at lower branch

The position of the neutral stability point affects the amplitude of the eigenmode, by changing the value of the integral of the growth rate $G(x)$. The favourable pressure gradient on the parabola moved the neutral stability point downstream, thus making the integral of the growth rate $G(x)$ more negative, hence decreasing the amplitude of the eigenmode. Consequently, we expect the adverse pressure gradient on the Rankine body to make the integral of $G(x)$ less negative, hence increasing the amplitude of the eigenmode as A increases. By considering tables 6.4, 6.5, 6.6 and figure 6.3, we see that this is in fact the case.

Tables 6.4, 6.5 and 6.6 show the amplitudes of the 1^{st} eigenmode, $|C_1^{-1}\psi_1^I|$ at the lower branch neutral stability point for $\epsilon = 0.05$, 0.1 and 0.2, along with the amplitude of the T-S mode, $|\psi_1^I|$, where

$$|\psi_1^I| = \left| C_1 \psi_{LR}(\xi_{LE}) \exp\left(\int_{\xi_{LE}}^{\xi_{NS}} G(x) dx \right) \right|.$$

The value of the receptivity coefficient, $|C_1|$, for the Rankine body tends to zero much faster than for the parabola (Nichols, 2001). We can see this if we consider the values $S = 0.05$ and 0.1 which correspond to $A = 0.033$ and 0.067. For $S = 0.05$ the value of $|C_1|$ for the parabola (see §5.2) is 0.95 and the corresponding value for the Rankine body

A	$\lvert C_1^{-1}\psi_1^I\rvert \times 10^{121}$	$\lvert C_1\rvert$	$\lvert\psi_1^I\rvert \times 10^{121}$
0.0	1.105	0.9662	1.068
0.005	1.632	0.82	1.338
0.01	2.658	0.61	1.621
0.015	4.341	0.40	1.736
0.02	7.071	0.22	1.556
0.025	11.64	0.12	1.397
0.0275	14.95	0.11	1.644
0.033	24.27	0.13	3.156
0.04	46.24	0.12	5.552
0.05	130.5	0.08	10.44
0.055	215.6	0.06	12.94
0.06	340.9	0.04	13.64
0.067	958.7	0.01	9.587
0.07	993.2	0.01	9.932

Table 6.4: Eigenfunction amplitudes at lower branch for the Rankine body, for varying A with $\epsilon = 0.05$. The values of the receptivity coefficient, $|C_1|$ are taken from Nichols (2001).

A	$\lvert C_1^{-1}\psi_1^I\rvert \times 10^{18}$	$\lvert C_1\rvert$	$\lvert\psi_1^I\rvert \times 10^{18}$
0.0	1.728	0.9662	1.670
0.005	2.082	0.82	1.707
0.01	2.768	0.61	1.689
0.015	3.678	0.40	1.471
0.02	4.906	0.22	1.079
0.025	6.559	0.12	0.7870
0.03	8.825	0.11	0.9707
0.04	17.97	0.12	2.156
0.05	34.70	0.08	2.770
0.055	48.33	0.06	2.900
0.06	66.91	0.04	2.677
0.07	130.7	0.01	1.307

Table 6.5: Eigenfunction amplitudes at lower branch for the Rankine body, for varying A with $\epsilon = 0.1$. The values of the receptivity coefficient, $|C_1|$ are taken from Nichols (2001).

is 0.13. Similarly for $S = 0.1$, the receptivity coefficient for the parabola is 0.78 and for the Rankine body it's 0.01.

The amplitude of the T-S mode for the Rankine body is much more interesting than for

A	$\lvert C_1^{-1}\psi_1^I\rvert \times 10^4$	$\lvert C_1\rvert$	$\lvert\psi_1^I\rvert$
0.0	1.989	0.9662	1.922
0.005	2.085	0.82	1.710
0.01	2.234	0.61	1.363
0.015	2.411	0.40	0.9645
0.02	2.610	0.22	0.5743
0.025	2.801	0.12	0.3361
0.03	3.095	0.11	0.3404
0.04	3.687	0.12	0.4414
0.05	4.336	0.08	0.3469
0.055	4.715	0.06	0.2829
0.06	5.077	0.04	0.2031
0.07	5.963	0.01	0.05963

Table 6.6: Eigenfunction amplitudes at lower branch for the Rankine body, for varying A with $\epsilon = 0.2$. The values of the receptivity coefficient, $|C_1|$ are taken from Nichols (2001).

the parabola, because there is a conflict between the increasing eigenmode amplitude, as A increases, and a decrease in the receptivity coefficient. The resulting T-S mode amplitudes can be seen in figure 6.3. While the eigenmode amplitudes appear to be straight lines, the T-S mode amplitude has a double maximum as a function of A. For the case $\epsilon = 0.05$ in figure 6.3(a), this double maximum is very clear, with maxima around $A = 0.015$ and $A = 0.055$, with the second being almost a factor of 10 larger than the first. The case $\epsilon = 0.1$ has a slightly different appearance, because the increase of the eigenmode amplitude is less than the $\epsilon = 0.05$ case, while the values of the receptivity coefficients remain unchanged. Hence in this case the first maximum of the T-S mode amplitude appears to occur closer to $A = 0$ and in fact the amplitude appears to be almost constant between $A = 0$ and $A = 0.015$. We still get another maximum around $A = 0.05$, but the relative increase in this maximum compared to the first one is much smaller than for the $\epsilon = 0.05$ case, and is only a factor of 1.8 times larger in this case. Figure 6.3(c) shows the same graph again except this time for $\epsilon = 0.2$, and we see a decay of the T-S mode away from $A = 0$, and the second maximum which occurs around $A = 0.04$ has in fact a lower magnitude than the one at $A = 0$. So as ϵ increases the growth of the eigenmode with respect to A decreases, and hence for the $\epsilon = 0.05$ case, we find the two maxima are

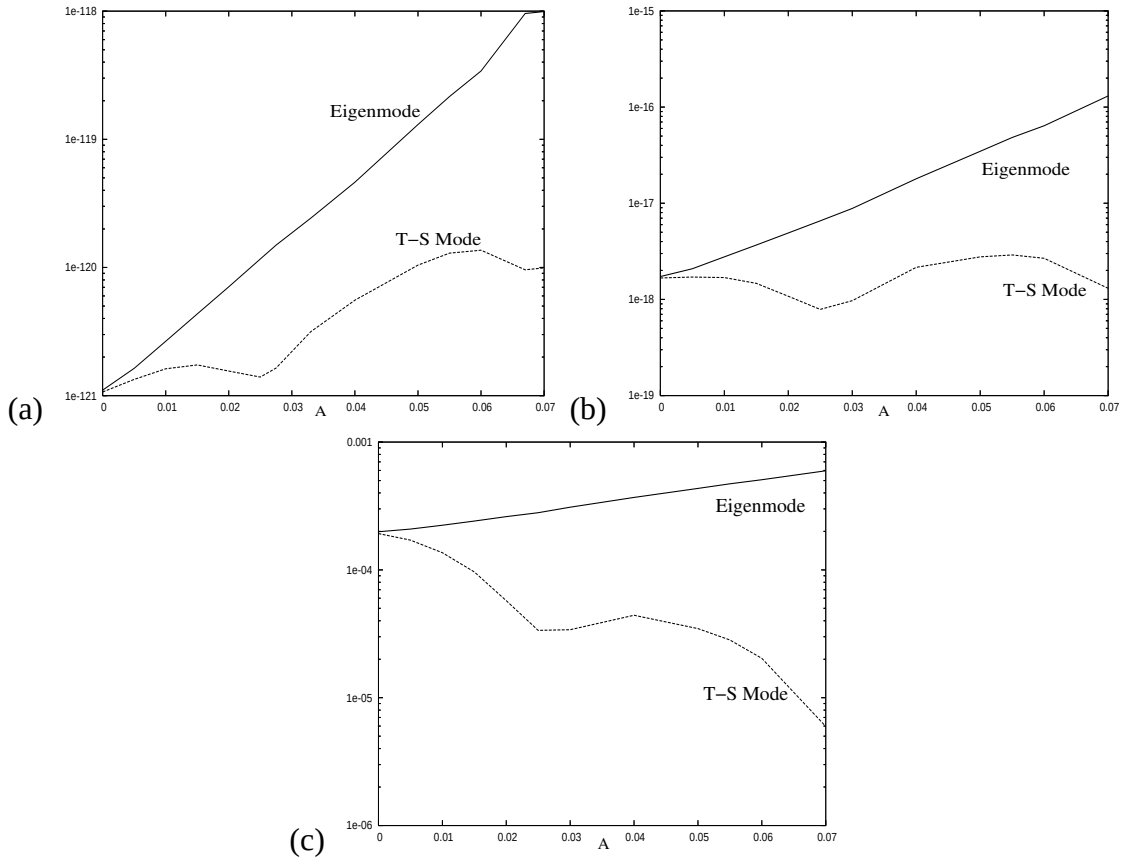

Figure 6.3: Plot on a log scale for the eigensolution, $|C_1^{-1}\psi_1^I|$, and the T-S mode, $|\psi_1^I|$, amplitudes on a Rankine body at lower branch, as a function of A for (a) $\epsilon = 0.05$, (b) $\epsilon = 0.1$ and (c) $\epsilon = 0.2$.

larger than the flat plate value, whereas for $\epsilon = 0.2$, the first maximum now corresponds to the flat plate value, and the second maximum has a value lower than the flat plate value.

In the next section we look at the physical properties of the parabola and the Rankine body, in an attempt to get a better idea of what results may be expected for a MSE.

6.2 Comparison of experimental and numerical bodies

In this section, we discuss both the parabola and Rankine body, compare their pressure gradients and slip velocities, and where we can, compare these with the MSE which is used so much in experimental and numerical studies.

6.2.1 Body geometry

The equation for the upper surface of the Rankine body, $x_c = x_c(y_c)$, was derived in appendix F, and given by

$$x_c = A - y_c \cot\left(\frac{y_c}{A}\right). \tag{6.19}$$

The equations for the upper surface of the parabola and MSE, $y_c = y_c(x_c)$, are

$$y_c = (2Sx_c)^{\frac{1}{2}}, \tag{6.20}$$

$$y_c = \begin{cases} b\left(1 - \left(\frac{a-x_c}{a}\right)^m\right)^{\frac{1}{2}}, \quad m = 2 + \left(\frac{x_c}{a}\right)^2 & x_c < a \\ b & x_c > a \end{cases}, \tag{6.21}$$

respectively, where S is the Strouhal number defined in (5.1), b is the semi-width of the flat plate on which the MSE is drilled, and a is the length of the elliptical part of the nose, as shown in figure 6.4. The ratio $a : b$ is known as the aspect ratio for the MSE, and typical values used in experimental and numerical works such as Saric and White (1998) and Wanderley and Corke (2001) are $20 : 1$ or $40 : 1$. For a regular elliptical nose considered by Saric and Rasmussen (1992), $m = 2$ in (6.21).

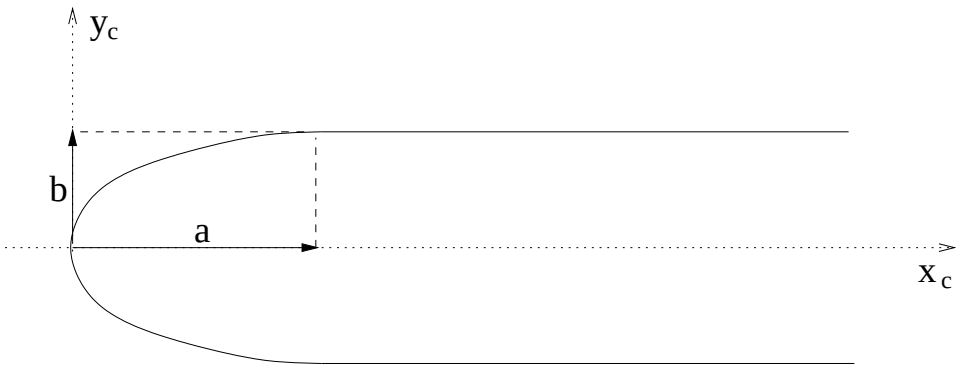

Figure 6.4: Sketch of MSE to show the definitions of a and b in (6.21).

To be able to compare these three bodies, we have to find a suitable parameter which describes all three bodies. A suitable choice for this is to calculate the dimensionless nose radius for each body. This is defined as

$$r(0) = r(x = 0) = \left.\frac{\left(1 + \left(\frac{dx_c}{dy_c}\right)^2\right)^{\frac{3}{2}}}{\frac{d^2x_c}{dy_c^2}}\right|_{x=0}. \tag{6.22}$$

Calculating the nose radius for these three bodies we find

$$r_P = S, \tag{6.23}$$

$$r_R = \frac{3A}{2}, \tag{6.24}$$

$$r_{MSE} = \frac{b^2}{a}, \tag{6.25}$$

where the subscripts P, R and MSE correspond to the parabola, Rankine body and MSE respectively. Thus for a given A it is straightforward to convert to a value of S, and vice versa. However for the MSE, the situation is a little bit more complicated. For a Rankine body and a MSE, we have two choices, we can either fix the nose radius of the Rankine body, or we can fix the aspect ratio of the MSE. If we fix the nose radius of the Rankine body, i.e. we stipulate A, then the thickness of the body is automatically fixed at $2A\pi$ ($b = A\pi$ for the MSE), as noted in the previous section. Thus if we form a MSE with the same nose radius as the Rankine body, with thickness $b = A\pi$, this leads to the value of a being

$$a = \frac{2b^2}{3A} = \frac{2\pi^2 A}{3}, \tag{6.26}$$

which fixes the aspect ration of the MSE at $2\pi/3$.

On the other hand, if we start with a MSE of thickness b, and if we fix the aspect ratio to be $a : b$, then we find from comparing the nose radii of the MSE and the Rankine body that

$$A = \frac{2b^2}{3a}, \tag{6.27}$$

and hence the nose radius of the Rankine body is fixed at $2b^2/(3a)$.

When modeling a MSE using a Rankine body, it seems logical to require that we make the nose radii the same so that the leading edge receptivity results are the same, however when we move downstream into the stability region, it would be more appropriate to fix the aspect ratio of the bodies, so that the far downstream forms are similar. The parabola, Rankine body and MSE with the same nose radius, for the case $A = 0.1$, have been plotted in figure 6.5. We see that the parabola increases in thickness as x_c increases and it also always lies outside the MSE. The Rankine body on the other hand tends to the flat plate of the MSE from inside, and always lies inside the MSE. Thus the geometry of the

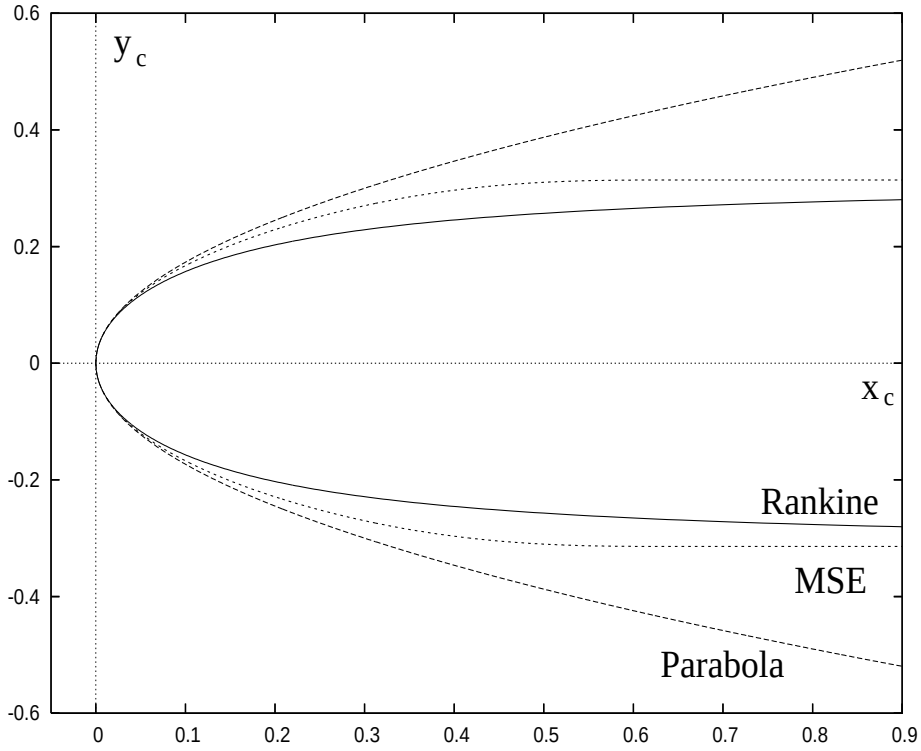

Figure 6.5: The shapes near the nose of the parabola, the Rankine body and the Modified Super Ellipse for the case $A = 0.1$.

MSE lies between the parabola and the Rankine body. However the stability properties of the bodies rely on the form of the pressure gradient, so just considering the geometry of the bodies won't give us an insight into the stability properties of the MSE.

As well as comparing the physical shape of the bodies, we can also compare the curvature too. We define the curvature as

$$\kappa = -\frac{\frac{d^2 y_c}{dx_c^2}}{\left(1 + \left(\frac{dy_c}{dx_c}\right)^2\right)^{\frac{3}{2}}}. \tag{6.28}$$

The curvature as a function of x_c, for the case $A = 0.1$, for these three bodies can be seen in figure 6.6. We can see that the Rankine body's curvature is higher than the parabola's up until $x_c \approx 0.475$ and then the parabola has the larger curvature. The MSE on the other hand has a curvature similar to that of the parabola up to $x_c \approx 0.1$, then the MSE has a region of constant curvature before decaying to zero at $x_c = a$, which in this case equals $2\pi^2/30$.

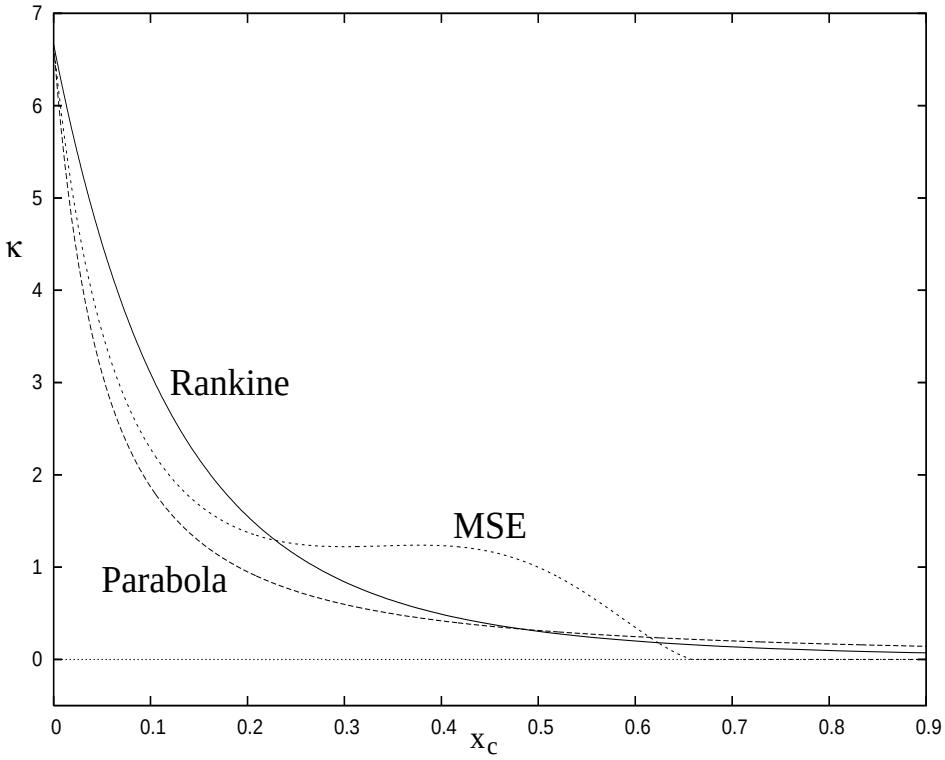

Figure 6.6: Plot of the curvature of the parabola, Rankine body and the MSE, for the case $A = 0.1$, as a function of x_c.

We can prove that the parabola's curvature tends to zero slower than the Rankine body's, by looking at the large x_c form of the curvature. Using the same method and variables as in §6.1.1, with $p = A\pi - y_c$, we see that the small p asymptotic limit of the Rankine body's geometry is

$$x_c \sim \frac{A^2\pi}{p} - \frac{\pi}{3}p + \frac{1}{3A}p^2 - \frac{\pi}{45A^2}p^3 + O(p^4),$$

and thus inverting this, we find that to leading order

$$y_c = A\pi - \frac{A^2\pi}{x_c} + O(x_c^{-2}). \tag{6.29}$$

Therefore as $x_c \longrightarrow \infty$, the leading order curvature terms for the parabola and Rankine body are

$$\begin{aligned} \kappa_P &\sim \frac{S^{\frac{1}{2}}}{(2x_c)^{\frac{3}{2}}}, \\ \kappa_R &\sim \frac{2A^2\pi}{x_c^3}, \end{aligned}$$

which when we use the fact that

$$S = \frac{3A}{2},$$

we find

$$\begin{aligned} \kappa_P &\sim \frac{(3A)^{\frac{1}{2}}}{4x_c^{\frac{3}{2}}}, \\ \kappa_R &\sim \frac{2A^2\pi}{x_c^3}, \end{aligned}$$

so clearly the Rankine body's curvature tends to zero much faster than the parabola's.

Just by looking at the geometries and body curvature, it's very difficult to tell how the receptivity disturbances will behave on the MSE. To get a better idea of this, we need to consider the pressure gradients for the three bodies.

6.2.2 Slip velocity and pressure gradient

Although comparing the body geometries gives as an insight into how the receptivity disturbances will behave as they move downstream, the best insight into how they will behave comes from comparing the slip velocity, U_f, and the pressure gradient, β. Figure 6.7 shows a comparison of the slip velocity and pressure gradient for the parabola and the Rankine body as a function of x, the coordinate along the body's surface from the leading edge, for the case $A = 0.1$.

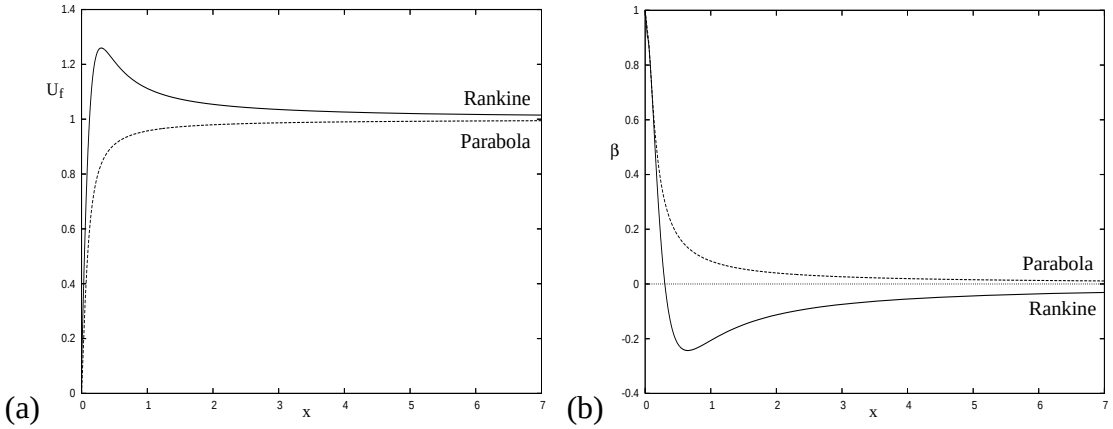

Figure 6.7: Plot of (a) $U_f(x)$ and (b) $\beta(x)$ for a Rankine body and a parabola for $A = 0.1$.

The maximum value of the slip velocity for the Rankine body occurs close to where the parabola's slip velocity becomes constant. Similarly the minimum in β occurs near the point where the parabola's pressure gradient turns sharply and tends to zero. The pressure gradient for the parabola tends to zero faster than for the Rankine body, which perhaps is not as expected, as the curvature of the Rankine body is less than the parabola far downstream, see figure 6.6.

In a way similar to the treatment of the curvature of the two bodies, we can prove that the pressure gradient for the parabola tends to zero faster than that of the Rankine body, by using the large x asymptotic form of $\beta(x)$. From §6.1.1 we found that for the Rankine body $\alpha = A$ and $\gamma = A^2$, hence from (2.45), we can write the large ξ form of $\beta_R(\xi)$ as

$$\beta_R(\xi) \sim -\frac{2A}{\xi} - 4A^2\frac{\ln\xi}{\xi^2} + O(\xi^{-3}\ln^2(\xi)).$$

The corresponding large ξ form of $\beta_P(\xi)$ for the parabola comes from (5.6) and is

$$\beta_P(\xi) \sim \frac{S}{2\xi} - \frac{S^2}{4\xi^2} + \frac{S^3}{8\xi^3} + O(\xi^{-4}).$$

Hence using the fact that $\xi \sim x$ as $\xi \longrightarrow \infty$ for both bodies, and that $S = 3A/2$, we see that to leading order

$$\begin{aligned} \beta_R &= -\frac{2A}{x}, \\ \beta_P &= \frac{3A}{4x}. \end{aligned}$$

Thus both pressure gradients tend to zero like $1/x$, however the pressure gradient on the parabola will tend to zero faster than for the Rankine body, due to the smaller constant multiplying the $1/x$ term. These expressions also show the difference in sign of β for the Rankine body and the parabola as shown in figure 6.7(b).

Calculating the slip velocity, and hence the pressure gradient on a MSE is a non-trivial exercise, but is possible via a full numerical inviscid simulation. However, we would like to gain an analytic approximation to the slip velocity of the form (2.41). A possible method to calculate this would be to increase the number of sources on the real axis, until the streamline through the stagnation point resembles the geometry of the MSE. The next section on slender body theory discusses how this is possible.

6.2.3 Slender body theory

Consider first the flow produced by a source, strength $2\pi K$, at $z = \pi K$ and a sink, strength $2\pi K$, at $z = 2\pi K$ in a uniform stream of unit strength. The complex potential, w, for this flow is

$$w(z) = z + K\ln(z - \pi K) - K\ln(z - 2\pi K), \tag{6.30}$$

where $z = x + iy$.

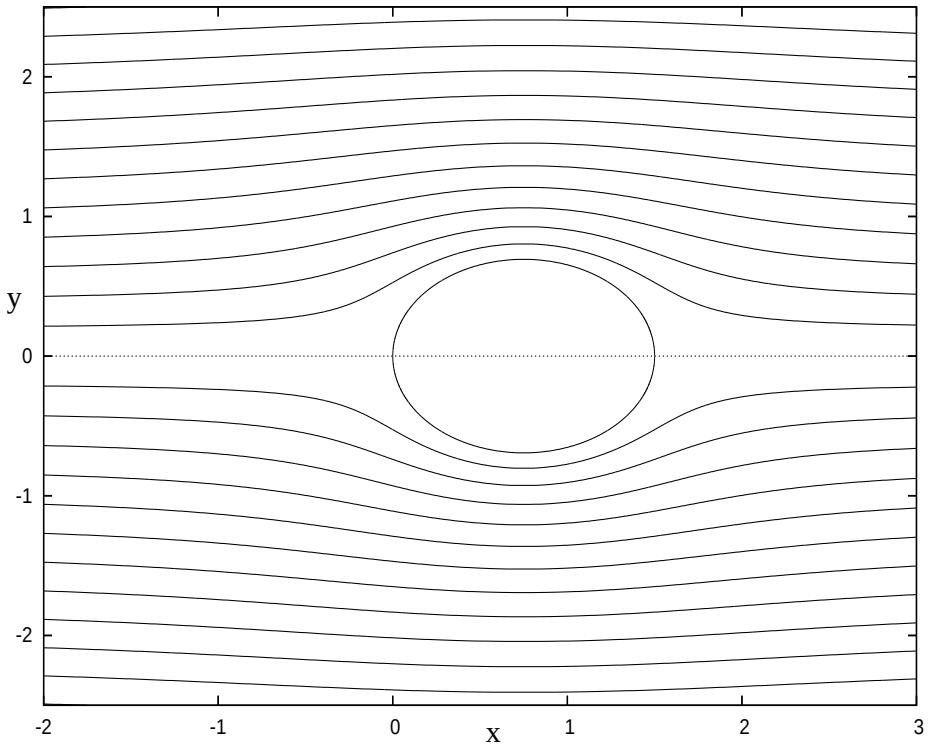

Figure 6.8: Plot of the streamlines for the complex potential (6.30) for the case $K = 1$.

The streamlines for this flow when $K = 1$ are shown in figure 6.8. We can see that this flow produces a closed streamline, which can be replaced by a solid body, so the flow can be thought of as the uniform flow of unit strength, past that body. Slender body theory extends this idea to put a continuous distribution of sources and sinks on the real axis to produce a streamline which matches, or in some cases, approximates, the surface of the body we wish to model the flow around.

Here we consider a symmetric body, of length $2b$, with the uniform flow at zero angle of attack, although this theory can be extended to incorporate cambered bodies and bodies at non-zero attack angles.

Following Thwaites (1964), the complex potential for a line source of strength $m\delta x_1$ at $z = z_1 = x_1 + iy_1$ is

$$w(z) = \frac{m\delta x_1}{2\pi} \ln(z - z_1).$$

If we consider this line source to be on $y_1 = 0$, and integrate over the continuous distribution of sources in the interval $x_1 \in [0, 2b]$, we have

$$w(z) = Uz + \int_0^{2b} \frac{m(x_1)}{2\pi} \ln(z - x_1) dx_1, \tag{6.31}$$

where the Uz term is the complex potential for a uniform stream of strength U, and the length of the body we wish to model is $2b$. For the body formed to be closed, we also require

$$\int_0^{2b} m(x_1) dx_1 = 0. \tag{6.32}$$

However this does not have to hold if we consider bodies similar to the Rankine body which tend to a flat plate downstream, but this is only relevant for $b \longrightarrow \infty$.

The velocity field produced by the presence of the body will have the form

$$\mathbf{u} = (U + u)\hat{\mathbf{x}} + v\hat{\mathbf{y}},$$

where (u, v) is the perturbed velocity in the $\hat{\mathbf{x}}$ and $\hat{\mathbf{y}}$ directions respectively, which are unit vectors in the horizontal and vertical directions respectively. On the body, inviscid theory says that the velocity $\mathbf{u}$ is tangential to the body's surface, so the boundary condition is

$$\left.\frac{dy}{dx}\right|_{y=F(x)} = \frac{dF}{dx} = \frac{v}{U + u},$$

where $y = F(x) \ll 1$ is the equation for the upper surface of the body. For a slender body we expect only small changes in the horizontal velocity, hence we expect $u \ll U$, hence

$$\frac{dF}{dx} = \frac{v}{U},$$

approximately. Using the fact that $u - iv = dw/dz$, we can write this boundary condition as

$$Im\left(\frac{dw}{dz}\right) = -U\frac{dF}{dx}. \tag{6.33}$$

Differentiating (6.31) with respect to z gives

$$u - iv = \frac{dw}{dz} = U + \int_0^{2b} \frac{m(x_1)}{2\pi}\frac{1}{z - x_1}dx_1,$$

which on the introduction of $z = x + iy$ we find that the imaginary part gives

$$v = \frac{1}{2\pi}\int_0^{2b} \frac{m(x_1)y}{(x - x_1)^2 + y^2}dx_1.$$

Evaluating this on $y = F(x)$ we find

$$\frac{1}{2\pi}\int_0^{2b} \frac{m(x_1)F}{(x - x_1)^2 + F^2}dx_1 = U\frac{dF}{dx}. \tag{6.34}$$

We split this integral up into three integrals, to carefully treat the integrand around the point $x_1 = x$, giving

$$\frac{F(x)}{2\pi}\left(\int_0^{x-\delta} \frac{m(x_1)}{(x - x_1)^2 + F^2}dx_1 + \int_{x+\delta}^{2b} \frac{m(x_1)}{(x - x_1)^2 + F^2}dx_1 + \int_{x-\delta}^{x+\delta} \frac{m(x_1)}{(x - x_1)^2 + F^2}dx_1\right) = U\frac{dF}{dx},$$

where $0 < \delta$.

For $F \ll 1$, the first two integrals are much smaller than the third, as in the third integral, the integrand is very large near $x = x_1$, hence we can ignore the contribution from the first two integrals. The third integral, under the approximation that δ is small compared with $2b$, but $\delta \gg F(x)$, can be approximated using a Taylors series expansion for $m(x_1)$,

$$m(x_1) = m(x) + (x_1 - x)\left.\frac{dm}{dx_1}\right|_{x_1=x} + O((x_1 - x)^2),$$

for $x_1 \in [x - \delta, x + \delta]$.

Hence to leading order we have

$$\frac{F(x)m(x)}{2\pi}\int_{x-\delta}^{x+\delta} \frac{dx_1}{(x_1 - x)^2 + F^2} = U\frac{dF}{dx},$$

which can be integrated to give

$$\frac{m(x)}{2\pi}\left(\tan^{-1}\left(\frac{\delta}{F}\right)-\tan^{-1}\left(-\frac{\delta}{F}\right)\right)=U\frac{dF}{dx}.$$

In the slender body limit ($F \longrightarrow 0$ with δ fixed), we find

$$m(x)=2U\frac{dF}{dx}. \tag{6.35}$$

Thus given any slender body geometry, we can find the source distribution to approximate the flow around this body in a uniform flow.

6.2.4 Approximating the MSE using Slender body theory

Using the analysis from §6.2.3, we write the dimensional complex potential for the inviscid flow past a MSE as

$$w^*=U_\infty z^*+\frac{U_\infty}{\pi}\int_0^\infty \frac{dF^*}{dx_1^*}\ln(z^*-x_1^*)dx_1^*,$$

where $y^* = F^*(x^*)$ is the dimensional form of the equation for the MSE's surface and U_∞ is the free-stream velocity. Introducing the non-dimensional quantity $z = \omega z^*/U_\infty$, the dimensionless body geometry $F = \omega F^*/U_\infty$, and changing the integration variable to $x_1 = \omega x_1^*/U_\infty$, gives

$$w^*=\frac{U_\infty^2}{\omega}z+\frac{1}{\pi}\frac{U_\infty^2}{\omega}\int_0^\infty \frac{dF}{dx_1}\left(\ln(z-x_1)+\ln\left(\frac{U_\infty}{\omega}\right)\right)dx_1.$$

We define the dimensionless complex potential $w = \omega w^*/U_\infty^2$, and use the fact that the upper surface of the MSE in Cartesian coordinates is given by $y_c = F(x_c)$, where

$$F(x_c)=\begin{cases} b\left(1-\left(\frac{a-x_c}{a}\right)^m\right)^{\frac{1}{2}} \quad m=2+\left(\frac{x_c}{a}\right)^2 & x_c<a \\ b & x_c>a \end{cases}, \tag{6.36}$$

where a and b are defined in §6.2.1, to simplify the complex potential to

$$w=z+\frac{1}{\pi}\int_0^a \frac{dF}{dx_1}\ln(z-x_1)dx_1+\frac{b}{\pi}\ln\left(\frac{U_\infty}{\omega}\right). \tag{6.37}$$

As a complex potential is defined up to an arbitrary constant, the constant term from (6.37) can be dropped without loss of generality. The upper limit of integration has been changed from ∞ to a, because $dF/dx_1 = 0$ for $x_1 > a$.

The velocity field is calculated from (6.37), and is

$$u - iv = \frac{dw}{dz} = 1 + \frac{1}{\pi}\int_0^a \frac{dF}{dx_1}\frac{1}{z - x_1}dx_1. \tag{6.38}$$

Due to the assumptions of slender body theory, (6.37) and (6.38) do not give the exact flow past the body $y_c = F(x_c)$. This can be seen by looking at the flow close to the nose, where the slip velocity $\longrightarrow \infty$ (see §6.2.5).

Equations (6.37) and (6.38) can be integrated by parts to make them more convenient to use, giving

$$u - iv = \frac{dw}{dz} = 1 + \frac{b}{\pi((x_c - a) + iy_c)} - \frac{1}{\pi}\int_0^a \frac{F(x_1)}{((x_c - x_1) + iy_c)^2}dx_1, \tag{6.39}$$

$$w = z + \frac{b}{\pi}\ln((x_c - a) + iy_c) + \frac{1}{\pi}\int_0^a F(x_1)\frac{(x_c - x_1) - iy_c}{(x_c - x_1)^2 + y_c^2}dx_1 + \frac{b}{\pi}\ln\left(\frac{U_\infty}{\omega}\right). \tag{6.40}$$

From (6.40) it is now straightforward to write down the velocity potential, ϕ, and the stream function, ψ, as

$$\phi = x_c + \frac{b}{2\pi}\ln((x_c - a)^2 + y_c^2) + \frac{1}{\pi}\int_0^a \frac{F(x_1)(x_c - x_1)}{(x_c - x_1)^2 + y_c^2}dx_1 + B, \tag{6.41}$$

$$\psi = y_c + \frac{b}{\pi}\arg((x_c - a) + iy_c) - \frac{y_c}{\pi}\int_0^a \frac{F(x_1)}{(x_c - x_1)^2 + y_c^2}dx_1, \tag{6.42}$$

where $B = b/\pi \ln(U_\infty/\omega)$ is a constant.

Although we wish to calculate the flow around the MSE, the actual body shape formed by the slender wing theory is not quite that of the MSE. We can see this more clearly if we consider the v component of velocity given by (6.38),

$$v = \frac{y_c}{\pi}\int_0^a \frac{dF}{dx_1}\frac{1}{(x_c - x_1)^2 + y_c^2}dx_1.$$

If we consider the limit as $x_c \longrightarrow \infty$, then $y_c \longrightarrow b$, and

$$v \sim \frac{b}{\pi}\int_0^a \frac{dF}{dx_1}\left(\frac{1}{x_c^2} + \frac{2x_1}{x_c^3} + O(x_c^{-4})\right)dx_1,$$

$$v \sim \frac{b^2}{\pi}\frac{1}{x_c^2} + O(x_c^{-3}).$$

Hence we see that v only tends to 0 as x_c gets large, whereas on an MSE, v would be identically zero on the flat plate part, and hence the slender body approximation only tends to a flat plate far downstream, whereas the MSE is exactly a flat plate. Thus rather than just assuming the body geometry is that of a MSE, we calculate the body shape found

by the theory. This is done by solving $\psi = C$ where C is a constant, and ψ is given in (6.42). The streamline corresponding to the surface of the body is obtained by considering the body far downstream, $x_c \longrightarrow \infty$, when $y_c \longrightarrow b$. From (6.42), $\psi_C \longrightarrow b$ in this limit, and hence the streamline corresponding to the upper surface of the body is given by the solution of

$$y_c + \frac{b}{\pi}\arg((x_c - a) + iy_c) - \frac{y_c}{\pi}\int_0^a \frac{F(x_1)}{(x_c - x_1)^2 + y_c^2}dx_1 = b. \tag{6.43}$$

Care must be taken with the choice of the argument function. This takes the form

$$\begin{aligned}
\arg((x_c - a) + iy_c)) &= \tan^{-1}\left(\frac{y_c}{(x_c - a)}\right) \quad \text{for} \quad x_c > a, \\
\arg((x_c - a) + iy_c)) &= \pi - \tan^{-1}\left(\frac{y_c}{|x_c - a|}\right) \quad \text{for} \quad x_c < a.
\end{aligned}$$

Equation (6.43) is not valid in the vicinity of the leading edge, and in this region we approximate the equation of the surface by a parabola of the form

$$y_c = \left(\frac{2b^2}{a}x_c\right)^{\frac{1}{2}}.$$

The reason that (6.43) is not valid in the vicinity of the leading edge, is because the slender body assumption that $dF/dx_c \ll 1$ is no longer correct. As we approach the leading edge of a blunt body such as a MSE, the gradient of the surface becomes infinite, and hence violates this assumption. Figures 6.9 and 6.10 show the breakdown of (6.43) as the leading edge is approached, and they also show the matching between the leading edge parabolic solution and the slender body solution. For the smaller, $20 : 1$, aspect ratio in figure 6.9, we see a relatively small matching region between the two solutions, but as the aspect ratio increases to $100 : 1$ in figure 6.10 we see that the length of the matching region, between the two solutions, increases. This is due to the slender body theory becoming a better approximation to the MSE, because a larger aspect ratio means that the body is more slender, i.e. the gradient of the surface is smaller. This leading edge region, and the breakdown of the slender body theory are discussed in more detail in §6.2.5, when we consider the slip velocity and pressure gradient produced by the slender body theory.

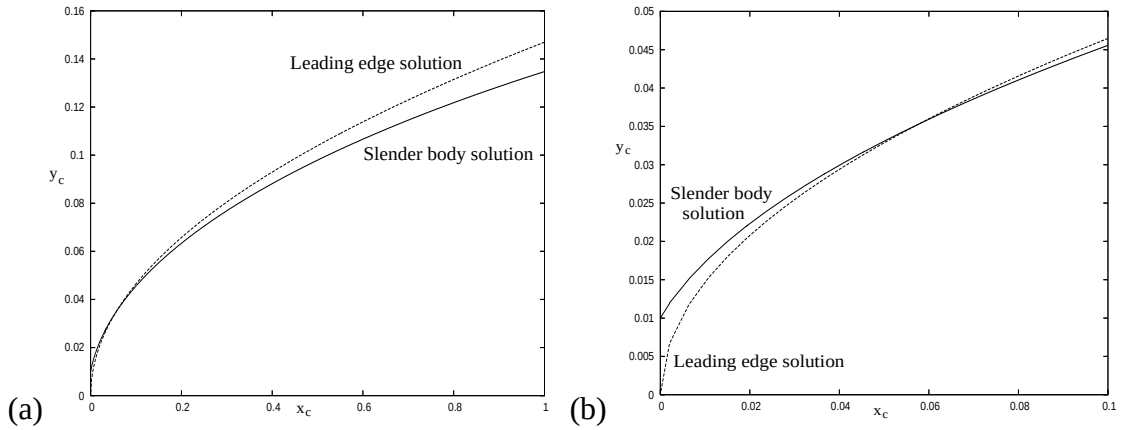

Figure 6.9: Plot of the matching between the leading edge parabolic solution (dotted line) and the slender body solution (solid line) for a $20 : 1$ MSE. Figure (b) shows a more detailed plot of figure (a).

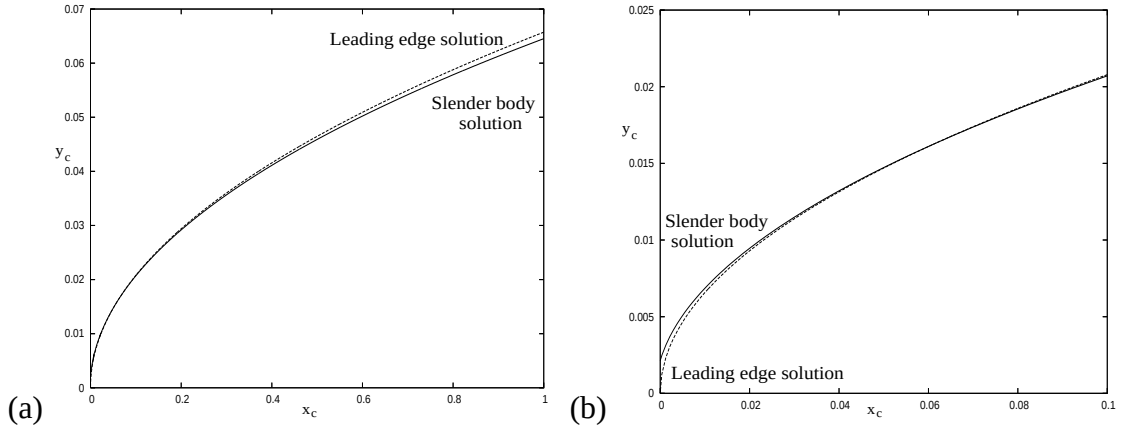

Figure 6.10: Plot of the matching between the leading edge parabolic solution (dotted line) and the slender body solution (solid line) for a $100 : 1$ MSE. Figure (b) shows a more detailed plot of figure (a).

A selection of body shapes for different aspect ratios is plotted in figure 6.11, and in figure 6.12 we see two different aspect ratios plotted with the corresponding MSE that they are approximating. In both these figures, the leading edge is approximated by a parabolic body. We see that as the aspect ratio increases, the slender body approximation becomes much more accurate. This is because the higher aspect ratio means the body is becoming more 'slender' in the sense that dF/dx_c is becoming much smaller. The agreement between the MSE and the higher aspect ratio slender body theory can also be

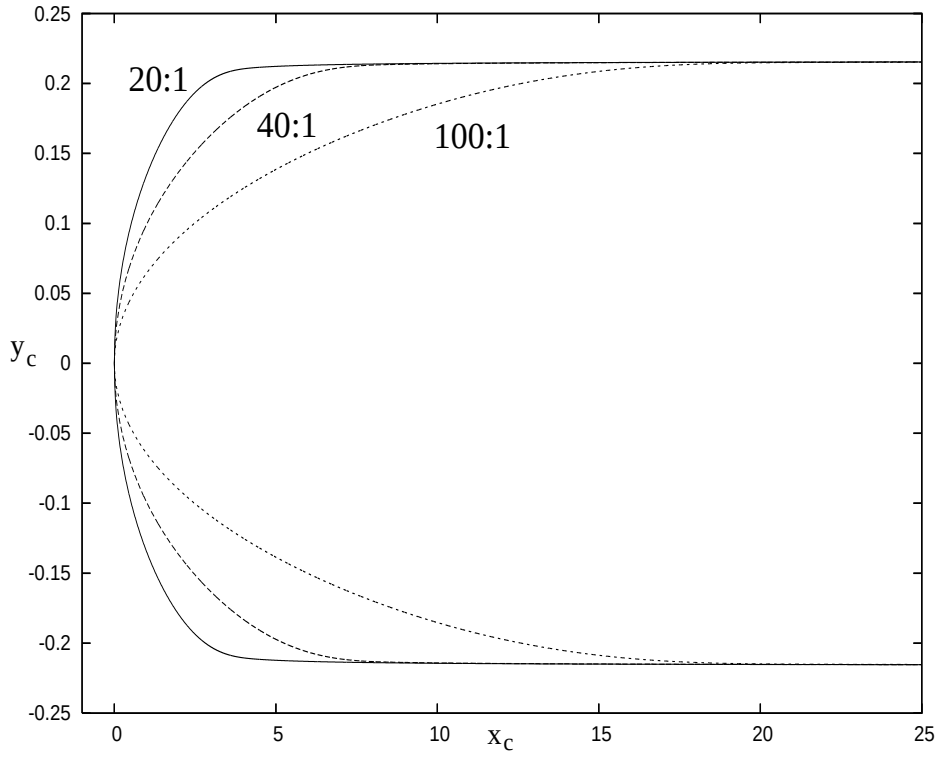

Figure 6.11: Plot of the approximations to the MSE for the three different aspect ratios, $20:1$, $40:1$ and $100:1$.

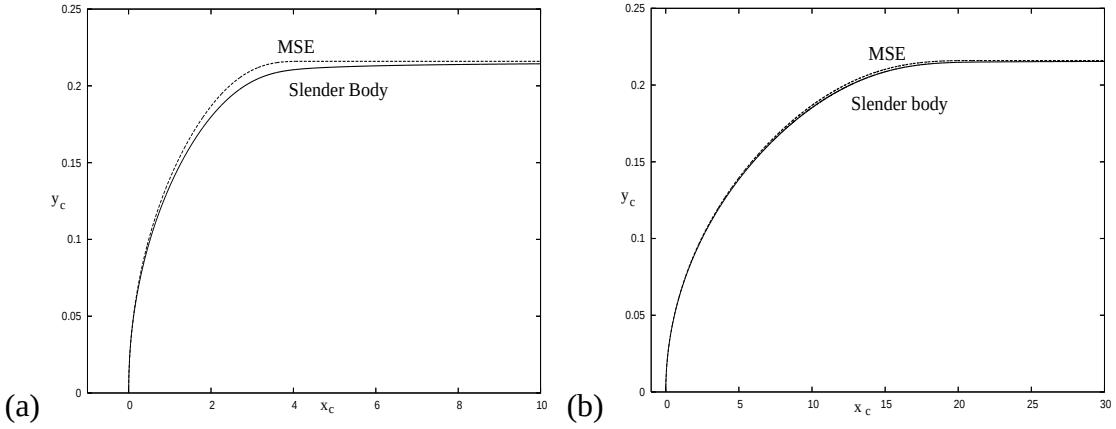

Figure 6.12: Plot of a comparison of the upper body surface for the MSE and the slender body approximation to the MSE for the aspect ratios (a) $20:1$ and (b) $100:1$.

seen in figure 6.13, which shows a plot of the curvature for the two aspect ratios, $20:1$ and $100:1$, where the curvature κ is defined by (6.28). We see that for the $20:1$ aspect ratio, the MSE and the slender body have good agreement up to the point where the curvature

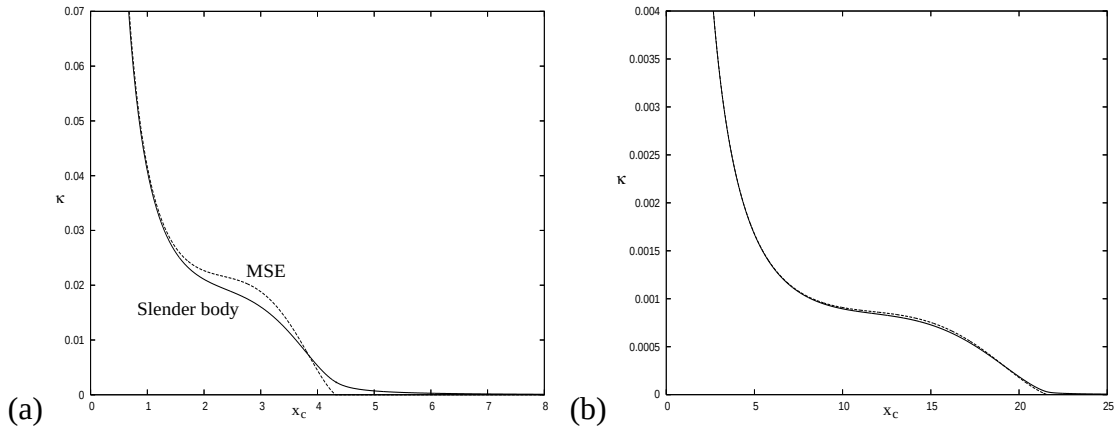

Figure 6.13: Plot of a the curvature comparing the slender body theory (solid line) with the MSE (dotted line) for the aspect ratios (a) $20:1$ and (b) $100:1$.

starts to become constant, but then the slender body's curvature tends to zero at a more constant rate than the MSE. For the $100:1$ MSE on the other hand, we observe very good agreement between the MSE and the slender body, for all x_c considered.

6.2.5 Slip velocity and pressure gradient

The steady slip velocity, U_f, on a MSE is given by

$$U_f = (u^2 + v^2)^{\frac{1}{2}}, \tag{6.44}$$

where u and v are given by

$$\begin{aligned} u &= 1 + \frac{1}{\pi}\left(\frac{b(x_c-a)}{(x_c-a)^2+y_c^2} - \int_0^a \frac{F(x_1)((x_c-x_1)^2-y_c^2)}{((x_c-x_1)^2+y_c^2)^2}dx_1\right), \\ v &= \frac{y_c}{\pi}\left(\frac{b}{(x_c-a)^2+y_c^2} + 2\int_0^a \frac{F(x_1)(x_1-x_c)}{((x_c-x_1)^2+y_c^2)^2}dx_1\right). \end{aligned}$$

If we consider the complex form of the velocity (6.39) evaluated at $x_c = 0$,

$$u - iv = 1 - \frac{b}{\pi a} - \frac{1}{\pi}\int_0^a \frac{F(x_1)}{x_1^2}dx_1, \tag{6.45}$$

we find that for blunt bodies, i.e. for bodies where there is no discontinuity in curvature at the nose, we get infinite velocities at this point, and hence we need a local solution about the nose, which has to be matched to the slender body solution. The MSE is a blunt body,

and the small x_c expansion of (6.36) is

$$F(x_c) \sim s_1 x_c^{\frac{1}{2}} + s_3 x_c^{\frac{3}{2}} + s_5 x_c^{\frac{5}{2}} + s_7 x_c^{\frac{7}{2}} + O(x_c^{\frac{9}{2}}), \tag{6.46}$$

where

$$\begin{aligned} s_1 &= b\left(\frac{2}{a}\right)^{\frac{1}{2}}, \\ s_3 &= -\frac{b}{4a}\left(\frac{2}{a}\right)^{\frac{1}{2}}, \\ s_5 &= \frac{7b}{32a^2}\left(\frac{2}{a}\right)^{\frac{1}{2}}, \\ s_7 &= -\frac{41b}{128a^3}\left(\frac{2}{a}\right)^{\frac{1}{2}}. \end{aligned}$$

Local solution near the nose

For the local solution near the nose, we introduce scaled variables, scaled on the dimensionless nose radius, $r = r_{MSE}$, given by (6.25). The local solution, to leading order, is flow past a parabola as discussed in detail in chapter 5, so we just present the results here.

The variables, Z, in the nose region are related to the slender body variables, z, by

$$z = \frac{r}{2}(Z^2 + 1),$$

and the complex potential, w, in the vicinity of the nose is

$$w = \frac{1}{2}Ur(Z - i)^2,$$

where the surface of the body is given by $Im(Z) = 1$ and U is a constant. Thus we can write the slip velocity in terms of $x_c = Re(z)$ as

$$U_f = \frac{U x_c^{\frac{1}{2}}}{(x_c + \frac{r}{2})^{\frac{1}{2}}}. \tag{6.47}$$

This solution is then matched with the slender body solution (6.39) to give

$$U = 1 - \frac{b}{\pi a} + \frac{s\sqrt{2b}}{\pi a} - \frac{1}{\pi}\int_0^a \left(F - b\left(\frac{2}{a}\right)^{\frac{1}{2}} x_1^{\frac{1}{2}}\right)\frac{1}{x_1^2}dx_1, \tag{6.48}$$

From (6.44) it is straightforward to plot the slip velocity as a function of x_c, however in previous chapters, we plotted the slip velocities with respect to ξ which is defined in

(2.33). To make the calculation of ξ more straightforward, we change the variable of integration from x to x_c, where x is measured along the body. Hence we have

$$\xi = \int_0^{x_c} U_f(x_c) \left(1 + \left(\frac{dy_c}{dx_c}\right)^2\right)^{\frac{1}{2}} dx_c. \tag{6.49}$$

In the local leading edge region, we find $\xi = Ux_c$, where U is given by (6.48). Elsewhere we evaluate the integral by means of the trapezoidal rule. Figure 6.14(a) shows the

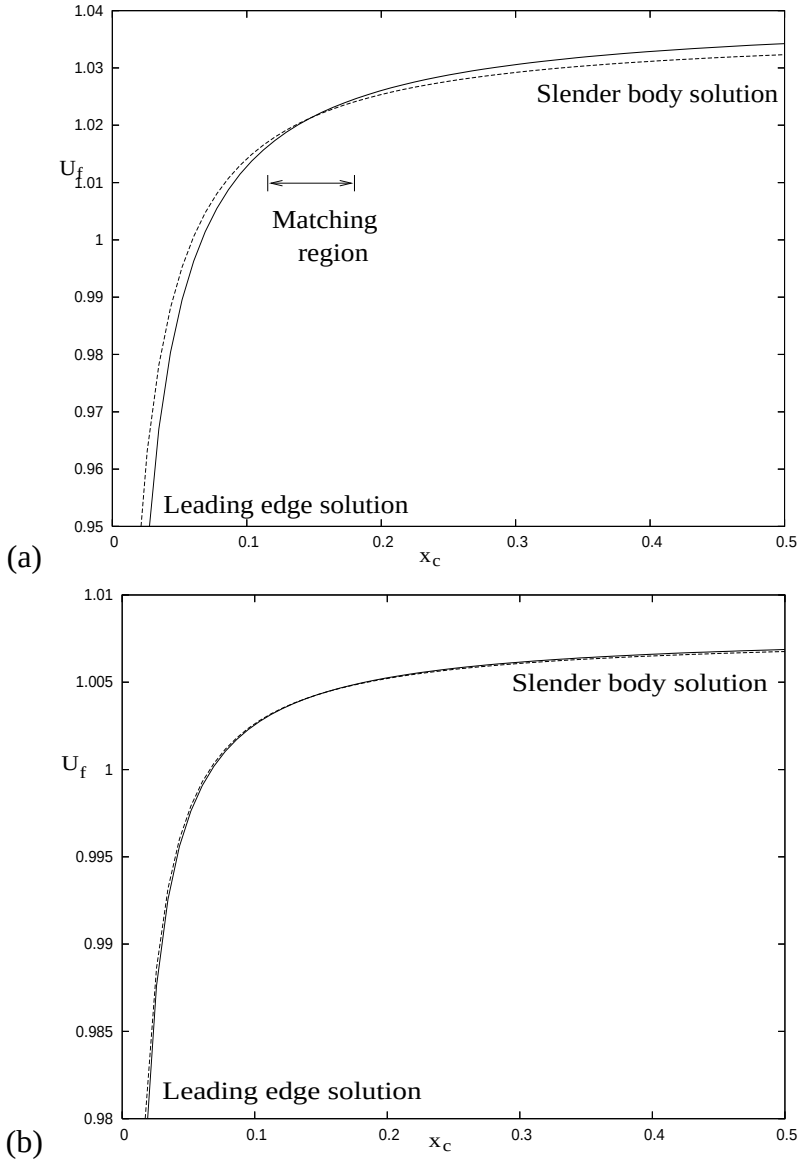

Figure 6.14: Plot of the slip velocity on (a) a $20 : 1$ MSE and (b) a $100 : 1$ MSE as a function of x_c, showing the matching region between the leading edge region (solid line) and the slender body theory (dotted line).

matching region between the slender body theory, and the solution in the nose region for a $20 : 1$ MSE. The overlap region is very hard to see, due to the chosen large value of $\epsilon = (90 \times 10^{-6})^{\frac{1}{6}}$. This value is the same as that used in figure 6.15, and is chosen so that results can be easily compared with those of Wanderley and Corke (2001). The size of this over lap region increases as the aspect ration of the MSE increases, and this can be seen in figure 6.14(b) which shows the two slip velocities for a $100 : 1$ MSE. For the $100 : 1$ MSE, the overlap region is hard to see because the two solutions are close to each other over the whole region considered, however it is clearer than for the $20 : 1$ MSE.

Figure 6.15 shows a plot of the slip velocity from the slender body theory approximation of the MSE for different aspect ratios, as a function of ξ for the case $\epsilon^6 = 90 \times 10^{-6}$. The constant ϵ only affects the unsteady solution, whereas the steady solution is independent of ϵ, however the value of ϵ enters the streamwise length scale ξ, and hence we have to consider it in the steady solution too. The slip velocity is made up of the two solutions, given by (6.44) in the main region, and (6.47) close to the nose. Figure 6.15(a) shows the slip velocity, as it rises from 0 at $\xi = 0$, however on this scale, we see very little detail of the curves outside the nose region, as their maximums are actually quite small. Thus figure 6.15(b) shows a close up of the curves around $U_f = 1$, where we can see a rapid increase in the slip velocity until it reaches a value close to its maximum, and then a slow growth until it reaches it's maximum, before decaying away to 1. The value of ξ where the maximum occurs increases as the aspect ratio increases, and also the maximum value of U_f itself decreases. The maximum value of U_f and its corresponding ξ value can be see in table 6.7. For the smaller aspect ratios, the maximum is reached earlier compared to the larger aspect ratios, and also the slip velocity tends to 1 faster for the smaller aspect ratios. The results presented in figure 6.15 are calculated with $\epsilon^6 = 90 \times 10^{-6}$, however changing the value of ϵ doesn't affect the shape of the curves, all this affects is the value of ξ, i.e. changing ϵ acts like multiplying ξ by a function of ϵ. The steady base flow would be independent of ϵ if it were plotted against the variable $x_w = Rex_c/R_L$, used by Wanderley and Corke (2001), where $Re = \epsilon^{-6}$ and R_L is the Reynolds number based on the length of the body. The reason we do not use this variable here is because,

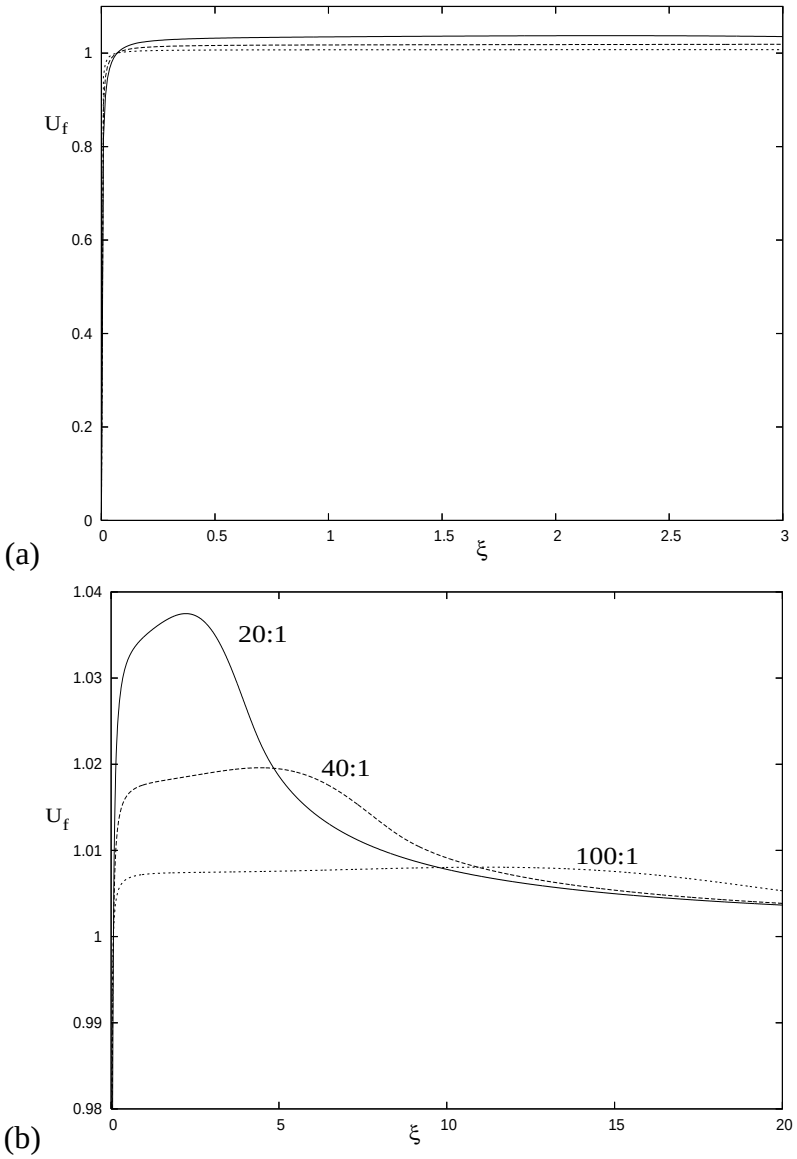

Figure 6.15: Plot of the slip velocity from the slender body theory approximation to the MSE as a function of ξ, for the aspect ratios $20 : 1$, $40 : 1$ and $100 : 1$, and with $\epsilon^6 = 90 \times 10^{-6}$. Figure (b) is a more detailed plot of figure (a).

our analysis in the leading edge region was non-dimensionalised using a different length scale to Wanderley and Corke, which left the ϵ scaling in. To keep the variables used in this section consistent with the variables from chapters 4 and 5, we decided against using the x_w variable.

Experimentalists typically report pressure distributions rather than fluid velocities, hence we don't have any experimental data to compare our results with. However a more

$a:b$	$\xi_{\max}$	$U_f(\xi_{\max})$
$20:1$	2.223	1.037
$40:1$	4.447	1.020
$100:1$	11.146	1.008

Table 6.7: Values of the maximum value of U_f for the MSE for the case $\epsilon^6 = 90 \times 10^{-6}$ and the corresponding value of $\xi_{\max}$.

suitable quantity to measure in experiments is the pressure on the surface of the body, and it is this which Wanderley and Corke (2001) compares in their numerical model. We define the pressure coefficient, C_p to be

$$C_p = \frac{2(p^* - p^*_\infty)}{\rho U^2_\infty}, \tag{6.50}$$

where p^* is the dimensional pressure on the plate and p^*_∞ is the dimensional pressure as $x_c \longrightarrow \infty$. The numerical calculations of C_p here agree with those of Wanderley and Corke (2001), but there is a typing error in equation (3) of Wanderley and Corke, and a factor of 2, present in (6.50), is missing from their equation for C_p. The form of the surface pressure can be found by considering the steady part of the slip velocity in (2.15), and integrating with respect to x to give

$$p = -\frac{1}{2}U_f^2 + C.$$

This form of the non-dimensional pressure is the same as that given by Bernoulli's equation along the streamline at the surface of the airfoil. Putting this pressure into dimensional form, and then evaluating it far downstream, where $U_f \longrightarrow 1$, to find p^*_∞ gives the two equations

$$\begin{aligned} p^* &= -\frac{1}{2}\rho U^2_\infty U_f^2 + C', \\ p^*_\infty &= -\frac{1}{2}\rho U^2_\infty + C', \end{aligned}$$

where $C' = \rho U^2_\infty C$.

Substituting these dimensional pressures into (6.50) gives the pressure coefficient as

$$C_p = 1 - U_f^2. \tag{6.51}$$

The resultant plots for C_p using the slender body theory are given in figure 6.16(b), and they are of identical shape to the ones given in figure 4 of Wanderley and Corke (2001), which is also presented in figure 6.16(a). The pressure distribution for the slender body

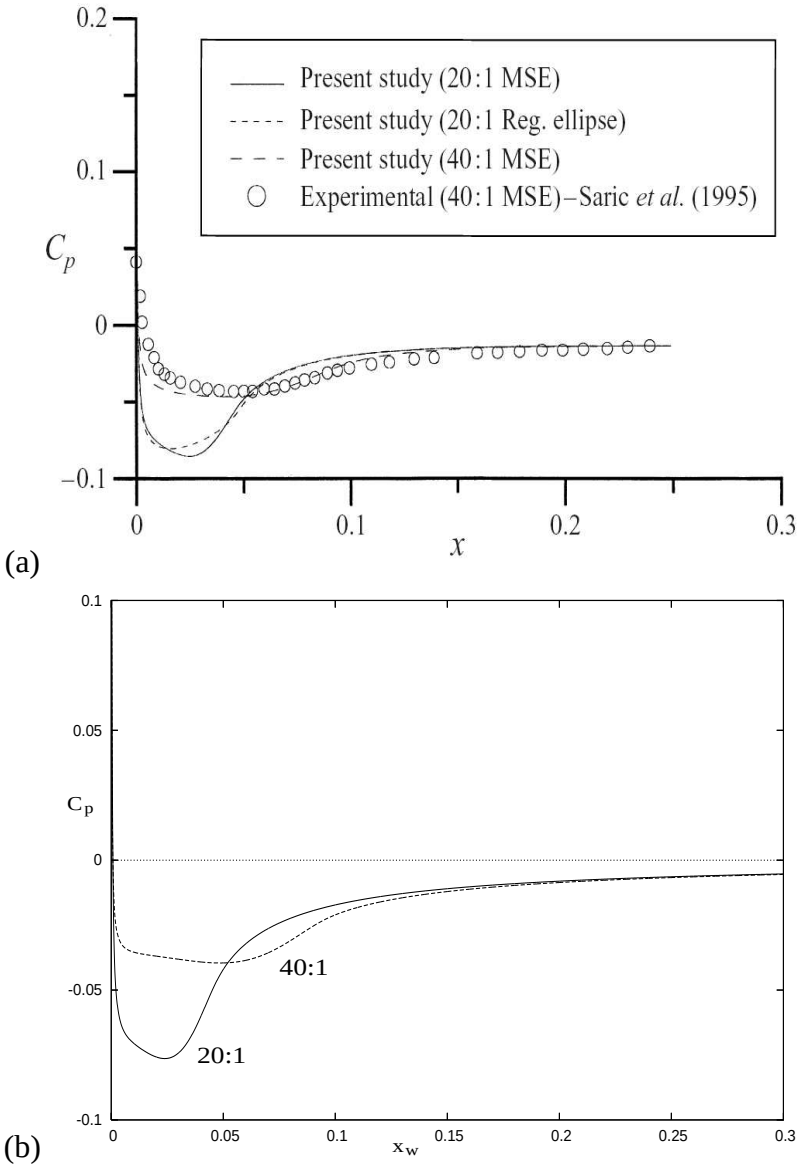

Figure 6.16: Figure showing the surface pressure distribution, C_p on a MSE as a function of x_w, which is the streamwise variable of Wanderley and Corke (2001) defined in §4.6.3. (a) is figure 4 taken from Wanderley and Corke, and (b) is the same plot produced with our slender body theory. The 'present study' shown in figure (a) refer to the numerical solutions of Wanderley and Corke.

approximation to the $20:1$ MSE in figure 6.16(b) is compared to the solid line in 6.16(a), and the $40:1$ aspect ratio MSE result is compared to the long dashed line in 6.16(b). For

the $20 : 1$ case, we see that the minimum of the pressure distribution is approximately -0.09 for Wanderley and Corke's work, and -0.075 for the slender body approximation. Similarly for the $40 : 1$ MSE, the minimum pressure distributions are approximately -0.05 for Wanderley and Corke's work, and -0.04 for the slender body approximation. Thus as the aspect ratio increases, the body becomes more slender, and hence the slender body approximation gives a better approximation to the MSE.

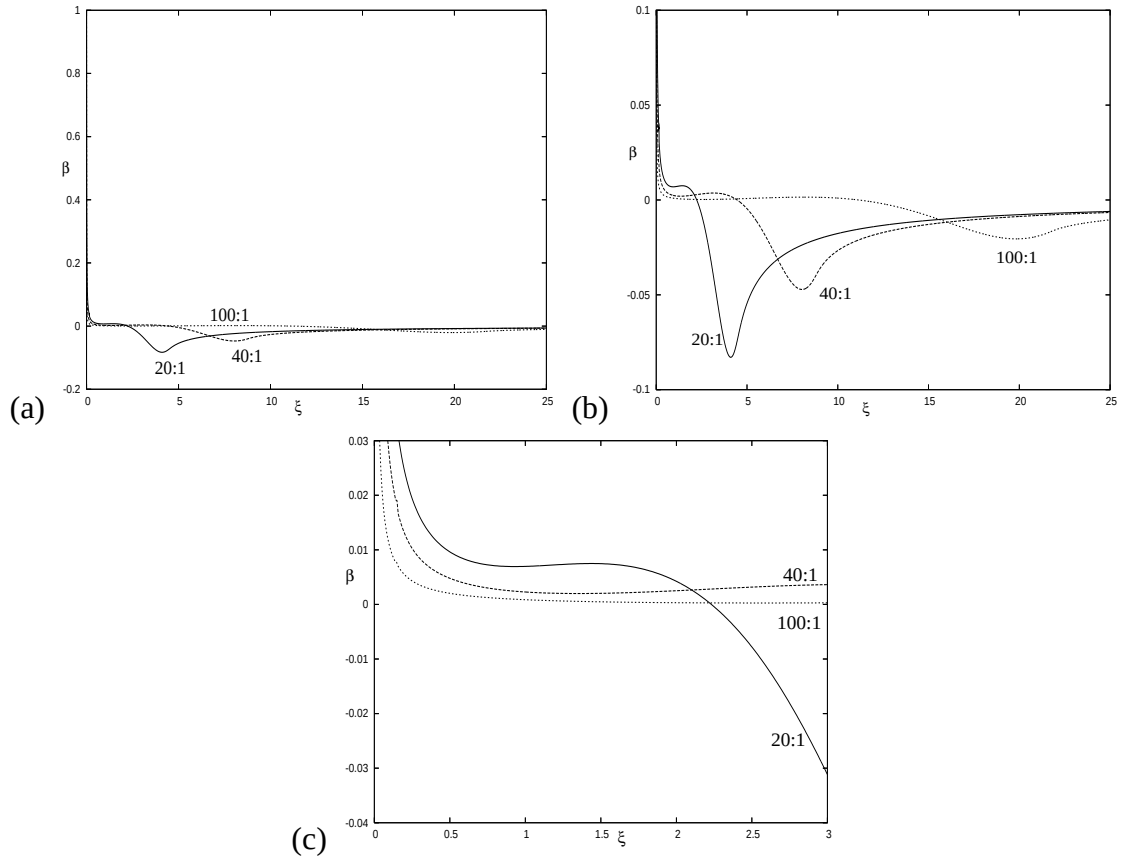

Figure 6.17: Plot of the pressure gradient, β, for the slender body theory approximation to the MSE as a function of ξ, for the aspect ratios $20 : 1$, $40 : 1$ and $100 : 1$. Figure (b) is a more detailed plot of figure (a). Figure (c) shows a close up of figure (b) to make the first minimum in β clearer.

Now that we have calculated the slip velocity for a MSE, we can now convert this into the pressure gradient, β given by (2.36). By changing variables from ξ to x_c to simplify the algebra, we find

$$\beta = \frac{2\xi}{U_f^2}\left(1 + \left(\frac{dy_c}{dx_c}\right)^2\right)^{-\frac{1}{2}} \frac{dU_f}{dx_c}. \tag{6.52}$$

The form of β in the nose region ($x_c \ll r$) can be found simply as

$$\beta = \frac{r}{2x_c + r},$$

where $r = r_{MSE} = b^2/a$. The resulting calculations for β can be seen in figure 6.17. As for the slip velocity plots, figure 6.17(a) shows the pressure gradient as it decays from 1 down to zero, but to get a better view of what is happening around $\beta = 0$, we have plotted figure 6.17(b). As for the Rankine body, we observe a region of favourable pressure gradient close to the nose, and then a region of adverse pressure gradient further downstream. The pressure gradients decay from 1 towards zero, and then reach a minimum value, greater than 0, rise slightly, and then decay to another minimum which is less than 0 before increasing again towards zero. The first minimum for the $20:1$ MSE is seen more clearly in figure 6.17(c). As the aspect ratio is increased, we find that both the minimums are shifted downstream, and that both the values at these minimums are closer to $\beta = 0$. The ξ values for both these minimums and the corresponding values of β are given in table 6.8. As with the slip velocity, a change in the value of ϵ just acts as a scaling factor on the value ξ, and doesn't actually affect the shape of the curves. The link between the

$a:b$	ξ_1	$\beta(\xi_1)$	ξ_2	$\beta(\xi_2)$
$20:1$	0.932	0.006939	4.107	-0.08292
$40:1$	1.356	0.001977	8.034	-0.04768
$100:1$	2.560	0.000264	19.830	-0.02050

Table 6.8: Values of the minimum values of β for the MSE for the case $\epsilon^6 = 90 \times 10^{-6}$ and the corresponding values of ξ_1 and ξ_2.

pressure gradient β and the geometry of the MSE can be seen in figure 6.18, which plots the pressure gradient and the curvature, κ, against the chord length x_c for a $20:1$ MSE. The first minimum which occurs around $x_c = 1$, along with the next maximum, are due to the curvature of the body becoming more constant, and decaying much slower. Once this happens, the pressure gradient becomes adverse, and starts to decay to the second minimum. This second minimum occurs around $x_c = 4$ which is the point at which the curvature is almost 0, and the body resembles that of a flat plate. Over the rest of the body we see the pressure gradient recovering to the value for a flat plate.

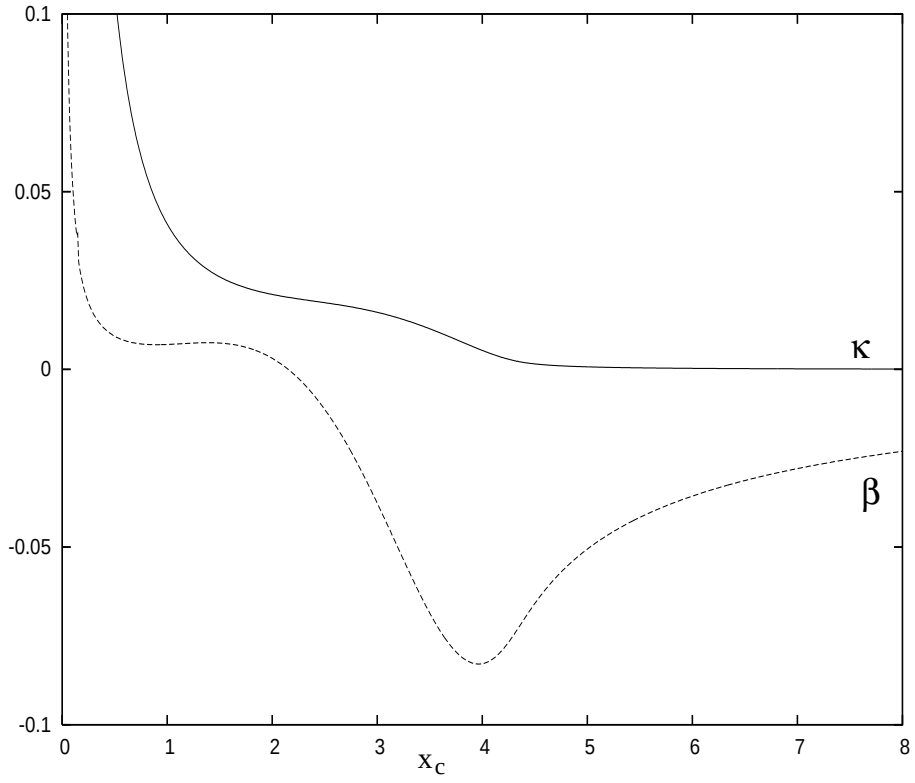

Figure 6.18: Plot of the the pressure gradient, β and the curvature κ for a $20:1$ MSE generated using slender body theory.

In order to use the PSE to calculate the T-S wave growth rate for the MSE, we require the large x form of $U_f(x)$ to find the constant, α multiplying the x^{-1} term in (2.41). In the analysis below, the variable x is again the streamwise variable along the body, and x_c is the usual Cartesian coordinate. The large x_c form of (6.44) is

$$U_f \sim 1 + \frac{b}{\pi x_c} + \left(\frac{ab}{\pi} - \frac{1}{\pi} \int_0^a F(x_1) dx_1 \right) \frac{1}{x_c^2} + O\left(x_c^{-3}\right), \tag{6.53}$$

where we have used the fact that

$$y_c \sim b - \frac{b^2}{\pi x_c} + O\left(x_c^{-2}\right),$$

as $x_c \longrightarrow \infty$. To write the slip velocity in terms of x, rather than x_c, we use the fact that

$$\frac{dx}{dx_c} = \left(1 + \left(\frac{dy_c}{dx_c} \right)^2 \right)^{\frac{1}{2}},$$

to show that

$$x \sim x_c - \frac{b^4}{6\pi^2 x_c^3} + O\left(x_c^{-4}\right),$$

for large x_c, and consequently that

$$x_c \sim x + \frac{b^4}{6\pi^2 x^3} + O\left(x^{-4}\right),$$

as $x \longrightarrow \infty$. Substituting this into (6.53) gives the large x form of the slip velocity as

$$U_f \sim 1 + \frac{b}{\pi x} + \left(\frac{ab}{\pi} - \frac{1}{\pi}\int_0^a F(x_1)dx_1\right)\frac{1}{x^2} + O\left(x^{-3}\right). \tag{6.54}$$

Thus, comparing (6.54) with (2.41) we see that for the MSE, $\alpha = b/\pi$, which is independent of a, and hence independent of the aspect ratio. This may seem a little counter intuitive, however, we are in a region far from the leading edge of the body, and so the affect of the aspect ratio has diminished. This behavior has been observed before by Nichols (2001), who found that for a body generated by a source and a sink, the $O\left(x^{-1}\right)$ correction term to the slip velocity was in fact the body half thickness divided by π.

Using the fact that $\alpha = b/\pi$, we can calculate the form of the lowest order Lam-Rott eigenmode from (2.70) and (2.87), by setting $j = 1$. This initial mode shape and the initial eigenmode given by $dT_1/d\xi$, where T_1 is given in (2.75), are then used as initial conditions to the PSE (2.102) which can be marched to lower branch to give the eigenmode amplitude there. To complete the calculation of the T-S wave amplitude at lower branch, the receptivity coefficient needs to be calculated. This is done by using the method of Nichols (2001), who compares the asymptotic solution with the full numerical solution in the leading edge region in a part of the complex plane, where the lowest order eigenmode dominates the solution. Nichols conducted this numerical procedure for a source and a sink in a uniform flow, and this method can be extended by adding more sources and sinks along the real axis, until we have the same source distribution as we do for our slender body theory.

6.3 Summary

In this chapter, we have presented T-S wave amplitude calculations at lower branch for a Rankine body, as we did for the parabola in chapter 5. We also presented the method of slender body theory, to approximate the geometry of the MSE, and allow us to calcu-

late the inviscid slip velocity, U_f, and the pressure gradient, β, at the outer edge of the boundary layer.

Unlike the parabola, the Rankine body has a pressure gradient which starts off favourable at the nose, then becomes adverse downstream, tending to zero far downstream. This behaviour moves the neutral stability point upstream of the corresponding flat plate value, and for the Rankine body we also found that as the nose radius increases, the amplitude of the eigenmode, excluding the receptivity coefficient, also increases. However, this combined with the rapid decrease in the receptivity coefficient for the Rankine body produces T-S wave amplitudes which have a double maximum appearance as the nose radius increases, for certain values of ϵ. For small values of ϵ this behaviour is clearly seen, however as ϵ increases to values more readily found in wind tunnel experiments, then this behaviour disappears, and we are left with a T-S amplitude which decreases from the flat plate value. Thus if experiments were carried out on the Rankine body, it is unlikely that parameter ranges which exhibit this double maximum would be attainable and it would be expected that only the decrease in amplitude compared to the flat plate value would be seen.

When comparing the shape of the parabola, Rankine body and the MSE, it was shown that the geometry of the MSE lies between the other two bodies. However, the MSE exhibits a very different surface curvature, due to the removal of the junction of the elliptical edge and the flat plate, and this produces a different form of the pressure gradient compared to the parabola and the Rankine body.

The MSE itself is modelled using slender body theory and the results for the slip velocities and pressure distributions proved to be very satisfactory, when compared to the work of Wanderley and Corke (2001). The pressure distributions have a minimum close to the nose, which decreases for larger aspect ratios, although the pressure tends to zero faster for the smaller aspect ratio. The pressure gradients on the other hand have a small positive maximum before decreasing to their minimum adverse pressure gradient. Both this maximum and the minimum move closer to the zero pressure gradient line, as the aspect ratio increases. The slip velocities obtained have a similar property to the pressure

gradient, with the largest slip velocity occurring for the smallest aspect ratio.

Using the slender body theory, we made comparisons of the pressure distribution with the calculations of Wanderley and Corke (2001), and found good agreement as the aspect ratio reduced. When the slender body theory is extended to give the form of the Lam-Rott eigenmode in the leading edge region, and when we can use the PSE to march this solution downstream, we will be able to make further comparisons with Wanderley and Corke. Firstly, we will be able to make comparisons of the position of the lower branch neutral stability point, and the neutral curve in general. Secondly, we will be able to calculate the amplitude of the T-S wave at lower branch as ϵ varies, and compare these results with figure 9 from Wanderley and Corke.

Chapter 7

Conclusions

In this work, we have focused our attention on the propagation of Tollmien-Schlichting waves, through the Orr-Sommerfeld region of a two-dimensional boundary-layer on an airfoil. In particular we have considered the propagation of T-S waves generated by an energy conversion process in a region at the nose of the body, where the body has continuous curvature and where the inviscid slip velocity tends to a constant far downstream. The disturbances in the nose region for a flat plate were found to be Lam-Rott eigenmodes (Lam and Rott, 1960). For more general bodies, these disturbances were generalizations of these Lam-Rott eigenmodes, with added components to account for the mean pressure gradient. We were only concerned with the propagation of the lowest order eigenmode of this set, as it is this mode which matches (in the matched asymptotic sense) to the T-S wave, which exhibits spatial growth downstream in the Orr-Sommerfeld region. The main aim of this work was to compare results for T-S wave amplitudes in the Orr-Sommerfeld region with existing direct numerical schemes and experiments, in order to help to bridge the gap between numerical and experimental results.

All of the results are discussed in more detail at the end of the appropriate chapter, so only the more important results are discussed here. In chapter 2 we formulated the asymptotic form of the generalized Lam-Rott eigenmodes, including the outer inviscid layer, where this had not previously been derived. We also derived the generalized form of the Parabolized Stability Equation, for non-zero pressure gradients, for which the Lam-Rott eigenmodes provide us with a suitable upstream boundary condition. Both these

results are valid for bodies for which the Navier-Stokes equations can be approximated by the plane wall boundary-layer equations to leading order. The two methods are completely determined by the inviscid slip velocity in its far downstream limiting form, and in fact, we only require the coefficient multiplying the first correction term, to produce results to the desired order. Hence, combining the asymptotics in chapter 2 with the numerics in chapter 3, allows us to solve a huge range of receptivity problems, where the slip velocity is known fully in terms of the streamwise variable.

For the case of a semi-infinite flat plate, we were able to utilize the asymptotic form of the wavenumber and mode shape of the T-S wave given in Goldstein (1983), to justify fully our PSE results in chapter 4. For sufficiently large values of the Reynolds number, we were able to show that the PSE method is problem free, because of the well defined matching region. For smaller values of the Reynolds number, we found inconsistencies in our results when compared with the asymptotics, and this was attributed to the difficulties in deriving the $O(\epsilon^3)$ term of the asymptotics (Goldstein, 1982). Thus, we concluded that even if this term is correct to the desired order, it is impractical to try to extend the asymptotics to other bodies.

In chapter 4 we also examined the occurrence of initial transients which appear in the solution to the PSE for particular values of the Reynolds number and step size. No specific cause for these transients was found, although we found strong evidence to suggest that these transients are consequences of having small contributions from higher Lam-Rott eigenmodes in the initial condition to the PSE. The higher eigenmodes enter via the composite solution of the three deck eigenmode structure. These higher Lam-Rott modes match onto higher T-S modes in the Orr-Sommerfeld region, which initially decay more slowly than the unstable T-S wave, and so we have a region where they may dominate the solution. It is this domination that we believe is the cause of these transients.

The T-S wave amplitude calculations at the lower branch neutral stability point for the parabola, in chapter 5, were consistent with experiments, where the amplitude was seen to decrease with increasing Strouhal number. This has been attributed to the favourable pressure gradient which exists along the whole boundary of the parabola. For the values

of the Reynolds number considered, it was seen that the slight increase in receptivity coefficient for small Strouhal numbers, noted by Hammerton and Kerschen (1996), makes very little difference to the amplitude of the T-S wave, due to the fact that the amplitude of the eigensolution had decayed by a sufficient amount to force the amplitude of the T-S wave to decay from the flat plate value. However, corresponding results for the Rankine body in chapter 6 are much more interesting, as the T-S wave amplitude was found to increase and decrease depending on the values of both the Reynolds number and the nose radius. This is due to the adverse pressure gradient along the body, which forces the eigensolution's amplitude to increase with increasing nose radius, which is in direct conflict with the decreasing value of the receptivity coefficient. However, experimentalists may not be able obtain this result in wind tunnel experiments, because the wind tunnel has a restriction on the range of Reynolds number that it can produce. Thus the experimentalists will probably just observe a decrease in T-S wave amplitudes at lower branch, as the nose radius is increased, similar to the parabola.

The slender body theory work on the Modified Super Ellipse (MSE) has a lot of scope for further work. Although very little work has been carried out on the MSE in this thesis, we believe that a detailed study of how the slender body work relates to numerical and experimental data will be of huge benefit. The most interesting work will possibly be on the far downstream section, where the slender body theory is tending to a flat plate, whereas the MSE is exactly a flat plate in this region. Work in this thesis concludes that this makes very little difference to the pressure field along the surface of the body, but this could still lead to large differences in the amplitude of the T-S wave downstream. The MSE extension could also be taken as far as to calculate downstream amplitudes in a similar way as we did for the parabola and the Rankine body. However the receptivity coefficient for an MSE would have to be calculated first, using methods similar to Nichols (2001).

This work could also be extended to look at other airfoil geometries such as cambered airfoils (Hammerton and Kerschen, 2005) or Joukowski airfoils. A relatively simple extension might be to consider a parabola at an angle of attack to the free-stream, as then

results could be compared with those of Corke and co-workers (Haddad and Corke, 1998, Erturk and Corke, 2001, Erturk *et al.*, 2004 and Haddad *et al.*, 2005). The asymptotic/PSE method described in this thesis could also be extended to consider other mechanisms of receptivity, such as the receptivity due to an element of surface roughness. Our PSE method is linear, so we can compare the evolution of T-S waves from each receptivity mechanism separately. Thus we can make a comparison of the amplitudes of T-S waves generated at the leading edge and waves generated at surface roughness elements, and see which type of wave dominates at the neutral stability point, as the position of the roughness element is changed. However, a simple starting place for further research would be to use the source/sink bodies studied by Nichols (2001) to look at the effect of pressure gradients on the overall T-S wave amplitude downstream.

To summarize, we have developed a method to calculate T-S wave amplitudes at streamwise positions along a body via the numerical solution of the Parabolized Stability Equation, which uses the leading edge asymptotic result as its initial condition. Using this method we have obtained T-S wave amplitudes for various body shapes, which agree with other numerical and experimental schemes, where these results are available. This method has the potential to solve many receptivity problems, some of which are described in this chapter, and contribute greatly to this area of applied mathematics. The recent developments described in this thesis and in other papers addressed in this work, in my opinion, show that the area of receptivity and stability has a bright and exciting future.

Appendix A

Derivation of the Orr-Sommerfeld equation

In this appendix, we derive the Orr-Sommerfeld equation, which is the governing equation for parallel flow problems. The dimensional Navier-Stokes equations for the fluid velocity vector, $\tilde{\mathbf{u}}^*_{\mathbf{T}} = (U, V, W)$, in Cartesian (x^*, y^*, z^*) coordinates is

$$\frac{\partial \tilde{\mathbf{u}}^*_{\mathbf{T}}}{\partial t^*} + \tilde{\mathbf{u}}^*_{\mathbf{T}} \cdot \nabla^* \tilde{\mathbf{u}}^*_{\mathbf{T}} = -\frac{1}{\rho}\nabla^* \tilde{p}^*_T + \nu \nabla^{*2} \tilde{\mathbf{u}}^*_{\mathbf{T}}, \tag{A.1}$$

$$\nabla^* \cdot \tilde{\mathbf{u}}^*_{\mathbf{T}} = 0, \tag{A.2}$$

where ρ is the fluid density, ν is the kinematic viscosity, $\tilde{p}^*_T$ is the pressure, and

$$\nabla^* = \left(\frac{\partial}{\partial x^*}, \frac{\partial}{\partial y^*}, \frac{\partial}{\partial z^*} \right),$$

where $*$ denotes a dimensional quantity.

Using suitable dimensionless variables, the Navier-Stokes equations become

$$\frac{\partial \tilde{\mathbf{u}}_{\mathbf{T}}}{\partial t} + \tilde{\mathbf{u}}_{\mathbf{T}} \cdot \nabla \tilde{\mathbf{u}}_{\mathbf{T}} = -\nabla \tilde{p}_T + \frac{1}{Re}\nabla^2 \tilde{\mathbf{u}}_{\mathbf{T}}, \tag{A.3}$$

$$\nabla \cdot \tilde{\mathbf{u}}_{\mathbf{T}} = 0, \tag{A.4}$$

where Re is the Reynolds number, which is defined by,

$$Re = \frac{U_0 L}{\nu},$$

where U_0 is a common velocity scale, and L is a common length scale. Typical velocity scales could be a constant velocity, in a constant flow over a wing, or a mean velocity,

in channel flow. Similarly a typical length scale could be the width of a channel, or the length of an airfoil etc.

For parallel flows, we assume the velocity has the form

$$\tilde{\mathbf{u}}_{\mathbf{T}} = U(y)\hat{\mathbf{x}} + \epsilon\tilde{\mathbf{u}}(\mathbf{x}, t), \tag{A.5}$$

where $U(y)$ is the purely parallel part of $\tilde{\mathbf{u}}_{\mathbf{T}}$, $\tilde{\mathbf{u}}$ is the perturbation velocity, and ϵ is a small parameter. The pressure has a main component which drives the parallel flow, and a perturbation component, in the form

$$\tilde{p}_T = P + \epsilon\tilde{p}. \tag{A.6}$$

Substituting (A.5) and (A.6) into (A.3) gives,

$$\epsilon\frac{\partial\tilde{\mathbf{u}}}{\partial t} + \epsilon U\frac{\partial\tilde{\mathbf{u}}_{\mathbf{T}}}{\partial x} + \epsilon\tilde{\mathbf{u}}_{\mathbf{T}}\cdot\nabla(U\hat{\mathbf{x}}) = -\nabla P - \epsilon\nabla\tilde{p} + \frac{1}{Re}(\nabla^2 U)\hat{\mathbf{x}} + \frac{\epsilon}{Re}\nabla^2\tilde{\mathbf{u}} + O(\epsilon^2). \tag{A.7}$$

Equating the coefficients of ϵ^0 gives

$$-\nabla P + \frac{1}{Re}\frac{d^2U}{dy^2}\hat{\mathbf{x}} = 0.$$

The $\hat{\mathbf{y}}$ and $\hat{\mathbf{z}}$ components imply $P = P(x)$, hence the $\hat{\mathbf{x}}$ component gives,

$$\frac{dP}{dx} = \frac{1}{Re}\frac{d^2U}{dy^2}.$$

The right hand side of this equation is a function of y only, and the left hand side is a function of x only, hence both sides must be a constant. So the base flow must have a constant pressure gradient, and the velocity profile must be quadratic,

$$U(y) = ry^2 + sy + t, \tag{A.8}$$

where r, s and t are constants, and $r = Re/2\ dP/dx$.

The $O(\epsilon)$ equation from (A.7) gives

$$\frac{\partial\tilde{\mathbf{u}}}{\partial t} + U\frac{\partial\tilde{\mathbf{u}}}{\partial x} + \tilde{v}U'\hat{\mathbf{x}} = -\nabla\tilde{p} + \frac{1}{Re}\nabla^2\tilde{\mathbf{u}}, \tag{A.9}$$

where $\tilde{\mathbf{u}} = (\tilde{u}, \tilde{v}, \tilde{w})$, and $U' = dU/dy$.

We can now separate the variables of this equation by taking independent normal modes of the form

$$\tilde{\mathbf{u}} = (u(y), v(y), w(y))e^{i(kx+lz-\alpha ct)}, \tag{A.10}$$

$$\tilde{p} = p(y)e^{i(kx+lz-\alpha ct)}, \tag{A.11}$$

where k and l are the streamwise and transverse wavenumbers and c is the wave speed.

Substituting these into (A.9) gives

$$(D^2 - \alpha^2 - (ik\ Re)(U-c))u = ik\ Re\ p + Re\ U'\ v, \tag{A.12}$$

$$(D^2 - \alpha^2 - (ik\ Re)(U-c))v = Re\ Dp, \tag{A.13}$$

$$(D^2 - \alpha^2 - (ik\ Re)(U-c))w = il\ Re\ p, \tag{A.14}$$

where $\alpha = (k^2 + l^2)^{\frac{1}{2}}$ and $D \equiv d/dy$. The continuity equation gives

$$iku + Dv + ilw = 0. \tag{A.15}$$

We now use Squire's transformation to simplify the system. This transformation reduces the problem from a 3D problem to a 2D one. Squire's transform is

$$\begin{aligned} \alpha\bar{u} &= ku + lw, \\ \bar{p} &= \frac{\alpha}{k}p, \\ \bar{v} &= v, \\ \bar{Re} &= \frac{k}{\alpha}Re, \end{aligned}$$

where the quantities on the left-hand side are the new transformed variables.

Now using this transform, and eliminating u, w and p from (A.12), (A.13), (A.14) and (A.15), and dropping the bar for clarity, we get the equation

$$(U-c)(D^2-\alpha^2)v - U''v = \frac{1}{i\alpha Re}(D^2-\alpha^2)^2 v. \tag{A.16}$$

This equation is known as the **Orr-Sommerfeld** equation. This is a fourth order equation, and hence we need four boundary conditions. As with most viscous fluid problems, the

boundary conditions are, no flow at the solid boundaries $y = y_1$ and $y = y_2$. The no normal flow condition is simply

$$v(y_1) = v(y_2) = 0.$$

To find the condition for no tangential flow, we take (A.15), use Squire's transformation and drop the bar for clarity. Doing this we find

$$Dv = -\alpha u,$$

hence $u = 0$ at $y = y_1, y_2$ implies

$$Dv(y_1) = Dv(y_2) = 0.$$

Hence the boundary conditions are

$$v(y_1) = v(y_2) = Dv(y_1) = Dv(y_2) = 0,$$

where y_1 and y_2 can be infinite. If y_1 and/or y_2 are infinite, then we use the condition that the perturbation velocity has decayed to zero at infinity.

Appendix B

Airy functions

Airy functions are solutions of

$$\frac{d^2w(z)}{dz^2} - zw(z) = 0, \tag{B.1}$$

which is known as Airy's (differential) equation, in the complex z plane. It has three pairs of linearly independent solutions

$$\begin{aligned} Ai(z) &, \quad Bi(z), \\ Ai(z) &, \quad Ai(ze^{\frac{2\pi i}{3}}), \\ Ai(z) &, \quad Ai(ze^{-\frac{2\pi i}{3}}). \end{aligned}$$

For real x, the function $Ai(x)$ and its derivative $Ai'(x)$ are plotted in figure B.1. Both these functions tend to zero exponentially as $x \longrightarrow \infty$, and as $x \longrightarrow -\infty$, $Ai(x) \longrightarrow 0$. The function $Bi(x)$ and its derivative $Bi'(x)$, which are plotted in figure B.2, both have exponential growth as $x \longrightarrow \infty$, but again $Bi(x) \longrightarrow 0$ as $x \longrightarrow -\infty$.

The Wronskian of the linearly independent functions $Ai(z)$ and $Bi(z)$ is

$$W(Ai(z), Bi(z)) = Ai(z)Bi'(z) - Ai'(z)Bi(z) = \frac{1}{\pi}. \tag{B.2}$$

For more information on the Airy functions and their properties, see Abramowitz (1964), page 446.

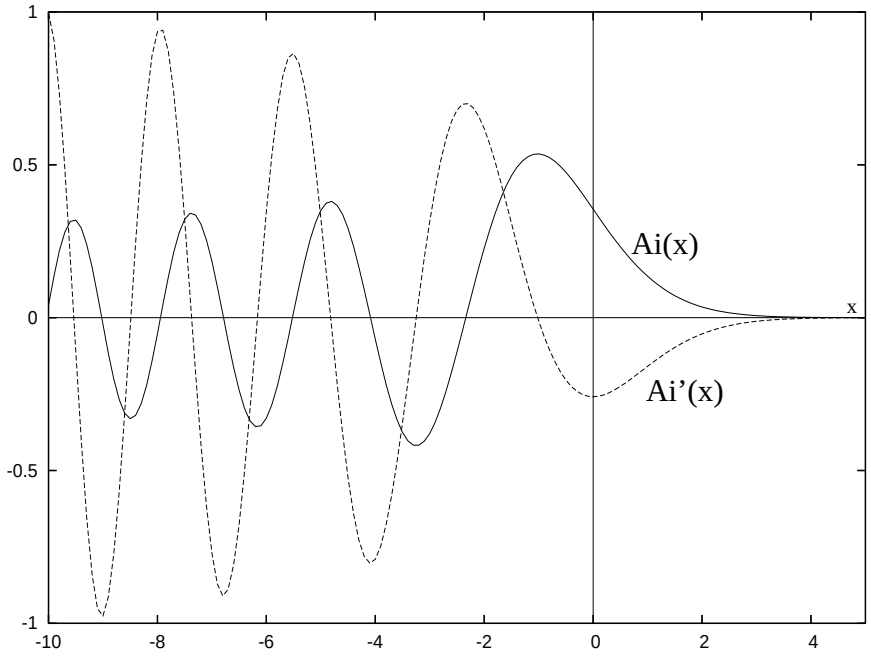

Figure B.1: $Ai(x)$, $Ai'(x)$

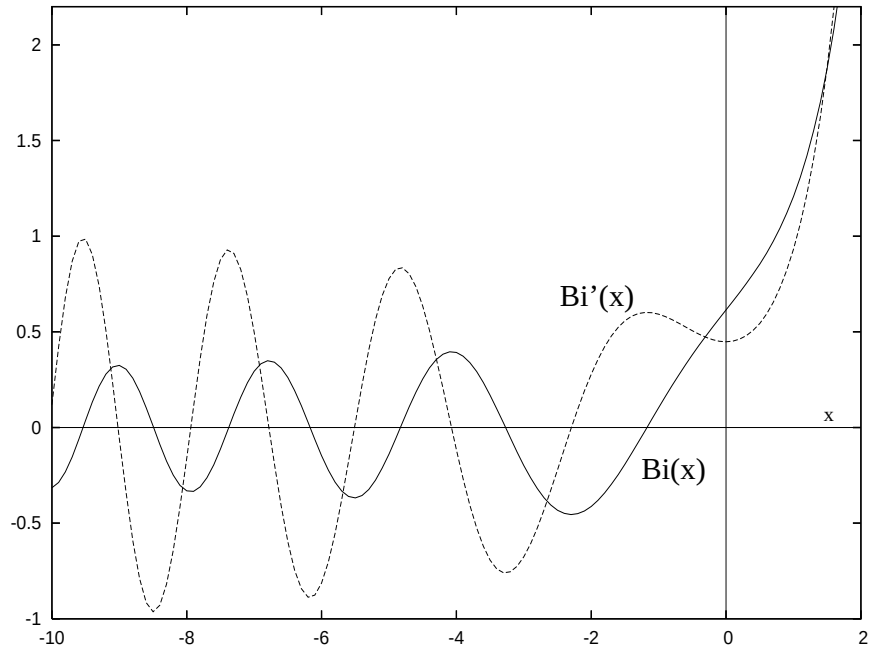

Figure B.2: $Bi(x)$, $Bi'(x)$

Appendix C

Chebyshev polynomials

Chebyshev polynomials are widely used in spectral collocation problems, especially in parallel flow problems, where the domain can be mapped to the $[-1, 1]$ domain, where these polynomials are valid.

Chebyshev polynomials are an orthogonal set of polynomials which satisfy the differential equation,

$$(1 - x^2)\frac{d^2y}{dx^2} - x\frac{dy}{dx} + n^2 y = 0, \tag{C.1}$$

where n is an integer. We define the n^{th} Chebyshev polynomial of the first kind by

$$T_n(x) = \cos(n \cos^{-1} x). \tag{C.2}$$

These polynomials are orthogonal, with respect to the weighting function

$$w(x) = (1 - x^2)^{-\frac{1}{2}},$$

and satisfy the orthogonality condition,

$$\int_{-1}^{1} (1 - x^2)^{-\frac{1}{2}} T_n T_m dx = \begin{cases} 0, & n \neq m \\ \frac{\pi}{2}, & n = m \neq 0 \\ \pi, & n = m = 0 \end{cases} . \tag{C.3}$$

If we write $\cos\theta = x$, and use the trigonometric identity

$$\cos n\theta + \cos(n-2)\theta = 2\cos\theta\cos(n-1)\theta,$$

then we see that Chebyshev polynomials satisfy the recurrence relation for $n \geq 2$

$$T_n(x) = 2xT_{n-1}(x) - T_{n-2}(x). \tag{C.4}$$

From (C.2) we can easily see that

$$\begin{aligned} T_0(x) &= 1, \\ T_1(x) &= x. \end{aligned}$$

Then using (C.4) we can write down the first few Chebyshev polynomials.

$$\begin{aligned} T_2(x) &= 2x^2 - 1, \\ T_3(x) &= 4x^3 - 3x, \\ T_4(x) &= 8x^4 - 8x^2 + 1, \\ T_5(x) &= 16x^5 - 20x^3 + 5x, \end{aligned}$$

which are plotted in figure C.1. Note that the odd numbered polynomials are odd functions, and the even numbered ones are even functions. This fact comes in handy when solving symmetric problems.

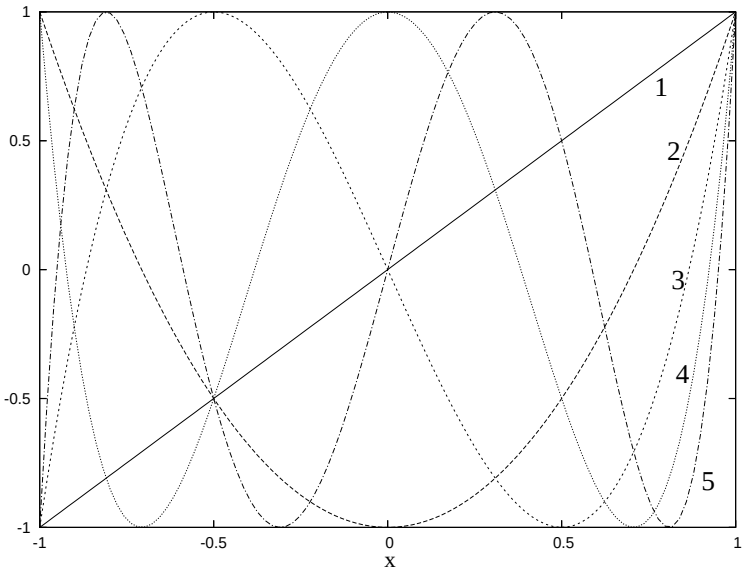

Figure C.1: Plot of the Chebyshev polynomials, $T_n(x)$, for $n = 1, 2, 3, 4, 5$.

Another fact which follows from (C.2) is that Chebyshev polynomials satisfy the condition

$$\frac{c_n}{n+1}T'_{n+1}(x) - \frac{d_{n-2}}{n-1}T'_{n-1}(x) = 2T_n(x) \tag{C.5}$$

for $n \geq 0$, where $c_n = d_n = 0$ if $n < 0$, $c_0 = 2$, $d_0 = 1$, and $c_n = d_n = 1$ if $n > 0$.

We can represent a function $g(x)$, defined on $x \in [-1, 1]$, as a series of Chebyshev polynomials,

$$g(x) = \sum_{i=0}^{N} a_i T_i(x),$$

where the a_i are constants. To find a_i we use (C.3), so that

$$\begin{aligned} a_i &= \frac{2}{\pi}\int_{-1}^{1}(1-x^2)^{-\frac{1}{2}}g(x)T_i(x)dx, \\ a_0 &= \frac{1}{\pi}\int_{-1}^{1}(1-x^2)^{-\frac{1}{2}}g(x)dx. \end{aligned}$$

For more information on Chebyshev Polynomials, see Rivlin (1974).

Appendix D

Derivation of equation (4.54)

This equation is merely stated in Goldstein (1982), however its derivation is important, and is derived here.

We define

$$\Gamma^{\dagger} = \pi i U_0' \zeta_0 \left(Ai(\zeta) \int_{\zeta_0}^{\zeta} gBi(\xi)d\xi - Bi(\zeta) \int_{\infty_1}^{\zeta} gAi(\xi)d\xi \right) + \frac{\bar{\eta}^2 U_0'}{2} \left(1 - \frac{(a_1 + \bar{c})\zeta_0}{\bar{c}\zeta} \right), \tag{D.1}$$

where $g = \bar{H}_1 \frac{d\ln(A)}{dx_1} + \bar{H}_2$.

Changing the variable from $\bar{\eta}$ to ζ we find

$$-\frac{\bar{c}}{\zeta_0 U_0'} \int_0^{\infty} \Gamma^{\dagger} d\bar{\eta} = \int_{\zeta_0}^{\infty} \Gamma^{\dagger} d\zeta.$$

Integrating the first term of $\Gamma^{\dagger}$ by parts and using (4.55), we end up with

$$\begin{aligned} \int_{\zeta_0}^{\infty} \Gamma^{\dagger} d\zeta = \pi i U_0 \zeta_0 \left[\int_{\infty_1}^{\zeta} Ai(\zeta)d\zeta \int_{\zeta_0}^{\zeta} gBi(\zeta)d\zeta - \int_{\zeta_0}^{\zeta} Bi(\zeta)d\zeta \int_{\infty_1}^{\zeta} gAi(\zeta)d\zeta \right]_{\zeta_0}^{\infty_1} \\ -\pi i U_0' \zeta_0 \int_{\zeta_0}^{\infty_1} \frac{Wi}{\pi} g \, d\zeta + \int_{\zeta_0}^{\infty_1} \frac{\bar{\eta}^2 U_0'}{2} \left(1 - \frac{(a_1 + \bar{c})\zeta_0}{\bar{c}\zeta} \right) d\zeta. \end{aligned} \tag{D.2}$$

Let us consider the first part of (D.2). We note that as $\bar{\eta}\ (\text{or}\ \zeta) \longrightarrow \infty$,

$$g \sim g_{\infty} = \lambda_0 + \lambda_1 \zeta + \lambda_2 \zeta^2 + \lambda_3 \zeta^3,$$

where

$$\lambda_0 = -\frac{i\bar{c}}{U_0'}\left(\frac{\bar{c}}{\zeta_0^3}+\frac{(a_1+\bar{c})}{2}\right), \tag{D.3}$$

$$\lambda_1 = \frac{i\bar{c}}{U_0'\zeta_0}(a_1+\frac{3}{2}\bar{c}), \tag{D.4}$$

$$\lambda_2 = -\frac{i\bar{c}}{2U_0'\zeta_0^2}(a_1+3\bar{c}), \tag{D.5}$$

$$\lambda_3 = \frac{i\bar{c}}{2U_0'\zeta_0^3}. \tag{D.6}$$

Note that in the first part of (D.2), the zero limit gives a zero contribution, but to evaluate the infinite limit, we have to insert g_∞ for g, and carry out the resulting integrals, noting that

$$\int zBi(z)dz = Bi'(z), \tag{D.7}$$

$$\int z^2Bi(z)dz = zBi'(z)-Bi(z), \tag{D.8}$$

$$\int z^3Bi'(z)dz = z^2Bi(z)-2zBi(z)+2\int Bi(z)dz, \tag{D.9}$$

and similar results hold for $Ai(z)$.

We now define

$$I_1 = \int_{\infty_1}^{\zeta} Ai(\zeta)d\zeta \int_{\zeta_0}^{\zeta} g_\infty Bi(\zeta)d\zeta, \tag{D.10}$$

$$I_2 = \int_{\zeta_0}^{\zeta} Bi(\zeta)d\zeta \int_{\infty_1}^{\zeta} g_\infty Ai(\zeta)d\zeta. \tag{D.11}$$

So using (D.7), (D.8) and (D.9) we find

$$\begin{aligned} I_1-I_2 &= \lambda_1\left(Bi'(\zeta)\int_{\infty_1}^{\zeta}Ai(\zeta)d\zeta - Ai'(\zeta)\int_{\zeta_0}^{\zeta}Bi(\zeta)d\zeta\right) \\ &+ \lambda_2\left(\zeta\left(Bi'(\zeta)\int_{\infty_1}^{\zeta}Ai(\zeta)d\zeta - Ai'(\zeta)\int_{\zeta_0}^{\zeta}Bi(\zeta)d\zeta\right)\right. && \text{(D.12)} \\ &- \left.\left(Bi(\zeta)\int_{\infty_1}^{\zeta}Ai(\zeta)d\zeta - Ai(\zeta)\int_{\zeta_0}^{\zeta}Bi(\zeta)d\zeta\right)\right) && \text{(D.13)} \\ &+ \lambda_3\left(\zeta^2\left(Bi'(\zeta)\int_{\infty_1}^{\zeta}Ai(\zeta)d\zeta - Ai'(\zeta)\int_{\zeta_0}^{\zeta}Bi(\zeta)d\zeta\right)\right. && \text{(D.14)} \\ &- \left.2\zeta\left(Bi(\zeta)\int_{\infty_1}^{\zeta}Ai(\zeta)d\zeta - Ai(\zeta)\int_{\zeta_0}^{\zeta}Bi(\zeta)d\zeta\right)\right)+EST, && \text{(D.15)} \end{aligned}$$

which upon using (4.55) becomes

$$I_1-I_2 = \frac{1}{\pi}\left(\lambda_1 Wi' + \lambda_2\zeta Wi' - \lambda_2 Wi + \lambda_3\zeta^2 Wi' - 2\lambda_3\zeta Wi\right). \tag{D.16}$$

This is now differentiated with respect to ζ, so that it can be put under an integral sign, which gives

$$\begin{aligned}\frac{d}{d\zeta}(I_1 - I_2) &= \frac{1}{\pi}\left(\left(\lambda_1\zeta + \lambda_2\zeta^2 + \lambda_3\zeta^3 - 2\lambda_3\right)Wi + \left(\lambda_1 + \lambda_2\zeta + \lambda_3\zeta^2\right)\right), \\ &= \frac{1}{\pi}\left(\left(g_\infty - \lambda_0 - 2\lambda_3\right)Wi + \left(\lambda_1 + \lambda_2\zeta + \lambda_3\zeta^2\right)\right), \qquad \text{(D.17)}\end{aligned}$$

where we have used the fact that $Wi'' - \zeta Wi = 1$.

If we now write part 3 of (D.2) in terms of ζ and λ_i we find

$$\frac{\bar{\eta}^2 U_0'}{2}\left(1 - \frac{(a_1 + \bar{c})\zeta_0}{\bar{c}\zeta}\right) = -iU_0'\zeta_0\left(\lambda_1 + \lambda_2\zeta + \lambda_3\zeta^2 + \frac{\bar{c}(a_1 + \bar{c})}{2iU_0'\zeta}\right), \qquad \text{(D.18)}$$

which on combining with part 1 of (D.2) and (D.17), we achieve (4.51).

Appendix E

Free-stream disturbances at an incident angle

This appendix considers the effect on the receptivity coefficient if the free-stream disturbance interacts with the body at a non-zero incident angle, θ. In chapters 4 and 5 we have been able to ignore the length of the body, however, when the incoming flow is not symmetric, the length of the body affects the local flow at the leading edge. Hence, we consider a body of length $2b$ with a dimensional nose radius of r_n, shown in figure 5.7, where the leading edge is assumed to be parabolic.

From equation (5.5) we see that the non-dimensional Cartesian (x_c, y_c) coordinates are related to our parabolic (ξ, N) coordinates by

$$x_c + iy_c = \frac{1}{2}\left((Z + iS^{\frac{1}{2}})^2 + S\right),$$

where $Z = \left((2\xi)^{\frac{1}{2}} + i\epsilon^3 N\right)$. Under this conformal mapping, the parabola in figure 5.1 gets mapped to flow in a right angle corner in the $Z-$plane, as shown in figure E.1.

In the $Z-$plane, the complex potential for this flow is given by

$$\begin{aligned} w(Z) &= \frac{1}{2}Z^2, \\ &= \frac{1}{2}\left((2\xi)^{\frac{1}{2}} + i\epsilon^3 N\right)^2, \end{aligned}$$

and hence the velocity field is given by

$$u - iv = \frac{dw}{dz} = \frac{dw}{dZ}\frac{dZ}{dz} = \frac{Z}{Z + iS^{\frac{1}{2}}}.$$

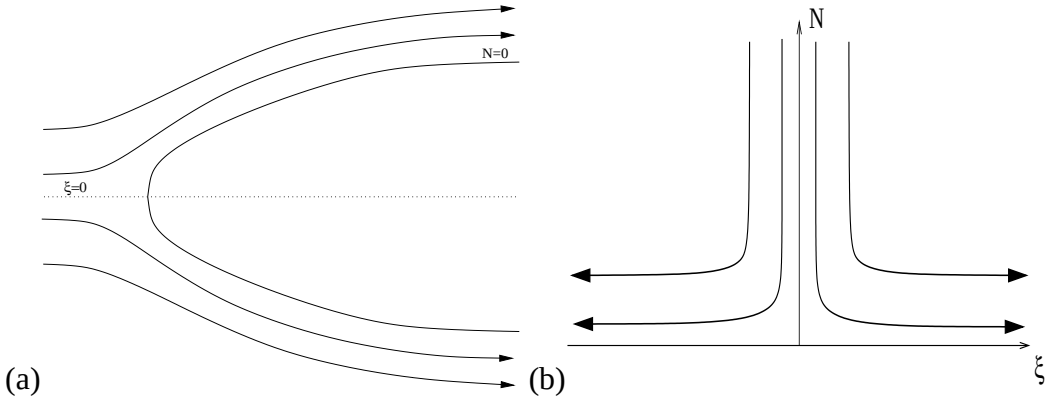

Figure E.1: Figure showing the symmetric flow around a parabolic body (a) in the $z-$plane, and (b) in the $Z-$plane.

The unsteady, inviscid slip velocity on the body ($N = 0$) is then given by

$$U_d(\xi) = \left|\frac{dw}{dz}\right| = \left|\frac{(2\xi)^{\frac{1}{2}}}{(2\xi)^{\frac{1}{2}} + iS^{\frac{1}{2}}}\right| = \frac{(2\xi)^{\frac{1}{2}}}{(2\xi + S)^{\frac{1}{2}}}, \tag{E.1}$$

which is the same as for the steady component, U_f, as we noted in §5.1. This form of the slip velocity is the symmetric part, which represents flow along $\xi = 0$ and around the body as shown in figure E.1(a). We now need to consider the antisymmetric flow which moves parallel to the plate from the bottom surface to the top surface as shown in figure E.2(a).

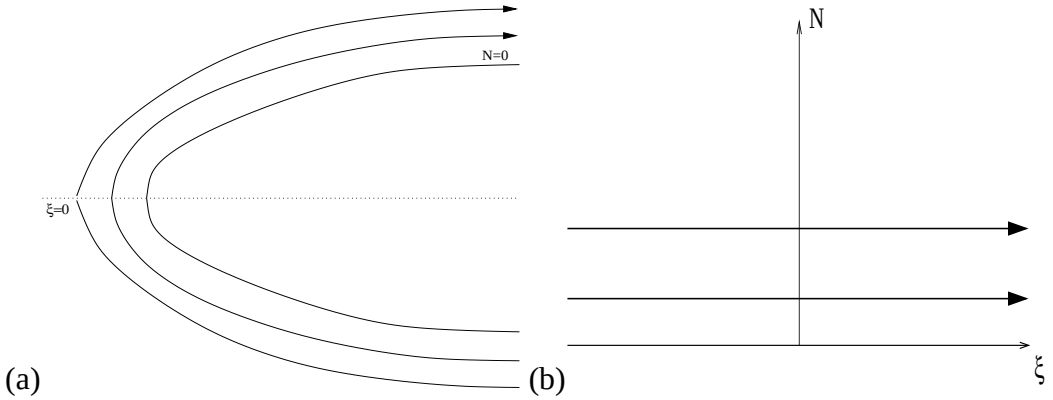

Figure E.2: Figure showing the anti-symmetric flow around a parabolic body (a) in the $z-$plane, and (b) in the $Z-$plane.

The complex potential for the anti-symmetric flow in the $Z-$plane is given by

$$w(Z) = Z,$$

which leads to an antisymmetric unsteady slip velocity of

$$U_d^{anti}(\xi) = \frac{1}{(2\xi + S)^{\frac{1}{2}}}. \tag{E.2}$$

For low Mach numbers, the acoustic wavelength $2\pi c/\omega$, where c is the speed of sound, is long compared to the hydrodynamic length scale U_∞/ω. Thus, outside the boundary-layer, the flow can be assumed to be inviscid and irrotational, so the complex potential theory above shows that the local flow has a slip velocity of the form

$$U_d(\xi) = \kappa_s(\theta)\frac{(2\xi)^{\frac{1}{2}}}{(2\xi + S)^{\frac{1}{2}}} + \kappa_a(\theta)\frac{1}{(2\xi + S)^{\frac{1}{2}}}. \tag{E.3}$$

The coefficients κ_s and κ_a multiplying these eigensolutions are independent of the Strouhal number, and only depend on θ. Substituting the form of (E.3) into (2.37) and using (5.6) gives

$$F(\phi_2) = \kappa_s\left(i(2\xi + S) - \frac{2S}{2\xi + S}\right) + \frac{\kappa_a}{(2\xi)^{\frac{1}{2}}}\left(i(2\xi + S) + \frac{2\xi - S}{2\xi + S}\right), \tag{E.4}$$

where $F(\phi_2)$ is the LUBLE operator defined by

$$\begin{aligned} F(\phi_2) \equiv \phi_{2NNN} &+ \phi_{2NN}\left(\phi_1 + 2\xi\phi_{1\xi}\right) + \phi_{2N}\left(i(2\xi + S) - \frac{2S}{2\xi + S}\phi_{1N} - 2\xi\phi_{1N\xi}\right) \\ &+ \phi_2\phi_{1NN} + 2\xi\left(\phi_{1NN}\phi_{2\xi} - \phi_{1N}\phi_{2N\xi}\right). \end{aligned} \tag{E.5}$$

Hence if we write $\phi_2 = \kappa_s\phi_s + \kappa_a\phi_a$, then it follows that the receptivity coefficient on the upper body of the surface is given by

$$C_1(S, \theta) = \kappa_s(\theta)C_s(S) + \kappa_a(\theta)C_a(S), \tag{E.6}$$

where the solutions for C_s and C_a are found by solving

$$F(\phi_s) = \left(i(2\xi + S) - \frac{2S}{2\xi + S}\right), \tag{E.7}$$

$$F(\phi_a) = \frac{1}{(2\xi)^{\frac{1}{2}}}\left(i(2\xi + S) + \frac{2\xi - S}{2\xi + S}\right), \tag{E.8}$$

respectively. The corresponding receptivity coefficient for the lower surface can be found by replacing θ by $-\theta$.

The symmetric and antisymmetric flow coefficients, κ_s and κ_a, are found by asymptotically matching the local velocity field near the nose, given by (E.3), to a global velocity

field given by complex potential theory. The solution of these two coefficients depends upon the reduced acoustic frequency $k = \omega b/c$, where again c is the speed of sound in the undisturbed fluid. Sedov (1965) describes how to calculate the velocity field about a thin wing, including the effects of compressibility, but in general, no simple form of the inviscid slip velocity can be obtained. We consider two cases which do lead to simple slip velocities. The first being when $k \ll 1$ which is the case of very small Mach numbers, when the acoustic wavelength is long compared to both the hydrodynamic length scale U_∞/ω and the length of the airfoil chord. This leads to the flow being analyzed using classical unsteady airfoil theory for incompressible flow. The second case is where $k \gg 1$, which is when the acoustic wavelength is long compared to the hydrodynamic length scale, but shorter than the airfoil itself, and this case is analysed using acoustic diffraction theory.

E.1 Small Mach numbers ($k \ll 1$)

We assume that the airfoil semi-chord is the relevant length scale for this problem, and since this is the relevant length scale for unsteady aerodynamic interaction, we can ignore the thickness of the airfoil, except in the region of the nose, and hence it reduces to a zero-thickness flat plate. The complex potential for this flow consists of two parts, a non-circulatory part, and a part which is due to the circulation induced by vorticity shed from the sharp trailing edge. The shed vorticity gets convected downstream from the body, so we assume it takes the form $\gamma(x,t) = \hat{\gamma} e^{i(ax-t)}$, where $a = \omega b/U_\infty$ is the aerodynamic reduced frequency.

The flat plate is mapped to a circle in the $Z-$plane by the conformal mapping

$$z - 1 = \frac{1}{2}\left(Z + \frac{1}{Z}\right),$$

which has an inverse mapping of

$$Z = z - 1 + (z(z-2))^{\frac{1}{2}}.$$

The non-dimensional complex potential, w is then written as

$$w(Z) = \frac{e^{-it}}{2}\left(e^{-i\theta}Z + \frac{e^{i\theta}}{Z}\right) - \frac{i\hat{\gamma}e^{-it}}{2\pi}\int_2^\infty e^{iax_0}\ln\left(\frac{Z-Z_0}{Z-1/Z_0}\right)dx_0, \tag{E.9}$$

where the second term is given by Milne-Thomson's circle theorem, excluding the term at $Z = 0$, which is used to eliminate any circulation induced by using this theorem (Acheson, 1990). We can do this because we are going to fix the value of $\hat{\gamma}$ by using the unsteady Kutta condition at the trailing edge. The unsteady Kutta condition states that the velocity is finite at the trailing edge of the flat plate ($Z = 1$), and this is achieved if

$$\hat{\gamma} = \frac{2\pi\sin\theta}{\int_2^\infty e^{iax_0}\left(\frac{x_0}{x_0-2}\right)^{\frac{1}{2}}dx_0}. \tag{E.10}$$

We wish to match this with the local solution given in (E.3), so we require the small x expansion of the velocity evaluated on the airfoil's surface, where x is the variable along the body without any geometric effects. Doing this we find

$$u(x,0\pm) \sim \left(\pm\frac{\sin\theta}{\sqrt{2}}(1+J(a))x^{-\frac{1}{2}} + \cos\theta + O(x^{\frac{1}{2}})\right)e^{-it} \quad \text{as} \quad x \longrightarrow 0, \tag{E.11}$$

where $J(a)$ is an effect of the vorticity shed from the trailing edge and is given by

$$J(a) = \frac{\int_2^\infty e^{iax_0}\left(\frac{x_0-2}{x_0}\right)^{\frac{1}{2}}dx_0}{\int_2^\infty e^{iax_0}\left(\frac{x_0}{x_0-2}\right)^{\frac{1}{2}}dx_0} = O(a^{-1}) \quad \text{as} \quad a \longrightarrow \infty. \tag{E.12}$$

The area we are interested in, is that of high reduced frequencies, so the effect of the shed vortices in the vicinity of the leading edge is then much smaller than the contribution of the non-circulatory part, by the factor of $O(a^{-1})$. Hence matching (E.11) with (E.3) as $\xi \longrightarrow \infty$ gives, at $O(x^{-\frac{1}{2}})$ and $O(1)$,

$$\begin{aligned} \frac{\sin\theta}{\sqrt{2}} &= \frac{\kappa_a}{\sqrt{2a}}, \\ \cos\theta &= \kappa_s, \end{aligned}$$

hence we see that

$$\kappa_s = \cos\theta, \quad \kappa_a = a^{\frac{1}{2}}\sin\theta. \tag{E.13}$$

We see from this, that close to the nose, except when θ is near 0 or π, the slip velocity is dominated by the antisymmetric part of the flow, and in fact the maximum flow speed of

$(b/r_n)^{\frac{1}{2}}$ is reached at the nose of the body. Also in the $k \ll 1$ limit, we note that the flow near the nose, and hence the receptivity coefficient, is the same if the body has a rounded trailing edge as well as a sharp trailing edge.

E.2 Use of acoustic diffraction theory ($k \gg 1$)

In this case, the acoustic wavelength is short compared to the length of the airfoil, and the interaction can be analysed by taking the airfoil to be a semi-infinite flat plate. Similar to the above case, on the scale of the acoustic wavelength, the airfoil appears as a zero-thickness flat plate, so the problem reduces to the classical Sommerfeld diffraction problem (Noble, 1958). The velocity potential for this unsteady flow is given by

$$\phi(x,y) = \left(-\frac{i}{k} e^{ik(x\cos\theta + y\sin\theta)} - \sin\left(\frac{\theta}{2}\right) \frac{\mathrm{sgn}(y)}{\pi(2k)^{\frac{1}{2}}} \int_{-\infty}^{\infty} \frac{\exp(-(\lambda^2-k^2)^{\frac{1}{2}}|y| - i\lambda x)}{(\lambda + k\cos\theta)(\lambda+k)^{\frac{1}{2}}} d\lambda \right) e^{-it}, \tag{E.14}$$

where the function $\mathrm{sgn}(y)$ is the sign function defined as

$$\mathrm{sgn}(y) = \begin{cases} -1 & \text{for} \quad y < 0, \\ 0 & \text{for} \quad y = 0, \\ 1 & \text{for} \quad y > 0. \end{cases}$$

Differentiating (E.14) with respect to x, leads to a slip velocity on the body ($y = 0$) of

$$u(x,0\pm) = \left(\cos\theta e^{ikx\cos\theta}(1 \mp \mathrm{erf}\Phi) \pm \sin\left(\frac{\theta}{2}\right) \frac{\sqrt{2}e^{i\pi/4}}{(\pi k)^{\frac{1}{2}}} x^{-\frac{1}{2}} \right) e^{-it}, \tag{E.15}$$

where $\Phi = e^{i\pi/4}(2kx)^{\frac{1}{2}} \sin\left(\frac{\theta}{2}\right)$, and erf is the error function, and is defined as

$$\mathrm{erf}(z) = \frac{2}{\sqrt{\pi}} \int_0^z e^{-t^2} dt.$$

As we let $x \longrightarrow 0$,

$$u(x,0\pm) \sim \left(\pm \sin\left(\frac{\theta}{2}\right) \frac{\sqrt{2}e^{i\pi/4}}{(\pi k)^{\frac{1}{2}}} x^{-\frac{1}{2}} + \cos\theta + O(x^{\frac{1}{2}}) \right) e^{-it}. \tag{E.16}$$

Thus matching (E.16) with (E.3) as $\xi \longrightarrow \infty$, we find

$$\kappa_s = \cos\theta, \qquad \kappa_a = \frac{2e^{i\pi/4}}{(\pi M_\infty)^{\frac{1}{2}}} \sin\left(\frac{\theta}{2}\right), \tag{E.17}$$

where $M_\infty = U_\infty/c$ is the Mach number of the mean flow, which we have assumed to be small. We again see that the antisymmetric component dominates the flow, except near

$\theta = 0$, however this time the slip velocity has a maximum value of $2e^{i\pi/4}(c/\pi\omega r_n)\sin\left(\frac{\theta}{2}\right)$ at the leading edge, which is independent of the semi-chord of the airfoil, b. We also note that for the case $k \ll 1$, both the symmetric and anti-symmetric components were in phase, but in this case, the antisymmetric component lags the symmetric component by $\pi/4$ because of the effect of compressibility.

Appendix F

Rankine body formulation

The Rankine body is formed by considering a line source in a uniform flow, so we can write the dimensional complex potential, w^* as

$$w^* = U_\infty z^* + \frac{K}{2\pi} \ln\left(z^* - \frac{K}{2\pi U_\infty}\right), \tag{F.1}$$

where $K > 0$ is the strength of the source, and $z^* = x_c^* + iy_c^*$, where the subscript c denotes that these are the usual Cartesian coordinates. In (F.1) we have located the source at $K/2\pi U_\infty$, so that the leading edge occurs at $z^* = 0$. The following theory also holds for the source at any point on the z^* axis. Introducing the same non-dimensional quantities as we did for the formulation of the governing equations in chapter 2, (F.1) becomes

$$w = z + A\ln(z - A) + A\ln\left(\frac{U_\infty}{\omega}\right), \tag{F.2}$$

where $w^* = U_\infty^2 w/\omega$, and

$$A = \frac{K\omega}{2\pi U_\infty}. \tag{F.3}$$

We note that the complex potential $w = \phi + i\psi$, where ϕ is the velocity potential, and ψ is the stream function. Equating the real and imaginary parts of (F.2) leads to

$$\phi = x_c + A\ln(|z - A|) + A\ln\left(\frac{U_\infty}{\omega}\right), \tag{F.4}$$

$$\psi = y_c + A\arg(z - A). \tag{F.5}$$

We can also work out the velocity field by differentiating (F.2) with respect to z to give

$$u - iv = 1 + \frac{A}{z - A}. \tag{F.6}$$

Equation (F.6) can be solved to show that the stagnation point of this flow occurs at $z = 0$. The streamlines for the flow are given from (F.5) as $\psi = c_i$, where c_i are constants, and the argument of z is taken to lie in the range $\arg(z) \in (-\pi, \pi]$. The streamline which passes through the stagnation point will be replaced by a solid body, and the other streamlines shall then represent the flow around that body. At the stagnation point, (F.5) is evaluated to give $\psi = A\pi$, hence the equation of the body is then given by

$$y_c + A\arg(z - A) = A\pi. \tag{F.7}$$

We note from (F.6) that the flow velocity has a singularity at the point $z = A$. This however is of no concern to us, as it lies inside the streamline, which we are replacing by an impermeable surface, and hence the singularity lies inside the body. Outside the body, the velocity field is finite. The body is symmetric, so we need only concern ourselves with the derivation of the equation for the upper surface. From (F.7) we see that the equation for the body can be written as

$$y_c + A\tan^{-1}\left(\frac{y_c}{x_c - A}\right) = A\pi, \tag{F.8}$$

where $\tan^{-1}$ is defined so that $\tan^{-1}(p/q) \in [0, \pi/2]$ for $p, q \geq 0$. We can then rearrange this to give the equation of the upper surface of the body as

$$x_c = A - y_c \cot\left(\frac{y_c}{A}\right). \tag{F.9}$$

We note that the function $y_c \cot(y_c/A)$ has poles at $y_c = nA\pi$, where $n = 1, 2, 3, ...$, and it has a periodic behavior for $y_c > A\pi$. Thus to make the equation of the upper surface of the body single valued, we restrict $y_c \in [0, A\pi)$. We note from (F.8) that far downstream, $x_c \longrightarrow \infty$, $y_c \longrightarrow A\pi$, so the asymptotic thickness of the body as $x_c \longrightarrow \infty$ is $2A\pi$.

To find the form of the slip velocity on the surface of the Rankine body, we substitute

(F.9) into (F.6). Hence we find that

$$\begin{aligned} U_f &= |u - iv|, \\ &= \left| \frac{x_c + iy_c}{(x_c - A) + iy_c} \right|, \\ &= \left(\frac{x_c^2 + y_c^2}{(x_c - A)^2 + y_c^2} \right)^{\frac{1}{2}}, \\ &= \left(1 + \frac{A^2}{y_c^2} \sin^2 \left(\frac{y_c}{A} \right) - \frac{A}{y_c} \sin \left(\frac{2y_c}{A} \right) \right)^{\frac{1}{2}}, \end{aligned} \tag{F.10}$$

and we note that the slip velocity is parameterised by the parameter y_c. In the formulation of the main governing equations, we introduced the variable ξ in (2.33) as a variable along the surface of the body. We defined ξ as the integral of the slip velocity along the body from the leading edge, to a point x, where x is also measured along to body. In this case, the slip velocity is only known in terms of the Cartesian parameter y_c, hence by a change of variables, we can define

$$\xi = \int_0^{y_c} U_f(y_c') \frac{dx}{dy_c}(y_c') dy_c', \tag{F.11}$$

where

$$\frac{dx}{dy_c} = \left(1 + \left(\frac{dx_c}{dy_c} \right)^2 \right)^{\frac{1}{2}} = \left(1 + \left(-\cot \left(\frac{y_c}{A} \right) + \frac{y_c}{A} \mathrm{cosec}^2 \left(\frac{y_c}{A} \right) \right)^2 \right)^{\frac{1}{2}}. \tag{F.12}$$

From these definitions, we can then see that the functions $\beta(\xi)$ and $\Omega(\xi)$ defined in (2.36) and (2.38) are also functions of y_c.

F.1 Introduction of scaled variables

As in chapter 5, we can introduce scaled variables so that we remove the dependence on A from the equation of the body and the slip velocity. Here we define the scaled variables $\hat{z} = z/A$ and $\hat{w} = w/A$. Thus introducing these and following the analysis through from the above section, we find that the equation of the body's upper surface is given by

$$\hat{x}_c = 1 - \hat{y}_c \cot(\hat{y}_c - \hat{c}_i), \tag{F.13}$$

where $\hat{c}_i$ is a constant which corresponds to the streamlines of the flow and the streamline for which $\hat{c}_i = \pi$ corresponds to the surface of the body. Under these new variables, the components of velocity become

$$\begin{aligned} \hat{u} - i\hat{v} &= \frac{d\hat{w}}{d\hat{z}} = \frac{1}{A}\frac{dz}{d\hat{z}}\frac{dw}{dz} = u - iv, \\ &= 1 + \frac{1}{\hat{z} - 1}. \end{aligned} \tag{F.14}$$

The streamlines for flow past a Rankine body in these scaled variables is shown in figure F.1. We note that the streamlines external to the body are given by $\hat{c}_i > \pi$ in the upper half plane, and $\hat{c}_i < -\pi$ in the lower half plane.

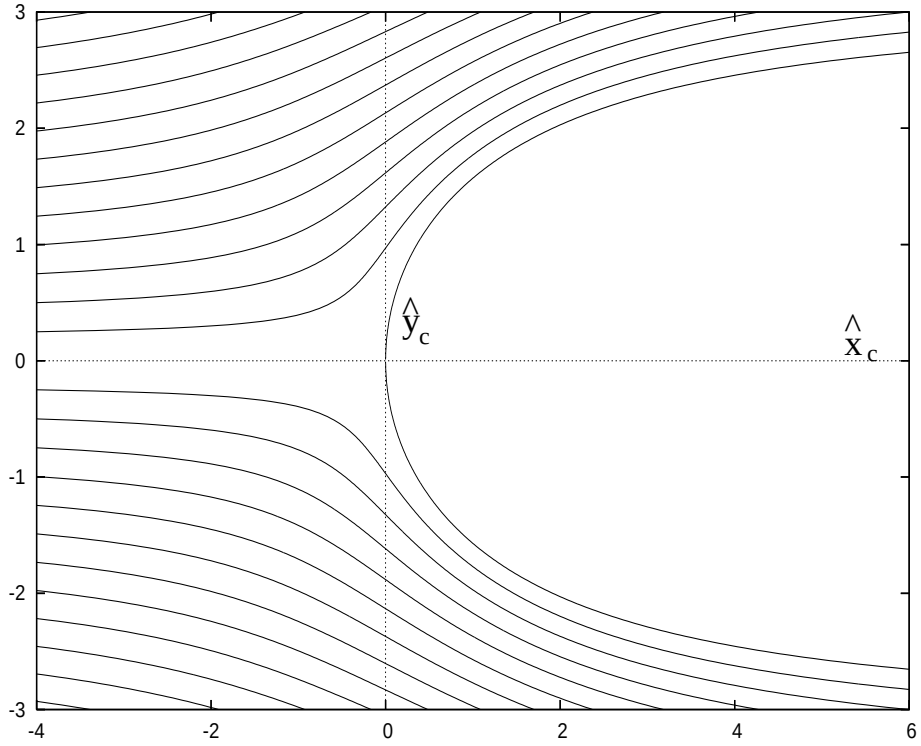

Figure F.1: Figure showing the streamlines around a Rankine body in the $(\hat{x}_c, \hat{y}_c)$ plane. Note that the streamline $\hat{c}_i = \pi$ denotes the surface of the Rankine body.

Under this change of variables, the slip velocity U_f and dx/dy_c become

$$U_f(\hat{y}_c) = \left(1 + \frac{\sin^2(\hat{y}_c)}{\hat{y}_c^2} - \frac{\sin(2\hat{y}_c)}{\hat{y}_c}\right)^{\frac{1}{2}}, \tag{F.15}$$

$$\frac{dx}{dy_c}(\hat{y}_c) = \left(1 + \left(-\cot(\hat{y}_c) + \hat{y}_c \mathrm{cosec}^2(\hat{y}_c)\right)^2\right)^{\frac{1}{2}}. \tag{F.16}$$

Thus we can actually remove the dependence on A from the pressure gradient $\beta(\xi)$ as we did for the parabolic body. This is achieved by introducing the variable $\hat{\xi} = \xi/A$, where

$$\hat{\xi} = \int_0^{\hat{y}_c} U_f(\hat{y}_c) \frac{dx}{dy_c}(\hat{y}_c) d\hat{y}_c, \tag{F.17}$$

then we see that

$$\beta(\xi) = \frac{2\xi}{U_f}\frac{dU_f}{d\xi} = \frac{2A\hat{\xi}}{U_f}\frac{d\hat{\xi}}{d\xi}\frac{dU_f}{d\hat{\xi}} = \beta(\hat{\xi}). \tag{F.18}$$

However, we can go further than this, by writing

$$\frac{dU_f}{d\hat{\xi}} = \frac{1}{U_f}\frac{d\hat{y}_c}{dx}\frac{dU_f}{d\hat{y}_c},$$

then we see that

$$\beta(\hat{y}_c) = \frac{2\hat{\xi}}{U_f^3}\frac{d\hat{y}_c}{dx}\left(\frac{\sin(2\hat{y}_c)}{\hat{y}_c^2} - \frac{\sin^2(\hat{y}_c)}{\hat{y}_c^3} - \frac{\cos(2\hat{y}_c)}{\hat{y}_c}\right). \tag{F.19}$$

References

Abramowitz, M. & Stegun, I. A. (1964). *Handbook of Mathematical Functions*. Dover.

Acheson, D. J. (1990). *Elementary Fluid Dynamics*. Oxford University Press.

Ackerberg, R. C. and Phillips, J. H. (1972). The unsteady laminar boundary layer on a semi-infinite flat plate due to small fluctuations in the magnitude of the free-stream velocity. *J. Fluid Mech.*, **51**, 137–157.

Andersson, P., Henningson, D. S., and Hanifi, A. (1998). On a stabilization procedure for the parabolic stability equations. *J. Engrg. Math.*, **33**(3), 311–332.

Anton, H. (1994). *Elementary Linear Algebra*. Wiley.

Bertolotti, F. P., Herbert, T., and Spalart, P. R. (1992). Linear and nonlinear stability of the Blasius boundary layer. *J. Fluid Mech*, **242**, 441–474.

Bodonyi, R. J., Welch, J. C., Duck, P. W., and Tadjfar, M. (1989). A numerical study of the interaction between unsteady free-stream disturbances and localized variations in surface geometry. *J. Fluid Mech.*, **209**, 285–308.

Bridges, T. J. and Morris, P. J. (1984). Differential eigenvalue problems in which the parameter appears nonlinearly. *J. Comput. Phys.*, **55**(3), 437–460.

Bridges, T. J. and Vaserstein, L. N. (1986). The local evaluation of the derivative of a determinant. *J. Comput. Phys.*, **65**(1), 107–119.

Brown, S. N. and Stewartson, K. (1973). On the propagation of disturbances in a laminar boundary layer. *Proc. Camb. phil. Soc*, **73**, 493–514.

Buckingham, R. J. (2004). Receptivity of Boundary-Layers to Vortical Disturbances. *PhD Thesis, University of East Anglia, Norwich, United Kingdom*.

Cebeci, T. and Cousteix, J. (2005). *Modeling and Computation of Boundary-Layer Flows: Laminar, Turbulent and Transitional Boundary Layers in Incompressible and Compressible Flows*. Springer.

Choudhari, M. and Streett, C. (1992). A finite Reynolds number approach for the prediction of boundary-layer receptivity in localized regions. *Phys. Fluids A*, **4:2**, 495–514.

Collis, S. S. and Dobrinsky, A. (1999). Evaluation of adjoint based methods for the prediction of linear and nonlinear receptivity. *Proceedings of the 5th IUTAM Symposium on Laminar-Turbulent Transition*, Springer.

Crouch, J. D. (1992). Non-localized receptivity of boundary layers. *J. Fluid Mech.*, **244**, 567–581.

Crouch, J. D. & Spalart, P. R. (1995). Study of non-parallel and nonlinear effects on the localized receptivity of boundary layers. *J. Fluid Mech.*, **290**, 29–37.

Dobrinsky, A. and Collis, S. S. (2000). Adjoint methods for receptivity prediction in nonparallel flows. *Submitted to Phys. of Fluids*.

Erturk, E. and Corke, T. C. (2001). Boundary layer receptivity to sound at incident angles. *J. Fluid Mech.*, **444**, 383–407.

Erturk, E., Haddad, O. M., and Corke, T. C. (2004). Laminar incompressible flow past parabolic bodies at angles of Attack. *AIAA Journal*, **42**(11), 2254–2265.

Fuciarelli, D. A., Reed, H. L., and Lyttle, I. (1998). DNS of leading-edge receptivity to sound. *AIAA Paper* 98-2644.

Gaster, M. (1974). On the effects of boundary-layer growth on flow stability. *J. Fluid Mech.*, **66**, 465–480.

Giannetti, F. (2002). Boundary Layer Receptivity. *PhD Thesis, University of Cambridge, Cambridge, United Kingdom*.

Goldstein, M. E. (1982). Generation of Tollmien-Schlichting waves by free-stream disturbances at low Mach numbers. *NASA TM 83026*.

Goldstein, M. E. (1983). The evolution of Tollmien-Schlichting waves near a leading edge. *J. Fluid Mech.*, **127**, 59–81.

Goldstein, M. E. (1985). Scattering of acoustic waves into Tollmien-Schlichting waves by small streamwise variations in surface geometry. *J. Fluid Mech.*, **154**, 509–529.

Goldstein, M. E. and Hultgren, L. S. (1987). A note on the generation of Tollmien-Schlichting waves by sudden surface-curvature change. *J. Fluid Mech.*, **181**, 519–525.

Goldstein, M. E. and Hultgren, L. S. (1989). Boundary-layer receptivity to long-wave free-stream disturbances. *Annu. Rev. Fluid Mech.*, **21**, 137–166.

Goldstein, M. E., Sockol, P. M., and Sanz, J. (1983). The evolution of Tollmien-Schlichting waves near a leading edge. Part 2. Numerical determination of amplitudes. *J. Fluid Mech.*, **129**, 443–453.

Goldstein, M. E., Leib, S. J., and Cowley, S. J. (1992). Distortion of a flat-plate boundary layer by free-stream vorticity normal to the plate. *J. Fluid Mech.*, **237**, 231–260.

Haddad, O. M. and Corke, T. C. (1998). Boundary layer receptivity to free-stream sound on parabolic bodies. *J. Fluid Mech.*, **368**, 1–26.

Haddad, O. M., Erturk, E., and Corke, T. C. (2005). Acoustic receptivity of the boundary layer over parabolic bodies at angles of attack. *J. Fluid Mech.*, **536**, 377–400.

Hammerton, P. W. (1999). Comparison of Lam-Rott and Brown-Stewartson eigensolutions of the boundary-layer equations. *Quart. J. Mech. Appl. Math.*, **52**(3), 373–385.

Hammerton, P. W. and Kerschen, E. J. (1996). Boundary-layer receptivity for a parabolic leading edge. *J. Fluid Mech.*, **310**, 243–267.

Hammerton, P. W. and Kerschen, E. J. (1997). Boundary-layer receptivity for a parabolic leading edge. Part 2. The small-Strouhal-number limit. *J. Fluid Mech.*, **353**, 205–220.

Hammerton, P. W. and Kerschen, E. J. (2005). Leading-edge receptivity for bodies with mean aerodynamic loading. *J. Fluid Mech.*, **535**, 1–32.

Herbert, T. (1993). Parabolized Stability Equations. *AGARD Rep.*, 4-1 to 4-34.

Herbert, T. (1997). Parabolized Stability Equations. *Annu. Rev. Fluid Mech.*, **29**, 245–283.

Hill, D. C. (1995). Adjoint systems and their role in the receptivity problem for boundary layers. *J. Fluid Mech.*, **292**, 183–204.

Hill, D. C. (1997). Receptivity in non-parallel boundary layers. *Proceedings of the 1997 ASME Fluids Engineering Division Summer Meeting*, FEDSM97-3108.

Itoh, N. (1974a). A power series method for the numerical treatment of the Orr-Sommerfeld equation. *Trans. Japan Soc. Aero. Space Sci*, **17**, 65–75.

Itoh, N. (1974b). Spatial growth of finite wave disturbances in parallel and nearly parallel flows. Part 2. The numerical results for the flat plate boundary layer. *Trans. Japan Soc. Aero. Space Sci*, **17**, 175–186.

Itoh, N. (1986). The origin and subsequent development in space of Tollmien-Schlichting waves in a boundary layer. *Fluid Dyn. Res.*, **1**, 119–130.

Kachanov, Y. S. (1994). Physical mechanisms of laminar-boundary-layer transition. *Annu. Rev. Fluid Mech.*, **26**, 411–482.

Klebanoff, P. S., Tidstrom, K. D., and Sargent, L. M. (1962). The three-dimensional nature of boundary-layer instability. *J. Fluid Mech.*, **12**, 1–34.

Lam, S. H. and Rott, N. (1960). Theory of linearized time-dependent boundary layers. *Cornell University GSAE Rep. AFOSR*, pages TN–60–1100.

Lam, S. H. and Rott, N. (1993). Eigen-functions of linearized unsteady boundary layer equations. *Journal of Fluids Engineering*, **115**, 597–602.

Leehey, P. and Shapiro, P. J. (1980). Leading edge effect in laminar boundary layer excited by sound, *Laminar-Turbulent Transition*. Springer.

Li, F. and Malik, M. R. (1994). Mathematical nature of Parabolized Stability Equations, *Laminar-Turbulent Transition. Proc. 4th IUTAM Symposium Sendai/Japan*. Springer, 205-212.

Li, F. and Malik, M. R. (1996). On the nature of the PSE approximation. *Theor. Comp. Fluid Dyn.*, **8**, 253–273.

Li, F. and Malik, M. R. (1997). Spectral analysis of Parabolized Stability Equations. *Computers and Fluids*, **26**(3), 279–297.

Libby, P. A. and Fox, H. (1963). Some perturbation solutions in laminar boundary-layer theory. Part 1. The momentum equation. *J. Fluid Mech.*, **17**, 433–449.

Lighthill, M. J. (1954). The response of laminar skin friction and heat transfer to fluctuations in the stream velocity. *Proc. Roy. Soc. London. Ser. A.*, **224**, 1–23.

Lin, N., Read, H. L., and Saric, W. S. (1992). Effect of leading-edge geometry on boundary-layer receptivity to free-stream sound, *Instability, Transition and Turbulence.* Berlin: Springer, 421-440.

Luchini, P. and Bottaro, A. (1998). Görtler vortices: a backward-in-time approach to the receptivity problem. *J. Fluid Mech.*, **363**, 1–23.

Miles, J. W. (1962). A note on the inviscid Orr-Sommerfeld equation. *J. Fluid Mech.*, **13**, 427–432.

Morkovin, M. V. (1969). On the many faces of transition. In *Viscous Drag Reduction*, ed. C. S. Wells. New York: Plenum.

Morkovin, M. V. (1985). *Guide to experiments on instability and laminar-turbulent transition in shear layers*. Cincinnati, Ohio.

Murdock, J. W. (1980). The generation of a Tollmien-Schlichting wave by a sound wave. *Proc. Roy. Soc. London. Ser. A.*, **372**, 517–534.

Nayfeh, A. H. (1973). *Perturbation Methods*. Wiley, New york.

Nayfeh, A. H. and Ashour, O. N. (1994). Acoustic receptivity of a boundary layer to Tollmien-Schlichting waves resulting from a finite-height hump at finite Reynolds numbers. *Phys. Fluids*, **6**, 3705–3716.

Nichols, D. E. (2001). Boundary Layer Receptivity of a Flat Plate with a Rounded Leading Edge. *PhD Thesis, University of East Anglia, Norwich, United Kingdom.*

Nishioka, M. and Morkovin, M. V. (1986). Boundary-layer receptivity to unsteady pressure gradients: experiments and overview. *J. Fluid Mech.*, **171**, 219–261.

Noble, B. (1958). *Methods Based on Wiener-Hopf Technique*. Pergamon.

Orszag, S. A. (1971). Accurate solution of the Orr-Sommerfeld equation. *J. Fluid Mech.*, **50**, 689–703.

Polykov, N. F. (1973a). Aerophysical research, issue 2. *Sb. nauch. trudov* [Collected Scientific Works] p88. *Institute of Theoretical and Applied Mechanics, Siberian Section USSR Academy of Sciences, Novosibirsk.*

Polykov, N. F. (1973b). Method of study of flow characteristics in low turbulence wind tunnel and transition phenomena in an incompressible boundary layer. *Candidate's dissertation, Institute of Theoretical and Applied Mechanics, Siberian Section USSR Academy of Sciences, Novosibirsk*.

Reed, H. L. (1994). Direct numerical simulation of transition: the spatial approach. *Progress in Transition Modelling, AGARD report 793.* Paris: NATO, 6.1-46.

Reed, H. L., Lin, N., and Saric, W. S. (1990). Boundary layer receptivity to sound: Navier-Stokes computations. *Appl. Mech. Rev.*, **43**(5), S175–S180.

Reshotko, E. (1976). Boundary-layer stability and transition. *Annu. Rev. Fluid Mech.*, **8**, 311–349.

Reynolds, O. (1883). An experimental investigation of the circumstances which determine whether the motion of water shall be direct or sinuous, and of the law of resistance in parallel channels. *Phil. Trans. Roy. Soc. Lond. A*, **186**, 123–164.

Rivlin, T. J. (1974). *The Chebyshev Polynomials*. Wiley.

Rosenhead (1963). *Laminar Boundary Layers. An account of the development, structure and stability of laminar boundary layers in incompressible fluids, together with a description of the associated experimental techniques*. Clarendon Press, Oxford.

Ross, J. A., Barnes, F. H., Burns, J. G., and Ross, M. A. S. (1970). The flat plate boundary layer. Part 3. Comparison of theory with experiment. *J. Fluid Mech.*, **43**, 819–832.

Salwen, H. and Grosch, C. E. (1981). The continuous spectrum of the Orr-Sommerfeld equation. Part 2. Eigenfunction expansions. *J. Fluid Mech.*, **104**, 445–465.

Saric, W. and Nayfeh, A. (1975). Nonparallel stability of boundary-layer flows. *Phys. Fluids*, **18**, 945–950.

Saric, W. and Nayfeh, A. (1977). Nonparallel stability of boundary layers with pressure gradients and suction. *AGARD CP-224*, 6/1-21.

Saric, W. S. and Rasmussen, B. K. (1992). Boundary layer receptivity: Freestream sound on an elliptic leading edge. *Bull. Am. Phys. Soc.*, **37**, 1720.

Saric, W. S. and White, E. B. (1998). Influence of high-amplitude noise on boundary-layer transition to turbulence. *AIAA Paper* 98-2645.

Saric, W. S., Reed, H. L., and Kerschen, E. J. (1994). Leading edge receptivity to sound: experiments, DNS, and theory. *AIAA Paper* 94-2222.

Saric, W. S., Wei, W., and Rasmussen, B. K. (1995). Effect of leading-edge on sound receptivity. *Laminar-Turbulent Transition, (IUTAM Sendai, 1994, ed. R. Kobayashi)*, Springer, 413-420.

Saric, W. S., Reed, H. L., and Kerschen, E. J. (2002). Boundary-layer receptivity to freestream disturbances. *Annu. Rev. Fluid Mech.*, **34**, 291–319.

Schensted, I. V. (1960). Contributions to the theory of hydrodynamic stability. *PhD dissertation, University of Michigan*.

Schmid, P. J. and Henningson, D. S. (2001). *Stability and Transition in Shear Flows*. Springer.

Schubauer, G. B. and Skramstad, H. F. (1947). Laminar boundary layer oscillations and the stability of laminar flow. *J. Aero. Sci.*, **14**, 69–78.

Sedov, L. I. (1965). *Two-Dimensional Problems in Hydrodynamics and Aerodynamics*. Interscience Publishers.

Shapiro, P. J. (1977). The influence of sound upon laminar boundary layer instability. *MIT Acoustics and Vibration Lab Rep. 83458-83560-1*.

Smith, F. T. (1979). On the non-parallel flow stability of the Blasius boundary layer. *Proc. Roy. Soc. London. Ser. A.*, **366**, 91–109.

Stewartson, K. (1957). On asymptotic expansion in the theory of boundary layers. *J. Math. Phys.*, **36**, 173–191.

Stewartson, K., Smith, F. T., and Kaups, K. (1982). Marginal separation. *Stud. Appl. Maths*, **67**, 45–61.

Thwaites, B. (1964). *Incompressible Aerodynamics*. Oxford.

Turner, M. R. (2006). Far downstream analysis for the Blasius boundary-layer stability problem. *In preparation*.

Turner, M. R. and Hammerton, P. W. (2006). Asymptotic receptivity analysis and the Parabolized Stability Equation : a combined approach to boundary layer transition. *Accepted by J. Fluid Mech.*

Van Dyke, M. (1964a). Higher approximations in boundary-layer theory. Part 3. Parabola in uniform stream. *J. Fluid Mech.*, **19**, 145–159.

Van Dyke, M. (1964b). *Perturbation Methods in Fluid Mechanics*. Academic Press.

Vorob'Yev, N. F., Polykov, N. F., Shashkina, G. N., and Shcherbakov, V. A. (1976). Physical gasdynamics. *Sb. nauch. trudov* [Collected Scientific Works] p101. *Institute of Theoretical and Applied Mechanics, Siberian Section USSR Academy of Sciences, Novosibirsk*.

Wanderley, J. B. V. and Corke, T. C. (2001). Boundary layer receptivity to free-stream sound on elliptic edges of flat plates. *J. Fluid Mech.*, **429**, 1–21.

Zhigulev, V. N. and Fedorov, A. V. (1987). Boundary-layer receptivity to acoustic disturbances. *J. of Appl. Mech. Tech. Phy.*, **28**, 28–34.